
**Infrared Spectroscopy of Water bearing
interstellar Ice Analogues**
From molecular Oxygen to the Structure of Ice Mantles

Birgitta Luise Maria Müller



München 2022

**Infrared Spectroscopy of Water bearing
interstellar Ice Analogues**
From molecular Oxygen to the Structure of Ice Mantles

Birgitta Luise Maria Müller

Dissertation
der Fakultät für Physik
der Ludwig-Maximilians-Universität
München

vorgelegt von
Birgitta Luise Maria Müller
aus Vilsbiburg, Deutschland

München, den 10. Januar 2022

Erstgutachter: Prof. Dr. Paola Caselli

Zweitgutachter: Prof. Dr. Barbara Ercolano

Tag der mündlichen Prüfung: 10. Februar 2022

*To my father, who taught me to be patient and persistent.
To my mother, who taught me to appreciate all facets of hard work.
To my sister, who taught me to take care of the people I love.*

*Für meinen Vater, der mich gelehrt hat, geduldig und ausdauernd zu sein.
Für meine Mutter, die mich gelehrt hat, harte Arbeit in allen Facetten zu wertschätzen.
Für meine Schwester, die mich gelehrt hat, auf die Menschen, die ich liebe, Acht zu geben.*

Contents

Zusammenfassung	xiii
Abstract	xv
1 Introduction	1
1.1 Formation of low-mass stars	1
1.1.1 Molecular clouds in gas phase	7
1.1.2 Taurus-Auriga and L1544	10
1.2 Astrochemical Network of interstellar Ices	11
1.2.1 Physical processes	12
1.2.2 The interplay of gaseous and solid phases	15
1.2.3 Ice chemistry	18
1.3 Spectroscopic studies	20
1.3.1 Closed-cycle He Cryostat	21
1.3.2 Fourier Transform Infrared Spectrometer	23
1.3.3 THz time-domain Spectrometer	27
1.3.4 Gas-line System	29
1.4 This Thesis	31
1.5 Bibliography	31
2 O₂ signature in thin and thick O₂-H₂O ices	33
2.1 Abstract	33
2.2 Introduction	33
2.3 Methods	36
2.4 Results	39
2.4.1 O ₂ features in thin and thick ice samples	39
2.4.2 Dangling bonds	43
2.5 Discussion	46
2.6 Astrophysical implications	48
2.6.1 Chemical modelling	48
2.6.2 Astronomical observability	50
2.7 Conclusions	52

3	Spectroscopy of CH₃OH in layered and mixed ices	55
3.1	Abstract	55
3.2	Introduction	56
3.3	Experimental methods	58
3.3.1	Cryogenic set-up	58
3.3.2	Ice preparation	58
3.4	Results	59
3.4.1	Water and methanol	59
3.4.2	Water, methanol, and CO	62
3.4.3	Water, CO ₂ , CO, and methanol	63
3.4.4	Warm-up	63
3.4.5	Inverse deposition	67
3.5	Discussion and comparison with previous work	69
3.6	Conclusions	72
4	Laboratory spectroscopy of theoretical pre-stellar core ices	75
4.1	Abstract	75
4.2	Introduction	76
4.3	Model description and theoretical predictions	77
4.4	Experimental methods	78
4.4.1	Preparation of the pre-stellar icy mantle analogues	78
4.5	Results	82
4.5.1	Layered and mixed ices	82
4.5.2	N ₂ and O ₂	86
4.6	Discussion	87
4.6.1	Comparison with previous work	87
4.6.2	Ice feature observability with JWST	89
4.7	Conclusion	94
5	Direct measurement of the complex refractive index of CO ice using THz TDS	95
5.1	Abstract	95
5.2	Introduction	96
5.3	Experimental and theoretical methods	97
5.3.1	Cryogenic set-up	98
5.3.2	Terahertz time-domain spectrometer	98
5.3.3	Ice preparation	100
5.4	Derivation of the optical constants	102
5.4.1	Ice parameters modelling	103
5.4.2	Laser interference technique	105
5.4.3	Reconstruction of the THz response	107
5.5	Discussion	107
5.6	Conclusions	113

6	Conclusion	115
6.1	Summary	115
6.2	Future work	117
6.2.1	Raman Microscope	118
A	Complementary Material for Chapter 4	123
A.1	Layered ice - Comparison of measurements and computational addition	123
B	Complementary Material for Chapter 5	125
B.1	THz-TDS optics	125
B.2	Reconstruction of the terahertz dielectric permittivity	126
B.3	Opacity model benchmark	130
B.3.1	Dielectric constants	130
B.3.2	Absorption coefficients	131
B.3.3	Opacities	131
	Acknowledgments	142
	Danksagung	145

List of Figures

1.1	HI gas all-sky column density map of from EBHIS and GASS data	2
1.2	Observation of the J = 1 - 0 CO transition mapped in the whole Milky Way	5
1.3	The various stages of low-mass star formation from dense cores to a planetary system	6
1.4	The Milky Way in the visible light obscured by dark clouds	7
1.5	Selective and total extinction as a function of λ^{-1} with the prominent local maximum at $4.6 \mu\text{m}^{-1}$ (2175 \AA)	8
1.6	CO 2.6 mm line map of Taurus-Auriga	11
1.7	The closed-cycle He cryostat: complete as well as close view on the sample holder and the radiation shield	21
1.8	Transmission of KBr with a thickness of 2 mm and of HRFZ-Si with a thickness of 5 mm	22
1.9	Sketch of the cooling chamber arrangement for the FTIR spectrometer and the THz TDS	24
1.10	Sketch of the complete movable rack system, enabling the coupling of the cryocooler either with the FTIR spectrometer or with the THz TDS	25
1.11	Schematic arrangement of a Michelson interferometer with a chemical probe in front of the detector	25
1.12	Complete view on the Fourier Transform Infrared Spectrometer	27
1.13	View on the THz time-domain spectrometer with the integrated cooling chamber	28
1.14	The gas-line system: complete view and sketch of the gas-line components	30
2.1	Sketch of the cryocooler set-up.	37
2.2	Spectra of all H ₂ O-O ₂ composition ratios for thick ice with same deposition time of 1 min each	40
2.3	Magnification of spectra of Fig. 2.2 around the O ₂ feature for all H ₂ O-O ₂ mixtures for thick ice	41
2.4	Magnified spectra of H ₂ O:O ₂ = 2:1 mixture around the O ₂ feature; the ice thicknesses is between 0.022 and 0.053 μm for thin ice.	42
2.5	Magnified spectra of H ₂ O:O ₂ = 2:1 mixture around the O ₂ feature; the thicknesses is between 0.008 and 0.022 μm for thin ice.	43
2.6	Thick-ice absorption spectrum of H ₂ O:O ₂ mixtures compared to pure water	45

2.7	Behaviour of the O ₂ feature for H ₂ O:O ₂ = 2:1 while heating the ice from 10 K to 50 K	47
2.8	Model ice thickness (in monolayers) vs. time in L1544. The ‘methanol peak’ is located 4000 AU away from the core centre.	49
2.9	Absorption coefficients of the 3280 cm ⁻¹ , 2200 cm ⁻¹ , 1660 cm ⁻¹ , 760 cm ⁻¹ water and 1551 cm ⁻¹ O ₂ bands for the different mixture ratios of O ₂ and H ₂ O	51
2.10	Calculated O ₂ /H ₂ O of L1544 as a function of the radial distance for t = 1.6 × 10 ⁵ yr.	52
3.1	Spectra of pure methanol and water ices, CH ₃ OH on top of H ₂ O ice layers (CH ₃ OH/H ₂ O) and H ₂ O-CH ₃ OH mixture (CH ₃ OH:H ₂ O)	61
3.2	Spectra of pure methanol ice layered on top of water ice compared with CH ₃ OH:CO ice layered on top of water ice	62
3.3	Spectra of methanol in CO mixture with varying relative abundances layered on top of water ice	64
3.4	Spectra of pure methanol and water ices compared with CH ₃ OH:CO ice layered on top of CO ₂ :H ₂ O ice and a mixed CO ₂ :H ₂ O:CH ₃ OH:CO ice	65
3.5	Heating of methanol layered on top of water ice and mixed CH ₃ OH:H ₂ O ice	66
3.6	Heating of CH ₃ OH:CO/H ₂ O ices	67
3.7	Heating of CH ₃ OH:CO layered on top of CO ₂ :H ₂ O ice and mixed CH ₃ OH:CO:CO ₂ :H ₂ O ice	68
3.8	OH dangling bonds in pure methanol and water ices compared with CH ₃ OH:CO ice layered on top of CO ₂ :H ₂ O ice and a mixed CO ₂ :H ₂ O:CH ₃ OH:CO ice	73
4.1	Predicted molecular fractional abundances for each layer of an ice mantle in a region close to the dust peak	79
4.2	Spectra of mixed and layered ices with layer 1, layer 2 and layer 2 on top of layer 1	83
4.3	Zoomed-in spectra of mixed and layered ices with layer 1, layer 2 and layer 2 on top of layer 1	84
4.4	Zoomed-in spectra around the N ₂ and O ₂ bands of mixed and layered ices with layer 1, layer 2 and layer 2 on top of layer 1	86
5.1	Sketch of the vacuum chamber of the cryostat coupled to the THz beam at the CAS	99
5.2	A schematic of the THz-TDS set-up and spectra of THz waveforms	101
5.3	Time-distance diagram illustrating the THz wave propagation through the HRFZ-Si substrate with ice films deposited on its surface	104
5.4	Time delays between the THz pulses and estimates for the thicknesses of the two ice films	106
5.5	Reference and sample waveforms and their corresponding Fourier spectra	108
5.6	Real and imaginary parts of the complex refractive index and dielectric permittivity	109
5.7	Calculated and reference opacities of astrophysical dust with CO ice and ice mixtures	112
6.1	Structure of CO ice after fast deposition	118

6.2	Anti-Stokes lines for residue material produced in an UV irradiation experiment of a $\text{CH}_4:\text{N}_1 = 1:8$ mixture.	119
6.3	The Raman microscope. Complete view and illustration of the combined Raman microscope and customized cryostat	120
6.4	Raman mapping of a $\text{CH}_4:\text{N}_2 = 1:8$ irradiation residue and CO ice structure after fast and slow deposition	122
A.1	Comparison of experimentally and computationally added layered ices	124

List of Tables

1.1	Reactants that destroy H_2D^+ their associated products and observed deuterium fractions in L1544	20
1.2	Selection of spectral regions for various molecular vibrations of interest	26
2.1	Gas mixture composition, expressed as partial pressure ratio, the water column density ($N_{\text{H}_2\text{O}}$), the water ice thickness $d_{\text{H}_2\text{O}}$ and O_2 column density (N_{O_2}) after a total deposition time of 1 min for thick ice for each experiment presented in this paper. The uncertainty for $N_{\text{H}_2\text{O}}$ and $d_{\text{H}_2\text{O}}$ lie within 20-30 %.	39
2.2	Band strength of O_2 for the different O_2 - H_2O ice compositions	44
2.3	Gas mixture composition and position of the dangling bonds (with shoulder feature position where present) for each experiment presented in this paper.	44
2.4	Optical depth and transmittance of the modelled L1544 in the area with $\text{O}_2/\text{H}_2\text{O} > 10^{-6}$	51
3.1	List of experiments performed in the present work	60
3.2	Peak wave number (cm^{-1}) of the 3.54 and 9.75 μm methanol bands in the experiments presented in the paper, recorded at 10 K	70
3.3	Peak wave number (cm^{-1}) of the 3.54 and 9.75 μm methanol bands in the experiments presented in the paper, during warm-up	72
4.1	Average fraction of molecules in the ice mantles based on the presented model . .	80
4.2	Ice composition during the experiments compared to predicted ratios based on the model	81
4.3	Position of all observed molecular bands in the experiments presented in the paper, recorded at 10 K	88
4.4	Optical depth and transmittance of the modelled ice features in L1544	91
4.5	Full width half maximum, line strength S , observation time and signal-to-noise ratio S/N of the bands included in the JWST exposure time calculator.	93
5.1	Opacities calculated at selected wavelengths and parameters of the fitting function	111

Zusammenfassung

Seit langem fragt sich die Menschheit, wie Sterne, Planeten und – im besonderen Fall unseres Sonnensystems – das Leben entstanden ist. Zahlreiche Forschungsgruppen haben dieses Thema behandelt, aber auch wenn wir ein gutes Grundwissen über die Entwicklung von Planetensystemen erlangt haben, gibt es immer noch viele offene Fragen, die für die Verbindung der unterschiedlichen Stadien der Sternentstehung wichtig sind. Weltweit untersuchen Wissenschaftler diese offenen Probleme mithilfe von Beobachtungen, Modellen und Studien im Labor. In dieser Arbeit präsentiere ich meine Forschung an der Chemie von Eis in Molekülwolken, prästellaren Kernen und Nachbarregionen von Protosternen, welche ich durch die Nutzung der Vorteile von Infrarot (IR)-Spektroskopie und THz Zeitdomäne-Spektroskopie (eng. "time-domain spectroscopy"; TDS) erhalten habe. Die vorgelegte experimentelle Arbeit basiert auf astronomischen Beobachtungen und theoretischen Vorhersagen und verbindet die drei Forschungsmethoden in einem großen Kreis der Einheit.

Im ersten Teil dieser Arbeit präsentiere ich die Stärke des Absorptionsbands von molekularem Sauerstoff in interstellaren Eisanaloga, wenn es in einer Wassermatrix mit variablen $O_2:H_2O$ -Verhältnissen gebettet ist. Ich habe die erhaltenen Daten verwendet, um die Beobachtbarkeit von O_2 in Eismänteln am Beispiel des vor kurzem erfolgreich gestarteten James-Webb-Weltraumteleskops (eng. "James Webb Space Telescope"; JWST) einzuschätzen. Wenn O_2 – in seiner reinen Form IR inaktiv – in einer polaren Umgebung, wie etwa H_2O , platziert wird, kann das Wirtsmolekül ein Dipolmoment auf das homonukleare diatomische Molekül übertragen, welches dann als schwaches Absorptionsband sichtbar wird. Ich zeige, wie die steigende Stärke des O_2 -Absorptionsbands vom $O_2:H_2O$ -Mischverhältnis abhängig ist und ich berechne die notwendige Beobachtungsdauer mit JWST basierend auf der modellierten Häufigkeit von O_2 im Innern des prästellaren Kerns L1544.

Die Struktur von Eismänteln ist Thema im zweiten Teil dieser Arbeit. Basierend auf Beobachtungen von Methanol (CH_3OH) im Serpens Sternentstehungsgebiet niedriger Masse und im prästellaren Kern L1544, welche auf eine geschichtete Morphologie des Eises hinweisen, habe ich einen Satz an Experimenten verwendet, um den Effekt von geschichteten oder gemischten Kompositionen der Eisanaloga auf die spektralen Merkmale zu untersuchen. Mit einer steigenden Komplexität der Proben, die sich der reichen Vielfalt von interstellarem Eis annähert, habe ich die Unterschiede in Gestalt und Position der CH_3OH Absorptionsbänder analysiert. CH_3OH wurde in verschiedenen Konfigurationen von Eisanaloga, welche eine oder mehrere Stoffe aus dem Angebot von H_2O , CO und CO_2 enthalten, aufgetragen. Während der Untersuchung der aufgenommenen Daten fand ich, dass geschichtete oder gemischte Strukturen des Eises in Form

von Bandverschiebungen und Änderungen im Bandprofil unterscheidbar sind. Diese Veränderungen können sogar einen Hinweis auf die Temperatur des interstellaren Eises geben und mit spektralen Auflösungen, wie sie von JWST bereitgestellt werden, werden dessen Instrumente geeignet sein, um selbst die kleinsten während der Experimente beobachteten Verschiebungen zu detektieren.

Während ich die Motivation der ersten beiden Projekte kombinierte, verwendete ich ein chemisches Modell von L1544, um Experimente mit den theoretisch häufigsten Molekülen sowie, in ihrer reinen Form, infrarot-inaktiven Molekülen durchzuführen. Zu diesem Zweck wurden H_2O , CH_3OH , CO , O_2 und N_2 in geschichteten und gemischten Konstellationen untersucht. Viele der untersuchten Bänder stellen Informationen über molekulare Interaktionen, die entweder von der gleichzeitigen Anwesenheit mehrerer Stoffe oder dem Mischverhältnis der Moleküle abhängig sind, bereit. Daher bieten meine experimentellen Beobachtungen verwendbare Hinweise auf die strukturelle Natur von interstellaren Eismänteln in L1544. Ich treffe außerdem Vorhersagen über die Beobachtungsdauer der schwachen O_2 - und N_2 -Bänder und zeige, dass die Detektion von molekularem Stickstoff durchführbar ist, während dies für molekularen Sauerstoff nicht der Fall ist.

THz TDS ist ein leistungsfähiges Werkzeug zur direkten Messung optischer Konstanten. In Zusammenarbeit mit dem Prokhorov General Physics Institute habe ich einen Satz an Experimenten mit CO durchgeführt und Veränderungen in der Intensität und Phase von THz-Pulsen, die durch dicker werdende Eisschichten wandern, gemessen. Die aufgenommenen Daten wurden verwendet, um die Eisdicke zu bestimmen, sowie den komplexen Brechungsindex und die dielektrische Permittivität ohne die Nutzung der Kramers-Kronig-Beziehung zu rekonstruieren. Die Staub-Opazität wurde dann von den gemessenen Daten abgeleitet. Vergleiche mit theoretischen Berechnungen zeigen Unterschiede zwischen experimentellen und theoretischen Ergebnissen, was die Bedeutung von THz TDS-Messungen für die Interpretation der Emission im Staub-Kontinuum und des Strahlungstransports unterstreicht.

Zukünftige Arbeiten werden mehr Informationen über den Effekt von Molekülen wie CO oder CO_2 auf die Bandstärke von O_2 bereitstellen und die direkte Messung der optischen Konstanten verschiedener Moleküle wird ein fortlaufendes Projekt sein, das dabei helfen wird, die Emission und den Energietransfer in interstellaren Quellen zu verstehen. Auch werden Diffusionsprozesse untersucht, um physikalische und chemische Prozesse in der festen und gasförmigen Phase zu verbinden.

Abstract

For a long time, humankind has asked how stars, planets, and – in the particular case of our solar system – life has formed. Numerous research groups have addressed this topic, but even though we have acquired good basic knowledge on the formation of planetary systems, there are still many open issues that are important for connecting different stages of star formation. Scientists globally investigate these open problems through observational, theoretical, and laboratory work. In this thesis, I present my research on the ice chemistry of molecular clouds, pre-stellar cores, and neighbouring regions of protostars obtained by using the advantages of infrared (IR) spectroscopy and THz time-domain spectroscopy (TDS). The presented experimental work is based on astronomical observations and theoretical predictions, connecting the three research methods in a big circle of unity.

In the first part of this thesis, I present the absorption band strength of molecular oxygen in interstellar ice analogues when it is embedded in a water matrix with varying $O_2:H_2O$ ratios. I used the obtained data to estimate the observability of O_2 in ice mantles when using the recently successfully launched James Webb Space Telescope (JWST). Placing O_2 – in its pure form IR inactive – in a polar environment, such as H_2O , then the hosting molecule can induce a dipole moment onto the homonuclear diatomic molecule which becomes observable as a weak absorption band. I show how the increasing strength of the O_2 absorption band is dependent on the $O_2:H_2O$ mixing ratio and I calculate the required observing time with JWST based on modelled abundances of O_2 throughout the pre-stellar core L1544.

The structure of ice mantles is subject of the second part of this work. Based on methanol (CH_3OH) observations in the Serpens low-mass star-forming region and the pre-stellar core L1544 that hint to a layered morphology of the ice, I used a set of experiments to examine the effects of a layered or mixed composition of the ice analogues on the spectral features. For an increasing complexity of samples that approaches the actual rich diversity of interstellar ices, I analysed differences in shape and position of CH_3OH absorption bands. CH_3OH was deposited in different configurations of ice analogues containing one or several species from the pool of H_2O , CO and CO_2 . Studying the recorded data, I found that layered or mixed structures of the ices are distinguishable in form of band shifts and changes in the band profiles. These changes can even give a hint to the temperature of interstellar ices and with spectral resolutions such as provided by JWST, its instruments will be suitable to detect even the smallest shifts observed during the experiments.

Combining the motivation of the first two projects, I used a chemical model of L1544 to conduct experiments with the theoretically most abundant molecular species as well as with, in

their pure form, IR inactive molecules. For this purpose, H₂O, CH₃OH, CO, O₂ and N₂ have been examined for spectral differences. Many of the studied bands provide information on molecular interactions that are either dependent on the contemporaneous presence of multiple species or the mixing ratio of the molecules. Hence, my experimental observations offer valuable clues on the structural nature of interstellar ice mantles in L1544. Moreover, I make predictions on JWST observing times of the weak O₂ and N₂ bands and show that detection of molecular nitrogen is feasible while detection of molecular oxygen is not.

THz TDS is a powerful tool to directly measure optical constants. In collaboration with the Prokhorov General Physics Institute, I have conducted a set of experiments with CO and measured changes in intensity and phase of THz pulses propagating through increasingly thicker CO ices. The recorded data were used to determine the ice thicknesses as well as to reconstruct the complex refractive index and dielectric permittivity without using the Kramers-Kronig relations. Then, dust opacities were derived from the obtained data. Comparison with theoretical calculations show differences between experimental and theoretical results, underlining the importance of THz TDS measurements for the interpretation of dust continuum emission and radiative transfer.

Future work will provide more information on the effect of molecular species such as CO and CO₂ on the band strength of O₂ and the direct measurement of optical constants for various molecules will be an ongoing project helping to understand the emission and energy transfer in interstellar sources. Also, diffusion processes will be examined in order to connect physical and chemical processes in solid and gas phase.

Chapter 1

Introduction

*"For a star to be born, there is one thing that must happen: a gaseous nebula must collapse.
So collapse. Crumble. This is not your destruction. This is your birth."*

- Zoe Skylar

1.1 Formation of low-mass stars

Settled in the interstellar medium (ISM), the space between stars within a galaxy, formation of low-mass stars and their planets starts in diffuse clouds, regions consisting of gas and dust that are relatively transparent to radiation from external sources. As the dust fraction usually contributes only 1 % to the total cloud mass, the 99 % of gaseous content is characterized by a low visual extinction of $A_V = 1$ mag, densities of $n_{tot} = 50 - 100 \text{ cm}^{-3}$, average temperatures of $T = 80 \text{ K}$ and typical sizes of 1 - 100 pc. Hydrogen constitutes the major mass contingent of gas (70 %) in diffuse clouds and it is present in the form of neutral atoms (HI). The energy E of a hydrogen atom is given by:

$$E = \frac{m_e m_p}{m_e + m_p} \frac{e^4}{2\hbar^2 n^2} = 13.6 \text{ eV } n^{-2}, \quad (1.1)$$

where m_e and m_p are the masses of an electron and a proton, respectively, e is the elementary charge, \hbar the reduced Planck constant and n the principal quantum number. The distribution of HI is dictated by the vertical gravitational force of the disc midplane that causes cold, denser clouds to settle closer to the Galactic plane. The scale height of the cold neutral medium (CNM) can be derived from the balance of gravity and the internal pressure gradient:

$$-\frac{1}{\rho_{HI}} \nabla P_{HI} - \nabla \Phi_g = 0, \quad (1.2)$$

where ρ_{HI} is the HI mass density, P_{HI} the pressure density and Φ_g the Galactic gravitational potential. ρ_{HI} and P_{HI} are connected by the equation of state for an ideal isothermal gas with the random internal motion velocity c_{HI} (also called speed of sound when the temperature is fixed):

$$P_{HI} = \rho_{HI} c_{HI}^2. \quad (1.3)$$

With z being the scale height we can derive by use of the unit vector \hat{z} :

$$\frac{1}{\rho_{HI}} \frac{\partial P_{HI}}{\partial z} = -\frac{\partial \Phi_g}{\partial z}. \quad (1.4)$$

HI can be detected in the regime of long wavelengths via the 21.1 cm hyperfine doublet transition of the $n = 1$ ground state, as was first done by Ewen & Purcell (1951). Over the years many surveys have detected HI in the Milky Way (e.g. Dickey & Lockman 1990; Kalberla et al. 2005; HI4PI Collaboration: et al. 2016), as depicted in Figure 1.1. It was found that 80 % of HI within a scale height of 100 pc in the galactic plane is present in the form of diffuse clouds.

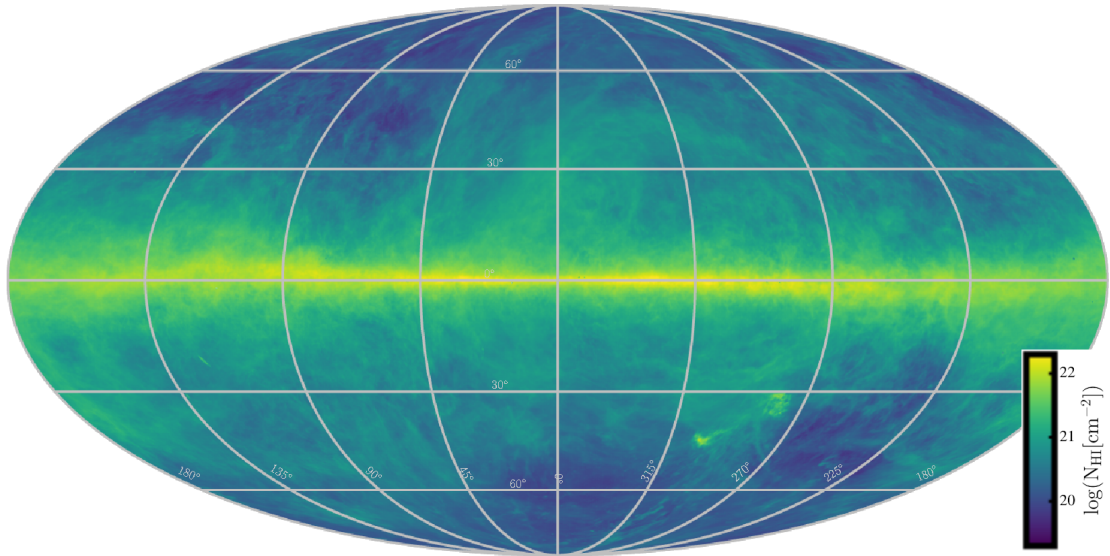


Figure 1.1: HI gas all-sky column density map of from the Effelsberg-Bonn HI Survey (EBHIS) and Galactic All-Sky Survey (GASS) data. Figure adapted from HI4PI Collaboration: et al. (2016).

When stars are present in the vicinity of gas clouds with low densities of 0.1 cm^{-3} , their emitted radiation can cause the ionization of hydrogen, denoted as HII. Warm regions of HII with temperatures of 10^4 K are traced, for example, with lines from the Balmer series of hydrogen, such as the most prominent $H\alpha$ line, with centimeter transition lines of even higher hydrogen levels or with dispersion of pulsar signals in the visible (VIS) and ultraviolet (UV) regime.

If the conditions are right, the internal pressure is overcome due to self-gravity at the next stage of star formation: the molecular cloud. Over the duration of 10^7 years molecular clouds can be stable due to an equilibrium of gravity as well as kinetic, thermal and magnetic pressure but they are still the sites where star formation is highly active. The temporal state of equilibrium can be expressed in terms of the virial theorem that takes all contributing quantities into account:

$$\frac{1}{2} \frac{\partial^2 I}{\partial t^2} = 2\mathcal{T} + 2U + \mathcal{W} + \mathcal{M}. \quad (1.5)$$

On the left hand side of the equation, I is the moment of inertia dependent on the spatial density distribution:

$$I \equiv \int \rho |\mathbf{r}|^2 d^3 \mathbf{x}. \quad (1.6)$$

and on the right hand side there is contribution of the total kinetic energy, a combination of rotational and turbulent motion:

$$\mathcal{T} = \frac{1}{2} \int \rho |\mathbf{u}|^2 d^3 \mathbf{x}, \quad (1.7)$$

of the energy of random, thermal motion:

$$U = \frac{3}{2} \int n k_B T d^3 \mathbf{x}, \quad (1.8)$$

of the the gravitational potential energy:

$$\mathcal{W} = \frac{1}{2} \int \rho \Phi_g d^3 \mathbf{x}, \quad (1.9)$$

and of the energy arising from magnetic fields:

$$\mathcal{M} = \frac{1}{8\pi} \int |\mathbf{B}|^2 d^3 \mathbf{x}, \quad (1.10)$$

where \mathbf{r} is the radius, \mathbf{u} is the velocity, n the number density, T the temperature and \mathbf{B} magnetic field. If these energies balance each other out, which means $\frac{1}{2} \frac{\partial^2 I}{\partial t^2} = 0$, then the cloud is in virial equilibrium. In order to estimate how much the kinetic, thermal and magnetic pressures work against gravitational forces, their ratios can be directly compared. Let ρ be the mass density, μ the molecular weight and m_H the mass of hydrogen, then $n \equiv \rho / \mu m_H$ and with $\mathcal{W} \approx -GM^2/R$, where G is the gravitational constant, M the mass and R the radius of the cloud, the ratio of thermal and gravitational energy is:

$$\begin{aligned} \frac{U}{|\mathcal{W}|} &\approx \frac{M k_B T}{\mu m_H} \left(\frac{G M^2}{R} \right)^{-1} \\ &= 3 \times 10^{-3} \left(\frac{T}{15 \text{ K}} \right) \left(\frac{M}{10^5 M_\odot} \right)^{-1} \left(\frac{R}{25 \text{ pc}} \right). \end{aligned} \quad (1.11)$$

Similarly, the ratio of magnetic and gravitational energy is:

$$\begin{aligned} \frac{\mathcal{M}}{|\mathcal{W}|} &\equiv \frac{|\mathbf{B}|^2 R^3}{6 \pi} \left(\frac{G M^2}{R} \right)^{-1} \\ &= 0.3 \left(\frac{B}{20 \mu\text{G}} \right)^2 \left(\frac{M}{10^5 M_\odot} \right)^{-2} \left(\frac{R}{25 \text{ pc}} \right)^4, \end{aligned} \quad (1.12)$$

while comparison of kinetic and gravitational energy yields:

$$\begin{aligned} \frac{\mathcal{T}}{|\mathcal{W}|} &\approx \frac{1}{2} M V^2 \left(\frac{G M^2}{R} \right)^{-1} \\ &= 0.5 \left(\frac{V}{4 \text{ km s}^{-1}} \right)^2 \left(\frac{M}{10^5 M_\odot} \right)^{-1} \left(\frac{R}{25 \text{ pc}} \right), \end{aligned} \quad (1.13)$$

where V is the mean value of random motion speed. Mostly, V is similar to the virial velocity $V_{vir} = (GM/R)^{1/2}$.

The marking criterion for cloud collapse is determined by the standing-wave perturbation of self-gravitating waves through an isothermal, uniform gas with density ρ_0 :

$$\rho(x, t) = \rho_0 + \delta\rho \exp[i(kx - \omega t)], \quad (1.14)$$

where x is the direction of propagation, $k = \frac{2\pi}{\lambda}$ the wave number corresponding to the wavelength λ and ω the frequency. Using Poisson's equation:

$$\nabla^2\Phi_g = 4\pi G\rho, \quad (1.15)$$

as well as equation 1.2 with the isothermal sound speed in the medium c_T , the dispersion relation can be expressed as:

$$\omega^2 = k^2 c_T^2 - 4\pi G\rho_0. \quad (1.16)$$

For short wavelengths, the approximation $\omega = kc_T$ is valid and with $\lambda_J \equiv 2\pi/k_0 = 2\pi c_T/\omega_0 = 2\pi c_T (4\pi G\rho_0)^{1/2}$ the Jeans length can be expressed as:

$$\lambda_J = \left(\frac{\pi c_T^2}{G\rho_0}\right)^{1/2} = 0.19 \text{ pc} \left(\frac{T}{10 \text{ K}}\right)^{1/2} \left(\frac{n_{H_2}}{10^4 \text{ cm}^{-3}}\right)^{-1/2}, \quad (1.17)$$

where n_{H_2} is the number density of H_2 . The Jeans length marks an exponential growth of amplitudes once the perturbation wavelength transcends this critical value. With $P_0 \equiv \rho_0 c_T^2$ and $m_1 = 1.18$, the critical Bonnor-Ebert mass that flags the boundary of gravitational instability:

$$M_{BE} = \frac{m_1 c_T^4}{P_0^{1/2} G^{3/2}}, \quad (1.18)$$

becomes:

$$M_J = \frac{m_1 c_T^3}{\rho_0^{1/2} G^{3/2}} = 1.0 M_\odot \left(\frac{T}{10 \text{ K}}\right)^{3/2} \left(\frac{n_{H_2}}{10^4 \text{ cm}^{-3}}\right)^{-1/2}, \quad (1.19)$$

also known as the Jeans mass. Clumps and cores with masses exceeding this threshold transition to gravitational collapse.

The increasing dust density and the correlated extinction of $A_V = 2$ mag protects the cloud from external irradiation and atoms can combine into molecules. Molecules in their gaseous state are found in large amounts in clouds with average sizes of 40 pc. This value however can vary just as the mass, density and temperature of the order of $10^5 M_\odot$, 100 cm^{-3} and 10 K, respectively. H_2 can collide with the abundant $^{12}C^{16}O$ and excite it to the $J = 1 - 0$ transition which is observable even across large distances. Thus, molecular clouds are usually traced by the 2.6 mm line that is emitted by this transition, as shown in Fig 1.2. While large linewidths indicate turbulent pressures in the molecular clouds, rotational transitions hint to spatial substructures throughout all scales of the clouds. Among them, dark cores with extinction values of $A_V = 5$ mag up to 10 mag, high densities of 10^4 cm^{-3} and masses between $10 M_\odot$ and $10^3 M_\odot$ form the nurseries of star formation within scales of ≈ 1 pc.

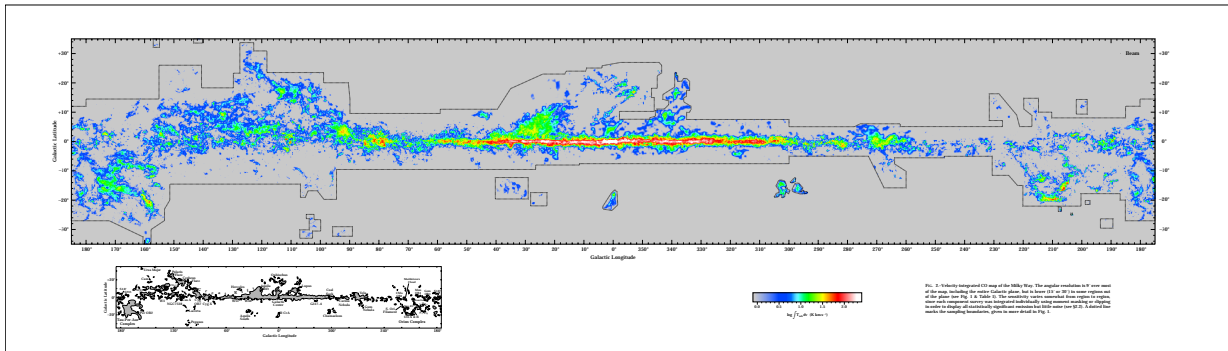


Figure 1.2: Observation of the $J = 1 - 0$ CO transition mapped in the entire Milky Way. Figure from Dame et al. (2001).

H_2 is presumably the main component of molecular clouds, but we cannot observe it due to the missing dipole moment. Nonetheless, astronomers have detected more than 200 molecules in the clouds mainly in the submillimeter regime of rotational transitions. Located in environments shielded by dust, these molecules are mostly simple chemical compounds, radicals or ions. Complex molecules, which means molecules with six or more atoms, represent a minor fraction of chemical species in space. As of November 2021, only 107 of the about 250 detected molecules in the interstellar medium or circumstellar shells – as listed in the Cologne Database for Molecular Spectroscopy (CDMS; <https://cdms.astro.uni-koeln.de/classic/molecules>) – contain six or more atoms.

Once the gravitational collapse starts, formation of a low-mass young stellar object (YSO) occurs in several stages, as seen in Figure 1.3.

In the phase of the **pre-stellar core**, which is a starless core that is about to begin star formation, dense regions contract from radii of ≈ 1 pc to cores of sizes ≈ 0.1 pc, $n = 10^4 - 10^7 \text{ cm}^{-3}$ and temperatures $T \approx 10$ K.

After typical time scales of $10^4 - 10^5$ yrs, the forming protostar has reached the stage of a **Class 0 protostar**, with typical sizes of several 1000 AU. These objects are so deeply embedded in gas and dust that they can only be observed in the millimeter and far-infrared (FIR) domain with peak intensities at $\lambda \approx 100 \mu\text{m}$, because the forming protostar emits absorbed radiation of infalling material as thermal radiation in direction of its poles.

As emitting jets grow stronger and the infalling material collects in a thick disc after $10^5 - 10^6$ yrs, Class 0 protostars transition to **Class I protostars**, that can be observed in the mid-infrared (MIR) around $24 \mu\text{m}$. They typically have radii of many 100 AU to 1000 AU.

The envelope has completely disappeared after $10^6 - 10^7$ years due to, for example, accretion flows and outflows, and the material has collected in a thin disc of radii of a few 100 AU. Observations now show two components of the **Class II protostar**, also known as a **classical T Tauri star**: the optical emission of the central pre-main-sequence star that has

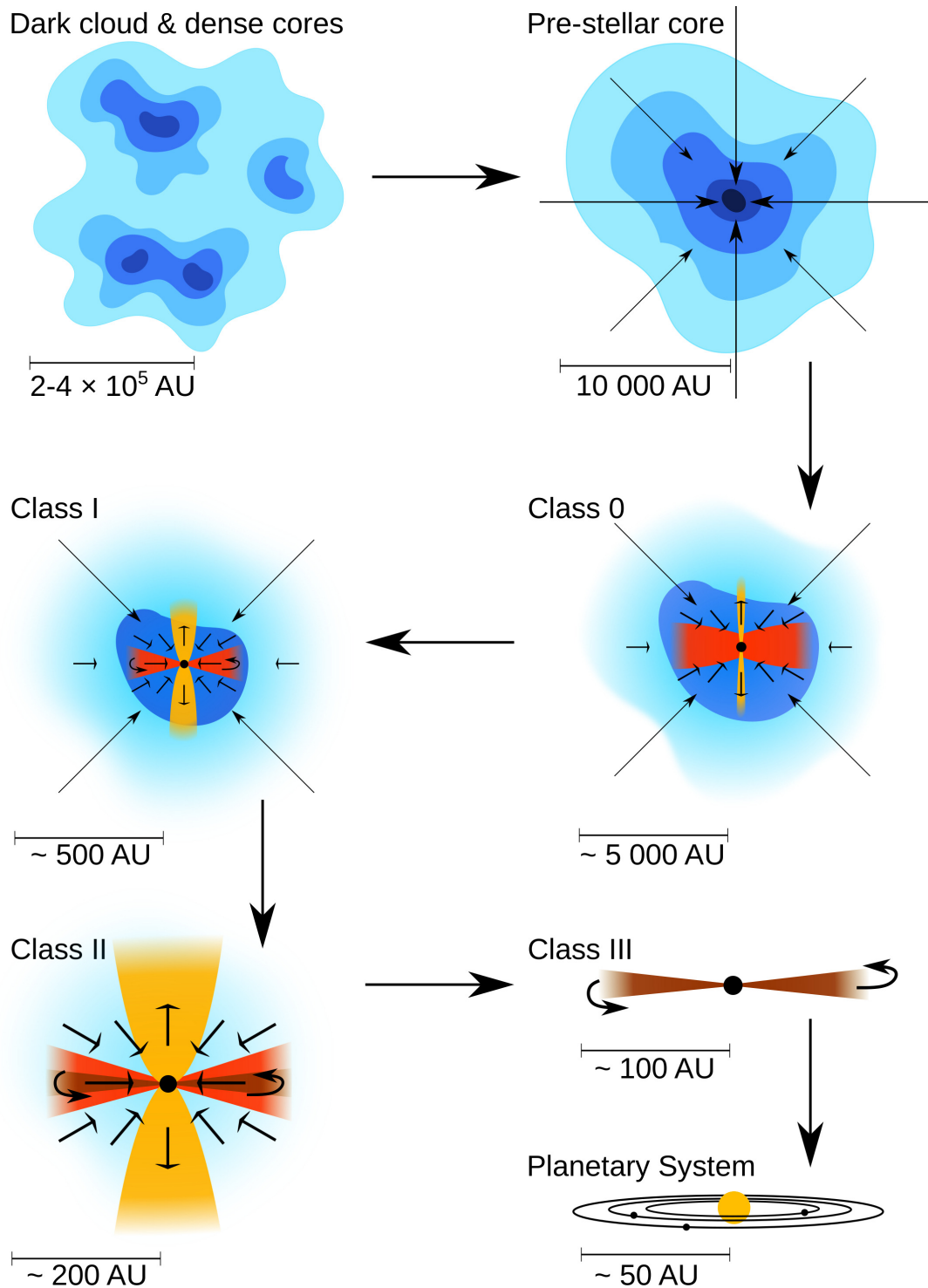


Figure 1.3: The various stages of star formation from dense cores to a planetary system. This figure was inspired by Persson (2014) and Klessen & Glover (2016).

started deuterium fusion in its centre and the infrared (IR) emission of the protoplanetary disc.

In the **Class III** or **evolved/weak T Tauri star** stage, material in the rotating midplane is almost completely gone and remnant gas and dust build the so called debris disc, eventually forming the planets of the planetary system. The young protostar has reached its final mass but is still contracting until it is dense and hot enough to start hydrogen fusion. This marks the birth of a new star.

1.1.1 Molecular clouds in gas phase

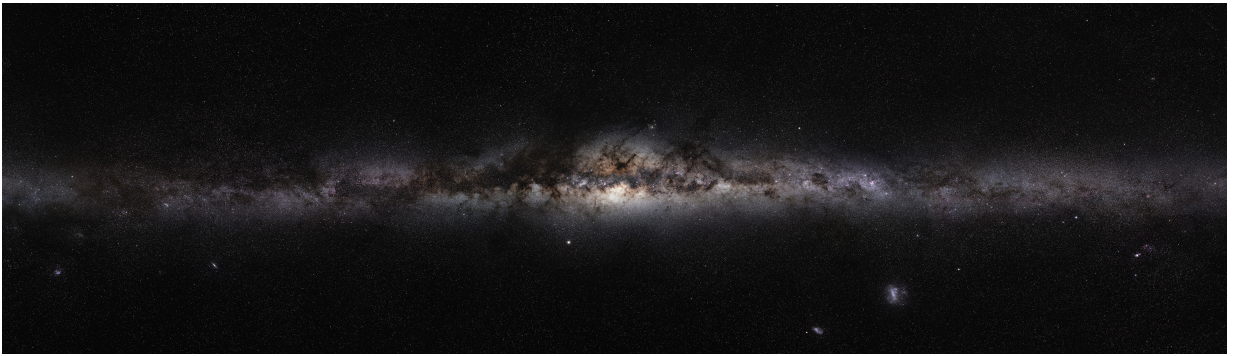


Figure 1.4: The Milky Way as observed at visible wavelengths. Dust grains in dark clouds obscure the light coming from background stars. Comparison with Figure 1.2 shows the interrelation of dark clouds protected by dust and the presence of CO. Credit: ESO/S. Brunier.

Even though dust grains represent only 1 % of the cloud's mass, their presence hugely impacts the physics and properties of the molecular cloud. On the one hand, light that traverses dust-containing regions experiences a red shift. Additional to reddening, dust effectively absorbs and scatters light with wavelengths smaller than the size of dust particles which can range from a few Å to 0.1 μm, as seen visually and quantitatively in Figure 1.4 and 1.5. The extinction is not only observable at visible wavelengths but also present across the whole electromagnetic spectrum and can be expressed dependent on the wavelength λ as:

$$m_{\lambda} = M_{\lambda} + 5 \log \left(\frac{r}{10 \text{ pc}} \right) + A_{\lambda}, \quad (1.20)$$

where m_{λ} and M_{λ} are the apparent and absolute magnitudes, r is the distance from the star and A_{λ} is the extinction at wavelength λ . The reddening effect of the light of background sources can be expressed in the interrelation of a decreasing A_{λ} when λ is increasing. Comparing eq. 1.20 for two wavelengths λ_1 and λ_2 for the same star, which means that r does not change, yields:

$$m_{\lambda_1} - m_{\lambda_2} = (M_{\lambda_1} - M_{\lambda_2}) + (A_{\lambda_1} - A_{\lambda_2}). \quad (1.21)$$

With $C_{12} \equiv m_{\lambda_1} - m_{\lambda_2}$ and $C_{12}^\circ \equiv M_{\lambda_1} - M_{\lambda_2}$, the color excess E_{12} can be defined as:

$$E_{12} \equiv C_{12} - C_{12}^\circ = A_{\lambda_1} - A_{\lambda_2}. \quad (1.22)$$

Considering a third wavelength λ_3 , the normalized selective extinction can be expressed as:

$$\frac{E_{32}}{E_{12}} = \frac{A_{\lambda_3}}{E_{12}} - \frac{A_{\lambda_2}}{E_{12}} = \frac{A_{\lambda_3}}{E_{12}} - R. \quad (1.23)$$

Connecting extinction and reddening, the ratio R , in terms of UB¹ filter names $R \equiv A_V/E_{B-V}$, has a value of 3.1 for the diffuse interstellar medium. In molecular clouds however, it can be much higher. In UB¹ terms and with an arbitrary wavelength λ , the selective extinction denoted as $E_{\lambda-V}/E_{B-V}$, as well as the total extinction $A_{\lambda_3}/E_{12} \stackrel{\text{UBV}}{=} A_{\lambda}/E_{B-V}$ are increasing with an increasing λ^{-1} , showing a local bump in the far-UV (FUV), as seen in Figure 1.5.

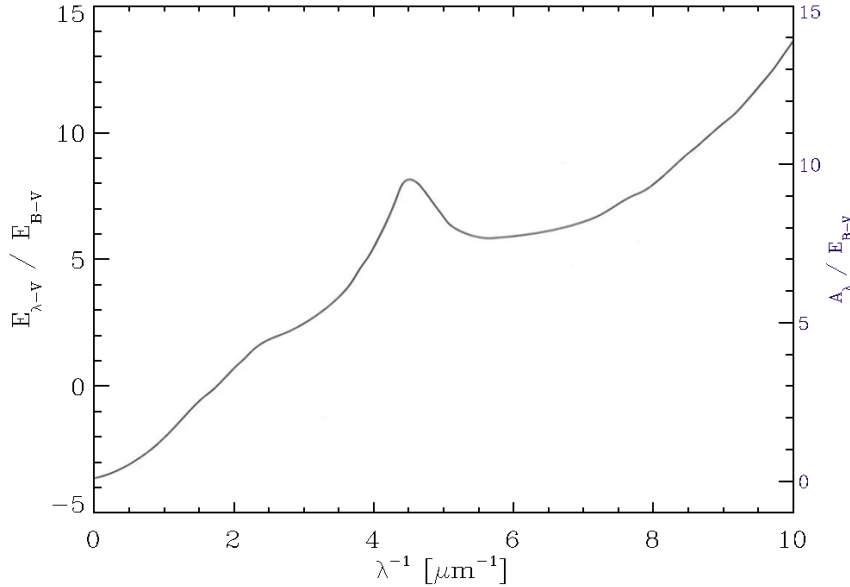


Figure 1.5: Selective and total extinction as a function of λ^{-1} with the prominent local maximum at $4.6 \mu\text{m}^{-1}$ (2175 \AA). The Figure is based on Stahler & Palla (2004).

Taking a closer look at the propagation of light through a dust containing medium, scattering, absorption and thermal emission influence the change in intensity I_ν of the traversing light with the frequency ν along a path of length Δs , which is given as:

$$\Delta I_\nu = -\rho \kappa_\nu I_\nu \Delta s + j_\nu \Delta s, \quad (1.24)$$

with κ_ν being the opacity and j_ν the emissivity.

$$\Delta \tau \equiv \rho \kappa_\nu \Delta s \quad (1.25)$$

¹The UB¹ photometric system refers to **ultraviolet, blue and visual** bands.

is called the optical depth, while $\rho\kappa_\nu$ is defined as the absorption coefficient α_ν . For values $\Delta\tau \gg 1$, as is the case in an optically thick medium, traversing light is very likely experiencing extinction whereas it can move freely through optically thin regions with $\Delta\tau \ll 1$. The equation of transfer can easily be derived from Eq. 1.24 as:

$$\frac{dI_\nu}{ds} = -\rho\kappa_\nu I_\nu + j_\nu \quad (1.26)$$

and in terms of $\Delta\tau$ the radiative transfer equation becomes:

$$\frac{dI_\nu}{d\tau_\nu} = -I_\nu + \frac{j_\nu}{\alpha_\nu} = -I_\nu + S_\nu. \quad (1.27)$$

S_ν is known as the source function and I_ν follows $I_\nu = I_0 e^{-\tau_\nu}$, where I_0 is the initial intensity of the star before traversing through a medium with optical depth τ_ν . For a uniform medium with constant j_ν and α_ν , I_ν can then be derived as:

$$I_\nu = I_0 e^{-\tau_\nu} + (1 - e^{-\tau_\nu}) S_\nu. \quad (1.28)$$

For the case of black body radiation governed by a thermal equilibrium, the source function follows the Planck formula given as:

$$S_\nu = B_\nu(T) = \frac{2h\nu^3}{c^2} \frac{1}{e^{h\nu/k_B T} - 1}, \quad (1.29)$$

where T (sometimes denoted as T_{eff}) is the surface temperature of the star, h the Planck constant and k_b the Boltzmann constant.

Chemical species in dense clouds with high optical depths are effectively shielded from UV light. This prevents molecular bond breaking through UV photodissociation, denoted as $AB + h\nu \rightarrow A + B$, allowing H_2 to form and the abundance of molecular hydrogen increases to $10^2 - 10^6 \text{ cm}^{-3}$, hence the name *molecular cloud*. Cooling processes are driven by molecular line and dust continuum emissions. In contrast to H_2 which does not have an effect on cooling, rotational line emission of CO, which is the most abundant molecule after H_2 in the gas phase, becomes dominant and the kinetic temperature of the gas settles to 8 - 15 K. The balance between cooling and heating is not dictated by UV irradiation anymore but by heating via energetic particles called cosmic rays (CR). With energies of at least 100 MeV nucleon⁻¹, the majority (89 %) of cosmic rays are protons with high energies of 1 - 10 GeV, while the other 11 % consist of energetic helium and other heavier elements as well as electrons. Low-energy CRs with energies from 100 MeV down to 1 MeV become the main drivers of heating and ionization of the gas. The ionization rate can best be derived from H_3^+ observations, following the production path of:



H_3^+ is lost by dissociation via electron recombination and reaction with polycyclic aromatic hydrocarbon (PAH) anions. As PAH neutralisation plays only a minor role, the cosmic-ray ionization rate can be expressed as:

$$\zeta_{\text{CR}} = \frac{k_e n_e n_{\text{H}_3^+}}{2.3 n(\text{H}_2)}, \quad (1.30)$$

where n_e , $n_{\text{H}_3^+}$, n_{H_2} are the densities of the corresponding components and k_e is the electron recombination coefficient, which is dependent on the temperature T as:

$$k_e = 10^{-6} T^{-0.45}. \quad (1.31)$$

Let the column density N_X of a species X be defined as:

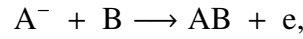
$$N_X = n_X \cdot L, \quad (1.32)$$

where L is the path length through the cloud. Then, the CR ionisation rate ζ_{CR} – under the assumption that the electrons mainly come from ionised C^+ – is:

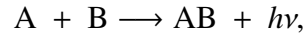
$$\zeta_{\text{CR}} = 7 \times 10^{-8} \frac{N_{\text{C}^+} N_{\text{H}_3^+}}{N_{\text{H}_2} L} = 7 \times 10^{-16} \left(\frac{\text{pc}}{L} \right) \text{cm}^3 \text{s}^{-1}. \quad (1.33)$$

Typical values for ζ_{CR} reach from a few $10^{-16} \text{cm}^3 \text{s}^{-1}$ for diffuse clouds down to $10^{-17} \text{cm}^3 \text{s}^{-1}$ for dense clouds.

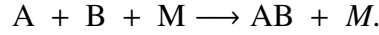
The formation of molecules in the gas phase becomes possible through associative detachment:



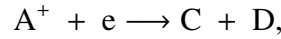
radiative association:



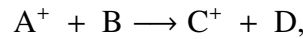
and collisional association:



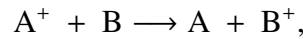
In dense regions, the most effective reaction that causes bond breaking is dissociative recombination:



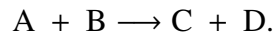
while molecular bondings can be restructured via ion-molecule reactions:



charge-transfer reactions:



and neutral-neutral reactions:



1.1.2 Taurus-Auriga and L1544

With a distance of 140 pc and a diameter of ≈ 30 pc, between the Taurus and Auriga constellations, lies one of the closest production sites for stars: the Taurus molecular cloud (TMC), depicted in Figure 1.6. With a total mass of molecular hydrogen $m_{\text{H}_2} = 10^4 M_{\odot}$, formation of low mass stars is very active here. While the Pleiades and Hyades, two young stellar clusters, can be found relatively close to the TMC, high-mass stars are not present in its vicinity. Among other

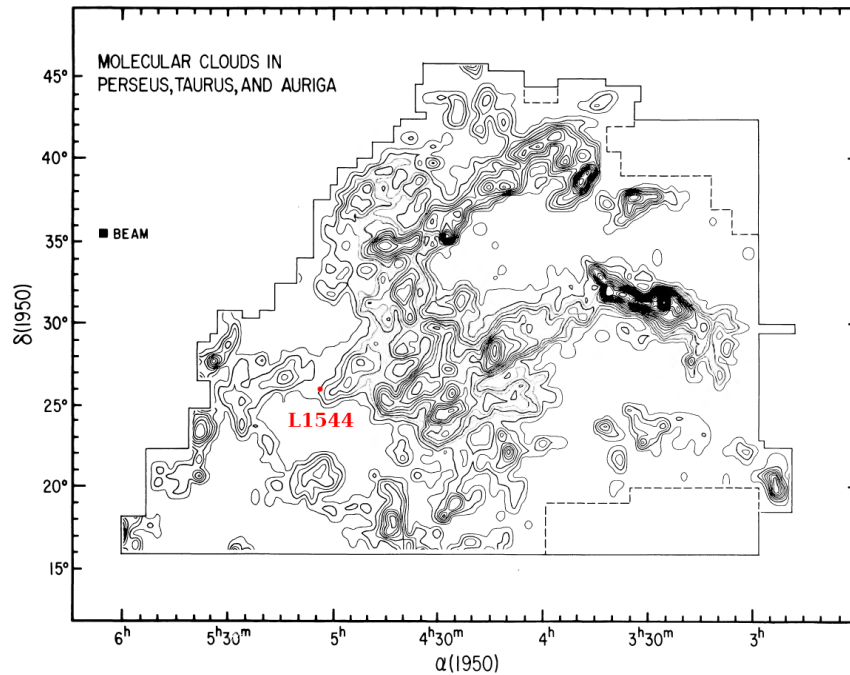


Figure 1.6: CO 2.6 mm line map of Taurus-Auriga. Figure from Ungerechts & Thaddeus (1987). The position of the pre-stellar core L1544 is marked on the map.

dense regions, starless cores like TMC-1 CP with a rich chemical diversity have been subject of many observations. Of special interest is the pre-stellar core L1544. With a cloud mass of $10 M_{\odot}$ (Tafalla et al. 1998), it has a central temperature of 6 K and a density $> 10^6 \text{ cm}^{-3}$ (Crapsi et al. 2007), which is higher than the critical threshold of 10^5 cm^{-3} that determines if a core can gravitationally collapse or not, as it was shown in Keto & Caselli (2008). Ward-Thompson et al. (1999) have analysed the density profile of L1544 and observed that the mass mainly accumulates in a somewhat filamentary structured core with a flat density gradient that becomes steeper only for radii larger than several 1000 AU. The major mass contingent of $8 M_{\odot}$ can be found in the core denoted as L1544 which is accompanied by the smaller cores L1544-E and L1544-W. Models show that contraction is happening in a quasi-equilibrium hydrostatic fashion (Keto et al. 2015). Observations following first detections of molecular species containing carbon, sulfur and nitrogen by Williams et al. (1999) and Ohashi et al. (1999) show a rich chemical variety of compounds in L1544.

1.2 Astrochemical Network of interstellar Ices

Already the radiative association of H atoms, $\text{H} + \text{H} \rightarrow \text{H}_2 + h\nu$, is very slow in the gas phase. An effective formation of H_2 and even more complex molecules can only happen on the surface of dust grains, where atoms and molecules can be adsorbed to form ice layers growing in thickness with time. The compounds of interstellar dust may originate from the last stages of

the stellar life cycle, when burned species are ejected from the interior of the star in the form of stellar winds or supernovae, for example. Refractive components such as oxygen, carbon, iron, silicon, magnesium or even titanium condense in the cooling atmosphere to eventually form SiO, silicates like olivines (e.g. $(\text{Mg,Fe})_2[\text{SiO}_4]$) or pyroxenes (e.g. $(\text{Mg,Fe})_2[\text{Si}_2\text{O}_6]$), PAHs and carbonaceous compounds such as SiC or TiC.

1.2.1 Physical processes

Chemical compounds can be adsorbed onto dust grains and subsequently removed from the gas phase, a process called depletion. Reactions on the grain surface can happen in two ways:

1. **Langmuir-Hinshelwood mechanism:** Adsorbed atoms and molecules move on the surface of dust because of thermal hopping or tunneling.
2. **Eley-Rideal mechanism:** A gaseous atom or molecule reacts with a partner on the grain after a direct hit.

The Eley-Rideal mechanism is unlikely to happen in interstellar clouds due to the low number density, which is why the Langmuir-Hinshelwood mechanism describes the dominant reaction procedure for adsorbed species.

The accretion rate, which is the ratio of an accreted species relative to the number of molecules on the dust grain, is given as:

$$k_{ac} = n_X \sigma_d \bar{v}_X S(T, T_d) \approx 10^{-17} \left(\frac{T}{10 \text{ K}} \right)^{1/2} n_X \text{ s}^{-1}, \quad (1.34)$$

where n_X is the number density of the accreting species in the gas phase. $\sigma_d = \pi a_d^2$ is the cross section of a dust grain with size a_d and \bar{v}_X the average speed of a molecule. The right hand side of the equation has been evaluated for CO at $T = 10 \text{ K}$. The sticking coefficient $S(T, T_d)$ is ≈ 1 for species heavier than H at low temperatures, while for atomic hydrogen it depends on the gas and dust temperature, T and T_d :

$$S(T, T_d) = \left[1 + 4 \times 10^{-2} (T + T_d)^{1/2} + 2 \times 10^{-3} T + 8 \times 10^{-6} T^2 \right]^{-1}. \quad (1.35)$$

Experiments have shown that $S = 0.8$ at 10 K and 0.5 at 100 K. Incorporated into the accretion rate is the time scale of a compound to arrive on a grain:

$$\tau_{ar} = \frac{1}{n_X \sigma_d \bar{v}_X} \approx 3 \left[\frac{10^4 \text{ cm}^{-3}}{n_X} \right] \left[\frac{1000 \text{ \AA}}{a_d} \right]^2 \text{ days}, \quad (1.36)$$

where the evaluation of the right hand side was done under the same assumptions as in Eq. 1.34.

The presence of mobile species is the key to the chemical reactivity on the dust surface. This is why the duration of a compound staying on the grain before it desorbs once more is an important factor. The duration is dependent on T_d , the adsorption energy E_b and the frequency of the adsorbed species ν_0 :

$$\tau_{des} = \frac{1}{\nu_0} e^{E_b/k_b T_d}. \quad (1.37)$$

Assuming a compound with mass m resides on a grain with a number density of surface sites N_S , which typically has a value of $\approx 2 \times 10^{15}$ sites cm^{-2} , the frequency in a symmetric harmonic potential is:

$$\nu_z = \left(\frac{2 N_S E_b}{\pi^2 m} \right)^{1/2}, \quad (1.38)$$

Meanwhile, the frequency of a mobile monoatomic gas ν_0 is dependent on f_z , the vibrational partition function in the mode perpendicular to the surface. f_z symbolises that an adsorbed species has traded one degree of translational freedom (in z direction) for a vibrational degree of freedom. ν_0 is then:

$$\nu_0 = \frac{k_b T}{h} \frac{1}{f_z}. \quad (1.39)$$

At high temperatures this mode is fully excited and $f_z = k_b T / h \nu_z$, which leads to $\nu_0 = \nu_z$. At low temperatures and therefore a non-excited mode, the vibrational partition function and the frequency are $f_z = 1$ and $\nu_0 = k_b T / h$, respectively. In case that the species is not mobile, all degrees of freedom must be taken into account and ν_0 can be expressed as:

$$\nu_0 = \frac{k_b T}{h} \frac{1}{f_x f_y f_z} \frac{2 \pi m k_b T}{N_S h^2}, \quad (1.40)$$

where the last factor expresses the distribution of the adsorbed species. The duration of species remaining on the dust surface is determined especially by the dust temperature. In molecular clouds with dust temperatures of ≈ 10 K, only H with $\tau_{ev,H} = 1.6 \times 10^3$ s and H_2 with $\tau_{ev,\text{H}_2} = 3 \times 10^7$ s desorb from a H_2O surface during the lifetime of the cloud, while for higher dust temperatures around 30 K, this is also the case for atoms such as C, N, O ($\tau_{ev} = 4 \times 10^{-1}$ s) or S ($\tau_{ev} = 4 \times 10^{13}$ s).

Once the species have adsorbed onto the dust grain, they can move via quantum mechanical tunneling, which is the case for hydrogen and deuterium at low temperatures, or via thermal hopping when the species is heavier than H. The tunneling time through a sink wall is:

$$\tau_t = \frac{1}{\nu_0} \exp \left[\frac{2 a}{\hbar} (2 m E_m)^{1/2} \right], \quad (1.41)$$

where a is the width of the wall and E_m its height for a particle with mass m . For H this is approximately 10^{-10} s, which is uncertain because of the poorly known value of E_m in the case of a dust grain covered by H_2O and partly by H_2 . On a silicate surface with a much higher binding energy E_b , experimental analysis has estimated τ_t to be of the order of 10^{-2} s.

The time for thermal hopping is also dependent on T_d as well as E_m , with $E_m \approx E_b/3$:

$$\tau_m = \frac{1}{\nu_m} \exp \left(\frac{E_m}{k_b T_d} \right). \quad (1.42)$$

The frequency for vibrational motion along the surface ν_m is similar to ν_0 . On dust grains covered by H_2O , migration time scales from one site to another have a wide range. At temperatures of 10 K, they can range from 10^{-2} s for atomic species up to 10^{12} s for CO, while species such as

CH₄ or H₂O never move at all during the lifetime of a molecular cloud. The migration time scales however are very sensitive to the temperature and already at T = 30 K, τ_m drops to 2×10^{-9} s for C, N and O, while H₂O becomes mobile with $\tau_m = 2 \times 10^5$ s. Species move on the grain surface in a random two dimensional fashion and visit $N/\ln N$ sites after N steps. The average time scale in which a particle moves over all grain surface sites N_t is:

$$\tau_{av} = (N_t \ln N_t) \tau_m. \quad (1.43)$$

On average, a dust grain of size 1000 Å has some 10^6 sites, which means that heavy atoms need several tens of hours to move over each position of the grain. This is a value similar to the accretion time scale for the very same species.

It has already been emphasized that the time scales of accretion, migration and desorption are dependent on the dust temperature. This quantity is determined by an equilibrium of absorption and emission energy. For a wavelength λ larger than a reference wavelength λ_0 the absorption efficiency follows a power law:

$$Q(\lambda) = Q_0 \left(\frac{\lambda_0}{\lambda} \right)^\beta, \quad (1.44)$$

where β is a constant, usually within a range of 1 to 2. In the case of amorphous materials it is equal to 1. Q_0 , another constant, and λ_0 can then be simplified to $Q_0 = 1$ and $\lambda_0 = 2\pi a_d$. The absorbed energy is then:

$$\Gamma_{abs} = 4 \pi \sigma_d \int_0^\infty Q(\lambda) J(\lambda) d\lambda, \quad (1.45)$$

where $J(\lambda)$ is the mean intensity of the radiation field and, correspondingly, the emitted energy is:

$$\begin{aligned} \Gamma_{em} &= 4 \pi \sigma_d \int_0^\infty Q(\lambda) B(T_d, \lambda) d\lambda \\ &= 4 \sigma_d \langle Q_P(T_d) \rangle \sigma T_d^4. \end{aligned} \quad (1.46)$$

$\langle Q_P(T_d) \rangle$ is the Planck mean efficiency and σ the Stefan-Boltzmann constant. Using Equations 1.29 and 1.44, the Planck mean efficiency can be written as:

$$\langle Q_P(T_d) \rangle = \frac{15}{\pi^4} (\beta + 3)! \zeta(\beta + 4) Q_0 \left(\frac{\lambda_0 k_b T_d}{h c} \right)^\beta, \quad (1.47)$$

where ζ is the Riemann zeta function defined as:

$$\zeta(s) \equiv \sum_{n=1}^{\infty} \frac{1}{n^s}. \quad (1.48)$$

Equating absorption and emission energy and denominating the integrated mean intensity as J , the resulting dust temperature of small amorphous grains ($\beta = 1$) in a diffuse cloud can be expressed as:

$$T_d = \left(\frac{h c}{k_b} \right) \left(\frac{4 \pi J}{384 \pi^2 a_d h c^2 \zeta(5)} \right)^{1/5}. \quad (1.49)$$

In case of silicate and graphite grains, approximations have shown that:

$$T_{\text{sil}} = 13.6 \left(\frac{1\mu\text{m}}{a_d} \right)^{0.06} \text{ K}, \quad (1.50)$$

and

$$T_{\text{gra}} = 15.8 \left(\frac{1\mu\text{m}}{a_d} \right)^{0.06} \text{ K}, \quad (1.51)$$

respectively. In diffuse clouds without a nearby star, typical dust temperatures for silicate and graphite grains range from ≈ 20 K to ≈ 30 K, depending on the grain size, while in dense clouds without radiation of VIS and UV photons, the temperature decreases to ≈ 10 K.

If there is additionally a star with luminosity L_* positioned at distance d to the cloud then the emitted radiation field is:

$$G_0 = 2.1 \times 10^4 \left(\frac{L_*}{10^4 L_\odot} \right) \left(\frac{0.1\text{pc}}{d} \right)^2. \quad (1.52)$$

In that case, dust temperatures rise and must be corrected for the present radiation field. In the case of a small grain with $\beta = 1$, the dust temperature becomes:

$$T_{d,*} = 33.5 \left(\frac{1\mu\text{m}}{a_d} \right)^{1/5} \left(\frac{G_0}{10^4} \right)^{0.2} \text{ K}. \quad (1.53)$$

For silicate grains with $T_{\text{sil}} < 250$ K and $T_{\text{gra}} < 65$ K it was found that:

$$\begin{aligned} T_{\text{sil},*} &= 50 \left(\frac{1\mu\text{m}}{a_d} \right)^{0.06} \left(\frac{G_0}{10^4} \right)^{1/6} \text{ K} \\ T_{\text{gra},*} &= 61 \left(\frac{1\mu\text{m}}{a_d} \right)^{0.06} \left(\frac{G_0}{10^4} \right)^{1/5.8} \text{ K}. \end{aligned} \quad (1.54)$$

1.2.2 The interplay of gaseous and solid phases

Accretion rate and time scales have already been discussed in context with the mobility of adsorbed species on the grain surface as a function of temperature. Furthermore, for dense clouds with dust temperatures of ≈ 10 K, where the assumptions hold that all compounds heavier than H stick to the dust grain ($S(T, T_d) = 1$) and never evaporate during the lifetime of a molecular cloud, the accretion rate can be equated with the arrival or growth rate k_{ar} , which can be expressed as a function a_d , abundance of condensable species X_c and gas density n :

$$k_{\text{ar}}(a_d) = k_{\text{ac}} = n_X \pi a_d^2 \bar{v}_X = 10^2 \left(\frac{a_d}{1000 \text{ \AA}} \right) \left(\frac{X_c}{10^{-4}} \right) \left(\frac{n}{10^4 \text{ cm}^{-3}} \right) \text{ yr}^{-1}. \quad (1.55)$$

Thus, the ice mantle grows in thickness with time and the dust grain gains mass according to:

$$\frac{dm_d(a_d)}{dt} = 4 \pi a_d^2 \rho_s \frac{da_d}{dt} = \pi a_d^2 n_X \bar{v}_X \bar{m}_X, \quad (1.56)$$

where ρ_s is the specific density of the grain and \bar{m}_X the mean mass of the eventually accreting species. Once the gaseous compounds have adsorbed onto the dust, they stay stuck on the surface and start to migrate if no other phenomenon causes the molecules and atoms to desorb again. Depending on the individual regions of a dense cloud however, particles can once more be ejected due to different processes.

1. **Sublimation:** When the dust temperature exceeds the sublimation temperature (dependent on the binding energy) of a pure ice species, said species will sublimate according to Eq. 1.37 with a rate of:

$$k_{\text{sub}} = \frac{1}{\tau_{\text{des}}} = v_0 e^{-(E_b/k_b T_d)}. \quad (1.57)$$

The sublimation temperature T_{sub} can be measured in the laboratory but it must be noted that the obtained values are noticeably higher than actual temperatures in clouds and protostars because of the greatly varying time scales of sublimation in the laboratory (of the order of minutes) and in space (10^5 yrs). For some species $T_{\text{sub,space}}$ is approximately $0.6 \times T_{\text{sub,lab}}$, as is the case for O_2 with $T_{\text{sub,lab}} = 22$ K and $T_{\text{sub,space}} = 13$ K, or for H_2O with $T_{\text{sub,lab}} = 150$ K and $T_{\text{sub,space}} = 90$ K. Furthermore, ice mantles are usually not composed of pure ices but consist of several different species that can become mixed - a state that can influence the sublimation temperature. This leads to separate desorption for species of similar amount or to evaporation at a later, hotter stage, when small portions of volatile species entrapped in a hosting ice matrix desorb only when the latter reaches its sublimation temperature.

2. **Photodesorption:** This process becomes significant at the outskirts of dense clouds where FUV radiation can still reach the ice mantles. Chemical species are then evaporated and the ice mantle loses mass dependent on the ice density ρ_s or correspondingly mean mass \bar{m}_s of the compound in question:

$$\frac{dm_d}{dt} = 4 \pi a^2 \rho_s \frac{da}{dt} = \pi a^2 Y_{pd} 4 \pi N_{\text{ISRF}} \bar{m}_s. \quad (1.58)$$

The corresponding decrease in size of the ice grain da/dt is:

$$\frac{da}{dt} = 2.2 \times 10^{-2} \left(\frac{Y_{pd}}{10^{-2}} \right) \text{Å yrs}^{-1} \quad (1.59)$$

Y_{pd} in Equations 1.58 and 1.59 is the photodesorption yield that expresses how many FUV photons are needed for one molecule or atom to desorb.

3. **Sputtering:** Energetic ions can knock out material from the dust grain or from the ice mantle, which is even easier due to lower binding energies. For light ions the minimum energy that enables sputtering is:

$$E_{sp} = \frac{E_b}{g(1-g)}, \quad (1.60)$$

with:

$$g = \frac{4 m_{ion} m_{tg}}{m_{ion} + m_{tg}}, \quad (1.61)$$

where m_{tg} is the mass of the target hit by the ion. For example, binding energies for ices, with values of 0.53 eV, are much smaller than those of dust grains with 5.7 eV for silicates. Measurements have shown that sputtering is already very effective for collisions with low-energy ions of ≈ 10 eV that are generated by shocks - high pressure regions generated for example by stellar winds - traversing through a cloud. Thus, shocks are assumed to be important contributors to desorption processes in molecular clouds.

4. **Thermal spikes and chemical desorption:** The discussion on the dust temperature in Section 1.2.1 has shown that T_d is strongly dependent on the grain size. Small compounds like PAHs that are struck by a UV photon heat up substantially so that bound molecules can desorb from the surface. Similarly, the heat produced during chemical reactions can be high enough for reactive species to sublime into the gas phase. Assuming that chemical desorption does not destroy the evaporation species or the ice grain, the process can be seen as an elastic collision where the total energy budget ΔH_R can be used in all degrees of freedom N . The kinetic energy fraction that is available for the species with mass m when it detaches from the ice grain with mass M is:

$$\epsilon = \frac{(M - m)^2}{(M + m)^2}, \quad (1.62)$$

and the total energy utilizable by the evaporating species perpendicular to the grain surface is:

$$E_{CD} = \frac{\epsilon \Delta H_R}{N}. \quad (1.63)$$

Then the probability for desorption can be expressed as:

$$P_{CD} = \exp\left(\frac{E_b}{\epsilon \Delta H_R / N}\right). \quad (1.64)$$

Experiments conducted by Minissale et al. (2016) have shown that the probability can differ greatly from theoretical calculations. In the case of the $O + H \rightarrow OH$ reaction, P_{CD} is predicted to be 68 %, while experiments have shown that chemical desorption from either non porous amorphous solid water or from a grain surface have a probability of 25 % or 50 %, respectively.

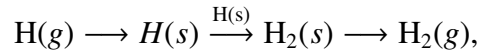
5. **Mantle explosions caused by cosmic rays:** CRs are present even in the densest part of an interstellar cloud and their collision with an ice grain can cause a strong temperature increase. For heavy species such as Fe, C, N or O with energies of 10 - 100 MeV nucleon⁻¹ the grain temperature can rise to 50 K or even 200 K. Time scales for collisions with a CR are dependent on the CR flux \mathcal{N}_{CR} :

$$\tau_{CR} = \frac{1}{4\pi \mathcal{N}_{CR} \pi a_d^2}. \quad (1.65)$$

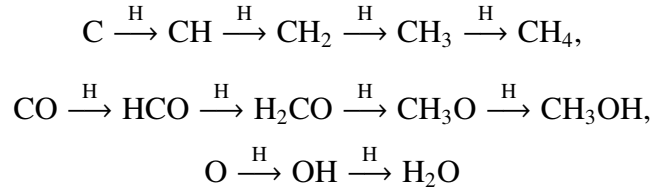
For CRs with $\mathcal{N}_{CR} \approx 10^{-4}$ particles $\text{cm}^{-2} \text{s}^{-1} \text{sr}^{-1}$, grains of sizes $> 50 \text{ \AA}$ will collide one or even several times during the molecular cloud stage.

1.2.3 Ice chemistry

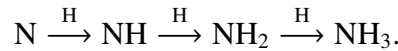
The composition of ice mantles is determined by the preceding abundances of chemical species in the gas phase. H_2 is by far the most abundant molecule, however because of CRs H is also present. These atoms are adsorbed onto dust grains and act as reactants with other species: oxygen, which is initially present in its atomic form; carbon, mainly present as CO with minor amounts of C (larger abundances in the early stages of the molecular cloud); and nitrogen, which is highly abundant as unreactive N_2 , while only small fractions of N serve as reaction agents. At low densities highly abundant atomic hydrogen becomes the primary reaction partner and enables several formation paths because of its reactivity. The main routes of hydrogenation are listed in the following passage.



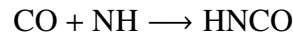
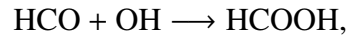
where (g) and (s) indicate if the species is present in the gas or solid phase. Other hydrogenation paths mainly happen in the solid phase on the surface of dust grains:



and



At higher densities, sufficient amounts of heavy species are present so that reactions with partners other than H become important. Complex molecules mainly form on dust grains and are then desorbed at a later stage. Some of the reactions highlighting the association of two molecules produced in the upper reaction paths are:

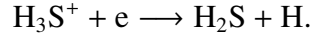
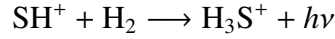
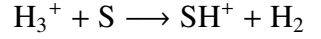


and



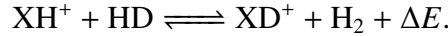
The chemistry of sulfur, another very abundant species in space is highly debated. While almost no sulfur was observed to be depleted in diffuse clouds, and the abundances are similar to the cosmic abundance, this changes drastically in dense regions. Observations of sulfur bearing molecules in cold dense cores (e.g. in form of OCS by Palumbo et al. 1997) show that only small amounts of S are present in the gas phase. However, depletion that could account for the missing

species is a current topic of discussion, as next to OCS only one more sulfur bearing molecule has been observed in solid phase: SO₂ (c.f. Zasowski et al. 2009). H₂S has been detected in the gas phase but its formation is very slow in gaseous reactions following the formation path:

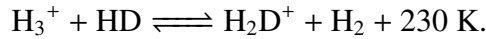


The formation of H₃S⁺ in a radiative association reaction is a minor process in the gas phase of cold clouds when compared to the electron recombination process of SH⁺. However, H₂S formation via the reactions of S⁺ + H₂ and SH⁺ + H₂ is endothermic and can only happen in shock regions when additional energy is provided. Thus, it is likely that H₂S forms on dust grains and is then later desorbed into the gas phase. This however has to be confirmed since H₂S has not yet been detected in ice mantles. As S⁺ does not react with H₂, it is more likely to bond with hydrocarbons to form species such as CS or CCS. Low abundances of such molecules have been observed in several sources in the gas phase (e.g. Vastel et al. 2018; Cernicharo et al. 2021), however no detection was reported for ice mantle observations.

Last named, deuterium is of special interest because its abundance comes mainly from nucleosynthesis during the first minutes after the Big Bang, while only small amounts are produced in protostars, pre-main-sequence stars and intermediate-mass stars. This means that the amount of deuterium overall no longer increases with time. Nevertheless, observations revealed that molecules in dense clouds are highly deuterated which is due to a higher stability when compared to H-bearing isotopologues. This is due to the fact that D is slightly more bound to the molecule than H, which is seen in reactions with the deuterated representative of molecular hydrogen, HD:



Since H₂ is the most abundant molecule in space, X = H₂ becomes especially important:



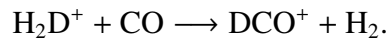
Gerlich et al. (2002) found a rate coefficient for this reaction of $k_f = 3.5 \times 10^{-10} \text{ cm}^3 \text{ s}^{-1}$ while the rate coefficient for the backwards reaction can be estimated as:

$$k_b = k_f \exp(-230 \text{ K}/T). \quad (1.66)$$

Denoting the Boltzmann constant in Eq. 1.67 as k to avoid confusion with the rate coefficient k_b , and assuming that the system is in a local thermodynamic equilibrium (LTE), the ratio of deuterated species to their non-deuterated equivalents is:

$$\frac{\text{H}_2\text{D}^+}{\text{H}_3^+} = \frac{\text{HD}}{\text{H}_2} e^{\Delta E/kT} \quad (1.67)$$

and this is $\gg 1$ for $T = 10 \text{ K}$. However, molecular clouds are not in local thermal equilibrium and recombination of H₃⁺ with present electrons hinders deuterium fractionation. Also, H₂D⁺ is destroyed when it collides with other species such as CO:



Thus, the deuterium fractionation is dependent on the abundance X of the corresponding reactants and the according reaction rate k_X :

$$\frac{X(\text{H}_2\text{D}^+)}{X(\text{H}_3^+)} = \frac{k_f X(\text{HD})}{k_b X(\text{H}_2) + k_e X(e) + k_{\text{CO}} X(\text{CO}) + \dots} \quad (1.68)$$

Table 1.1 shows some of the reaction partners that destroy H_2D^+ and compares deuterium fractionation ratios in L1544 to the elemental ratio of $X(\text{D}) / X(\text{H}) = 1.5 \times 10^{-5}$. The ratios for molecular species are several orders of magnitude higher and show how effective deuteration in ice mantles can be.

Table 1.1: Reactants that destroy H_2D^+ (column 1), their associated products (column 2) and observed deuterium fractions in the pre-stellar core L1544 (column 3).

Reactant	Products	deuterium fractionation (L1544) ^c
HD^a	$\text{D}_2\text{H}^+ + \text{H}_2$	
CO^a	$\text{DCO}^+ + \text{H}_2$ $\text{HCO}^+ + \text{HD}$	$X(\text{DCO}^+) / X(\text{HCO}^+) =$ 0.04
N_2^a	$\text{N}_2\text{D}^+ + \text{H}_2$ $\text{N}_2\text{H}^+ + \text{HD}$	$X(\text{N}_2\text{D}^+) / X(\text{N}_2\text{H}^+) =$ 0.2
HCN^b	$\text{DCN} + \text{H}_2^+$	
HNC^b	$\text{DNC} + \text{H}_2^+$	$X(\text{DNC}^+) / X(\text{HNC}^+) =$ 0.034

(a) For example in Millar (2005).

(b) For example in Millar (1992).

(c) Observed by Caselli et al. (2002a); Caselli et al. (2002b).

1.3 Spectroscopic studies

This section describes the spectroscopic methods that are used at the Center for Astrochemical Studies (CAS). Also, the experimental devices that were used for the measurements will be presented. Aimed at investigating interstellar ices, the core piece in all set-ups is one of two closed-cycle He cryostats that can be coupled to three spectrometers: the Fourier transform infrared (FTIR) spectrometer, the THz time-domain spectrometer (TDS) and the Raman microscope. While the Raman microscope will be described in more detail in Chapter 6, each one of these spectrometers has unique features that help to investigate different properties of interstellar ice analogues.

1.3.1 Closed-cycle He Cryostat

In order to investigate the different parameters of interstellar ice mantles, first it is necessary to create ice analogues in the laboratory under conditions that are as close as possible to those in space. The closed-cycle He cryostat, from now on simply referred to as the cryostat or cryocooler, provides the possibility to reach temperatures as low as 4.2 K using the powerful Gifford-McMahon refrigeration cycle. The cooling procedure is pneumatically driven by a differential of high and low pressure He gas which has the benefit of reducing vibrations compared to a mechanically driven cooling system, as described by Advanced Research Systems (ARS). Additionally, a damping interface is incorporated into the cryocooler that hinders almost all physical vibrations to reach the sample holder and affect measurements. This greatly improves the signal-to-noise (S/N) ratio.

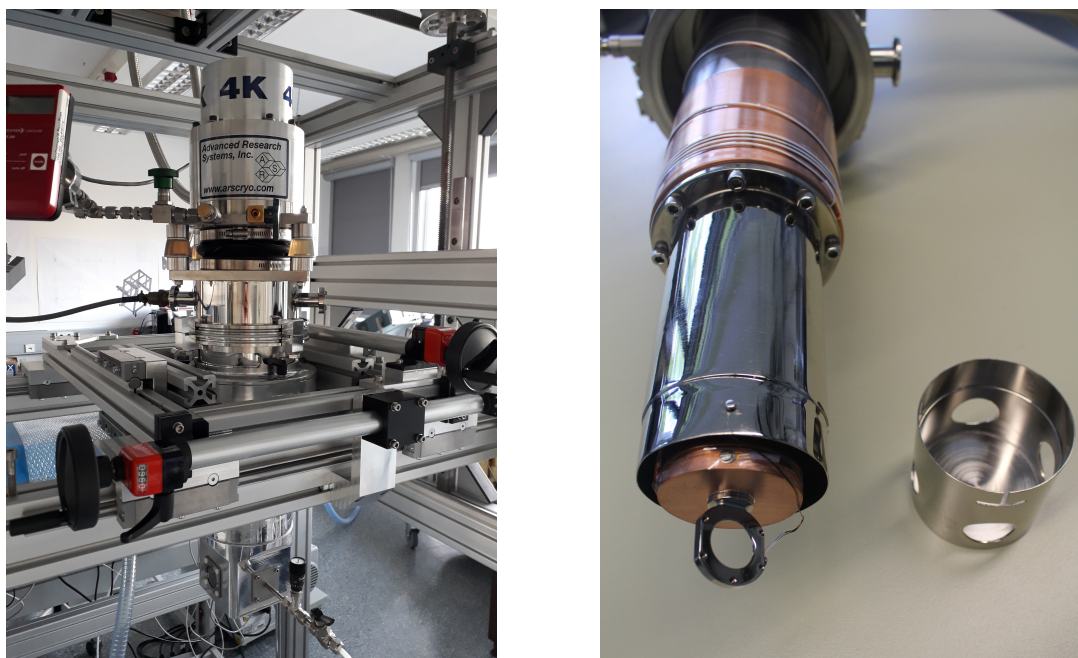


Figure 1.7: The closed-cycle He cryostat. Left: complete view. Right: close view on the sample holder and the radiation shield.

The sample holder, as seen in the right image of Figure 1.7, is attached to the end of the cold-head and optical windows with a diameter of $d = 20$ mm can be mounted on it. The material of the windows is chosen accordingly to the spectral region that is going to be examined. In the CAS ice laboratory, usually KBr is used for spectroscopy in the near-IR (NIR), MIR and partly in the FIR region. Transmission information provided by Edmund Optics show the big advantage that KBr enables transmission ≥ 90 % in the large wavelength (or wavenumber λ^{-1}) range of 400 nm (25000 cm^{-1}) to 20 μm (500 cm^{-1}) and still performs well down to 250 nm (40000 cm^{-1}) in the UV regime and up to 26 μm (384.6 cm^{-1}) in the FIR spectral range. For longer wavelengths that are observed using the THz TDS, high-resistivity float-zone silicon (HRFZ-Si) is the sample ma-

terial of choice since the only other suitable option would be the much more expensive diamond. Tydex specifies a transmission of the HRFZ-Si window with a thickness of 5 mm as 50 - 54 % in the range of 50 - 1000 μm ($200 - 10 \text{ cm}^{-1}$ or 6 - 0.3 THz) while this value drops to $\approx 40\%$ at 20 μm (15 THz). Technical information on the transmission is shown graphically in Figure 1.8.

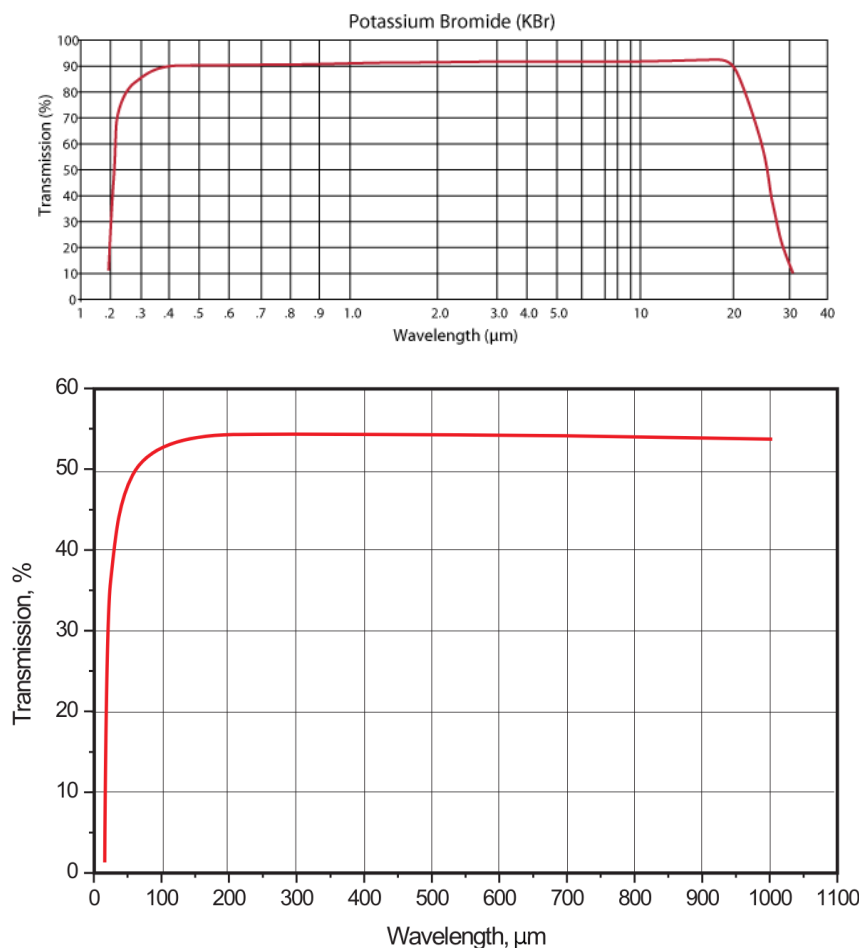


Figure 1.8: Transmission of KBr with a thickness of 2 mm (top) and of HRFZ-Si with a thickness of 5 mm (bottom). Transmission information is provided by Edmund Optics for KBr and by Tydex for HRFZ-Si.

After mounting the substrate window, a so called radiation shield, as seen next to the sample holder in the right panel of Figure 1.7, is attached to the cryostat. Residual water in the evacuated chamber can condense onto the radiation shield which makes cooling down to temperatures of 4.2 K possible. Experiments with the THz TDS, which are described in Chapter 5, have shown that the minimum temperature without the radiation shield is 14 K. The cooling system is closed by a cubic chamber of edge length 10 cm, as seen in the bottom part of the left panel in Figure 1.7 and it is then set under high vacuum that reaches 10^{-5} mbar at ambient temperature and 10^{-7} mbar at 10 K. With these settings it is possible to mimic conditions in dense regions of the ISM well enough to form ice analogues with a similar structure as in interstellar mantles so that

recorded and analysed data of the investigated ice compositions can assist in the interpretation of astronomical observations.

A cross section of the cooling chamber from a bird's eye view is shown both for the FTIR and THz TDS configuration in Figure 1.9. The main differences of the two set-ups are the different materials of the windows adjusted to the measurements in the corresponding spectral regions, the alignment of the substrate relative to the molecular beam coming from the inlet, the distance of the inlet from the substrate, and the presence of the radiation shield. The spatial arrangement in the THz experiments helps to avoid a directionality in the structure of the ice sample.

In the FTIR experiments, KBr is used only as a substrate. One reason for this is that thin windows are quite brittle and can easily break when not carefully mounted. Moreover, due to its hydrophilic nature the surface would go blind when it is exposed to moisture over a longer period of time. Thus, the optical windows on the outside of the cooling chamber are usually made of ZnSe which gives a lower transmission of $\approx 70\%$, as indicated by Edmund Optics, but is unaffected by the humidity in the air. In the THz experiments on the other hand, three HRFZ-Si windows with a total thickness of 6 mm are used as substrate and external windows.

The probes are deposited onto the substrate via an inlet that allows a gaseous mixture with the same composition as the desired ice analogue to meet the cooled substrate. Due to the large pressure differences of 7 - 8 orders of magnitude between the gas flow (1 - 20 mbar) and the vacuum chamber (10^{-7} mbar) the gas beam experiences adiabatic expansion in a supersonic jet. The sample holder is positioned in the zone of silence of the incoming gas flow where molecules do not collide with each other anymore and hence grow as amorphous solid ice on the substrate. As shown by Dohnálek et al. (2003), the density of the ice is dependent on the angle between gas flow and substrate and decreases with increasing angle, making the ice more porous. After deposition, the ice sample can be analysed at any desired temperature between 4.2 K and 300 K.

As shown in Figure 1.10, this cryocooler can be coupled with the FTIR spectrometer or with the THz TDS using a movable rack system that holds the rotatable cryostat as well as the shiftable THz TDS (blue in the sketch). A more detailed description of the two spectrometers will be presented in Section 1.3.2 and 1.3.3.

1.3.2 Fourier Transform Infrared Spectrometer

Fourier Transform Infrared (FTIR) Spectroscopy is an important tool necessary to identify molecular species in observed sources. In the CAS ice laboratory, molecular spectra of interstellar ice analogues are recorded with a FTIR spectrometer, which operates using the principles of a Michelson interferometer. Light of the wavelength λ_0 and intensity I_0 emitted by a coherent light source is divided into two equally intensive parts using a beam splitter that is mounted in a 45° angle relative to the incoming beam, as shown in Figure 1.11. Each of the beam parts is then reflected by a mirror but while one of the mirrors is a stationary one, the other moves along a path of length D . After reflection, the two beam parts experience interference at the beam splitter.

The interfering light is guided to a detector which observes a cosine shaped interferogram with a number of maxima N that depends on D as:

$$N = \frac{\lambda_0}{2} D. \quad (1.69)$$

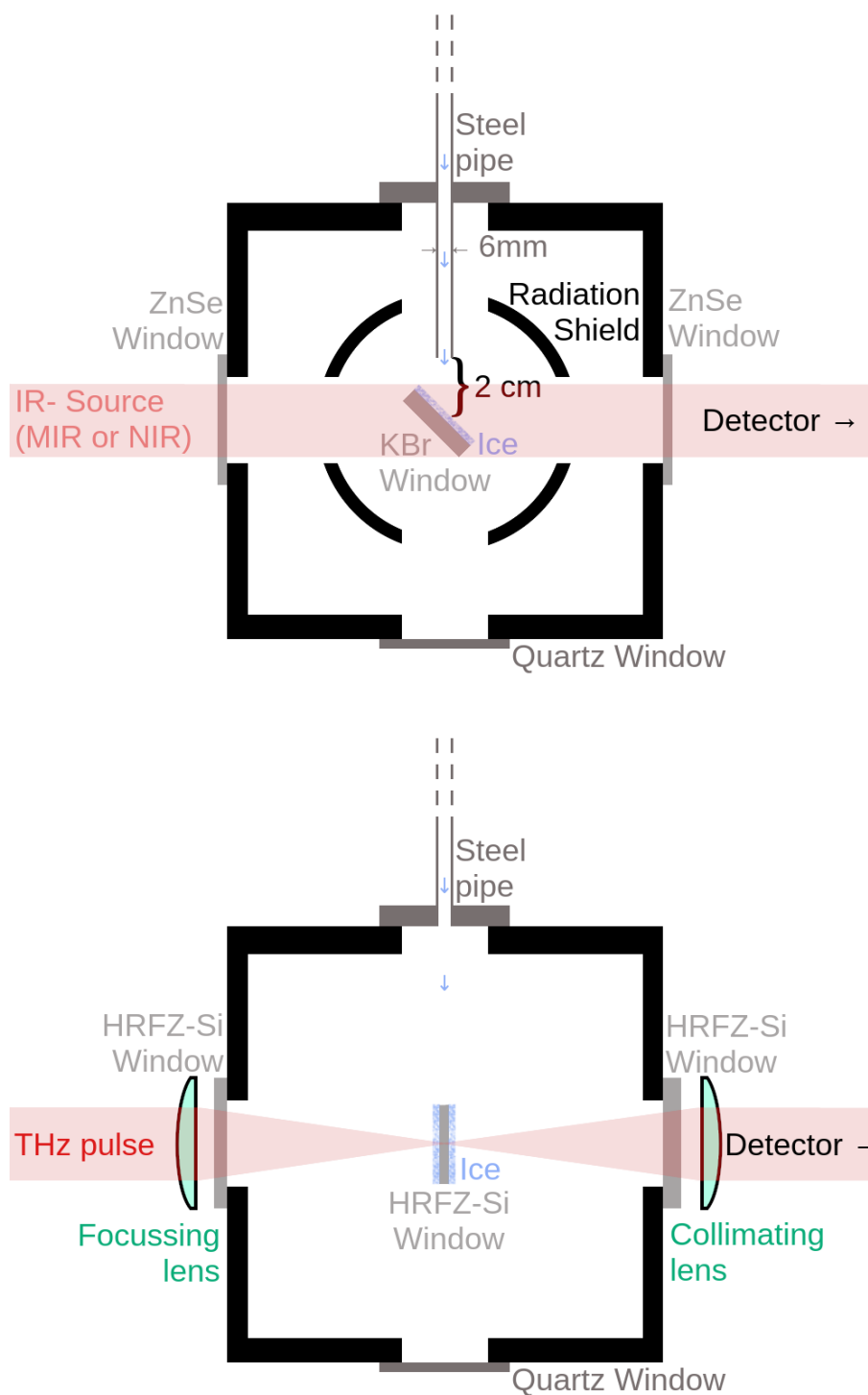


Figure 1.9: Sketch of the cooling chamber arrangement for the FTIR spectrometer (top) and the THz TDS (bottom).

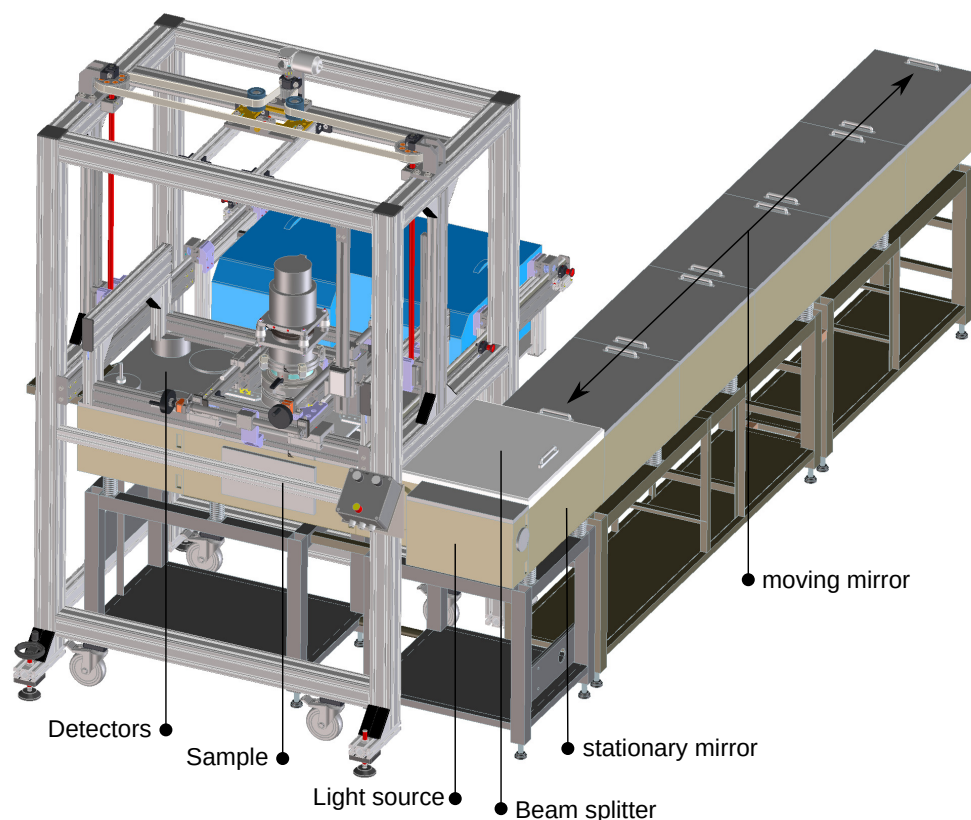


Figure 1.10: Sketch of the complete movable rack system, enabling the coupling of the cry-cooler either with the FTIR spectrometer or with the THz TDS. Credit: Christian Deysenroth.

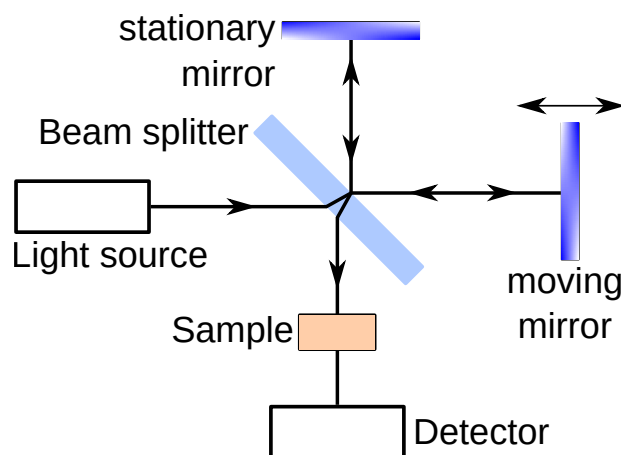


Figure 1.11: Schematic arrangement of a Michelson interferometer with a chemical probe in front of the detector. This Figure was inspired by Zinth & Zinth (2018).

The recorded interferogram of the laser with frequency $\nu_0 = 1/\lambda_0$ can be described with:

$$I(D) = \frac{I_0}{2} [1 + \cos(2\pi\nu_0 D)] \quad (1.70)$$

In the case of a FTIR spectrometer the light source is not a monochromatic laser but of polychromatic nature. I_0 then translates to $S(\nu) d\nu$ which is the input intensity $I(D = 0)$ at frequency $\nu + d\nu$. The resulting interferogram is then basically the sum of cosine waves of each monochromatic component and the spectrum can be retrieved as a Fourier transform of the incoming signal:

$$I(D) = \int_0^{\infty} \frac{I_p(\nu)}{2} [1 + \cos(2\pi\nu D)] d\nu. \quad (1.71)$$

The interferogram in a polychromatic source reads as $\tilde{I}(D) = 2I(D) - I(D = 0)$ and:

$$\tilde{I}(D) = \int_0^{\infty} S(\nu) \cos(2\pi\nu D) d\nu \quad (1.72)$$

generates the Fourier transform:

$$S(\nu) = \int_0^{\infty} \tilde{I}(D) \cos(2\pi\nu D) dD. \quad (1.73)$$

In the case that a sample is inserted into the beam path in front of the detector, the probe then absorbs those frequencies of the interfering light corresponding to the molecular vibrations of the compound and $S(\nu)$ becomes the absorption spectrum. If it is measured in a frequency range from ν_1 to ν_2 with $\nu_1 > \nu_2$ then the resolution is:

$$\delta\nu = \frac{\nu_1 - \nu_2}{N}. \quad (1.74)$$

This means that the resolution increases with a longer path length of the moving mirror. Some of the molecular vibrations can be expected in a certain frequency range so that astronomical observations of unknown molecules can give a first hint to what kind of chemical species might be a good candidate for laboratory inspection. A small selection of such frequency ranges and the corresponding molecular vibrations is shown in Table 1.2.

Table 1.2: Selection of spectral regions for various molecular vibrations of interest. Example values are given for pure ices.

Wavenumber (cm ⁻¹)	Bond	Example (cm ⁻¹)
3700 - 3100	OH & NH stretch	H ₂ O (3280) NH ₃ (3208 - 3375)
3000 - 2700	CH stretch	H ₂ CO (2884,2821) CH ₃ OH (2951, 2827)
2300 - 1900	X ≡ Y & X=Y=Z	CO (2139) CO ₂ (2343)
1300 - 1000	CO stretch	CH ₃ OH (1026)
900 - 500	OH, NH, NH ₂ bend	H ₂ O (760)

In the CAS ice laboratory it is possible to record high resolution $3.5 \times 10^{-3} \text{ cm}^{-1}$ spectra due to the long arm of the moving mirror, as seen in Figure 1.12. This is suitable for gaseous samples but for ice samples with broad absorption bands, such a resolution is not necessary and

experiments are usually conducted with $\delta\nu$ of 1 cm^{-1} or 2 cm^{-1} . After transmission through the sample, the incoming signal is recorded by one of five detectors: two working at room temperature, two which have to be cooled with liquid nitrogen ($T = 77 \text{ K}$) and one bolometer that can externally be attached to the FTIR spectrometer and must be cooled with liquid helium ($T = 4.2 \text{ K}$). The detectors that must be cooled are semiconductors of which the sensitivity increases with decreased working temperature.

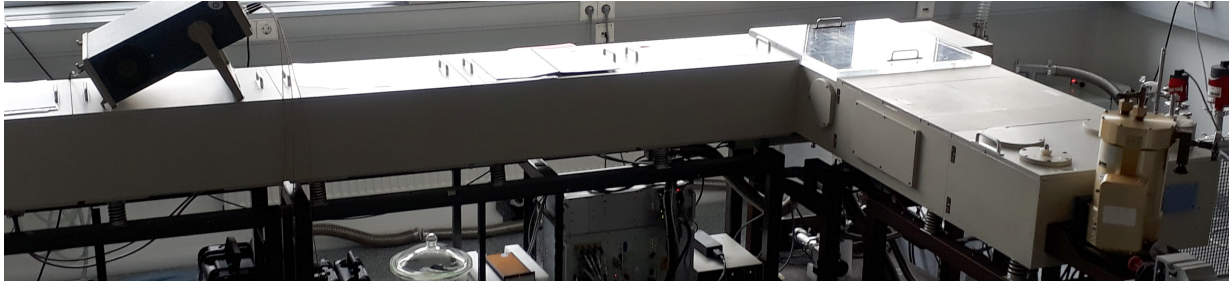


Figure 1.12: Complete view on the Fourier Transform Infrared Spectrometer. The arm for the movable mirror extends to the left part of the Figure while the beam splitter compartment is located below the reflecting cover. The sample compartment lies between the beam splitter and the detectors, seen at the right side of the Figure - including the external golden coloured bolometer.

1.3.3 THz time-domain Spectrometer

The knowledge of grain size and composition as well as of optical constants is an important part of describing physical processes in dense clouds. These quantities are needed to accurately describe continuum emission not only of dust but also of ice mantles that cover the dust grains. THz spectroscopy is not only able to investigate intermolecular vibrations and analyse the changes in the structure of the ice but it can also be used to measure dielectric properties. One quantity of special interest is the complex refractive index, that expresses how strongly light interacts with the medium:

$$n(\nu) = n'(\nu) + in''(\nu) = n'(\nu) + i \frac{c}{2\pi\nu} \alpha(\nu). \quad (1.75)$$

$n'(\nu)$ is the real part of the complex refractive index while $\alpha(\nu)$ is the already defined absorption coefficient. Directly related to the complex refractive index is the dielectric permittivity of an insulator, which relates how strongly a material gets polarised in the presence of an electric field:

$$\varepsilon(\nu) = n^2(\nu) = \varepsilon'(\nu) + i\varepsilon''(\nu). \quad (1.76)$$

These quantities can be derived using the advantages of THz spectroscopy, which compares an initial electric field $E_0(t)$ with the measured electric field $E_{tr}(t)$ after $E_0(t)$ traverses through a

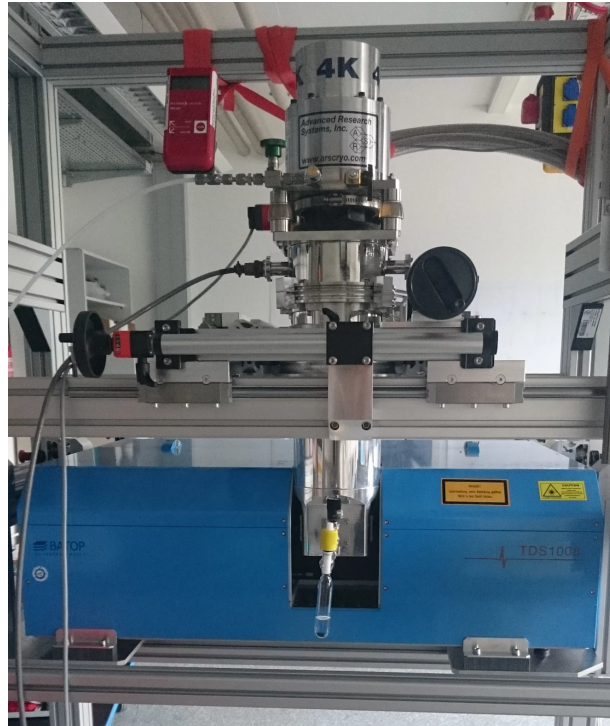


Figure 1.13: View on the THz time-domain spectrometer with the integrated cooling chamber. During measurements the spectrometer is sealed and purged with N_2 .

medium with a real-valued response function $G(t)$.

$$E_{tr}(t) = \int_{-\infty}^{\infty} G(t - t') E_0(t') dt'. \quad (1.77)$$

Using the Fourier transformation and substituting $2\pi\nu$ with ω , Eq. 1.77 in the frequency domain can be written as:

$$E_{tr}(\omega) = G(\omega) E_0(\omega). \quad (1.78)$$

The transit or more precisely the absorption and dispersion related to the complex refractive index of the material cause a drop in intensity as well as a phase shift of the incoming signal at the detector. $G(\omega) = E_{tr}(\omega)/E_0(\omega)$ is the resulting spectrum of the probe and the dielectric permittivity is related to $G(\omega)$ via the electric susceptibility $\chi(\omega)$:

$$\varepsilon(\omega) = \varepsilon_0 (1 + \chi(\omega)), \quad (1.79)$$

where ε_0 is the permittivity of vacuum and

$$\chi(\omega) = \chi'(\omega) + i\chi''(\omega) = \int_0^{\infty} G(t) e^{i\omega t} dt. \quad (1.80)$$

An important connection between $\chi'(\omega)$ and $\chi''(\omega)$ is made by the Kramers-Kronig relations:

$$\begin{aligned}\chi'(\omega') &= \frac{2}{\pi} \mathcal{P} \int_0^{\infty} \frac{\omega \chi''(\omega)}{\omega^2 - \omega'^2} d\omega \\ \chi''(\omega') &= -\frac{2\omega'}{\pi} \mathcal{P} \int_0^{\infty} \frac{\chi'(\omega)}{\omega^2 - \omega'^2} d\omega,\end{aligned}\tag{1.81}$$

where \mathcal{P} is the Cauchy principal value. Transferring this relation to $n'(\omega)$ and $\alpha(\omega)$ while simplifying the expression $\frac{c}{\omega} \alpha(\omega)$ to $k(\omega)$, also known as extinction coefficient, it holds that:

$$\begin{aligned}n'(\omega') - 1 &= \frac{2}{\pi} \mathcal{P} \int_0^{\infty} \frac{\omega k(\omega)}{\omega^2 - \omega'^2} d\omega \\ k(\omega') &= -\frac{2\omega'}{\pi} \mathcal{P} \int_0^{\infty} \frac{n'(\omega) - 1}{\omega^2 - \omega'^2} d\omega.\end{aligned}\tag{1.82}$$

Until recently the Kramers-Kronig relations were used to derive the complex refractive index knowing either $n'(\omega)$ or $k(\omega)$, but it must be noted that these are bound to the limitation $\omega > 0$. However, in collaboration with the Prokhorov General Physics Institute of the Russian Academy of Sciences I acquired the THz TDS data for a set of pure molecules, namely CO, H₂O, N₂ as well as CO₂ and it was possible for the first time to directly measure the complex refractive index and dielectric permittivity of CO using the changes in intensity and phase recorded with the THz TDS, which is shown in Figure 1.13.

The THz TDS in the CAS ice laboratory can operate at frequencies of 0.5 - 3.5 THz. In spite of its important benefit to enable direct measurements of optical constants, it has the disadvantage that the recorded signal is extreme sensitive to the humidity of air. Thus, the THz TDS compartment is purged by a strong N₂ gas flow, but up to this point it is only possible to safely measure spectra up to a frequency of 2.0 THz even though the humidity is $< 10^{-3} \%$. However, this factor will be improved in the future so that measurements within a bigger spectral range and better S/N ratios can be conducted.

1.3.4 Gas-line System

Before measurements of ice samples can be done, the composition of interest must first be prepared in the gas phase. For pure ices this is relatively easy as many compounds can be purchased with high purity, but as soon as the sample contains several species, the composition has to be prepared by mixing pure gases. The mixing ratio follows the ideal gas law:

$$pV = nRT,\tag{1.83}$$

where p is the pressure, V the volume, n the number of particles, R the ideal gas constant and T the temperature. The practical use proceeds under the premise that volume and temperature do not change, which indeed is true when the gases are slowly filled into a glass vessel. The mixing ratios of several compounds a, b, c, [...] can then be derived from their relative pressures:

$$\frac{n_i}{n_{\text{tot}}} = \frac{p_i}{p_{\text{tot}}},\tag{1.84}$$

where $i = a, b, c, [\dots]$ and $n_{\text{tot}} = n_a + n_b + n_c + [\dots]$ or $p_{\text{tot}} = p_a + p_b + p_c + [\dots]$, respectively.

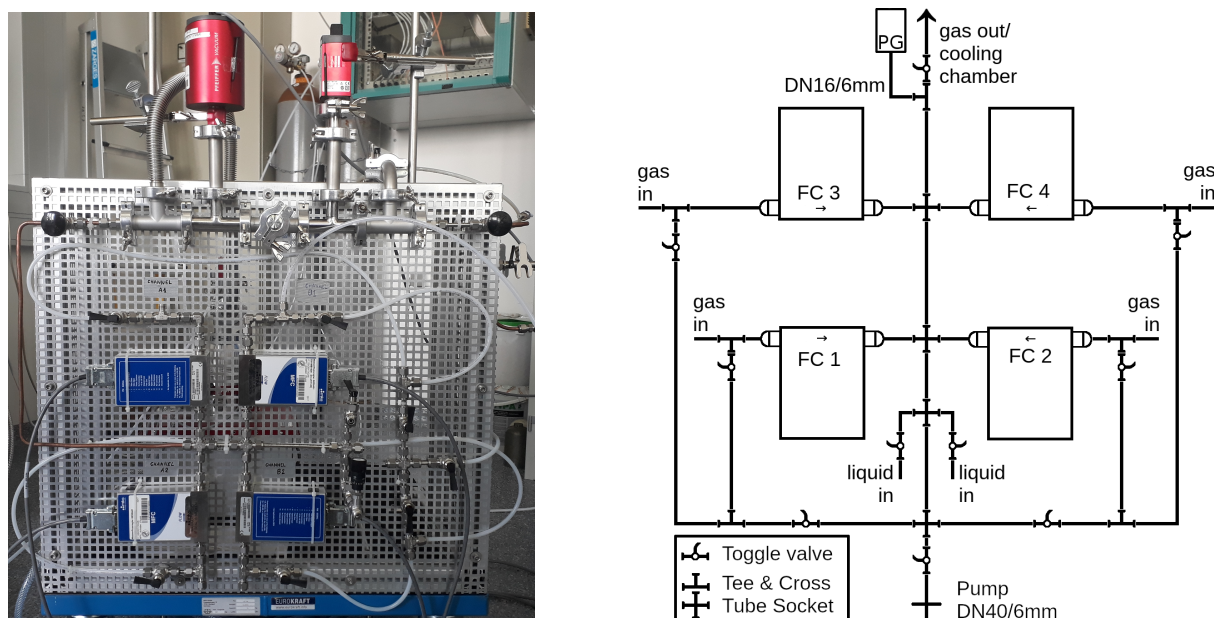


Figure 1.14: The gas-line system. Left: complete view after installation. Right: sketch of the gas-line components. FC: gas flow controller, PG: pressure gauge.

Another approach is the use of a gas-line system that controls the amount of chemical compounds entering the cooling chamber with gas flow controllers. Within the scope of my doctoral research, I designed and built a gas-line system that is theoretically able to produce gaseous mixtures of up to six components. The possibility to precisely control or even stop the flow allows the formation of not only mixed ices but also layered structures. As seen in Figure 1.14, the gas line system offers four ports for gaseous samples and two access points for liquid samples. The six connections then combine to one main line that is guided into the cooling chamber.

However, practical testing has revealed that the composition of the combined gas flow is changing during prolonged deposition and even the addition of an additional line that was supposed to help in the regulation of the gas flow could not improve the stability of the mixture. Therefore, instead of guiding the main line into the cooling chamber, the gas-line system is now used to prepare the gas mixtures in glass vessels, which are then connected to the gas inlet directed at the substrate. Using the gas-line system we were able to prepare mixtures of up to four components. Mixtures with a higher number of components are very challenging to prepare and even small aberrations from the partial pressures can lead to a gas mixing composition that is far off the desired ratios. Nevertheless, I was able to conduct experiments on mixed and layered ices that contain a number of compounds which reflect the actual composition in the ISM better than various laboratory work found in the literature.

1.4 This Thesis

After providing the theoretical and practical basis for this thesis, the following chapters will describe in detail the experiments that I conducted and address the results that I obtained during my analysis of the recorded data. My experiments focus on water based ices with different numbers of added components as well as changing ratios and structures. The description of my laboratory results is followed by a general conclusion and an outlook of subsequent work.

- **Chapter 2** describes experiments that aim to estimate the detectability of molecular oxygen in interstellar ices. In the IR regime, O₂ can be detected when it is sitting in a polar matrix, as is the case for H₂O. The strength of the O₂ absorption band dependent on the mixing ratios with H₂O is extracted from the recorded data and using theoretical predictions of the O₂:H₂O ratios in the pre-stellar core L1544, I calculated the observing time for the detection of O₂. I found that the detection of O₂ with JWST is not feasible with observation times > 100 h.
- **Chapter 3** discusses the spectral changes of CH₃OH absorption features in ices of increasing composition complexity as well as different structures which are of layered or mixed type. I present both shifts in the position of absorption maxima and changes in the band profiles that are caused by varying or missing interactions between the molecules dependent on the ice structure.
- **Chapter 4** focuses on the spectra of ice mantles of which the compositions are based on predictions of a L1544 chemical model. Layered and mixed ices are compared with each other and differences due to changing interactions between molecules are discussed. The experiments aim to help future observations in understanding the actual structure of ice mantles in L1544.
- **Chapter 5** describes methods for retrieving optical constants using THz TDS. The complex refractive index and dielectric permittivity are directly measured and compared to theoretical calculations found in the literature.
- **Chapter 6** presents the summary and conclusion of this thesis and provides an outlook on laboratory work that aims to continue the presented topics.

1.5 Bibliography

This introduction has been based on many books, articles and courses. If not denoted otherwise, then the descriptions of

- low mass star formation in Section 1.1 and the astrochemical network of ices in Section 1.2 were based on Stahler & Palla (2004), Tielens (2005), Cazaux et al. (2016), Klessen & Glover (2016), Yamamoto (2017) and the *Astrochemistry and Star/Planet Formation* IMPRS advanced course by Prof. Dr. P. Caselli.

- spectroscopic studies in Section 1.3 are based on Morse (1996) while spectroscopic methods in the IR regime (FTIR and Raman spectroscopy) are described in Bates (1978) and Colthup et al. (1990).
- THz TDS were based on Giuliano et al. (2019) and Peiponen & Zeitler (2017). The ideal gas law can be found in many literary works such as Halliday et al. (2010).

Chapter 2

O₂ signature in thin and thick O₂-H₂O ices

The contents of this chapter were published in the *Astronomy&Astrophysics* Journal.
Credit: Müller et al., A&A, 620, A46, 2018, reproduced with permission ©ESO

2.1 Abstract

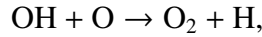
In this paper we investigate the detectability of the molecular oxygen in icy dust grain mantles towards astronomical objects. We present a systematic set of experiments with O₂-H₂O ice mixtures designed to disentangle how the molecular ratio affects the O₂ signature in the mid- and near-infrared spectral regions. All the experiments were conducted in a closed-cycle helium cryostat coupled to a Fourier transform infrared spectrometer. The ice mixtures comprise varying thicknesses from 8×10^{-3} to $3 \mu\text{m}$. The absorption spectra of the O₂-H₂O mixtures are also compared to the one of pure water. In addition, the possibility to detect the O₂ in icy bodies and in the interstellar medium is discussed. We are able to see the O₂ feature at 1551 cm^{-1} even for the most diluted mixture of H₂O:O₂ = 9:1, comparable to a ratio of O₂/H₂O = 10 % which has already been detected in situ in the coma of the comet 67P/Churyumov-Gerasimenko. We provide an estimate for the detection of O₂ with the future mission of the James Webb Space Telescope (JWST).

2.2 Introduction

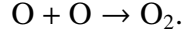
Astrochemical models have always dedicated special attention to molecular oxygen. With a cosmic abundance twice that of C, atomic O is the third most abundant element in space. In dense clouds, standard gas phase chemical models therefore suggest a comparable ratio of CO and O₂ after times $\geq 3 \times 10^5$ yr (e.g. Woodall et al. 2007), where O₂ is supposed to be formed especially via $\text{OH} + \text{O} \rightarrow \text{O}_2 + \text{H}$. The OH here can be formed by the dissociative recombination of H₃O⁺, $\text{H}_3\text{O}^+ + \text{e}^- \rightarrow \text{OH} + 2\text{H}$. However, observations with the Submillimeter Wave Astronomy Satellite (SWAS) by Goldsmith et al. (2000) towards Orion and with Odin by Larsson et al. (2007) towards ρ Oph A showed a significant difference between model predictions and measurements. The O₂ abundances found were more than 100 times smaller than those predicted by models

(Goldsmith et al. 2000). Better agreement with observations can be obtained if freeze-out of O atoms onto dust grains is taken into account in gas-grain chemical models (Bergin et al. 2000; Viti et al. 2001), with consequence surface production of H₂O and O₂, which may trap a significant fraction of oxygen, leaving only some atomic O and CO in the gas phase. Observations conducted by Liseau et al. (2012) led to a O₂ column density of $N(\text{O}_2) = 5.5 \times 10^{15} \text{ cm}^{-2}$ with an upper limit of abundance of $N(\text{O}_2)/N(\text{H}_2) \sim 5 \times 10^{-8}$ in warm gas ($T > 50 \text{ K}$) and to $N(\text{O}_2) = 6 \times 10^{15} \text{ cm}^{-2}$ with a little higher abundance in cold gas ($T < 30 \text{ K}$). Liseau et al. (2012) stated that detecting gas phase O₂ might be so difficult because the O₂ abundance is transient in ρ Oph A and O₂ is no longer detectable after $\sim 2 \times 10^5 \text{ yr}$. A relatively large amount of O₂ has only been found with *Herschel* in Orion as reported by Goldsmith et al. (2011). This source is quite warm ($\geq 180 \text{ K}$), leading to a grain temperature of $\geq 100 \text{ K}$. At this temperature the grains are warm enough to desorb H₂O ice and keep a large amount of oxygen with a big fraction in the form of O₂ in the gas phase. Another explanation for the high O₂ abundance found by Goldsmith et al. is that low-velocity C-shocks might be responsible for the increase of molecular oxygen in the gas phase.

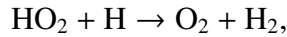
In the gas phase, the formation of O₂ via



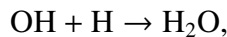
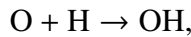
has been discussed by for example, Davidsson & Stenholm (1990) and Carty et al. (2006). According to Ioppolo et al. (2011), O₂ is formed in the solid state via



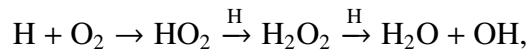
Possible other formation paths for molecular oxygen as suggested by Ioppolo et al. (2011) such as

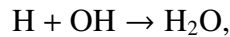


are still under discussion. With present CO molecules, Ioppolo et al. (2011) reports the formation of CO₂ rather than O₂. Also, the reaction $\text{HO}_2 + \text{H} \rightarrow \text{O}_2 + \text{H}_2$ can have a large activation barrier of 79.6 kJ mol^{-1} (Mousavipour & Saheb 2007) which makes it unlikely to proceed at low temperature in gas phase. Reaction-diffusion competition, however, increases the probability of overcoming the reaction barrier on the ice surface (Herbst & Millar 2008). In the solid state, O₂ is expected to form by the reaction of two O atoms, $\text{O} + \text{O} \rightarrow \text{O}_2$ (Tielens & Hagen 1982; Hama & Watanabe 2013). Dulieu et al. (2010) showed that the consecutive hydrogenation of O in the solid phase,

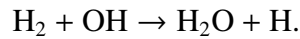
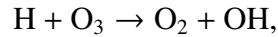
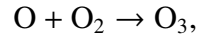


is a very efficient process. In addition to this path for water formation, molecular O₂ is an important component for the formation of H₂O on grains via the production of H₂O₂ (Ioppolo et al. 2008; Miyauchi et al. 2008),





or the formation of O_3 (Jing et al. 2012),



Cuppen & Herbst (2007) state that the reaction between H and OH represents the main route of H_2O formation in diffuse and translucent clouds as H is abundant in the gas phase there. In dense clouds, however, $\text{H}_2 + \text{OH}$ is the dominant path for H_2O formation while $\text{H} + \text{H}_2\text{O}_2$ also contributes significantly. OH radicals formed in the reactions $\text{H} + \text{O}_3$ and $\text{H}_2\text{O}_2 + \text{H}$ can then also react with H and H_2 as experimentally examined by Oba et al. (2012). While effective H_2O formation upon H irradiation of solid O_2 has been observed for temperatures of 12-28 K, Oba et al. (2009) showed that a co-deposition of H and O_2 on an Al substrate leads to formation of compact amorphous H_2O ice, consistent with astronomical observations in molecular clouds, as well as H_2O_2 up to a temperature of 40 K. Mokrane et al. (2009) and Romanzin et al. (2011) experimentally studied the reaction path of $\text{H} + \text{O}_3$ forming H_2O . Using dust grains as substrate, Mokrane et al. (2009) shows that the reaction of $\text{H} + \text{O}_3$ can efficiently form H_2O , while Romanzin et al. (2011) confirm this possible path working with a gold-coated copper substrate.

The detection of solid O_2 in the infrared (IR) is impeded as the molecular vibration of O_2 is infrared inactive. However, Ehrenfreund et al. (1992) have shown that, when O_2 is embedded in a matrix, the interaction with neighbouring molecules allows for the detection of a feature assigned to the vibration mode at 1551 cm^{-1} ($6.45 \mu\text{m}$). The band strength of this feature depends on the molecular composition of the matrix, in terms of the ratio between different components, and on the chemical polarity. In their work, Ehrenfreund et al. (1992) explored the effect of different ice compositions on the line position, line width and band strength of the O_2 feature. The authors find that strongly polar environments, such as water, as well as weakly polar environments such as CO, have no so strong effect on the O_2 molecule, as the presence of a non-polar environment, such as CO_2 molecules.

The search for molecular oxygen in solid form in astronomical objects using the O_2 infrared vibration was attempted in the late 1990s. Ehrenfreund & van Dishoeck (1998) observed a deeply embedded proto-stellar object, S140 in the S 140/L 124 complex, using the Short Wavelength Spectrometer (SWS) on-board the Infrared Space Observatory (ISO). Cold dense clouds were also observed with ISO-SWS and ground-based observations by Vandenbussche et al. (1999). However, the detection of solid O_2 appears to be a difficult task for these objects, and the mentioned studies resulted in the determination of upper limits. Recently, molecular oxygen in a concentration of up to 10 % relative to water has been found in the coma of the comet 67P/Churyumov-Gerasimenko, as Bieler et al. (2015) and Mousis et al. (2016) have recently reported. Successive work of Keeney et al. (2017) comparing line of sight measurements of O_2 conducted with the Alice far-ultraviolet spectrograph on Rosetta with in situ measurements of the Rosetta Orbiter Spectrometer for Ion and Neutral Analysis (ROSINA) hint to even higher abundances of 11-68 % with a mean value of 25 %, although the comparison is not easily done.

This detection opens new scenarios and raises interest in the possibility of detecting molecular oxygen in cometary and interstellar ice. Recent work by Taquet et al. (2016) show that solid O₂, with a molecular ratio to water ice similar to those measured in comet 67P, can be produced in molecular clouds with relatively low H to O abundance ratio in the gas phase, high densities ($\geq 10^5 \text{ cm}^{-3}$) and dust temperature around 20 K, higher than that typically measured in interstellar dark clouds (10-15 K).

In this paper, we implement new laboratory experiments based on the work of Breukers (1991) as presented in Ehrenfreund et al. (1992), where the 6.45 μm molecular oxygen feature was measured in an ice mixture of H₂O:CO:CO₂:O₂ = 2:2:0.5:1 with unknown thickness. On the basis of this experiment, we have extended our analysis to different molecular composition ratios, as well as to different thicknesses. We have limited our analysis to the ice mixtures composed of H₂O and O₂ to study solely the impact of the water matrix on the imbedded O₂ feature, even though this molecular composition is not necessarily representative of the average composition of astrophysical ice. Thus, we put strong emphasis on the dependence of the ice composition on the O₂ band strength. Further studies with different mixtures, inclusive of CO and CO₂ at a 20-25 % level, as found in interstellar ices (e.g. Boogert et al. 2015) will be presented in a future paper. This paper is structured as followed: We describe in Section 2.3 the methods and the setup used in the experiment. In Section 2.4 we present the experimental results and in Section 2.5 we discuss our measurements. Section 2.6 is dedicated to the astrophysical implications of our experiments.

2.3 Methods

The experiments were conducted in the recently developed cryogenic laboratory at the Center for Astrochemical Studies (Max Planck Institute for Extraterrestrial Physics) in Garching (Germany). The experimental setup is composed by a high power cryocooler, purchased from Advanced Research Systems (ARS), hosted in the sample compartment of a high resolution Bruker IFS 120/5HR Fourier Transform Infrared (FTIR) spectrometer.

The cryocooler consists of a cold finger situated into a vacuum chamber, with a final vacuum of 10^{-7} mbar. A sample holder (model SHO-1A, also from ARS) is placed at the end of the cold finger, suited to be cooled down to a minimum temperature of 4.2 K. The temperature is controlled by a Lake Shore Cryotronics (model 335) temperature controller, equipped with DT-670 Silicon Diodes sensors. The measured lowest temperature reached by the sample holder is 5 K. The sample holder can be complemented with substrates of different materials, on top of which the ices can be formed by condensation from the gas phase. The substrate used for this set of experiments is made of potassium bromide (KBr), which offers, with a transmission of $> 90\%$ through the whole observed spectral range, the best optical properties in the desired frequency range. The appropriate gas mixture is introduced into the cryocooler by an expansion through a 6 mm stainless steel pipe, attached to a gas reservoir. The exit of the pipe is placed at a distance of approximately 2 cm from the sample holder, facing the substrate. In this set of experiments the gas mixtures were deposited onto the substrate kept at a temperature of 10 K.

The vacuum chamber is complemented by two ZnSe optical windows, and one quartz window

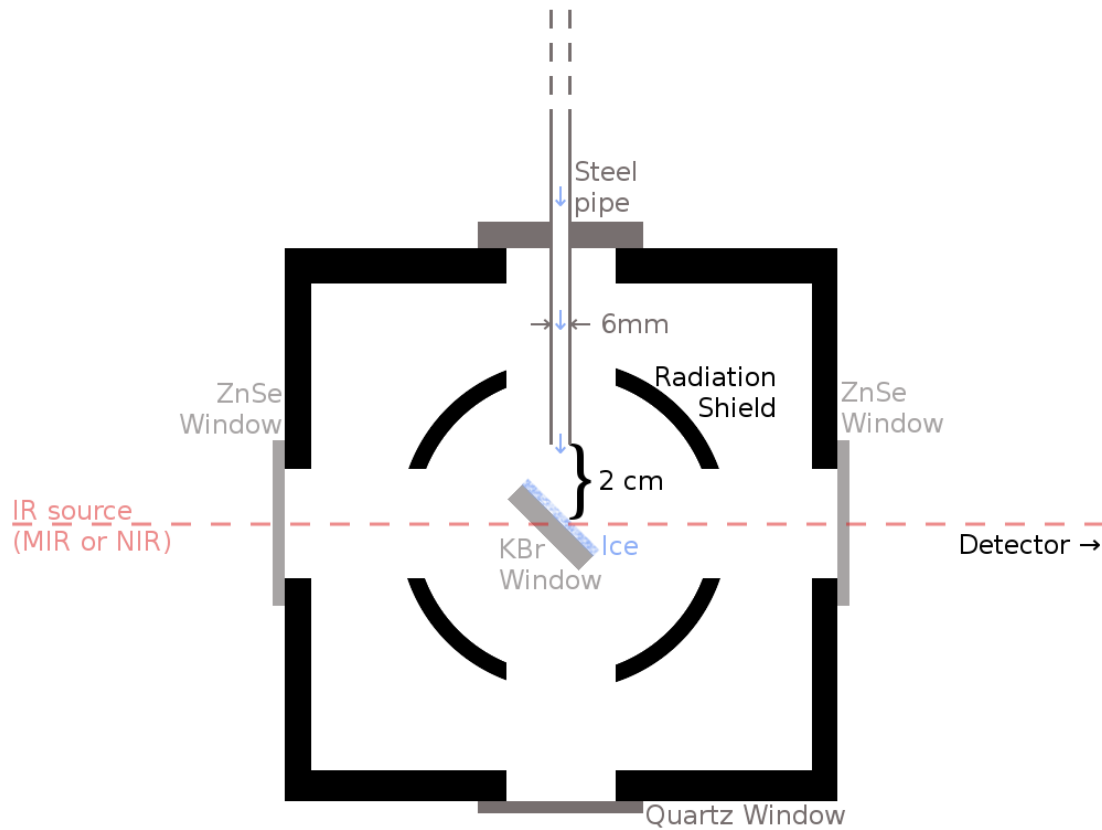


Figure 2.1: Sketch of the cryocooler set-up.

for visual inspection. For the measurements in the mid-infrared (MIR) and in the near-infrared (NIR) spectral regions, with a resolution of 2 cm^{-1} , a DTGS (deuterated triglycine sulphate) detector and a nitrogen cooled InSb detector, respectively, were used. A globar lamp was used as radiation source. A scheme of the arrangement of the cryocooler and its main components is illustrated in Figure 2.1.

The gas mixtures were prepared in a 2 liter glass flask by using standard manometric techniques. The ratios of H_2O to the O_2 were adjusted by measuring the pressure inside the glass flask following the ideal gas law

$$pV = nRT, \quad (2.1)$$

whereas the number of H_2O and O_2 particles is set by the isotherm relation

$$\frac{n_i}{n_{tot}} = \frac{p_i}{p_{tot}} = \frac{V_i}{V_{tot}}, \quad (2.2)$$

where n_i is the particle number, p_i the partial pressure and V_i the partial volume of the gas i , in our case H_2O and O_2 . The total pressure p_{tot} is the sum of all partial pressures $\sum_i p_i$, $n_{tot} = \sum_i n_i$ and $V_{tot} = \sum_i V_i$.

The gas mixture composition used for each experiment is outlined in Table 2.1. Distilled water that had been degassed in a freeze-pump-thaw cycle three times, and oxygen with a purity of 99.999 % were introduced in the cooling chamber under high vacuum with a base pressure of 10^{-6} mbar. The deposition time was varied starting with deposition times of 30 s, using a moderate deposition rate, and increasing the deposition time up to 3 min with fast deposition rate, so that thicknesses of $0.03 \mu\text{m}$ (~ 100 MLs) up to $3 \mu\text{m}$ (~ 10000 MLs), with an uncertainty of 20-30 %, could be analysed. In the fourth column of Table 2.1, the water column density for thick ice reached after 1 minute of deposition time for each ice mixture is listed; the derived water ice thickness and the oxygen column density are indicated in columns 5 and 6, respectively. We note that the latter has a high error for water rich ices due to limits in determining the area of the weak oxygen feature that is overlapped by the water bending vibration mode. Also, a comparison of $N_{\text{H}_2\text{O}}$ and N_{O_2} to estimate the real ice composition is difficult for oxygen rich ices due to monomer and dimer features in the water bands.

The thickness of the deposited ice has been calculated from the area of the three bands characteristic of the water ice spectral signature. First, the column density N has been estimated from the band area for the water component, following the relation

$$N = \ln(10) \cdot \frac{\text{Area}}{A}, \quad (2.3)$$

and for A using the band strength values from Hagen et al. (1981) and Gerakines et al. (1995). The factor $\ln(10)$ originates in the relation of the optical depth $\tau = Abs \cdot \ln(10)$ where Abs is the absorbance. τ is incorporated into the area. Then, the thickness d (cm) has been calculated assuming

$$d = \frac{N \cdot M}{\rho \cdot N_A}, \quad (2.4)$$

where N is the column density (molecules cm^{-2}), ρ the density (g cm^{-3}), N_A the Avogadro constant (molecules mol^{-1}) and M the molecular mass (g mol^{-1}). The total thickness has been estimated by considering the water to oxygen molecular ratio and scaling the thickness value accordingly. For this estimation we assumed that the ice molecular composition remains constant over the deposition time scale. There is no spectroscopic evidence which can prove that this assumption is correct, but assuming that the sticking coefficient is not varying significantly for the two components water and oxygen, we can estimate to produce a quite uniformly mixed ice. This is the general assumption used for this kind of experimental set-ups.

The cold KBr substrate is mounted with an angle of 45° with respect to the molecular beam direction. This configuration allows the deposition of the gas to take place simultaneously with the recording of the spectra. In the vacuum chamber, the molecules expand to a collisionless beam and the ice formed on the top of the substrate has a porous structure, with an expected density of approximately 0.8 g/cm^{-3} (Dohnálek et al. 2003; Snels et al. 2011). The thickness values provided for these experiments have been scaled to the direction normal to the substrate surface, to correct for the 45° angle of the substrate with respect to the spectroscopic path.

The measurements in our experimental setup work in transmittance and thus we would take an ice deposition on both sides of the substrate into account. Nevertheless, we experimentally confirm that ice was deposited only on the side of the substrate that faces the steel pipe. We

Table 2.1: Gas mixture composition, expressed as partial pressure ratio, the water column density ($N_{\text{H}_2\text{O}}$), the water ice thickness $d_{\text{H}_2\text{O}}$ and O_2 column density (N_{O_2}) after a total deposition time of 1 min for thick ice for each experiment presented in this paper. The uncertainty for $N_{\text{H}_2\text{O}}$ and $d_{\text{H}_2\text{O}}$ lie within 20-30 %.

Exp	H ₂ O	O ₂	$N_{\text{H}_2\text{O}}/10^{18}$ mol cm ⁻²	$d_{\text{H}_2\text{O}}$ (μm)	$N_{\text{O}_2}/10^{18}$ mol cm ⁻²
#1	9	1	1.94	0.68	0.02
#2	4	1	1.42	0.50	0.02
#3	3	1	1.12	0.39	0.07
#4	2	1	2.17	0.77	0.21
#5	1	1	0.95	0.33	0.28
#6	1	2	0.58	0.21	0.16
#7	1	4	0.25	0.09	0.32
#8	1	9	0.08	0.03	0.25

used the laser interference method to ensure that no significant amount of ice is deposited on the substrate face opposite to the gas inlet.

2.4 Results

2.4.1 O₂ features in thin and thick ice samples

Figure 2.2 shows the whole observed spectrum for the different composition ratios after same deposition time. The figure clearly shows the H₂O stretching mode at 3280 cm⁻¹, the H₂O combination mode at 2200 cm⁻¹, the H₂O bending mode at 1660 cm⁻¹ and the H₂O libration mode at 760 cm⁻¹. Moreover, the O₂ feature can be found at 1551 cm⁻¹. In spectra #2, #6, #7, and #8, features due to CO₂ contamination are present at 2343 cm⁻¹ and at 660 cm⁻¹. The H₂O:O₂ = 2:1 spectrum shows the saturation of the stretching mode because of different deposition conditions compared to the other experiments.

In the thick ice layer regime (estimated thicknesses ranging between 1 and 3 μm) the oxygen feature is visible at all the investigated molecular ratio. Our limit cases are the mixture in excess of water (experiment #1) and the mixture in excess of oxygen (experiment #8). It is convenient to divide the analysis into two parts, one for the experiments from #1 to #4, and a second for the experiments from #5 to #8. In the first part, excess of water at different molecular ratios is investigated. In these experiments, the oxygen feature is overlapped to the bending vibration mode of water, making its detection increasingly difficult as the water becomes predominant in the molecular ratio (cf. Figure 2.3). Nevertheless, even with a water to oxygen ratio of 9:1, the oxygen feature is still visible in our recorded spectrum, as it shown in Figure 2.3.

For the thin ice, we conducted separate experiments in order to monitor the dependence of the O₂ band position on the physical conditions of the thin ice. The spectrum of the thin H₂O:O₂ = 2:1 ice (thickness 0.022 - 0.053 μm) is shown enclosed around 1660 cm⁻¹ in Figure 2.4. Presenting even thinner ice, Figure 2.5 shows the first three deposition steps (thickness 0.008 -

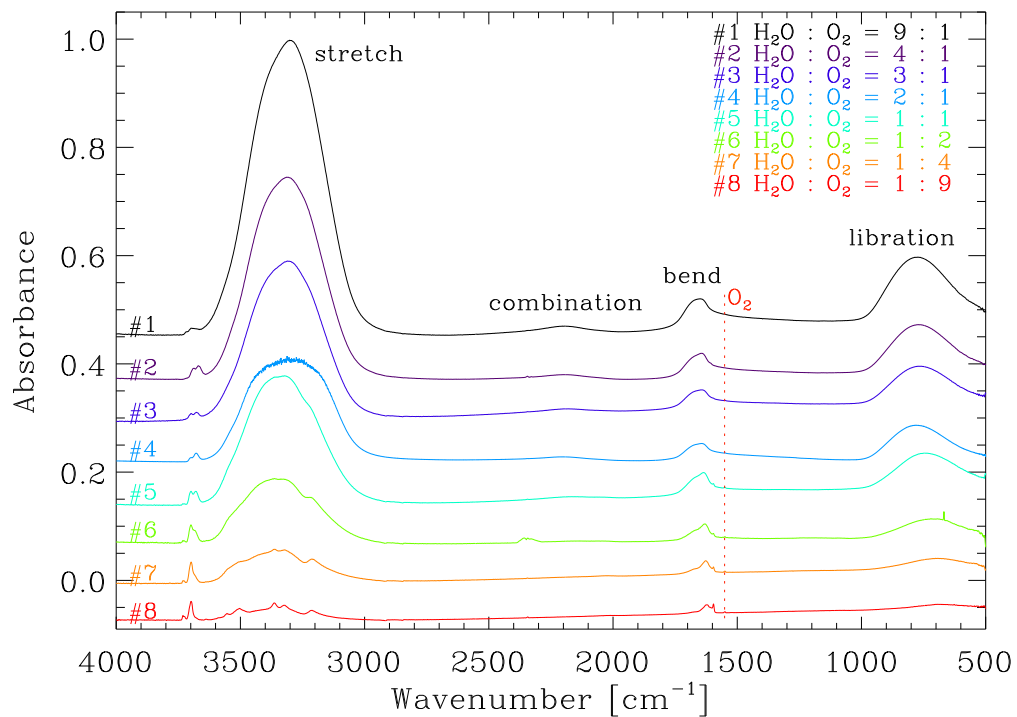


Figure 2.2: Spectra of all H₂O-O₂ composition ratios for thick ice with same deposition time of 1 min each. The number of H₂O monolayers here goes from 80 ML (thickness $\approx 0.03 \mu\text{m}$) for H₂O:O₂ = 1:9 to 1900 ML (thickness $\approx 0.68 \mu\text{m}$) for H₂O:O₂ = 9:1. The spectra for the different compositions are shifted in the absorbance scale for helping their visualization. The vertical red dashed line indicates the O₂ band position at 1551 cm⁻¹.

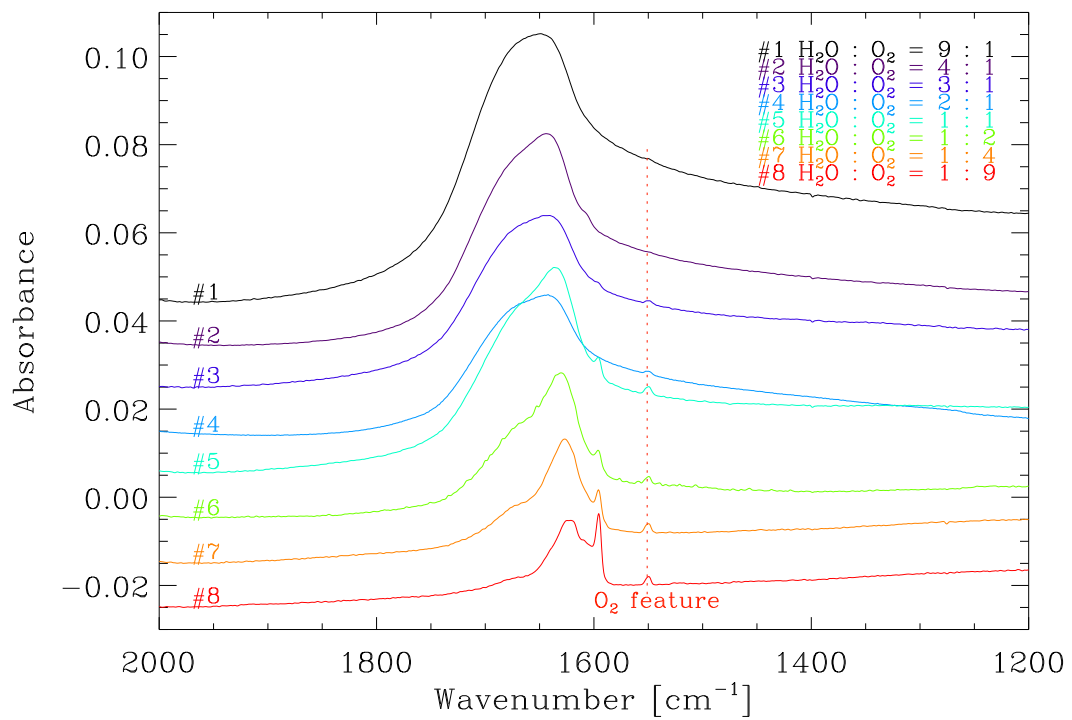


Figure 2.3: Magnification of spectra of Fig. 2.2 around the O₂ feature (marked by the vertical red dashed line) for all H₂O-O₂ mixtures for thick ice.

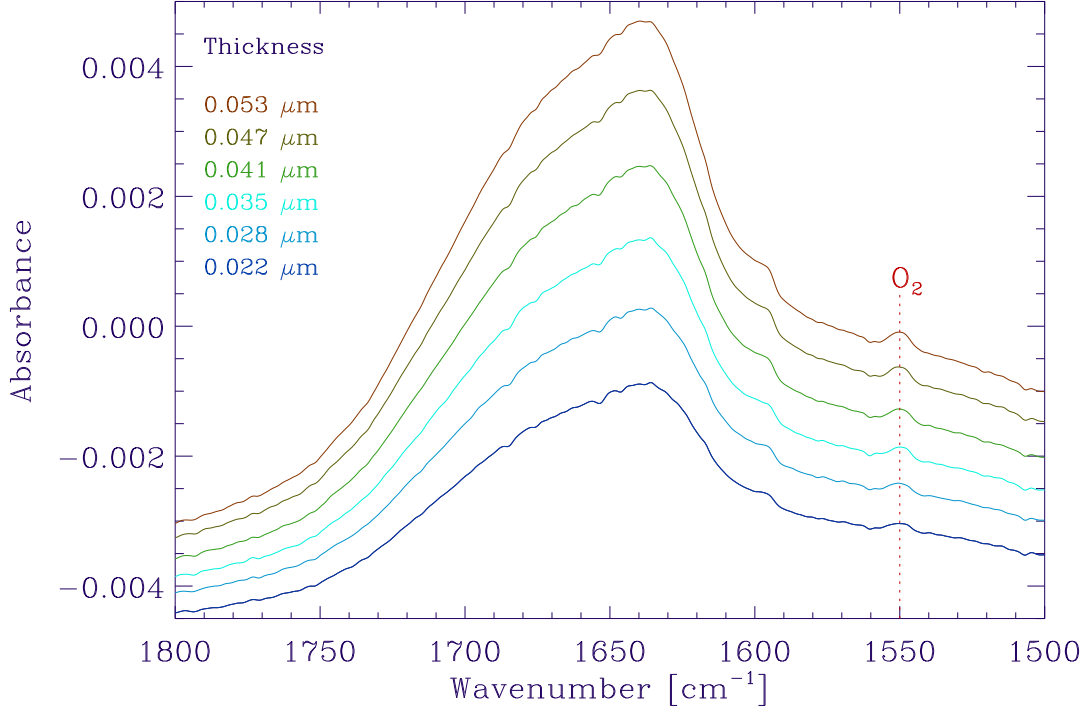


Figure 2.4: Magnified spectra of H₂O:O₂ = 2:1 mixture around the O₂ feature; the ice thicknesses is between 0.022 and 0.053 μm for thin ice.

0.022 μm) in order to enhance the visibility of the O₂ feature of which we see hints of the band at 1551 cm^{-1} also for the thinnest ice. The water bands assume the characteristic features of water trapped in a matrix, as can be observed from Ehrenfreund et al. (1996).

In the experiments in excess of oxygen, the O₂ feature is progressively isolated from the water bending feature. Its spectral characteristics, though, are not varying significantly with the change in the H₂O to O₂ ratio, in terms of frequency shift and band profile. Therefore, these spectra offer the best conditions for the estimate of the O₂ band strength. The band strength A is given as

$$A = \int \sigma(\tilde{\nu})d\tilde{\nu} = \frac{1}{N} \int \tau(\tilde{\nu})d\tilde{\nu}, \quad (2.5)$$

where $\sigma(\tilde{\nu})$ is the cross-section (cm^2) and $\tau(\tilde{\nu})$ the optical depth for a given wavenumber $\tilde{\nu}$ (cm^{-1}). Using

$$\tau = Abs \cdot \ln(10), \quad (2.6)$$

where Abs is the measured absorbance of the O₂ feature, we get

$$\int \tau(\tilde{\nu})d\tilde{\nu} \approx Abs \cdot \ln(10) d\tilde{\nu}. \quad (2.7)$$

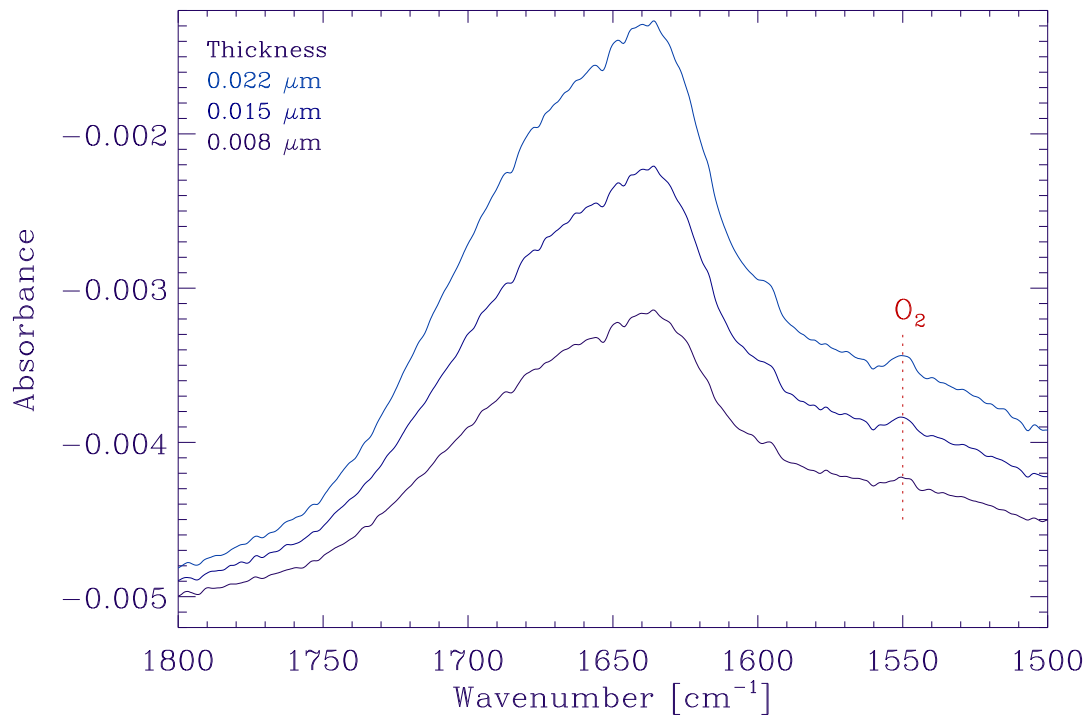


Figure 2.5: Magnified spectra of $\text{H}_2\text{O}:\text{O}_2 = 2:1$ mixture around the O_2 feature; the thicknesses is between 0.008 and $0.022 \mu\text{m}$ for thin ice.

We measured $d\tilde{\nu} = 10 \text{ cm}^{-1}$ and for O_2 the column density $N = 3.01 \times 10^{22} \text{ molecules cm}^{-3} \cdot d$. The derived band strengths for the different ice mixtures and a comparison with the values found by Ehrenfreund et al. (1992) can be found in Table 2.2.

For comparable experiments, where the values of $\text{H}_2\text{O}/\text{O}_2$ presented in this work are equal to those presented by Ehrenfreund et al. (1992), the values of the band strength agree with a factor of approximately two. This difference is most likely due to the influence of CO and CO_2 in the experiments conducted by Ehrenfreund et al. (1992), which enhance the oxygen band strength.

As the feature of solid O_2 is present at 1551 cm^{-1} , there exists the possibility for observable overtones in the NIR. While we don't expect to see any O_2 features near 3102 cm^{-1} ($3.22 \mu\text{m}$) due to the strong water signal, we looked for the next possible overtone at 4653 cm^{-1} ($2.15 \mu\text{m}$). Even, for the thick ice with $3 \mu\text{m}$ thickness, there is no O_2 feature to be found near 4653 cm^{-1} .

2.4.2 Dangling bonds

We note that in our experiments we dealt with a porous amorphous ice structure. For this reason, in the recorded spectra we observe the features assigned to the presence of the so-called dangling bonds, that is, features arising from the OH stretching vibration of water molecules that are not engaged in a intermolecular interaction with the ice bulk. Although the analysis of the spectral

Table 2.2: Columns 1 and 2: Band strength of O₂ for the different O₂-H₂O ice compositions. The values have been averaged for the analysis of different ice thicknesses.

H ₂ O : O ₂	A (cm molec ⁻¹)	Mixture ^a	Ratio ^a	A ^a (cm molec ⁻¹)
9 : 1	7.6e-21			
4 : 1	9.6e-21			
3 : 1	1.5e-20			
2 : 1	4.8e-20	H ₂ O : CO : CO ₂ : O ₂	2 : 2 : 0.5 : 1	1.0e-19
1 : 1	3.9e-20	H ₂ O : CO : O ₂	1 : 1 : 1	0.7e-19
1 : 2	6.4e-20			
1 : 4	1.6e-19			
1 : 9	3.2e-19			
		CO : O ₂	1 : 1	0.7e-19
		CO ₂ : O ₂	1 : 1	6.0e-19
		CO ₂ : O ₂	10 : 1	3.0e-18

^a Comparison with band strength as derived by Ehrenfreund et al. (1992). H₂O to O₂ ratios with equal values to those used in our work have been aligned to facilitate comparison.

signature of the dangling bonds is not directly applicable to the comparison with astronomical observations, for which no detection is currently available, we believe that studying the way in which the presence of oxygen affects the features ascribed to the dangling bonds can provide useful information for future laboratory experiments. In Figure 2.6 the spectral region of the dangling bonds for thick ice corresponding to the different H₂O-O₂ mixtures and the pure water is shown. The increasing steepness of the spectra towards 3500 cm⁻¹ relate to the increasing ratio of H₂O to O₂ as the stretch feature of water rises in intensity with increasing water abundance. The positions of the dangling bond features can be found in Table 2.3.

Figure 2.6 shows a red shift of the dangling bonds peaks going from the pure water to the

Table 2.3: Gas mixture composition and position of the dangling bonds (with shoulder feature position where present) for each experiment presented in this paper.

Exp	H ₂ O : O ₂	Dang. bond #1 (shoulder)/cm ⁻¹	Dang. bond #2 (shoulder)/cm ⁻¹
#1	9 : 1	3717	3698
#2	4 : 1	3689	3669
#3	3 : 1	3698	3678
#4	2 : 1	3693	3678
#5	1 : 1	3731 (3725)	3699 (3680)
#6	1 : 2	3731 (3727)	3699 (3686)
#7	1 : 4	3731 (3727)	3699 (3685)
#8	1 : 9	3731 (3725)	3699 (3680)

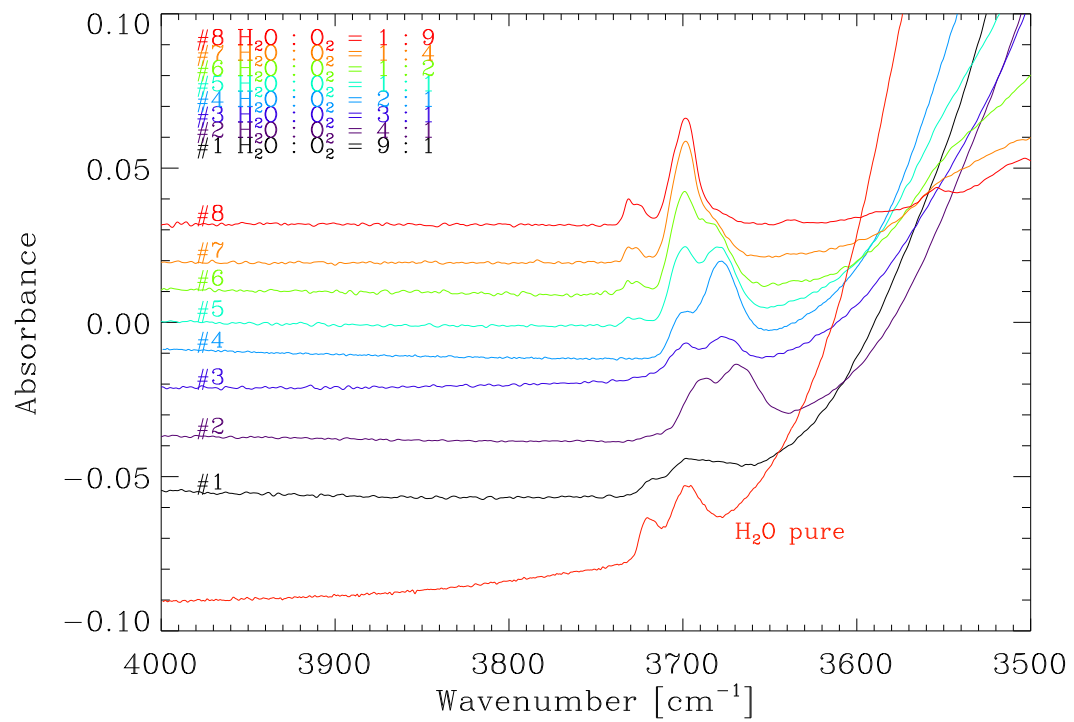


Figure 2.6: Thick-ice absorption spectrum of H₂O:O₂ mixtures compared to pure water. To enable a better overview, similar to Fig. 2.2, the spectra of the different mixtures have been shifted.

H₂O:O₂ = 2:1 mixture, from 3697 cm⁻¹ (2.705 μm) and 3683 cm⁻¹ (2.715 μm) to 3698 cm⁻¹ (2.704 μm) and 3678 cm⁻¹ (2.719 μm). The change in the spectroscopic feature of the dangling bonds for the water and oxygen ices with respect to pure water ice is in agreement with previous experiments performed by Palumbo et al. (2010), in which the effect on the profile of the dangling bond feature for an ice mixture of approximately 20 % of oxygen in water is reported. Their study can be compared to our H₂O:O₂ = 4:1 mixture. For oxygen-rich ice mixtures, the peak shape and position is probably influenced by the presence of water monomers and dimers embedded in the oxygen matrix, as reported in Ehrenfreund et al. (1996).

2.5 Discussion

We decided to limit our study to the case of the molecular oxygen complexes with water and to extend the amount of molecular ratio explored going from ice mixtures in excess of water to excess of oxygen, in order to have a complete overview of the molecular oxygen signature in different astrophysical environments. Furthermore, for each experiment we have analysed the IR spectra in the thin and thick ice layer regimes, showing that the oxygen spectral signature does not exhibit different characteristics, in terms of band position and shape, with respect to the two approaches. The molecular vibration of O₂ by itself is inactive in the infrared since the dipole moment doesn't change upon molecular vibration. Nevertheless, the interaction with the water matrix breaks the electron symmetry and induce a small dipole moment, which allows for the detection in the IR region.

In the thin ice layer regime, in which the thicknesses of the ice layer (estimated for the water component) varies between 0.008 and 0.053 μm, the oxygen feature has been observed only in the most favourable case, that is, the H₂O:O₂ = 2:1 mixture (experiment #4). In this molecular ratio, the band strength of the oxygen feature is enhanced, as shown by Ehrenfreund et al. (1992), the instrumental detection limit in dealing with a low column density is overcome, and the observation of a low intensity band is possible. For even thinner ices however, we don't expect the shape and position of the O₂ feature to change much, but the detection of O₂ depends on the total column density, so in the end it depends on the ice thickness as well as dust number density. In the remaining cases the low intensity of the band signal did not allow for a detection. The frequency position measured in the experiment #4 is 1551 cm⁻¹ (6.45 μm). In order to increase the S/N for the thin H₂O:O₂ = 2:1 ice, the recording of the spectra was performed with a higher number of recorded cycles (2048 record cycles; for comparison: 1184 record cycles for thick ice). That way, the noise was reduced in order to obtain a S/N ≲ 3 even for the thinnest ice.

In addition, we compared the dangling bond features of pure water with that of the H₂O:O₂ = 9:1 mixtures. As already observed by Palumbo et al. (2010), the profile of the dangling bond feature depends on the presence of other species mixed-in with water ice. The presence of oxygen affects the dangling bonds profile in term of intensity and shape. Their profile may be related to the microstructure of the deposited ice. As can be observed from Figure 2.6, the H₂O:O₂ ratio in the ice is affecting significantly the spectral characteristic of the water dangling bonds. Going from the water rich to oxygen rich mixtures, we observe a progressive change in the relative intensity of the two main features and a shift in their position. For oxygen rich

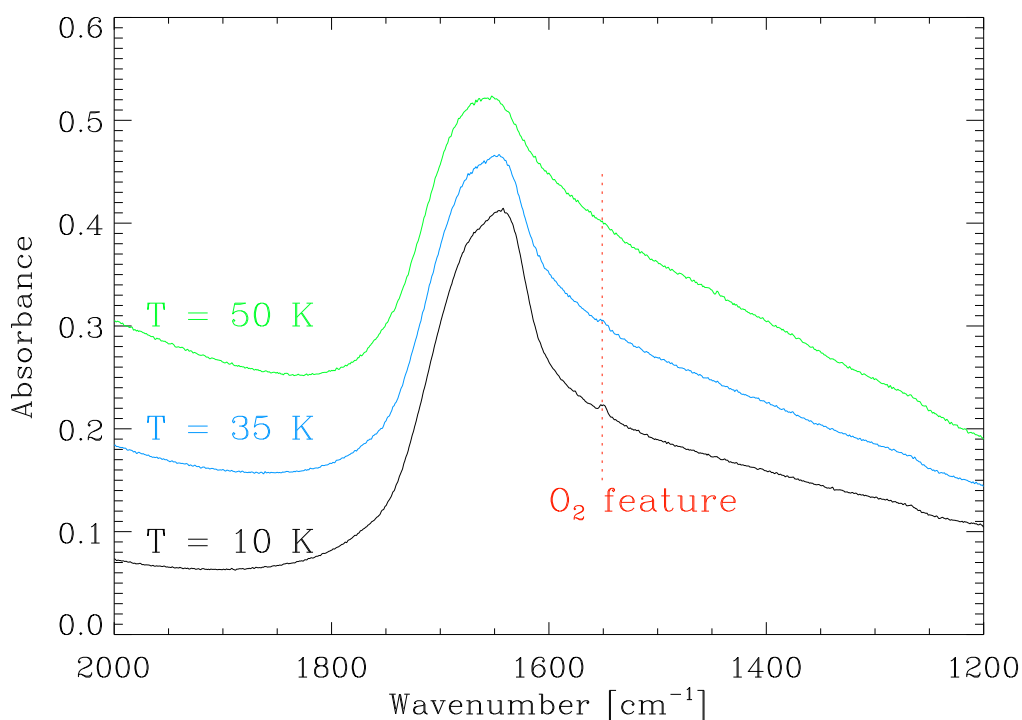


Figure 2.7: Behaviour of the O₂ feature (marked by the vertical dashed line) for H₂O:O₂ = 2:1 while heating the ice from 10 K to 50 K.

mixtures, we observe a predominant sharper feature at lower frequencies, while the water rich mixtures exhibit a smoother profile and similar relative intensities of the two components. The mixture with a similar water to oxygen ratio shows a profile which is in between the extremes. From this consideration we can relate the shape of the dangling bonds bands with the molecular composition of the bulk ice, allowing an identification of the enrichment of the ice in one or the other species. However, a detailed analysis of the effect of the structure of the ice on the dangling bond characteristic is outside the scope of this work.

Figure 2.7 shows the behaviour of the O₂ feature upon heating. Observed O₂ features started to vanish when the probes were heated to 35 K. At this temperature, the O₂ molecules trapped on the amorphous water ice matrix start to evaporate (cf. Bar-Nun et al. 1987). At a temperature of 50 K, the O₂ features were completely absent. Above this temperature the O₂ is not trapped by the porous amorphous solid water any more and the O₂ is desorbed from the deposited ice. This observation is consistent with the experiments conducted by Ayotte et al. (2001).

2.6 Astrophysical implications

Our experimental approach intends to explore astrophysical scenarios. The experiments dedicated to the thin ice layer regime (number of monolayers < 150; counted using the thickness and density of the ice) simulate the conditions in the dense interstellar medium more adequately (Öberg 2016), while the experiments in the thick layer regime attempt to extend the physical conditions relative to the centre of pre-stellar cores as well as in the midplane of protoplanetary disks, where pebbles and icy bodies precursors of comets and planetesimals with ice thicknesses > 200 ML form (e.g. Bieler et al. 2015). There is a lack of observational data proving the presence of molecular oxygen in ISM ice, while O₂ has been recently detected in the coma of the comet 67P/Churyumov-Gerasimenko (Bieler et al. 2015; Mousis et al. 2016).

Our experimental data show that the detection of the O₂ feature in thin ices is much more difficult compared to the thick ones, and the only molecular composition allowing the laboratory detection is the H₂O:O₂ = 2:1, which is unrealistic for the ISM ice composition. However, predictions by astrochemical models for pre-stellar cores, such as L1544, indicate that the icy mantles can reach thicknesses close to the thick ice regime in these experiments (e.g. Vasyunin et al. 2017). On the other hand, the mixture with a molecular ratio H₂O:O₂ = 9:1 will account for a realistic proportion like it was observed in the cometary coma of 67P/Churyumov-Gerasimenko with a mean value of 3.80 ± 0.85 %.

2.6.1 Chemical modelling

We studied which ice structure and composition is predicted by current astrochemical models, and how it is related to the observational data on O₂:H₂O ratio and ice thickness. For this purpose, we used results from Vasyunin et al. (2017). Briefly, this is a three-phase (gas-reactive ice surface - (less) reactive ice bulk) time-dependent astrochemical model that includes an extensive set of gas-phase and grain-surface chemistry. In Vasyunin et al. (2017), the model has been successfully applied to the explanation of observed distribution of complex organic molecules (COMs) in the prototypical pre-stellar core L1544. The authors find that the best agreement between the model and the observed data is reached after 1.6×10^5 years of chemical evolution of a static cloud with physical structure similar to one reproduced for L1544. The model also reproduced the enhanced abundances of COMs at the so-called methanol peak located ~ 4000 AU (~ 0.015 pc) away from the centre of the core (the peak of the dust emission), as observed by Bizzocchi et al. (2014).

At the time of maximum O₂/H₂O abundance, the modelled ice thickness is 70 monolayers, but it is growing with time, and stabilizes at the methanol peak at 200 monolayers after 10^5 years of evolution, as shown in Figure 2.8. As such, we believe that modelling results are in rough agreement with observed values for O₂/H₂O in the coma of 67P/Churyumov-Gerasimenko comet. Also, the modelling suggests that icy mantles in pre-stellar cores such as L1544 are relatively thick, and may reach several hundreds of monolayers. Finally, it is interesting to note that while the model by Vasyunin et al. (2017) predicts gas-phase O₂ abundance, at the time of the best agreement between the model and observed values of COMs, to be at least an order of magnitude lower than that of CO, the O₂ gas-phase abundance is still overestimated by an or-

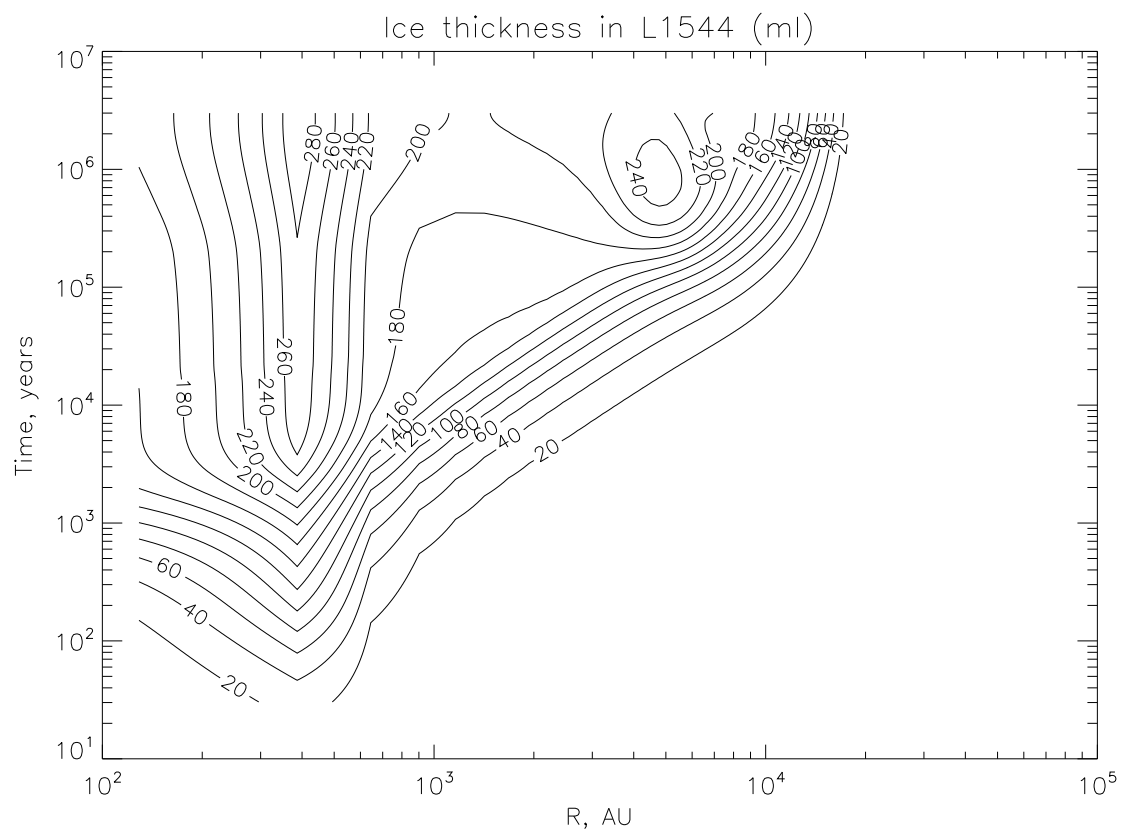


Figure 2.8: Model ice thickness (in monolayers) vs. time in L1544. The ‘methanol peak’ is located 4000 AU away from the core centre.

der of magnitude in comparison to observed upper limits in other environments (e.g. Goldsmith et al. 2000). The gas-phase O₂ abundance in the model by Vasyunin et al. (2017) is mainly controlled by the reactive desorption mechanism, whose efficiency under various conditions is currently a matter of debate (see e.g. Minissale et al. 2016; Chuang et al. 2018; He et al. 2017; Oba et al. 2018). Thus, gas-phase abundance of O₂ will be the subject of further theoretical and experimental studies.

2.6.2 Astronomical observability

Using absorbance and thickness data obtained in our experiments, we were able to calculate the absorption coefficient

$$\alpha = \frac{Abs \cdot \ln(10)}{d}, \quad (2.8)$$

for the different mixture ratios of O₂/H₂O. α as a function of the O₂/H₂O ratio can be found in Figure 2.9. The absorption coefficients for water are in good agreement with the derived values from Warren & Brandt (2008), considering a discrepancy in sample temperature, while we have no possibility to compare the calculated absorption coefficient for O₂ with the literature. In order to calculate α for all O₂ to H₂O ratios, the data were fit using two different methods for statistical comparison. The first method creates the fit by minimizing the χ^2 -error statistics. The second method uses the least absolute deviation method that minimizes the sum of absolute errors.

The calculated values were then used to derive the optical depth and the transmittance of L1544 using the model by Vasyunin et al. (2017) introduced in section 2.6.1 (cf. Figure 2.10). The transmittance of an area with a constant absorption coefficient can be calculated with

$$T = \frac{F}{F_0} = e^{-\int \alpha s} = e^{-\tau}, \quad (2.9)$$

where F_0 is the initial flux density received from the medium, F is the flux density transmitted by the medium, s is the size of the area with a certain absorption coefficient α . For our calculations, we divide the modelled cloud into subpaths s_n of constant absorption coefficients and obtain

$$\tau_{tot} = \sum_{s_n} \tau_{s_n}. \quad (2.10)$$

Following this, we get the total transmittance

$$T_{tot} = \prod_{s_n} T_{s_n}. \quad (2.11)$$

The optical depth and transmittance was computed only for the inner part of our modelled L1544 where O₂/H₂O is $> 10^{-6}$. The derived optical depth and transmittance for the different H₂O and O₂ can be found in Table 2.4.

Directly comparing the overlapping H₂O 1660 cm⁻¹ and O₂ 1551 cm⁻¹ bands we get a transmittance ratio of 0.946 for fitting method a) and b). The predicted transmittance of the O₂ band is then $\approx 5.4\%$ of the water band transmittance at 1660 cm⁻¹. In order to check the observability of

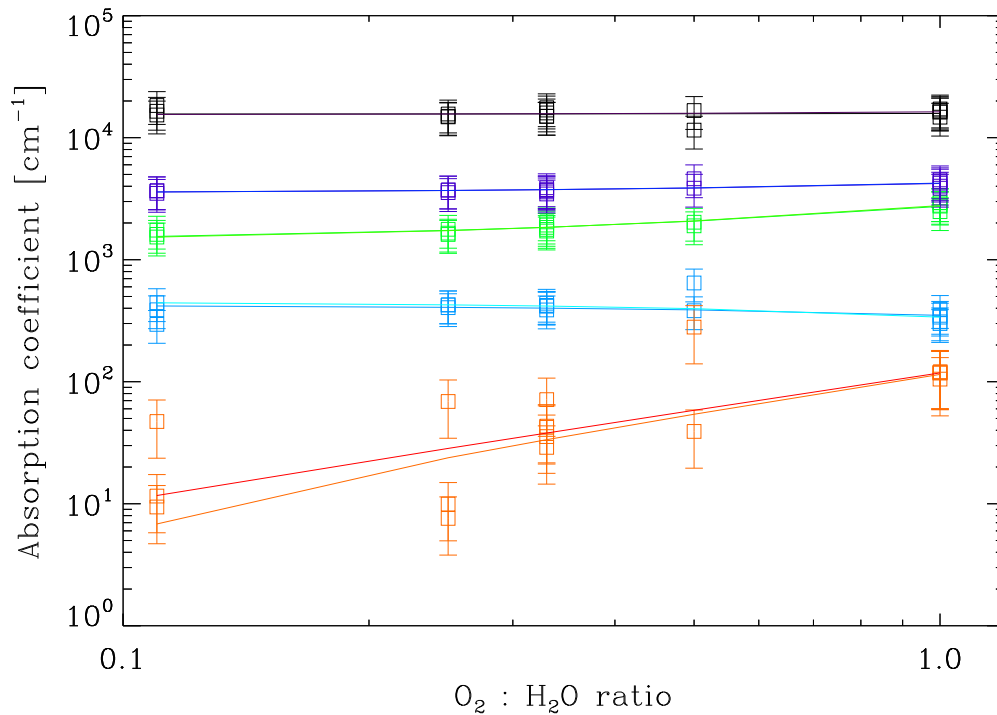


Figure 2.9: Absorption coefficients of the 3280 cm^{-1} (black), 2200 cm^{-1} (light blue), 1660 cm^{-1} (green), 760 cm^{-1} (dark blue) water and 1551 cm^{-1} (red) O_2 bands for the different mixture ratios of O_2 and H_2O . The data were fit using the a) minimizing χ^2 -error statistics (bright coloured fits) and b) ‘robust’ least absolute deviation method (dark coloured fits).

Table 2.4: Optical depth and transmittance of the modelled L1544 in the area with $\text{O}_2/\text{H}_2\text{O} > 10^{-6}$.

Band	τ (fitting method a)	τ (fitting method b)	T (fitting method a)	T (fitting method b)
3280 cm^{-1}	0.625 ± 0.006	0.611 ± 0.039	0.535 ± 0.005	0.543 ± 0.039
2200 cm^{-1}	0.017 ± 0.001	0.018 ± 0.002	0.982 ± 0.052	0.982 ± 0.093
1660 cm^{-1}	0.056 ± 0.002	0.055 ± 0.003	0.945 ± 0.024	0.946 ± 0.048
1551 cm^{-1}	$7.4 \times 10^{-4} \pm 8.1 \times 10^{-4}$	$1.0 \times 10^{-5} \pm 3.0 \times 10^{-6}$	0.999 ± 0.110	1.000 ± 0.337
760 cm^{-1}	0.140 ± 0.003	0.139 ± 0.006	0.869 ± 0.016	0.870 ± 0.035

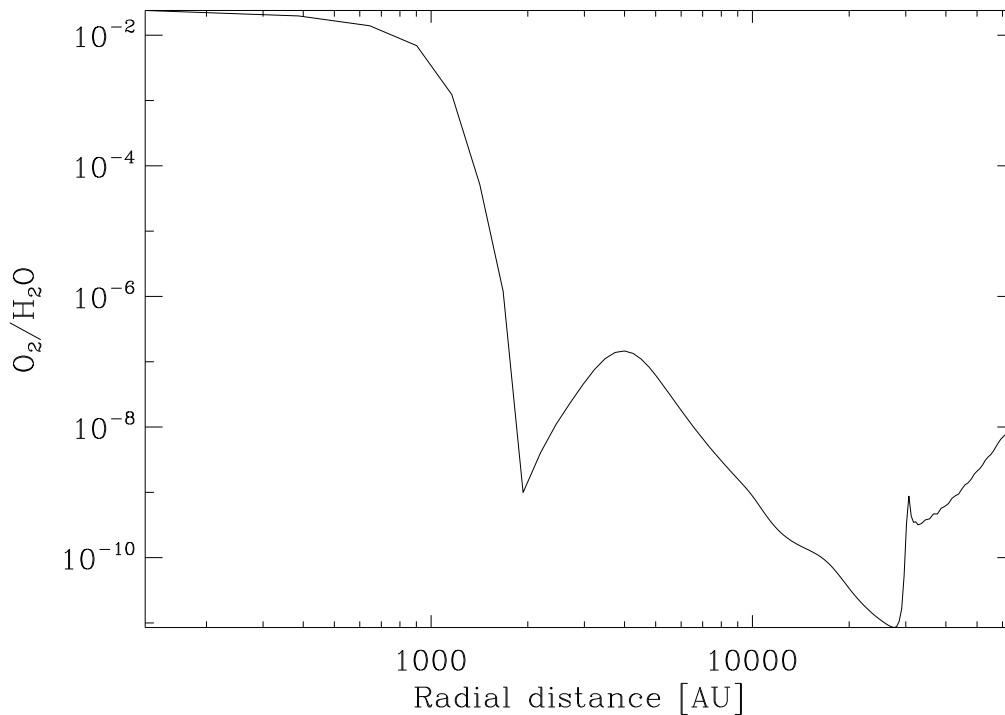


Figure 2.10: Calculated O₂/H₂O of L1544 as a function of the radial distance for $t = 1.6 \times 10^5$ yr.

this feature with the *James Webb Space Telescope* (JWST) the time calculator facility has been employed. For the prestellar core L1544, we calculated the time needed to detect the O₂ line at a 3σ level for the MIRI instrument in the Channel 1 (short) configuration and found that this requires more than 100 hours with JWST, meaning it is not feasible. This estimate is, however, conservative, as we expect, based on the experiments by Ehrenfreund et al. (1992), that the O₂ feature becomes stronger when ice mixtures are considered. We will quantify this in a future paper, where we will present the spectroscopic signatures of an ice mixture similar to the one predicted by Vasyunin et al. (2017).

2.7 Conclusions

This paper presents spectral features of solid molecular oxygen enclosed in a water matrix. The analysis is compared to previous studies reported by Ehrenfreund et al. (1992) and Palumbo et al. (2010), and extended to further molecular ratios and ice thicknesses, as motivated by the recent detection of O₂ in the comet 67P/Churyumov-Gerasimenko. In particular, we have explored the possibility of detecting O₂ in solid form towards pre-stellar cores for which gas-grain chemical model predictions were available.

In our experiments, O₂ is found at 1551 cm^{-1} for thick ice. Also, we find evidence for

the O₂ band at that position even for our thinnest ice. Because of their more heterogeneous composition, interstellar ices may, however, show the O₂ features around these values. The porous amorphous nature of the ice mixture produces the dangling bonds near the stretching mode of water. However, while their position and intensity depends on the ratio of H₂O and O₂, the lack of detection in space hint to the conclusion that the ice there is compact and not porous (e.g. Palumbo 2005). The O₂ feature can only be seen for temperatures ≤ 35 K.

The behaviour of the dangling bonds in dependence of the ice mixture composition has been discussed. The O₂:H₂O ratio not only has an effect on the intensity of the features but also on their position and shape. This is especially so for mixtures with an excess of O₂ that show a shoulder feature or even a second maximum near the two main bands.

The three-phase time-dependent astrochemical model of the pre-stellar core L1544, as introduced by Vasyunin et al. (2017) predicts thick ice (≈ 200 ML) and O₂/H₂O fractions close to those measured towards the comet 67P. Using JWST, it is not feasible to detect O₂ in solid phase via measuring the transmission ratio of L1544 using the MIRI instrument. New estimates for the O₂ detection in mixed ices with JWST, however, will be done in a future paper.

Chapter 3

Spectroscopic measurements of CH₃OH in layered and mixed interstellar ice analogues

The contents of this chapter were published in the *Astronomy&Astrophysics* Journal.
Credit: Müller et al., A&A, 652, A126, 2021, reproduced with permission ©ESO

3.1 Abstract

The molecular composition of interstellar ice mantles is defined by gas-grain processes in molecular clouds, with the main components being H₂O, CO, and CO₂. Methanol (CH₃OH) ice is detected towards the denser pre-stellar cores and star-forming regions, where large amounts of CO molecules freeze out and get hydrogenated on top of the icy grains. The thermal heating from nearby protostars can further change the ice structure and composition. Despite the several observations of icy features carried out towards molecular clouds and along the line of sight of protostars, it is not yet clear if interstellar ices are mixed or if they have a layered structure. We aim to examine the effect of mixed and layered ice growth in dust grain mantle analogues, with specific focus on the position and shape of methanol infrared bands, so dedicated future observations could shed light on the structure of interstellar ices in different environments. Mixed and layered ice samples were deposited on a cold substrate kept at a temperature of 10 K using a closed-cycle cryostat placed in a vacuum chamber. The spectroscopic features were analysed by Fourier transform infrared spectroscopy. Different proportions of the most abundant four molecular species in ice mantles, namely H₂O, CO, CO₂, and CH₃OH, were investigated, with a special attention placed on the analysis of the CH₃OH bands. We measure changes in the position and shape of the CH and CO stretching bands of CH₃OH depending on the mixed or layered nature of the ice sample. Spectroscopic features of methanol are also found to change due to heating. A layered ice structure best reproduces the CH₃OH band position recently observed towards a pre-stellar core and in star-forming regions. Based on our experimental results, we conclude that observations of CH₃OH ice features in space can provide information about the structure of interstellar

ices, and we expect the James Webb Space Telescope (JWST) to put stringent constraints on the layered or mixed nature of ices in different interstellar environments, from molecular clouds to pre-stellar cores to protostars and protoplanetary discs.

3.2 Introduction

The interpretation of astronomical observations relies on the contribution provided by laboratory data and theoretical modelling. The spectroscopic features of interstellar ice analogues recorded in the laboratory at infrared wavelengths provide important information to shed light on the composition and physical state of the icy mantles of interstellar dust grains. Many decades of laboratory investigations dedicated to the study of astrophysical relevant ice samples have offered a rich bibliography that makes information available for the most commonly observed ice mixtures, which can be found in commonly known databases.

Öberg et al. (2011) showed that the most realistic picture of ice mantles covering the dust grains is a layered model, in which the chemical composition of the ice changes as the ice accretes on the dust surface following the changes in the gas-phase chemical composition. This produces changes of the observed ice features depending on the environment probed. In Bottinelli et al. (2010), a comparison of low-mass young stellar objects observations (using the *Spitzer* InfraRed Spectrograph) with laboratory studies of ices containing NH₃ and CH₃OH indicates that CH₃OH ice is present mostly in pure form or mixed with CO and CO₂. The bombardment of icy mantles by energetic particles such as cosmic rays could already affect the ice structure (e.g. Leger et al. 1985; Dartois et al. 2020; Ivlev et al. 2015) in the pre-stellar phase, while protostellar activity (thermal heating and shocks) may also provide other mechanisms to mix a previously layered icy mantle onto dust grains.

In the past years, experiments on layered ice analogues have focussed on a number of components that are present in interstellar ices such as H₂O, CO, CO₂, CH₄, HCOOH, or CH₃OH. First laboratory studies by Givan et al. (1997), who compared pure water ice, water layered on top of Ar and Ne, as well as H₂O-Ar, H₂O-Ne and H₂O-CO ice mixtures, showed that the spectroscopic parameters are sensitive to structural modifications in the solid ice layers as well as sudden changes in the temperature.

Investigations on layered and mixed CO containing ice analogues by Fraser et al. (2004) and Fraser (2004) support the assumption that interstellar CO ice is present in mostly pure layers instead of mixed ices. Measurements of CO layered on top of other species conducted by Collings and McCoustra (Collings et al. 2003) observed entrapment of CO in pores of H₂O ice as well as a collapse of those pores during heating. Subsequent sub-monolayer coverage experiments characterised the band shifts of CO on top of crystalline and amorphous solid water (Collings et al. 2005) and on top of ¹³CO, CO₂, NH₃, CH₃OH, and H₂O (Collings et al. 2014). The results of Collings et al. (2014) for CO-CO₂ ices agreed well with those of van Broekhuizen et al. (2006), who measured changes and shifts in the CO and CO₂ bands of pure, mixed, and layered ice analogues. Allodi et al. (2014) examined the structure and dynamics of H₂O and CO₂ in pure, mixed, and layered ices and they were able to follow CO₂ segregation, which affected the shape and position of the H₂O bands. While experiments of CH₃OH and C₂H₅OH deposited on H₂O

by Wolff and Brown showed mixing and subsequent co-desorption during heating (Burke et al. 2008; Wolff et al. 2007), Bahr et al. (2008) observed that layered and reverse-layered depositions of CH₃OH and D₂O can affect the morphology of the top layers during annealing. Similarly to our experiments presented in the following sections, Dawes et al. (2016) measured band shifts of mixed and pure CH₃OH and H₂O ices, and their results agree well with our findings.

Many of the experimental works mentioned above focus on layered deposition and a comparison of layered and mixed ices is not always provided. Also, in none of the described experiments have more than two components been analysed, and some examine the ices at temperatures that are too high for comparison with, for example, dense molecular clouds of temperatures between 10 and 20 K. Only recently, Ciaravella et al. (2020) experimentally examined X-ray processing of two layered ices where CH₃OH and CO were deposited on top of an H₂O:CH₄:NH₃ ice at 12 K. They observed conversion of hydrogenated species and formation of new molecules both in the bottom and top layers.

More elaborated examination of the influence of pure and mixed ice layers on the spectral signatures is needed. Here, we focus our attention on solid CH₃OH features, as methanol has been detected in the gas phase of starless and pre-stellar cores (e.g. Tafalla et al. 2004, 2006; Bizzocchi et al. 2014; Chacón-Tanarro et al. 2019; Scibelli & Shirley 2020) and its distribution was recently modelled by Vasyunin et al. (2017). The gas-grain chemical code of Vasyunin et al. (2017) predicts that gas-phase CH₃OH is produced by the reactive desorption of surface methanol, produced on CO-rich ices at the location of the catastrophic CO freeze-out (e.g. Caselli et al. 1999); a significant fraction of solid CH₃OH is also predicted to accumulate on the ice mantle. In fact, Perotti et al. (2020) and Goto et al. (2021) recently detected solid methanol in the direction of the Serpens low-mass star-forming region and the pre-stellar core L1544, respectively.

While Perotti et al. (2020) had difficulties fitting the red wing of the L band between 3.0-3.7 μm because of a low signal-to-noise (S/N) ratio, Goto et al. (2021) found an interesting shift in the frequency of the 3.54 μm CH₃OH stretching band detected towards the pre-stellar core L1544 when compared to experimental data of ice mixtures examined by Hudgins et al. (1993). With an offset of + 0.01 μm , this observed methanol band differs from the experimentally measured peak wavelength of 3.53 μm . A similar behaviour was found by Dartois et al. (1999); while their observations of the protostars RAFGL7009S and W33A mark the methanol CH stretching band at 2827 cm^{-1} , laboratory data from Ehrenfreund et al. (1998) presenting ice mixtures containing methanol show optical depth maxima at positions > 2830 cm^{-1} . Moreover, Penteadó et al. (2015) present observations of methanol ice towards the young stellar object AFGL 7009S, showing a peak position at 3.53 μm instead of the actual absorption band maximum expected at 3.54 μm . They offer an explanation for this discrepancy stating that either a gradient of different ice compositions in the mantles exists or that mantles change in composition along the line of sight. As presented in the following sections, our experiments suggest a different explanation to the shifts in the ν_1 methanol band position observed by Dartois et al. (1999), Goto et al. (2021), and Penteadó et al. (2015): a layered ice structure.

We conducted experiments on ices with compositions resembling that of interstellar ices, where the most abundant species are H₂O, CO, and CO₂, and CH₃OH is a minor component, following observations of Öberg et al. (2011) in different environments. We provide accurate

spectroscopic measurements of ice features in layered and mixed ices containing CH₃OH, with the aim of assisting the interpretation of the above-mentioned observations of solid methanol. Moreover, we present the effect of heating on the shape of the vibrational bands in layered and mixed ices. We show that the layered or mixed structure can be deduced from the characteristic features of the observed bands.

The experimental methods employed are described in Sect. 3.3, followed by the presentation of the results in Sect. 3.4. A discussion about the measurements can be found in Sect. 3.5, while Sect. 3.6 addresses our conclusions.

3.3 Experimental methods

The experiments were performed using CASICE, the cryogenic set-up developed at the Center for Astrochemical Studies (CAS) located at the Max Planck Institute for Extraterrestrial Physics in Garching (Germany). The set-up is composed of a closed-cycle He cryostat purchased from Advanced Research Systems, coupled with a Bruker Fourier Transform Infrared (FTIR) spectrometer. A detailed description of the set-up can be found in Müller et al. (2018).

3.3.1 Cryogenic set-up

The cryostat is mounted in a stainless steel vacuum chamber of adequate dimensions to be hosted in the sample compartment of the spectrometer. A final vacuum of 10^{-7} mbar and a temperature of 10 K is attained after cooling.

The IR spectra were recorded in the $4800\text{--}500\text{ cm}^{-1}$ ($2.1\text{--}20\text{ }\mu\text{m}$) frequency range using a standard deuterated triglycine sulfate (DTGS) detector. A spectral resolution of 1 cm^{-1} has been used and the signal has been averaged over 128 scans, as is common practice. No significant differences were noted with spectra taken at higher resolutions (see van Broekhuizen et al. 2006; Gerakines & Hudson 2015). To obtain a good transmittance in the spectral range, KBr is used in these experiments as optical material for the substrate, while the vacuum chamber optical windows are made of ZnSe.

3.3.2 Ice preparation

The ice layers are prepared by expansion of suitable gaseous samples into the vacuum chamber followed by condensation on top of the cold substrate. A two-fold gas inlet was used to allow the gases into the CASICE vacuum chamber. The pure and mixed gases used for the ice layers' formation were connected to the two inlets and expanded in the vacuum chamber separately to allow the formation of a layered structure. No contamination from residual gas in the inlet pipe was observed.

The total thickness of the ice samples was kept below $1\text{ }\mu\text{m}$ to be as close as possible to the typical thicknesses for icy mantles in dense clouds and pre-stellar cores (e.g. Vasyunin et al. 2017). In our set-up, we reached this thickness after several minutes of gas deposition. The

contamination from residual water vapour contributes to an ice growth of four monolayers per hour and can be neglected.

Gas mixtures were prepared in glass bulbs using a separate gas line equipped with flow controllers and precision valves. Following the ideal gas law, the molecular ratio in the gas phase was controlled by measuring the partial pressure of each species.

After deposition, the relative abundance of the molecular species in the ice samples were calculated by converting the integrated absorption features into column density values by using band strength values tabulated in Hudgins et al. (1993) and Gerakines et al. (1995).

3.4 Results

In this work, we compare pure ices with layered and mixed ices and show the differences in the spectral features. The purpose is to investigate the change in band shape and position of the most prominent methanol features in mixed and layered ices.

In the following three sections, the results of three different sets of experiments are shown. The results of the heating and inverse deposition of selected experiments is presented in Sects. 3.4.4 and 3.4.5. The complete list of performed experiments is shown in Table 3.1, together with the estimated molecular composition and thickness expressed as number of monolayers. The chosen abundances of CH₃OH, CO, and CO₂ relative to H₂O are based on median values obtained in observations of cloud cores and high-mass protostars conducted by Öberg et al. (2011). All the spectra are presented in raw format, without baseline correction, in order to avoid the appearance of spurious features due to the correction procedure.

3.4.1 Water and methanol

As starting test, ices of pure water and pure methanol were deposited in separate experiments. The resulting spectra were then summed mathematically to obtain the resulting overlapped spectrum.

Similarly to Dawes et al. (2016), who compared pure and mixed ices, the overlapped spectrum was then compared to the spectra from the two different experiments in which the ice is deposited in layers or pre-mixed in the gas phase (exps. 1 and 2 in Table 3.1). The results are shown in Fig. 3.1, where sub-figures (b) and (c) present not only changes in the shape of the band profile but also clearly distinguishable shifts of the CH-stretch band as well as the CO-stretch band maxima position for mixed and layered ices in more detail.

The molecular ratio in the pre-mixed gas sample was chosen in order to match the relative abundance of water and methanol in the layered ice assuming that the ratios are similar in gas and solid phases. In Fig. 3.1, re-scaling was applied to the spectrum of the mixed CH₃OH-H₂O ice. Moreover, in Figs. 3.1b and 3.1c the spectra were shifted along the y-axis for better comparability of the bands. The re-scaling does not alter the shape of the spectrum and was chosen to guide the eye in the comparison. Table 3.2 presents the ν_3 CH-stretch and ν_8 CO-stretch absorption band positions of CH₃OH listed in frequency for the investigated ice samples.

Table 3.1: List of experiments performed in the present work. The number of monolayers has an error of 20% - 30%.

Experiment		$\chi_{\text{H}_2\text{O}}^{\text{a}}$	$\chi_{\text{CH}_3\text{OH}}^{\text{a}}$	$\chi_{\text{CO}}^{\text{a}}$	$\chi_{\text{CO}_2}^{\text{a}}$	Thickness (MLs)
Pure H ₂ O		100%	–	–	–	1739
Pure CH ₃ OH		–	6% ^b	–	–	103
1	1 st layer	100%	–	–	–	2344
	2 nd layer	–	5%	–	–	116
2	mixed	100%	4%	–	–	1530
3	1 st layer	100%	–	–	–	1598
	2 nd layer	–	3.5%	7% ^c	50%	850
4	1 st layer	100%	–	–	–	1352
	2 nd layer	–	5%	16% ^c	30%	470
5	1 st layer	100%	–	–	–	1453
	2 nd layer	–	10%	32% ^c	31%	596
6	1 st layer	100%	–	–	39%	489
	2 nd layer	–	5%	16% ^c	32%	351
7	mixed	100%	4%	14% ^c	28%	1650
8	1 st layer	100%	–	–	–	1598
	2 nd layer	–	10%	9% ^c	113%	1962
9	1 st layer	–	5%	–	–	134
	2 nd layer	100%	–	–	–	2437

^a Abundance of the molecular species in the ice with respect to H₂O.

^b Abundance of the molecular species in the ice with respect to the number of monolayers of pure H₂O.

^c Abundance of methanol in the ice with respect to CO.

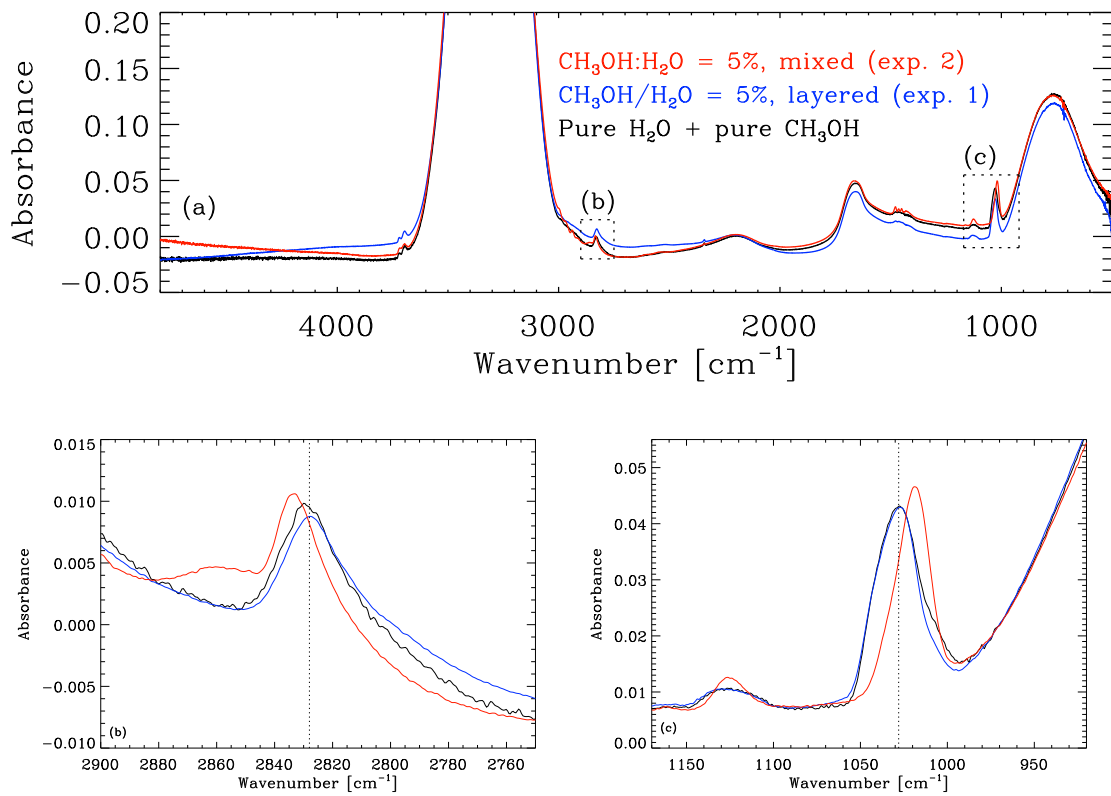


Figure 3.1: Spectra of pure methanol and water ices, CH₃OH on top of H₂O ice layers (CH₃OH/H₂O exp. 1 in Table 3.1) and H₂O-CH₃OH mixture (CH₃OH:H₂O exp. 2 in Table 3.1) in the full frequency range (a), zoomed-in around the 3.54 μm CH-stretch band (b) and zoomed-in around the 9.75 μm CO-stretch band (c). Re-scaling was applied to the spectrum of exp. 2, and in Figs. 3.1b and 3.1c the spectra are shifted along the y-axis.

3.4.2 Water, methanol, and CO

Figure 3.2 shows the comparison between the spectroscopic features of water and methanol layers (exp. 1 in Table 3.1) and layers of methanol diluted in CO on top of the water (exp. 4 in Table 3.1). Re-scaling was applied to the spectrum of exp. 4. In Figs. 3.2b and 3.2c, we show a zoomed-in image of the spectra around the CH- and CO-stretch features for better comparison.

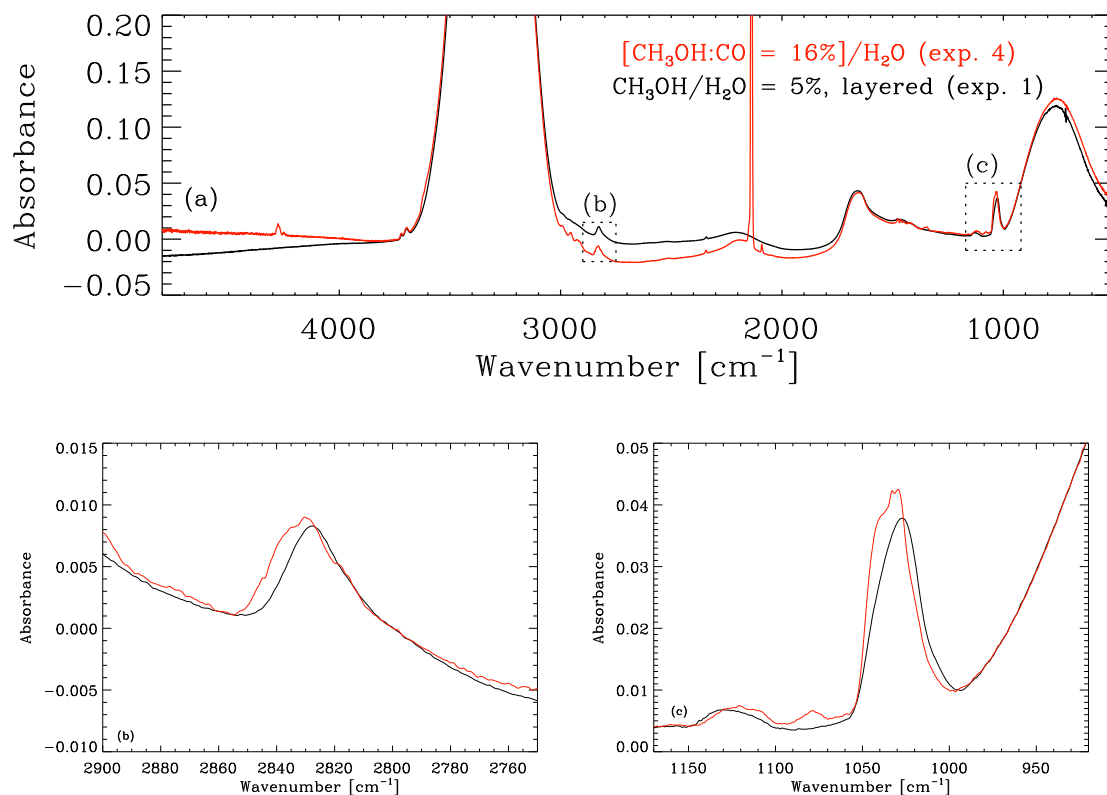


Figure 3.2: Spectra of pure methanol ice layered on top of water ice (exp. 1 in Table 3.1) compared with CH₃OH:CO ice layered on top of water ice (exp. 4 in Table 3.1) in the full frequency range (a), zoomed-in around the 3.54 μm CH-stretch band (b) and zoomed-in around the 9.75 μm CO-stretch band (c). Brackets in the labels within the panels mark species that are present in one ice layer as well as their mixture ratio. Re-scaling was applied to the spectrum of exp. 4, and in Figs. 3.2b and 3.2c the spectra are shifted along the y-axis.

As can be appreciated in these figures, the effect of diluting methanol in a CO matrix on the spectroscopic signature is different from the one observed when methanol is embedded in a water matrix. The presence of CO does not produce an appreciable shift in the frequency at the maximum of the main methanol features when compared to water.

Nevertheless, CO does have an effect on the profile of the absorption bands. To further investigate the observed effect on the band shape, we prepared gas mixtures of methanol diluted in CO in different proportions (exps. 3-5 in Table 3.1). Figure 3.3 illustrates the methanol band

profile for the CH- and CO-stretch features for three different proportions of methanol in CO. The effect of higher dilution of methanol (around 7%) results in a multi-component CH and CO stretch band profile that is smoothed out when the concentration of methanol is increased (from 16% up to 32%). The exact position of the absorption features is listed in Table 3.2.

3.4.3 Water, CO₂, CO, and methanol

In this section, we present the results for mixed and layered ices with the largest number of components examined. According to Öberg et al. (2011) and Boogert et al. (2015), water, carbon dioxide, carbon monoxide, and methanol are the major components of astronomical ices. The ice growth model proposed in the paper includes the formation of layers of different molecular compositions over the molecular cloud evolution. In particular, the water ice formation is associated with the presence of solid CO₂, while the formation of methanol ice is believed to occur in molecular clouds through the hydrogenation of CO-rich layers that accrete on the mantles in dense cloud cores and at the edge of pre-stellar cores (see also Vasyunin et al. 2017).

Therefore, two different ice mixtures were considered to simulate this ice structure in the laboratory, following the molecular ratio in Öberg et al. (2011). The first mixture (exp. 6 in Table 3.1) includes CO₂ in water at about 40% molecular abundance, whereas the second one consists of methanol diluted in CO at a ratio of about 15%. The two mixtures were deposited in layers, starting with the water-rich one and increasing the thickness of the CO-rich mixture until a relative proportion of approximately 30% between CO and water was reached. The recorded spectra are compared with an ice layer formed by condensation of a four components gas mixture (exp. 7 in Table 3.1) in equal relative proportion to that in exp. 6 (see Table 3.1).

Figure 3.4 illustrates the corresponding spectroscopic data, in the full experimental frequency range, and shows a zoomed-in view around the most prominent methanol features. Re-scaling was applied to the spectrum of the mixed CH₃OH-CO-CO₂-H₂O ice. Also, the comparison with the summed spectra of pure water and methanol is shown, corrected for the total ice thickness. We see clear shifts in the maximum band position of the CH-stretch band as well as the CO-stretch band for mixed and layered ices. The shape of the CO-stretch band for the layered ice shows similarities with exp. 4 in Table 3.1 (cf. Fig. 3.3). Since only the composition of the bottom layer is different for exps. 4 and 6 in Table 3.1, this hints at the assumption that there is no strong interaction between the species in the upper and lower layers.

3.4.4 Warm-up

In our experiments, we aim to characterise the change in the methanol spectroscopic features observed during ice warm-up, which is relevant for protostellar cores in the neighbourhood of the young stellar object. The layered and mixed ice samples were heated up to 150 K, the temperature at which the methanol ice desorbs and the water ice transitions to a crystalline state. The crystallisation can be accompanied by desorption of water ice following a desorption rate profile peaking around 180 K (cf. Potapov et al. 2018). Similar desorption temperatures were observed by Collings et al. (2004), who measured desorption temperatures around 160 K for a heating rate of 0.08 K s⁻¹.

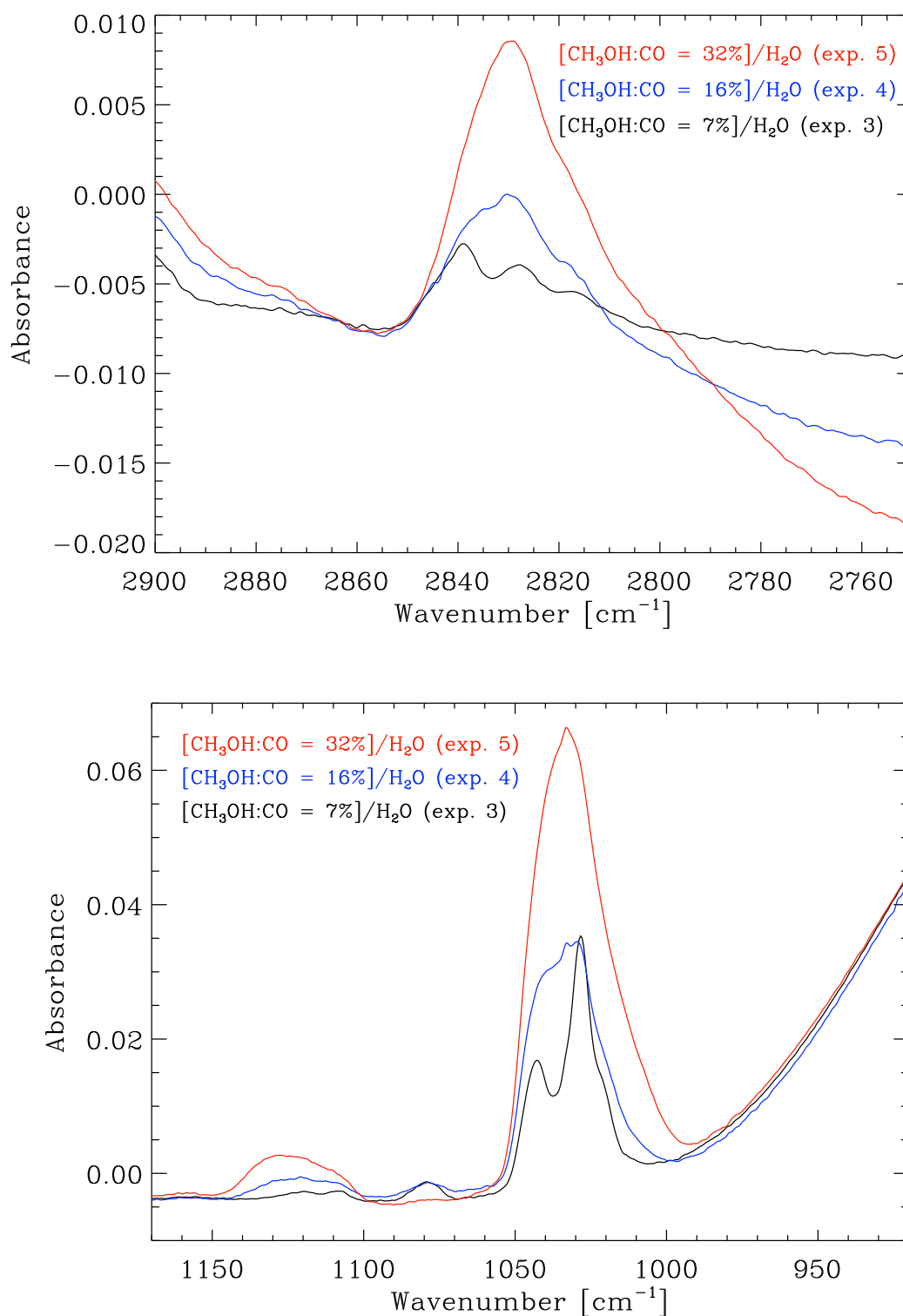


Figure 3.3: Spectra of methanol in CO mixture layered on top of water ice, zoomed-in on the 3.54 μm CH-stretch frequency range (top) and zoomed-in on the 9.75 μm CO-stretch frequency range (bottom). The spectra are shown for relative abundances of CH₃OH:CO = 7% (exp. 3 in Table 3.1), CH₃OH:CO = 16% (exp. 4 in Table 3.1), and CH₃OH:CO = 31% (exp. 5 in Table 3.1).

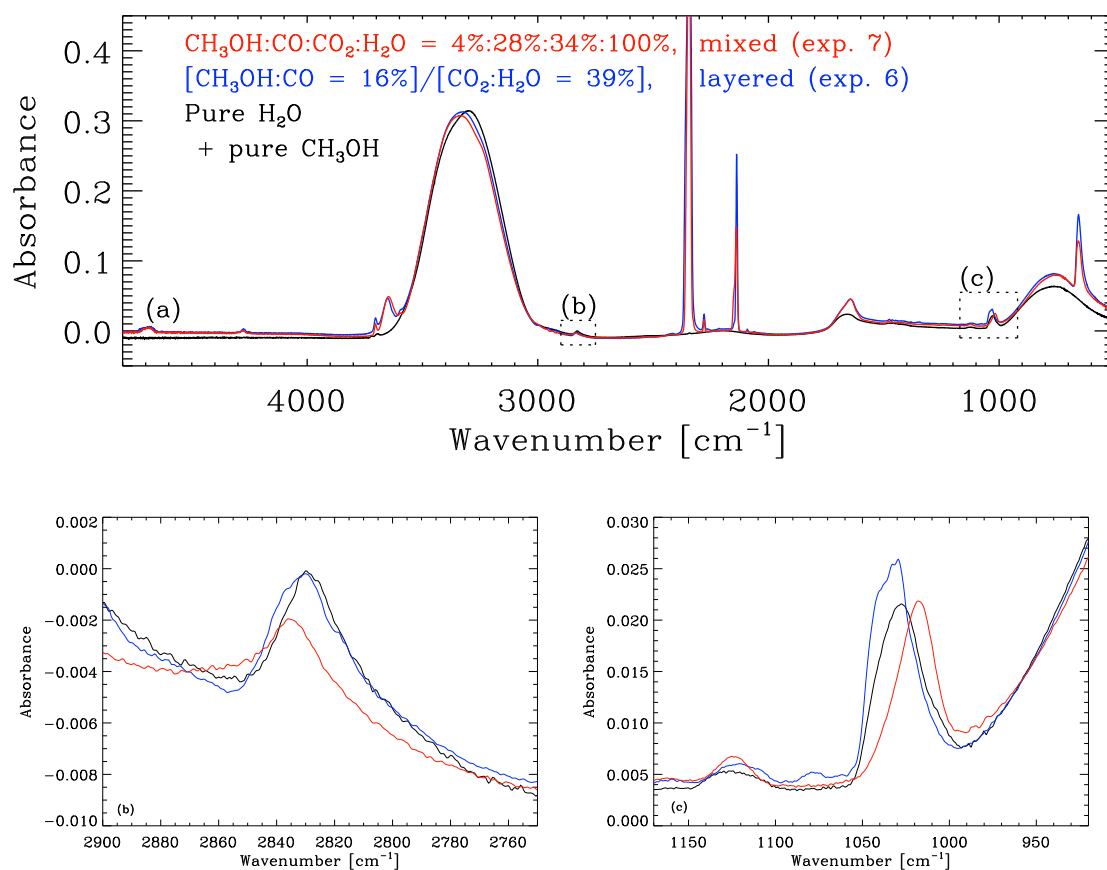


Figure 3.4: Spectra of pure methanol and water ices compared with CH₃OH:CO ice layered on top of CO₂:H₂O ice (exp. 6 in Table 3.1) and a mixed CO₂:H₂O:CH₃OH:CO ice (exp. 7 in Table 3.1) in the full frequency range (a), zoomed-in around the 3.54 μm CH-stretch band (b) and zoomed-in around the 9.75 μm CO-stretch band (c). Re-scaling was applied to the spectrum of exp. 7, and in Figs. 3.4b and 3.4c the spectra are shifted along the y-axis.

The first result we show in Fig. 3.5 is the effect of the heating of methanol layered on top of water ice as well as a mixed H₂O:CH₃OH in direct comparison. Comparing with Dawes et al. (2016), Fig. 3.5 shows that upon heating to 100 K the layered H₂O/CH₃OH ice is mixed, while the initially mixed H₂O:CH₃OH ice shows segregation of methanol.

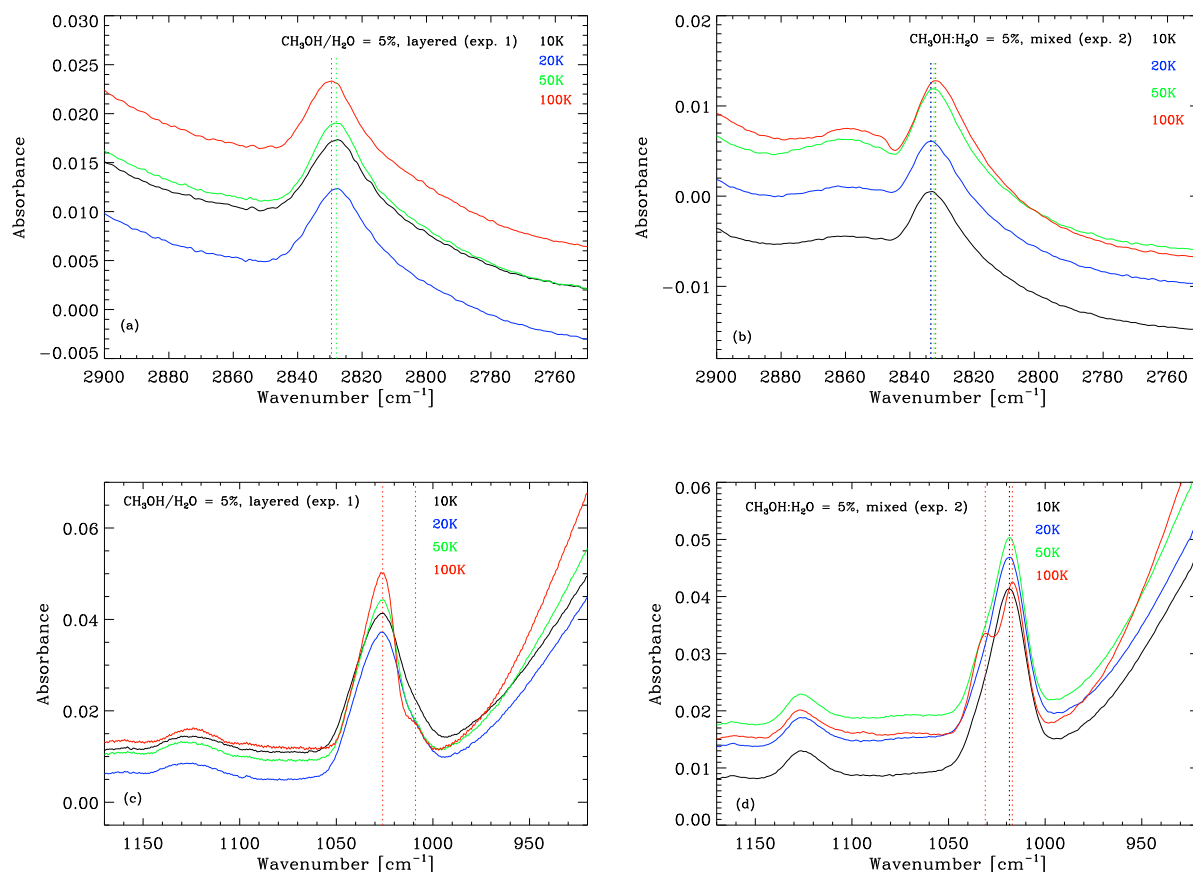


Figure 3.5: Heating of methanol layered on top of water ice (exp. 1 in Table 3.1) and mixed CH₃OH:H₂O ice (exp. 2 in Table 3.1), zoomed-in on the 3.54 μm CH-stretch band, layered (a) and mixed (b) ices, and zoomed-in on 9.75 μm CO-stretch band, layered (c) and mixed (d) ices. For heated samples, vertical coloured lines mark the position of local band maxima and shoulder features for the respective temperature.

Secondly, methanol diluted in CO was layered on top of water ice. For this particular experiment (see exp. 8 in Table 3.1), the proportion between water and methanol was increased to 10% as this is the methanol-to-water ratio constrained by Goto et al. (2021) after comparing their observations with laboratory work by Hudgins et al. (1993). The increase of the methanol-to-water ratio is followed by a consequent change in the H₂O:CO ratio to 113%, and methanol to CO ratio to 9%. In Fig. 3.6, the spectra recorded at 10, 20, 50, and 100 K are shown. For

10 K, we see no effect on the CH-stretch band or the CO-stretch band compared to exp. 3 in Table 3.1, which has a similar CH₃OH:CO ratio to exp. 8 in Table 3.1. The effect of the heating on the methanol band profile is quite significant, starting with very mild heating already at 20 K presenting a spectroscopic signature compatible with methanol segregation in the CO matrix.

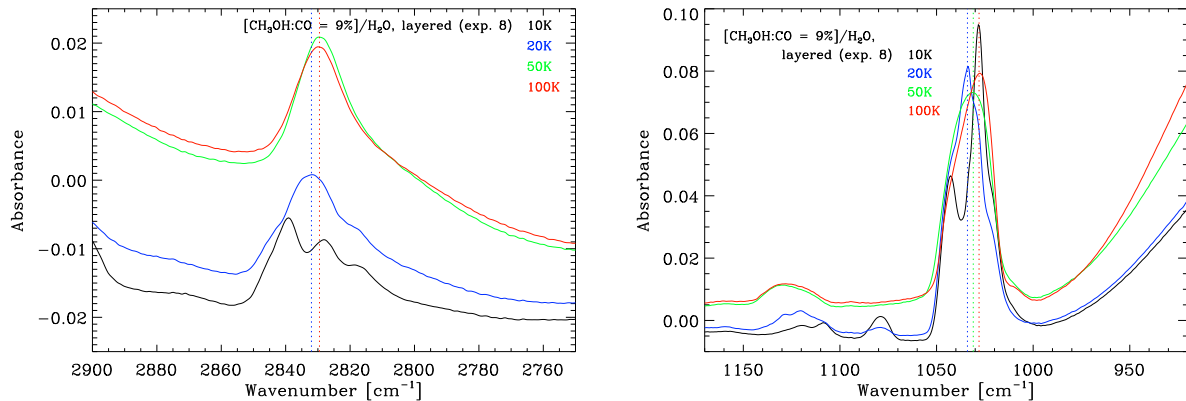


Figure 3.6: Heating of CH₃OH:CO/H₂O ices, zoomed-in on the 3.54 μm CH-stretch band (left) and 9.75 μm CO-stretch band (right). For heated samples, vertical coloured lines mark the position of the band maximum for the respective temperature.

The results of our measurements for the more complex H₂O:CO₂:CO:CH₃OH ice samples, up to 100 K, are shown in Fig. 3.7. The 3.54 μm (2828 cm⁻¹) and 9.75 μm (1026 cm⁻¹) methanol bands show different profiles when methanol is mixed in a water matrix compared to a layered structure.

In summary, for mixed and layered H₂O-CH₃OH ices (exps. 1 and 2 in Table 3.1) we are not able to deduce the ice temperature from the band shape and position for $T < 100$ K, where segregation or mixing begins. This changes for ices with an increased number of species where not only the presented CH₃OH band shapes but also the band positions are strongly affected by the temperature of the ice, even at $T = 20$ K (cf. exps. 6-8 in Table 3.1). Since these ice analogues are more similar to the expected ice composition of interstellar ices, the presented measurements can help to put constraints on the temperature of observed ices.

3.4.5 Inverse deposition

Following the approach presented by Gálvez et al. (2007), Maté et al. (2008), and Allodi et al. (2014), among other studies, we investigated the effect of inverse deposition (ID) of ice layers on their spectroscopic signature. We limited this study to the H₂O:CH₃OH samples, depositing a layer of water ice on top of a layer of methanol ice, keeping the relative proportion of methanol with respect to water to 5%. We then compared the spectra of the inverse deposited ice sample with the data from previous sequential deposition (exp. 1, Table 3.1), observing that there is no

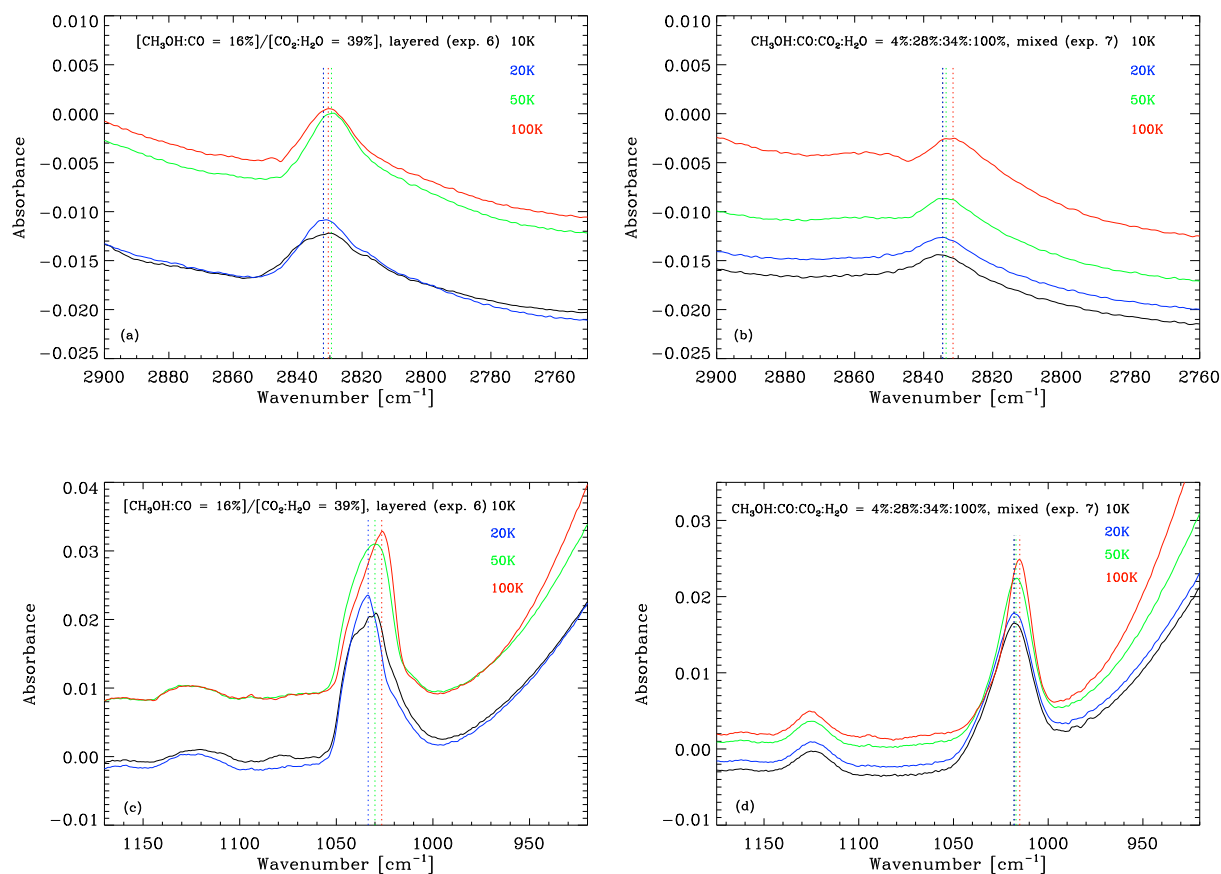


Figure 3.7: Heating of CH₃OH:CO layered on top of CO₂:H₂O ice (exp. 6 in Table 3.1) and mixed CH₃OH:CO:CO₂:H₂O ice (exp. 7 in Table 3.1), zoomed-in on the 3.54 μm CH-stretch band, layered (a) and mixed (b) ices, and zoomed in at 9.75 μm CO-stretch band, layered (c) and mixed (d) ices. For heated samples, vertical coloured lines mark the position of the band maximum for the respective temperature.

appreciable effect on the shape and position of the absorption bands due to the deposition order of the two components. We warmed up the ice samples to 150 K, in steps of 20, 50, and 100 K, and we find no difference in the spectroscopic features between sequential and inverse sequential deposition due to this heating.

3.5 Discussion and comparison with previous work

The spectroscopic features of the considered ices show some general trends when we compare the spectra recorded in layers with the ones for completely mixed ices. The chemical environment of a molecular species embedded in the ice can affect its spectral band shape due to the effect of the intermolecular interactions. It is therefore important to measure the changes in band features of abundant ice components, such as methanol ice, so that future sensitive observations can provide information about the ice structure and composition. As a result of the different interactions, we observe shifts in frequency, as well as changes in the band profile.

Intuitively, it is expected that the spectral features of molecular species deposited in layers are more similar to the spectra of the corresponding pure ices than the mixed equivalent. When methanol is premixed with other molecular species in the gas phase, its band shapes in the solid phase will diverge from those of the pure ice. This effect is caused by the interaction between the different species, which has an effect on the vibration of the molecular bonds and has been studied by various groups such as Sandford & Allamandola (1990) and Ehrenfreund et al. (1999). In contrast, when methanol is deposited as a layer on top of other species, the shape of the absorption bands stays close to that of the pure methanol since the molecular vibrations are more similar to those of pure ices due to the missing influence of other species.

This problem has been addressed in previous works (Gálvez et al. 2007; Herrero et al. 2010; Maté et al. 2009), in which the interaction of binary ice mixtures, sequentially or co-deposited, has been investigated. The molecular species considered in these studies were H₂O:CO₂, CO₂:CH₃OH and H₂O:CH₄. The analysis focussed on adsorption and diffusion processes between the investigated species, and it provided information on the spectral changes observed. These changes have been interpreted as variations in terms of the structure that the host species can adopt within the guest one. The results focussed on the CO₂ or CH₄ features as a probe for the change in the water or methanol environment. The authors conclude that the distortions of the molecular environment must be caused by weak interactions between the host and the guest species, where the porosity of the host matrix plays the main role in setting the guest absorption properties.

Sandford & Allamandola (1990) reported an investigation of CO₂ co-deposited with samples of different compositions and concentrations, including methanol. Similarly to our results, they observed significant variations in position and width of the CO₂ vibrational bands, which are associated with the relative concentration of the two species, as well as by heating from 10 to 150 K.

In recent observations of the L1544 starless core at 3 μ m by Goto et al. (2021), laboratory data from Hudgins et al. (1993) have been used to constrain the methanol to water ice ratio. These data were recorded for an ice mixture that has been co-deposited from the gas phase,

with the molecular composition of H₂O:CH₃OH:CO:NH₃ = 100:10:1:1, which might not be representative of the average ice composition in cold clouds. In particular, the effect of CO₂ and CO on water-rich ices was not taken into account, nor was the role of layered versus co-deposited ice samples on the spectral features.

The present work shows a new approach to the understanding of the ice structure as the experiments are based on compositions that resemble interstellar ices. We focus our attention on CH₃OH, as this was recently found to be quite abundant in the direction of the pre-stellar core L1544 (Goto et al. 2021). The main points addressed consider the effect of a layered structure versus a mixed one, how the increase of the number of components impacts the band peak frequency and shape, and the effect of heating on the spectroscopic changes.

In all the experiments performed, the layered ice structure has significantly changed the absorption features compared to the ice samples deposited from pre-mixed gases. The ice layers present strong similarities with the spectra from pure ice samples, while in mixed ices the frequency of the absorption bands can be shifted from those assigned to pure ices. In this case, the polarity of the major ice component, which acts as hosting matrix, is probably the main thing responsible for the spectroscopic changes. Table 3.2 shows the change in the absorption frequency positions in the different experiments. Our results, when compared with the observational work of Goto et al. (2021) and Dawes et al. (2016), favour a layered structure of interstellar ices.

Table 3.2: Peak wave number (cm⁻¹) of the 3.54 and 9.75 μm methanol bands in the experiments presented in the paper, recorded at 10 K. Multiple band assignments connect to several local maxima or shoulder features for one band. The error in the measured positions lies within 2 cm⁻¹.

Experiment ^a	Wave number (cm ⁻¹)	
	ν_3 CH stretch ^b	ν_8 CO stretch ^b
Pure CH ₃ OH	2829	1028
1	2828	1028
2	2833	1018
3	2839;2828;2817	1043;1028;1021
4	2830	1040;1033;1029
5	2830	1033
6	2832	1041;1038;1033;1029
7	2834	1018
8	2839;2828;2817	1043;1028;1021
9	2828	1030

(a) See Table 3.1.

(b) The vibrational assignment is taken from Sandford & Allamandola (1993), where ν_3 and ν_8 are assigned to 2827 cm⁻¹ and 1026 cm⁻¹, respectively.

By comparing the spectra of methanol diluted in water or the CO matrix, we see that the band shifts are significantly different (cf. Figs. 3.1, 3.2, and 3.4 relating to exps. 2, 4, 6, and 7 in

Table 3.1). The water matrix induces the largest shift, while no significant changes are observed in CO. Considering the very polar nature of methanol, which is prone to form hydrogen bonds, we could conclude that the intermolecular interactions with water are stronger than with CO, and this effect is reflected in the spectroscopic signature.

Dawes et al. (2016) compared CH₃OH band positions of pure CH₃OH, pure H₂O, and mixed CH₃OH-H₂O ices. They observed a blueshift of the C-H stretching band for mixed ices compared to pure CH₃OH, and they describe a red shoulder feature for the C-O stretching component that gets more dominant as methanol is more diluted in water. The described band positions agree well with our measurements of mixed H₂O and CH₃OH ices (exp. 2 in Table 3.1).

The degree of dilution of the minor ice component also has an effect on the band's appearance. The effect observed for three different methanol abundances in CO shows quite different band shapes, especially for the most diluted one. We could relate this effect to a major isolation of methanol in the CO environment, bringing it to different binding sites, while for the most concentrated mixtures the methanol can start to segregate, resembling more closely the features of the pure ice.

The heating of the most diluted CH₃OH:CO mixtures shows interesting results (Fig. 3.6). At a temperature of 20 K, the shape of the methanol bands already shows significant changes, presenting a spectroscopic signature compatible with the methanol segregation in the CO matrix. The positions of the band peaks during the warm-up phase are displayed in Table 3.3.

These effects have indeed been observed in previous studies by Öberg et al. (2009) and Cooke et al. (2018). The segregation mechanism and barriers in H₂O:CO and H₂O:CO₂ ice mixtures, as well as the CO diffusion into CO₂ ice, were studied in these papers, leading to the conclusion that the heating of the ice samples promotes the mentioned processes, which can be experimentally quantified.

Also, the diffusion of various molecular species in amorphous solid water has been investigated in a series of papers (He et al. 2017; He & Vidali 2018; He et al. 2018a,b), where the dependence of the segregation effect with respect to temperature and concentration has been analysed in detail.

The spectroscopic characterisation of H₂O:CO₂ ice mixtures, co-deposited and layered, has already been performed in several studies (Palumbo 2006; Öberg et al. 2007; Allodi et al. 2014), and an extensive study of H₂O:CH₃OH:CO₂ mixtures has been published by Ehrenfreund et al. (1999) and Palumbo & Baratta (2000). This previous literature can be studied for details on the effect of CO₂ addition to H₂O ice. Adding the CO₂ component in the water layer does not affect the methanol features in an appreciable way; however, in this work, the effect on the methanol features becomes important when the CO₂ is mixed as molecular component in the gas phase before ice condensation. In this case, the observed shift in the frequency position is consistent with the spectra measured for the simplest H₂O:CH₃OH case.

We also note that while the CO₂ component in the water layer does not affect the methanol features, it has a clear effect on the water dangling bond features at approximately 3650 cm⁻¹ and 3700 cm⁻¹, as shown in Fig. 3.8. The observed spectroscopic signature is in line with previous studies by Ehrenfreund et al. (1999), Palumbo (2006), and Öberg et al. (2007), although the band profile for the dangling bond vibration slightly varies in the different studies. This effect can be fully explained by the differences in the experimental conditions, such as temperature and

Table 3.3: Peak wave number (cm⁻¹) of the 3.54 and 9.75 μm methanol bands in the experiments presented in the paper, during warm-up. Multiple band assignments connect to several local maxima or shoulder features for one band. The error in the measured positions lie within 2 cm⁻¹.

Experiment ^a	Wave number (cm ⁻¹)		T (K)
	ν_3 CH stretch ^b	ν_8 CO stretch ^b	
1	2828	1026	20
	2828	1026	50
	2829	1026;1009	100
2	2833	1018	20
	2832	1018	50
	2832	1031;1017	100
6	2832	1033	20
	2829	1030	50
	2830	1026	100
7	2834	1018	20
	2833	1017	50
	2831	1015	100
8	2832;2817	1043;1033;1021	20
	2829	1028	50
	2829	1028	100

(a) See Table 3.1.

(b) The vibrational assignment is taken from Sandford & Allamandola (1993), where ν_3 and ν_8 are assigned to 2827 cm⁻¹ and 1026 cm⁻¹, respectively.

molecular composition, among the previous works, and it has not been the subject of further investigation.

3.6 Conclusions

The present study provides a detailed spectroscopic characterisation of the main features of methanol ice embedded in different ice components, with relative abundances reflecting observations in molecular clouds and star-forming regions (Öberg et al. 2011). In particular, the effect of layering methanol on top of water and the effect of a CO ice matrix were investigated. The purpose of the work is to present laboratory data that are representative of realistic astronomical ice structure, according to recent observations and astrochemical models, as well as to explore the conditions that could potentially identify the ice sample's composition and history from spectroscopic data. In our experiments, we were able to assign band shifts and changes in the band

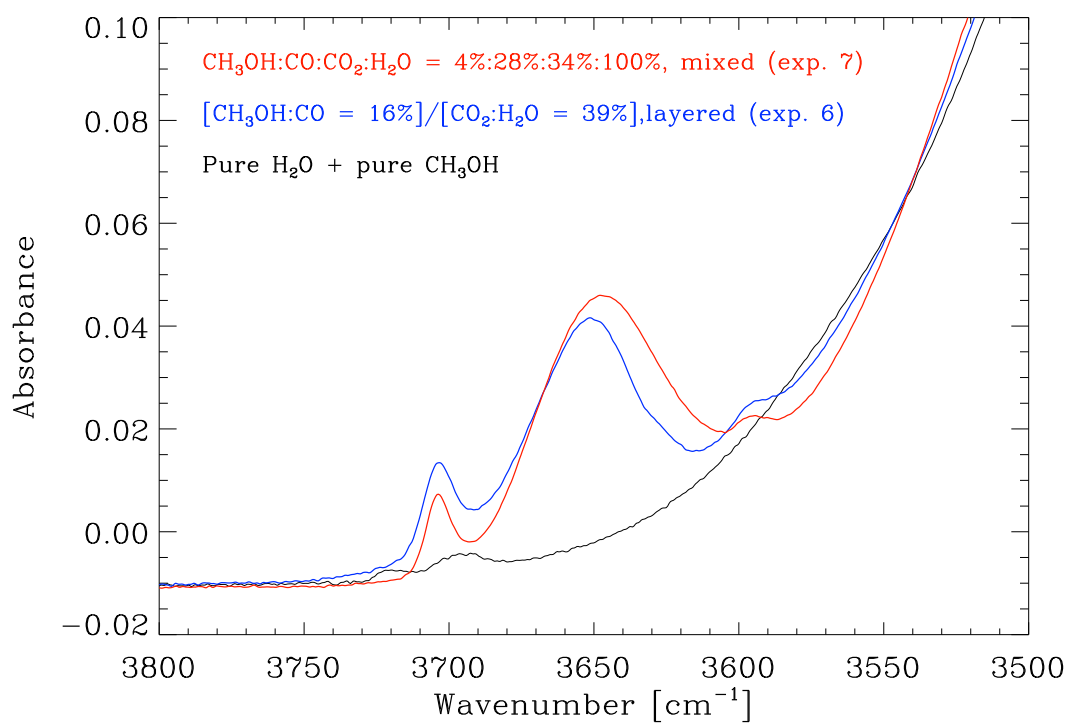


Figure 3.8: Spectra of pure methanol and water ices compared with CH₃OH:CO ice layered on top of CO₂:H₂O ice (exp. 6 in Table 3.1) and a mixed CO₂:H₂O:CH₃OH:CO ice (exp. 7 in Table 3.1), zoomed-in on the free OH-stretch frequency range (H₂O dangling bonds).

shape to the composition of layered and mixed ices. We see clear and distinguishable differences in the shape and peak position of the methanol CH- and CO-stretching bands, depending on the ice structure and chemical composition. Moreover, the spectral features undergo further changes during heating, providing information on the thermal history of the ice mantles. The measured methanol ν_1 band positions of layered ices agree well with the methanol bands observed by Goto et al. (2021) in a pre-stellar core and Penteado et al. (2015) toward young stellar objects. This therefore suggests that ices in quiescent environments and star-forming regions have a layered structure.

We expect our results to serve as a guide for future observations in the mid-infrared range, especially taking into account the expected performance of new facilities such as the James Webb Space Telescope (JWST). Our findings will allow us to infer information about the structure of ices in interstellar environments, which is important for putting stringent constraints on current theories of surface chemistry. The two methanol bands of interest can be observed with JWST's Near-Infrared spectrograph (NIRSpec) for the 3.54 μm CH-stretch band and the Mid-Infrared Instrument (MIRI) for the 9.75 μm CO-stretch band. With spectral resolutions of $R \sim 2700$ for NIRSpec with high resolution gratings ($\Delta\nu = 1.05 \text{ cm}^{-1}$ for the CH-stretch band) and $R \sim 2400 - 3600$ for MIRI ($\Delta\nu = 0.28 - 0.43 \text{ cm}^{-1}$ for the CO-stretch band), both instruments are able to observe the spectral changes in position and shape for the respective bands.

Chapter 4

Laboratory spectroscopy of theoretical pre-stellar core ices

The contents of this chapter have been submitted to the *Astronomy & Astrophysics* Journal. Credit: Müller, B., Giuliano, B. M., Vasyunin, A. and Caselli, P.

4.1 Abstract

The pre-stellar core L1544 has been subject of several observations conducted in the past years, complemented by modelling studies focused on its gas and ice-grain chemistry. The chemical composition of the ice mantles reflects the environmental physical changes along the temporal evolution, such as density and temperature. The investigation outcome hints at a layered structure of interstellar ices with abundance of H₂O in the inner layers and an increasing concentration of CO near the surface. The morphology of interstellar ice analogs can be investigated experimentally assuming a composition derived from chemical models. We present laboratory spectra of ice mantles predicted by state-of-the-art gas-grain models applied to the L1544 physical structure. We compare layered and mixed structures for the ice mantles, showing differences in position and shape of absorption bands. Moreover, we investigate the observability of these spectral changes using the James Webb Space Telescope.

Ice analogs spectra have been recorded at a temperature of 10 K using a Fourier transform infrared spectrometer. In case of the layered ice, we deposited a H₂O-CO-N₂-O₂ mixture on top of a H₂O-CH₃OH-N₂ ice while in the case of the mixed ice, we examined a H₂O-CH₃OH-N₂-CO composition. The selected species are the four most abundant ice components predicted by the chemical model. Following the changing composition and structure of the ice, we find differences in the absorption bands for most of the examined vibrational modes. Observable changes in the bands are suitable to analyse the structure of ice mantles in L1544 from future observations by the James Webb Space Telescope (JWST). Our spectroscopic measurements of interstellar ice analogues predicted by our state-of-the-art gas-grain chemical codes of pre-stellar cores will allow detailed comparison with upcoming JWST observations. This is crucial to put stringent constraints on the chemical and physical structure of dust icy mantles just before the

formation of stars and protoplanetary disks, as well as to elucidate on surface chemistry.

4.2 Introduction

The James Webb Space Telescope (JWST) is the next generation NASA telescope which is designed to work with enhanced sensitivity covering the infrared spectroscopic range. The applications of its capability are multiform, and among them the investigation of ice mantles in different astronomical environments, such as star-forming regions from the earliest phases represented by pre-stellar cores to protostars to planet-forming disks.

In preparation of upcoming JWST observations, preliminary work is required to simulate the conditions of the astronomical object of interest and acquire spectral laboratory data which will facilitate and reinforce the observational data analysis, once they became available. The interpretation of the observational data from telescope facilities can be greatly assisted by theoretical modeling and laboratory experiments. In this paper we present our custom-designed experiments, guided by chemical simulation on the pre-stellar core L1544. The aim of the work is to make available to the community a set of laboratory spectra which mimic the ice mantles composition on top of the dust grains following the chemical model predicted by Vasyunin et al. (2017).

L1544 is a prototypical pre-stellar core, with clear signs of contraction motions (e.g. Keto & Caselli 2010; Caselli et al. 2012) and a highly concentrated structure where the density goes up to about 10^7 H₂ molecules cm⁻³ and temperatures drop to about 6 K (Crapsi et al. 2007; Keto et al. 2015). Recent ALMA observations have detected a compact central region with radius ≈ 1400 au, called the "kernel" (Caselli et al. 2019), where almost all species heavier than He have been found to freeze-out onto dust grains (Caselli et al. 2021, submitted), as predicted by chemical models (Vasyunin et al. 2017; Sipilä et al. 2019).

By exploring different ice chemical composition and thicknesses we offer a tool to disentangle the contribution to the spectroscopic fingerprints from the internal region of the cloud, the kernel, from the entire line of sight. Provided the presence of a background star which is luminous enough to shine through the denser region with high extinction, namely the dust peak, and still be detected by the telescope, it will be therefore possible to utilize observational data to probe the ice mantles composition along the cloud depth.

We have previously investigated the spectroscopic signature of ice analogues in Müller et al. (2018) and Müller et al. (2021). In these studies, the chemical composition and physical state were adjusted to the available results from observational data (see references therein). In the present work, the novelty of our approach consists of the close synergy between the experiment and the chemical modeling, which is here applied for the first time to the representation of a pre-stellar core. Although a rich variety of spectroscopic data of ice mantles analogues are already accessible by the commonly known databases, data on the desired composition and structure predicted by chemical models can be retrieved only with a dedicated experiment. We provide laboratory results for both a layered and a mixed morphology of ice analogues.

In the next sections we will present a description of the model employed and its predictions (Section 4.3), followed by an overview of the experimental methodology in Section 4.4. The

discussion on the experimental results will be conducted in Section 4.5 and Section 4.6, followed by our conclusions in Section 4.7. Additionally, a comparison of the computationally added layer spectrum with the experimentally layered ices is addressed in the Appendix Section A.1.

4.3 Model description and theoretical predictions

The theoretical icy mantles are those obtained by Vasyunin et al. (2017) and we report here some basic description of the model, avoiding details that can be found there. Vasyunin et al. (2017) applied their 3-phase chemical model¹ to the physical structure (volume density, dust and gas temperature, velocity profiles) of L1544 as described in Keto et al. (2015). Rate equations, with modifications to take into account stochastic effects, are used. Modifications are particularly important, as hydrogen atoms and molecules (H and H₂) are assumed to quantum-tunnel across the icy mantles (see, e.g. Garrod et al. 2009).

Dust grains are assumed to be spherical, with size equal to 0.1 μm . Five desorption processes are included in the model: thermal desorption, cosmic-ray induced desorption, cosmic-ray induced photodesorption, photodesorption and reactive desorption, with only surface species allowed to desorb. Although the first four desorption mechanisms have been implemented using standard procedures (e.g. Hasegawa & Herbst 1993; Prasad & Tarafdar 1983), Vasyunin et al. (2017) implemented new experimental work from Minissale et al. (2016) to follow the reactive desorption during the chemical evolution of the pre-stellar core. The most important experimental finding of Minissale et al. (2016) was that the reactive desorption efficiency of a molecule formed onto the surface of a dust grain is a sensitive function of the surface composition, with CO-rich (H₂O-rich) ices allowing the most (least) efficient reactive desorption. This is especially important for methanol, which mainly forms on the surface of dust grains, via successive hydrogenation of CO. In fact, within the catastrophic CO-freeze-out zone of pre-stellar cores (which, in L1544, starts at a radius of ≈ 7000 au; Caselli et al. 1999), where more than 90% of CO molecules are adsorbed onto dust grains, CO-rich icy mantles allow efficient surface formation and reactive desorption of CH₃OH, in good agreement with observations (see also Jiménez-Serra et al. 2016, for detailed comparison of the model predictions with observations of other complex organic molecules within L1544).

This comprehensive gas-grain chemical network, applied to the L1544 physical structure, provides the chemical composition of the icy mantles at each radius of the pre-stellar core. An example of this output is shown in Figure 4.1, where the fractional abundances of the most abundant solid species within an icy mantle of a dust grain located 1160 au away from the L1544 center (representative of the icy mantle composition within the L1544 kernel), are plotted as a function of the number of monolayers. This figure will be discussed in the next section.

¹A 3-phase model indicates a gas-grain chemical model where three different environments are taken into account: (i) gas-phase; (ii) surface of icy mantles (represented by the first four monolayers, see Vasyunin & Herbst (2013)); and (iii) bulk of icy mantles (all monolayers below the surface).

4.4 Experimental methods

All the experiments presented in this paper were conducted at the Max Planck Institute for Extraterrestrial Physics in Garching (Germany), using the cryogenic set-up developed at the Center for Astrochemical Studies (CAS). A full description of the set-up can be found in Müller et al. (2018) and Müller et al. (2021); here we will describe the most relevant details for the presentation of our results.

The set-up is composed of a closed-cycle He cryostat (Advanced Research Systems), coupled with a Bruker Fourier Transform Infrared (FTIR) spectrometer. The sample compartment of the spectrometer hosts the cryostat mounted in a stainless steel vacuum chamber, which is able to achieve a minimum temperature of 10 K and a final vacuum of 10^{-7} mbar when cold. The vacuum chamber is equipped with ZnSe optical windows, while KBr is used as cold substrate window.

The IR spectra were recorded in the $4800\text{--}500\text{ cm}^{-1}$ ($2.1\text{--}20\text{ }\mu\text{m}$) frequency range using a standard deuterated triglycine sulfate (DTGS) detector. A spectral resolution of 1 cm^{-1} has been used and the signal has been averaged over 128 scans.

The ice formation is attained by condensation of a suitable gaseous mixture on top of the cold substrate. The following gases have been employed in these experiments: water vapour from double distilled water, methanol vapour from a liquid sample by Sigma Aldrich with 99,8 % purity, CO, N₂, and O₂ from gas bottles with over 99 % purity. Gases were pre-mixed in a glass bulb in relative proportion controlled by measuring the partial pressure of each species, following the ideal gas law. Two different gas mixtures were expanded separately into the vacuum chamber by using a two-fold gas inlet, to allow the formation of a layered structure. No contamination from residual gas in the inlet pipe was observed.

The relative abundance of the molecular species in the ice samples, after deposition, were estimated by the integrated absorption features calculating the corresponding column density from band strength values tabulated in Jiang et al. (1975), Hagen et al. (1981), D’Hendecourt & Allamandola (1986), Ehrenfreund et al. (1992), Hudgins et al. (1993), Gerakines et al. (1995) and Bernstein & Sandford (1999).

4.4.1 Preparation of the pre-stellar icy mantle analogues

The pre-stellar icy mantle analogues have been prepared based on the predictions of the gas-grain chemical model of Vasyunin et al. (2017), updated as explained in Section 4.3. The model provides the layer-by-layer molecular composition at different positions within the pre-stellar core. Figure 4.1 shows an overview of the predicted molecular abundances for each monolayer of the icy mantles present at a radius of 1160 au, representative region of the central kernel.

In the case of our layered ice analogue, we divided the modelled data into two parts. The molecular composition for the experimental first layer was obtained by averaging over the predicted inner 131 monolayers (ML) where high fractions of H₂O and CH₃OH are present. The three most abundant species were used for the ice mixture of layer 1. For the second layer, we averaged over the outer 30 MLs with high abundances of CO and O₂. Again, the three most abundant species as well as O₂ were incorporated into the ice mixture. Similarly, we averaged over

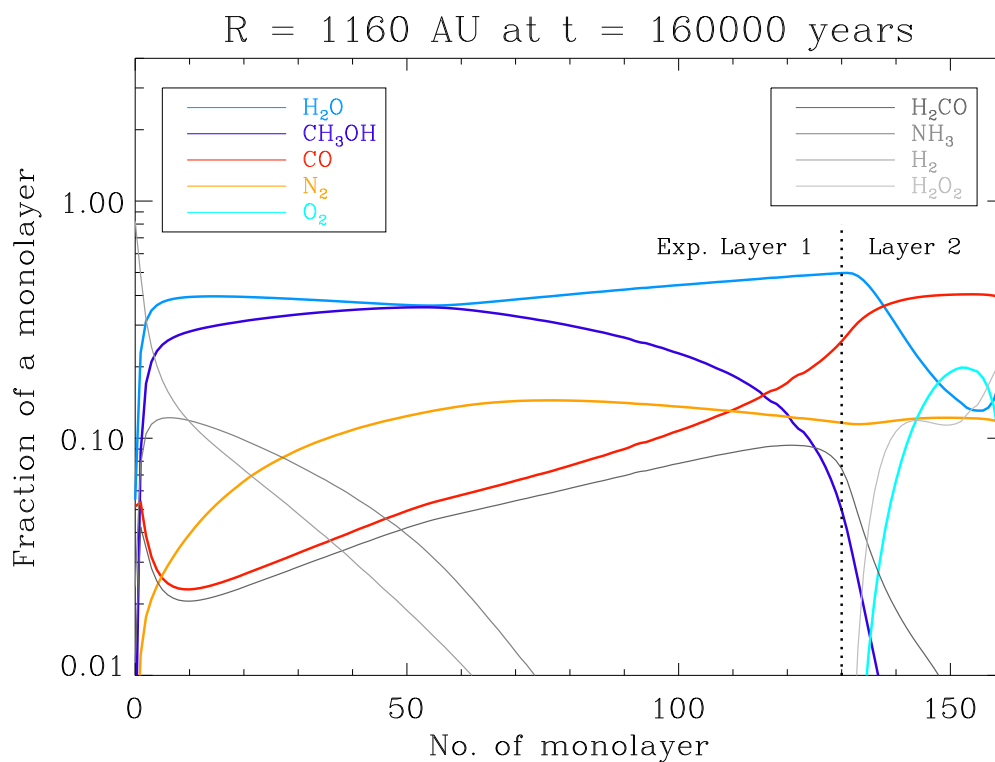


Figure 4.1: Predicted molecular abundances for each layer of an ice mantle in a region close to the dust peak. The vertical line marks the division of monolayers that were used for calculating the average composition in the experimental layers 1 and 2. Coloured fractions highlight the species used in our experiments.

all modelled ice layers and used the four most abundant species for the mixed ice. A detailed overview of the species present in the model is shown in Table 4.1 where molecular species used for the experiments are highlighted. Table 4.2 shows the actual ice composition during the experiments, with deviations $\lesssim 10\%$ from the predicted ratios.

Table 4.1: Average fraction of molecules in the ice mantles based on the presented model. Bold printed species were used for the ice compositions. Values in brackets show the molecular abundance relative to H₂O.

Molecule	Layered		Mixed
	Layer 1 (ML 0-130)	Layer 2 (ML 131-160)	(ML 0-160)
H ₂ O	40% (100%)	26% (100%)	38% (100%)
CH ₃ OH	27% (67.5%)	0.6% (2.3%)	22% (58%)
N ₂	11% (27.5%)	12% (46%)	11% (29%)
CO	8% (20%)	38% (146%)	14% (37%)
H ₂ CO	5% (12.5%)	2% (7.7%)	5% (13%)
NH ₃	4% (10%)	0.1% (0.4%)	3% (7.9%)
H ₂	4% (10%)	$2.5 \times 10^{-4}\%$ ($9.6 \times 10^{-4}\%$)	3% (7.9%)
H ₂ O ₂	$1.5 \times 10^{-3}\%$ ($3.8 \times 10^{-3}\%$)	11% (42.3%)	2% (5.3%)
O ₂	$2.6 \times 10^{-4}\%$ ($6.5 \times 10^{-4}\%$)	10% (38.5%)	2% (5.3%)

Table 4.2: Ice composition during the experiments compared to predicted ratios based on the model. The numbers of monolayers and consequential relative ratios have an error of 20% - 30%.

	$\chi_{\text{H}_2\text{O}}^{\text{a}}$		$\chi_{\text{CH}_3\text{OH}}^{\text{a}}$		$\chi_{\text{CO}}^{\text{a}}$		$\chi_{\text{N}_2}^{\text{a}}$		$\chi_{\text{O}_2}^{\text{a}}$		Thickness (MLs)
	Exp.	Model	Exp.	Model	Exp.	Model	Exp.	Model	Exp.	Model	
Layered Layer 1	100%	74.4%	67.5%	–	–	–	32.4%	27.5%	–	–	767
Layer 2	100%	–	–	143.7%	146%	–	47.5%	46%	40.5%	38%	160
Mixed	100%	56.9%	58%	32.9%	37%	–	32.2%	29%	–	–	894

^a Abundance of the molecular species in the ice with respect to H_2O .

We note that CO₂ is not a major component of the icy mantle composition predicted by our chemical model. Although this may not be correct, as CO₂ ice is well detected in molecular clouds, we decided here to focus on the exact model predictions relevant for the centre of pre-stellar cores, where it is not clear if CO₂ is indeed a dominant component and JWST observations are needed to confirm this.

4.5 Results

The results for the layered and mixed ices are presented in the next subsection, followed by a more detailed depiction of the weak N₂ and O₂ bands.

4.5.1 Layered and mixed ices

The experiments have been design in order to fit the molecular composition as well as the thickness ratio, estimated in number of monolayers, as close as possible to the model, for the inner and outer ice layers. A minimum ice thickness of ≈ 160 ML was necessary to reconfirm that the N₂:H₂O ratio in layer 2 deviates by less than 10 % from the predicted value, but the ML ratio of layer 1 to layer 2 varies less than 10 % from the modelled partition.

Figure 4.2 shows all recorded spectra in the whole frequency range for the inner layer 1, the outer layer 2, layer 2 deposited on top of layer 1 and the mixed ice. The positions of band maxima for pure H₂O, CH₃OH and CO ices as well as N₂ and O₂ embedded in a H₂O matrix are added to help the reader assign the bands to the respective species. The spectra in all presented figures were baseline corrected and shifted along the y-axis for a better comparison of mixed and layered ices and to enable a better understanding of how layer 1 and 2 contribute to the spectral features observed in the layered ice.

H₂O ice bands

Figure 4.3a shows a shift of the OH stretching band maximum towards higher frequencies for both mixed and layered ices when compared to the pure ices. While a weak right shoulder feature can be explained by the contribution of the CH₃OH OH stretching vibration as well as interactions with CO, we observe that the shift of the band maximum is bigger for higher CO:H₂O and O₂:H₂O ratios, as most prominently seen in the spectrum of layer 2.

The molecular composition has a strong effect on the position of the H₂O dangling bonds as well. The presence of CH₃OH which has a similar abundance in the mixed ice and layer 2, causes a shift from higher frequencies to 3686 cm⁻¹ and an increasing amount to CO leads to dangling bond features even closer to the OH stretching band, as seen in Fig. 4.3c.

In the case of the H₂O 1660 cm⁻¹ bending mode, we see conspicuous differences both in band shape and position depending on the species that are interacting with H₂O. Even though the total amount of MLs is similar for the mixed and layered ices, the band intensity as well as the area below the band is considerably smaller for the layered ice. Additionally, the interaction of CH₃OH with H₂O in layer 1 causes a split of the band into two components, in comparison

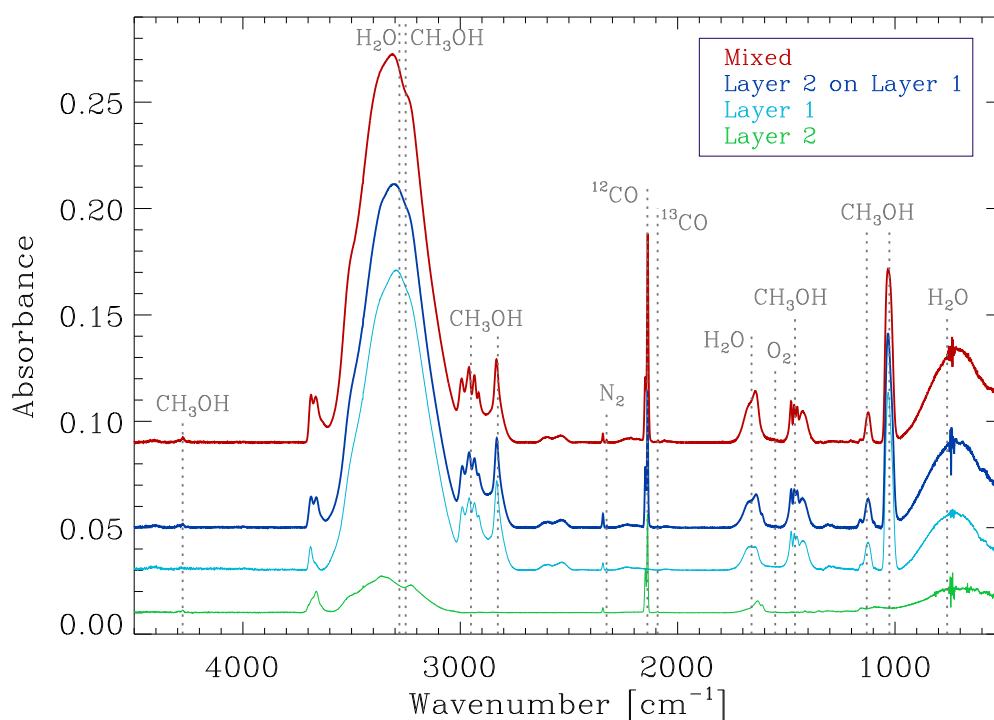


Figure 4.2: Spectra of mixed (red) and layered ices with layer 1 (light blue), layer 2 (green) and layer 2 on top of layer 1 (dark blue). Corresponding to Table 4.1, relative abundances for the mixed ice are $\text{H}_2\text{O}:\text{CH}_3\text{OH}:\text{N}_2:\text{CO} = 100\%:58\%:29\%:37\%$ and for the layered ice $\text{H}_2\text{O}:\text{CH}_3\text{OH}:\text{N}_2 = 100\%:67.5\%:27.5\%$ (Layer 1) and $\text{H}_2\text{O}:\text{N}_2:\text{CO}:\text{O}_2 = 100\%:46\%:146\%:38\%$ (Layer 2).

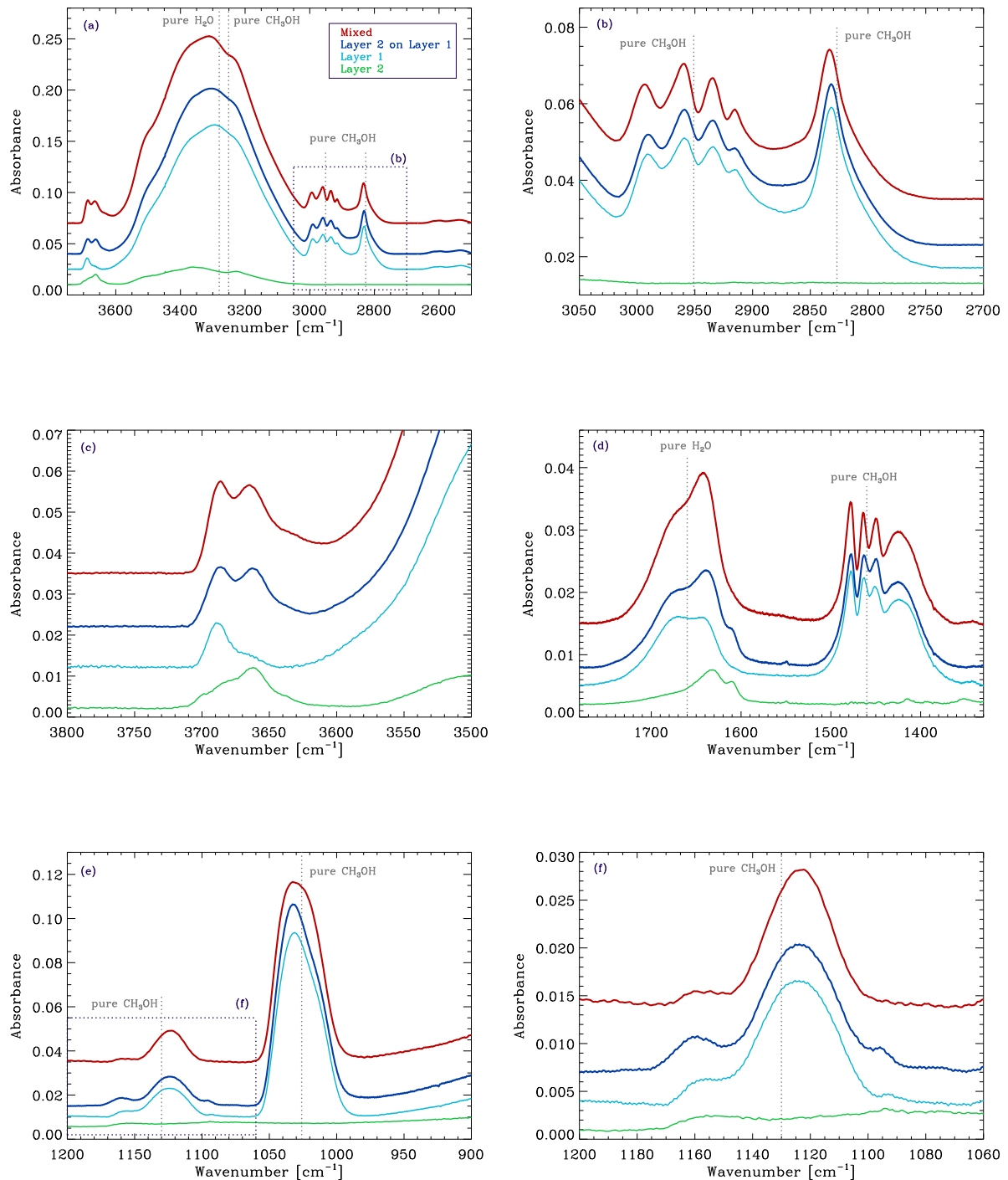


Figure 4.3: Spectra of mixed (red) and layered ices with layer 1 (light blue), layer 2 (green) and layer 2 on top of layer 1 (dark blue), zoomed-in around the OH-stretch (upper left), CH-stretch (upper right), H₂O dangling bonds (middle left) and OH-bend (middle right), CH₃OH CO-stretch (lower left) and CH₃-rock (lower left) bands. Corresponding to Table 4.1, relative abundances for the mixed ice are H₂O:CH₃OH:N₂:CO = 100%:58%:29%:37% and for the layered ice H₂O:CH₃OH:N₂ = 100%:67.5%:27.5% (Layer 1) and H₂O:N₂:CO:O₂ = 100%:46%:146%:38% (Layer 2).

with the spectral feature of the pure H₂O (c.f. Hagen et al. 1981). On the other hand, in layer 2 with high abundances of CO and O₂ we observe a shift of the water bending mode towards smaller frequencies and the emergence of a shoulder feature on the right wing, as seen in the right panel of Fig. 4.4.

CH₃OH ice bands

As the average composition of layer 1 was calculated by using 80 % of the modelled dust grain monolayers, the abundances of CH₃OH and N₂ relative to H₂O are very similar to those in the mixed ice. The major difference between these two CH₃OH containing ices analogues is the presence of CO that can be found in high amounts only in the outer layers of our model and thus is incorporated only in the mixed ice and layer 2, where the latter shows a considerably higher CO abundance relative to H₂O.

Since the CH₃OH:H₂O ratio is only slightly higher in layer 1 than in the mixed ice, interactions with CO are presumably the main reasons for the minor shifts in position of the CH₃OH CH stretching modes in the layered and mixed ices, at 2951 cm⁻¹ and 2827 cm⁻¹, as seen in Fig. 4.3b. When compared to pure CH₃OH ice however (e.g. Hudgins et al. 1993), we see the effect of the interacting H₂O and CH₃OH molecules in both the band shape and position. The maximum position is shifted to smaller frequencies and local maxima appear to be more prominent for the 2951 cm⁻¹ band (cf. Ehrenfreund et al. 1999). In the mixed ice, the presence of CO has a noticeable effect on the intensity, which is enhanced.

A similar behaviour is seen in Fig. 4.3d for the 1460 cm⁻¹ CH₃ stretching band. While the band strengths become more prominent with the presence of CO, the general appearance of the band for the mixed ice and layer 1 is very much alike. Interaction of H₂O and CH₃OH on the other hand causes not only a small blue shift but also a change in the band shape. Comparison with Ehrenfreund et al. (1999) shows that the relative intensity of the three local maxima at lower frequencies changes, with the left wing becoming the most intense. Also, the shoulder feature on the right wing of the pure methanol band gets more dominant.

In Fig. 4.3e and 4.3f no shifts in position of the CO stretching and CH₃ rocking bands are seen when comparing layered and mixed ices. While a small change in the 1026 cm⁻¹ band shape might be difficult to observe, the emergence of a local maximum on the right wing of the 1130 cm⁻¹ band in the layered ice, as well as the different shape of the left wing local maximum, enable a clear differentiation of the layered or mixed structure of the ice. Additionally, the interaction of H₂O and CH₃OH leads to a shift towards higher frequencies relative to the position of pure CH₃OH ice for the CO stretching mode while the CH₃ rock shifts towards smaller wavenumbers.

CO ice band

The presented model suggests that a considerable amount of CO freezes out within pre-stellar cores, in agreement with observations (e.g. Crapsi et al. 2005). CO is the most abundant species in the external layers of icy mantles in contrast with the composition of the bulk in which H₂O represents the largest fraction. In our experiments, this layered morphology of CO on top of H₂O

is represented in layer 1 and 2 and compared to the mixed ice with a considerably lower CO:H₂O ratio.

Figure 4.2 shows that position and shape of the CO ice bands are very similar in the layered and mixed ice analogues. For both spectra, we detect only a minor shift from 2139 cm⁻¹ to 2138 cm⁻¹ when compared to pure CO ice (e.g. Jiang et al. 1975). A second component is visible in the absorption band, due to the interaction with H₂O, for layered and mixed ices at 2148 cm⁻¹ or 2149 cm⁻¹, respectively (cf. Bouwman et al. 2007). Band shape and position are not affected by the presence of CH₃OH, N₂ and O₂. Thus, we find that CO spectral features are not bringing any information about the layered or mixed nature of our ice analogues.

4.5.2 N₂ and O₂

Pure N₂ and O₂ do not show vibrational bands in the IR region because homonuclear diatomic species have no dipole moment. A molecular stretching mode can only be induced via symmetry breaking by other polar species such as water, as shown by Ehrenfreund et al. (1992) and Bernstein & Sandford (1999).

N₂ is present in all layers of the considered ice mantle. Apart from the innermost bulk it shows a constant abundance throughout all numbers of monolayers and thus the average N₂ fractions of both layered and mixed ices are very similar. Nonetheless, in our layered ice experiment the N₂:H₂O ratio is higher for layer 2 than for layer 1 which is due to a decreasing abundance of H₂O towards the surface layers.

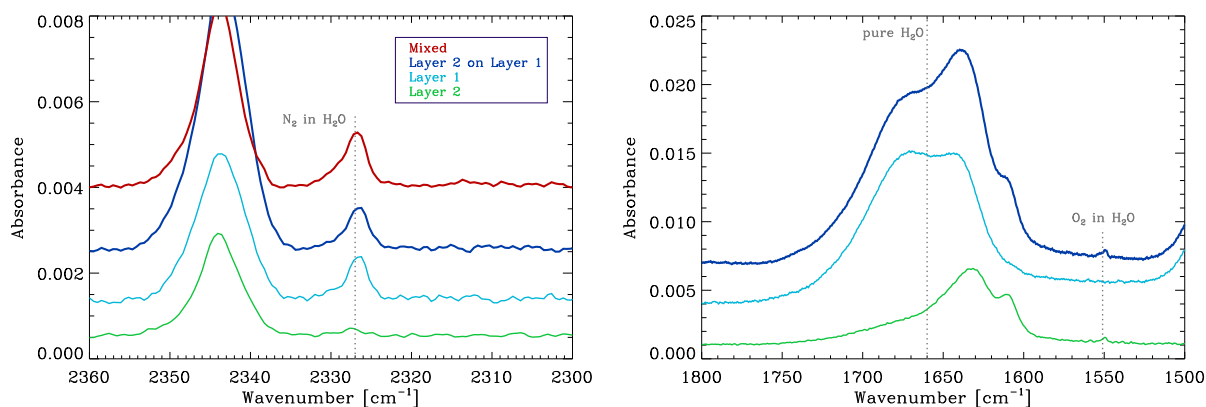


Figure 4.4: Spectra of mixed (red) and layered ices with layer 1 (light blue), layer 2 (green) and layer 2 on top of layer 1 (dark blue), zoomed-in around the N₂ (left) and O₂ (right) bands. Corresponding to Table 4.1, relative abundances for the mixed ice are H₂O:CH₃OH:N₂:CO = 100%:58%:29%:37% and for the layered ice H₂O:CH₃OH:N₂ = 100%:67.5%:27.5% (Layer 1) and H₂O:N₂:CO:O₂ = 100%:46%:146%:38% (Layer 2).

The left panel in Fig. 4.4 shows that the differences in the relative abundances of N₂ and

H₂O have no influence on the 2327 cm⁻¹ nitrogen band position and shape. The same is true for different ice compositions including CH₃OH, CO and O₂ in different composition ratios.

As already mentioned, we did not include CO₂ in our modelled experiments, as we follow the theoretical predictions of our pre-stellar core chemical model. Still, a weak CO₂ band is present in Fig. 4.4 due to residual contamination in the experimental set-up.

In the inner regions of L1544, O₂ is predicted to be present in high amounts of 10 % in the outer monolayers of the ice mantles. With an average abundance of H₂O = 26 % in these layers, and a relative abundance of O₂:H₂O = 38 %, the O₂ band becomes visible in layer 2 of our experiments. We find the O₂ band at a frequency of 1549 cm⁻¹ which differs from the 1551 cm⁻¹ when O₂ is present only in a two component O₂-H₂O ice mixture (c.f. Ehrenfreund et al. 1992; Müller et al. 2018).

4.6 Discussion

4.6.1 Comparison with previous work

We have seen that the structure and the molecular composition of the ice have an effect on the position and shape of absorption bands. Table 3.2 lists all examined band positions compared with the position values of pure H₂O, CH₃OH and CO ices, as well as N₂ and O₂ embedded in a water matrix. Some of the observed bands do not show any shifts when layered and mixed ices are compared. Nevertheless, our results show important deviations from the frequencies measured for pure ices. In this context, the observed broadening of the 1032 cm⁻¹ maximum in the mixed ice indicates the interaction of CH₃OH with CO, which was studied by Penteado et al. (2015) who recorded a shift towards higher frequencies when CH₃OH is interacting with CO. Our measurements show that the band profile of the 1464 cm⁻¹ CH₃ bending mode is another suitable indicator of the CH₃OH-CO interplay. Moreover, the particular profile of the CO double peak appears when CO and H₂O are present in an ice mixture of low temperature, as observed by Fraser et al. (2004).

Most of the H₂O and CH₃OH bands are applicable for characterising the layered or mixed nature of our ices. We are able to connect the band changes to the structure of our probes, in agreement with previous works in the literature, (e.g. Wolff et al. 2007; Bahr et al. 2008; Öberg et al. 2009).

Based on experimental results from Dawes et al. (2016) who examined band changes of CH₃OH in different ratios relative to H₂O, we expected to find the peak of the OH stretching band in an frequency range between the maximum position of 3280 cm⁻¹ for pure water and 3251 cm⁻¹ for pure methanol. Our results however show a blue shift towards frequencies ≥ 3304 cm⁻¹ and the emergence of a right wing shoulder feature. The appearance of the band can be explained by interactions of CO with the OH mode of H₂O and CH₃OH. Our observations agree well with Bouwman et al. (2007) who saw a similar behaviour for ices with an increasing CO:H₂O ratio and with experiments conducted by Müller et al. (2021) where CO is present in ice mixtures containing water and methanol.

Also, the appearance of a shoulder feature on the right wing of the H₂O 1660 cm⁻¹ bending

Table 4.3: Position of all observed molecular bands in the experiments presented in the paper, recorded at 10 K, with a spectral resolution of 1 cm^{-1} . Multiple band assignments refer to several local maxima or shoulder features for one band.

Molecule	Vibration mode	Wavenumber (cm^{-1})		
		Pure	Layered ^a	Mixed
H ₂ O	ν_1, ν_3 OH stretch	3280	3304	3314
	ν_2 OH bend	1660	1670, 1638, 1610	1674, 1642
	dangling bonds	3720, 3697	3686, 3662	3686, 3665
CH ₃ OH	OH & CH stretch	3251, 2951, 2827	3304, 2959, 2832	3314, 2960, 2834
	CH ₃ bend	1460	1464	1464
	ν_7, ν_{11} CH ₃ rock	1130	1160, 1124, 1096	1160, 1124
	ν_8 CO stretch	1026	1032	1032
CO	CO stretch	2139	2138, 2148	2138, 2149
N ₂		2327 ^b	2327	2327
O ₂		1551 ^b	1549	-

(a) Layer 2 on top of layer 1.

(b) Embedded in a H₂O matrix.

mode as well as the shift of the water dangling bonds towards lower frequencies is in good agreement with observations for similar CO:H₂O and O₂:H₂O ratios conducted by Bouwman et al. (2007) and Müller et al. (2018) who examined the interaction of H₂O with CO and O₂, respectively. Spectra presented in Müller et al. (2021) don't show any considerable effect of CH₃OH on the free OH dangling bonds but we note that the CH₃OH:H₂O ratio in that work is considerably lower than in the presented experiments. Considering reflection absorption infrared spectra (RAIRS) results from He et al. (2018b), who showed the shift of dangling bonds for a N₂:H₂O ratio similar to our mixtures, we deduce the remarkable band profile difference of the local maximum at 3686 cm⁻¹ from interactions of water with methanol.

The highly varying amount of CO represents the major difference in mixed and layered ices containing CH₃OH. Thus, differences in band shape and position of CH₃OH are mainly due to its interaction with CO. While the 2951 cm⁻¹ asymmetric CH stretching and 1460 cm⁻¹ CH₃ bending mode seem to be enhanced by this interaction, we observe only a significant change in the 1130 cm⁻¹ CH₃ rocking mode. Müller et al. (2021) found that shoulder features of the 1130 cm⁻¹ band tend to disappear when CH₃OH interacts with increasing abundances of CO. This behaviour can also be seen when we compare our layered ice, where CO and CH₃OH are present in different layers, with the mixed ice, where the presence of CO and methanol causes the decrease or even the disappearance of the left and right shoulder features. Apart from the shift towards smaller frequencies due to interactions of H₂O and CH₃OH we do not see any differences in the 2827 cm⁻¹ symmetric CH stretch when comparing layered and mixed ices. The shift of the 1026 cm⁻¹ CO stretching band towards higher frequencies agrees well with the results in Müller et al. (2021) that has a CO:CH₃OH ratio appropriate for comparison with our work. The present study however cannot confirm the shift of the CO stretching mode to 1018 cm⁻¹ as seen in Müller et al. (2021) for CH₃OH-H₂O mixtures when CO is not included in the ice matrix. The discrepancy however can be explained by the large difference in the ratio of CH₃OH:H₂O = 5 % in the previous work, compared to the present work, where CH₃OH:H₂O = 74.4 %.

Examining the CO stretching band we see that it is not affected by changing N₂:CO ratios, the presence of O₂ or CH₃OH in the mixed ice. However, when we compare to measurements conducted by Bouwman et al. (2007), we see that a mixture of CO and H₂O results in a feature on the left wing of the band, which increases for increasing H₂O:CO ratios, and shifts towards higher frequencies. Moreover, our observations agree well with the broadening of the band and decreasing intensity as recorded by Bouwman et al. (2007) for increasing abundances of H₂O.

4.6.2 Ice feature observability with JWST

We are interested in the observability of the weak N₂ and O₂ bands with JWST as both species are thought to be abundant in interstellar ices. Being not detectable in the IR region in their pure form, both species become visible at mid-IR wavelengths when they are embedded in a polar matrix (for example H₂O) that can induce the formation of a dipole moment.

The presented model predicts large amounts of molecular nitrogen in all ice layers forming on dust grains in the inner regions of L1544. In our analysis, the N₂ feature is not sensitive to the changes in ice composition or structure. This is confirmed by work from Bernstein & Sandford (1999) who analysed the nitrogen absorption band in binary mixtures with excess of N₂.

O₂ is thought to be found in fractions of a monolayer > 10 % in the outer layers of ice mantles located in central zones of the pre-stellar core. In our experiment, this correlates to a high O₂:H₂O ratio of 38.5 % and the band becomes detectable for the FTIR spectrometer. We find the O₂ band at a position of 1549 cm⁻¹ which differs from the frequency of 1551 cm⁻¹ that was recorded for binary O₂-H₂O mixtures by Ehrenfreund et al. (1992) and Müller et al. (2018). The difference in position can be explained with the interaction of O₂ with CO (c.f. Ehrenfreund et al. 1992)

In the case of our layered ice analogue, for some absorption bands we noticed differences in the band shape when we compared layer 1 and 2 with layer 2 deposited on top of layer 1. The differences are present in the water dangling bonds and bending mode as well as in the methanol CH₃ rocking mode. A comparison of the computationally added layer 1 and 2 with the experimentally layered ice is shown in appendix section A.1. The differences in band shape and position can be explained by interactions of molecules at the interface between the two layers.

For both the layered and the mixed ice, we estimate the observation times with JWST for a selection of the presented absorption bands, including the weak N₂ and O₂ bands. The optical depth τ and the transmittance T are related to each other by

$$T = e^{-\tau} = e^{-\int \alpha ds}, \quad (4.1)$$

where ds is the length of the path through which the light of a background star travels. Similar to Müller et al. (2018), the absorption coefficient α can be derived from absorbance values Abs and ice thicknesses d obtained during the experiments using

$$\alpha = \frac{Abs \cdot \ln(10)}{d}. \quad (4.2)$$

For our calculations of the whole pre-stellar core we sum up the optical depth of subpaths s_n along the line-of-sight and derive

$$\tau_{\text{tot}} = \sum_{s_n} \tau_{s_n} \quad (4.3)$$

and consequently

$$T_{\text{tot}} = \prod_{s_n} T_{s_n}. \quad (4.4)$$

In order to derive the total optical depth and transmittance of the modelled pre-stellar core, the ice composition and thickness at each subpath s_n has been taken into consideration. The model suggests that the proportions of icy species within a radius of 1675 au do not change much and that this is also true for ice mantles in the outer region of the modelled L1544. Thus, we decided to treat the ice mantles in the inner 1675 au as the same as our experimentally tested ice composition while we average over all chemical fractions for $R > 1675$ au. The calculated values for τ and T are shown in Table 4.4.

The transmitted fraction of the initial flux density F_v^* emitted by a background star is

$$F_{v,\text{tr}} = T \cdot F_v^* \quad (4.5)$$

Table 4.4: Optical depth and transmittance of the modelled ice features in L1544. The values have an error of 20% - 30%.

Molecule	Vibration mode	τ		T	
		Layered	Mixed	Layered	Mixed
H ₂ O	ν_1, ν_3 OH stretch	3.8082	3.8169	0.0222	0.0220
	ν_2 OH bend	0.3666	0.5052	0.6931	0.6034
CH ₃ OH	OH & CH stretch	3.8082	3.8169	0.0222	0.0220
	ν_7, ν_{11} CH ₃ rock	0.3156	0.2966	0.7293	0.7434
	ν_8 CO stretch	2.1560	1.7049	0.1158	0.1818
N ₂		0.0217	0.0257	0.9785	0.9746
O ₂		0.0178	-	0.9823	-

and the absorbed fraction is thus

$$F_{\nu,\text{abs}} = A \cdot F_{\nu}^* = (1 - T) \cdot F_{\nu}^*. \quad (4.6)$$

Finally, the line strength necessary for calculating the observation time is

$$S = \int_{\Delta\nu} F_{\nu,\text{abs}} d\nu, \quad (4.7)$$

where $\Delta\nu$ is the band width of the corresponding absorption band. Assuming that the band has the form of a Gaussian peak, the line strength is approximately $S \approx F_{\nu,\text{abs}} \cdot FWHM$, where $FWHM$ is the full width at half maximum.

In order to calculate the line strengths close to the dust peak, which are necessary to obtain observation times with JWST, apparent magnitudes from observations of L1544 with the Spitzer Space Telescope (SST) were used to derive flux densities for the SST Infrared Array Camera (IRAC) channels 2-4, which are suitable for observing the 1600 cm^{-1} H₂O bend, 1130 cm^{-1} CH₃OH rock, 2327 cm^{-1} N₂ and 1551 cm^{-1} O₂ bands. Close to the dust peak, the observed Vega magnitudes are $m_{\text{vega,IRAC2}} = 10.61$, $m_{\text{vega,IRAC3}} = 10.24$ and $m_{\text{vega,IRAC4}} = 10.16$. Converting to AB magnitudes, which are necessary for calculating the flux densities, gives $m_{\text{AB,IRAC2}} = m_{\text{vega,IRAC2}} + 3.26 = 13.87$, $m_{\text{AB,IRAC3}} = m_{\text{vega,IRAC3}} + 3.73 = 13.97$ and $m_{\text{AB,IRAC4}} = m_{\text{vega,IRAC4}} + 4.40 = 14.56$. The resulting flux density consequently is

$$F_{\nu}^* = 10^{-m_{\text{AB}}/2.5} \cdot F_{\nu 0}, \quad (4.8)$$

where $F_{\nu 0}$ is the zero magnitude flux density, which is in the case of SST equal to $F_{\nu 0, \text{IRAC2}} = 179.7 \text{ Jy}$, $F_{\nu 0, \text{IRAC3}} = 115.0 \text{ Jy}$ and $F_{\nu 0, \text{IRAC4}} = 64.9 \text{ Jy}$.

Together with the FWHM of the bands, the resulting line strength can be found in Table 4.5. Both quantities are necessary to generate a theoretical spectrum of the modelled L1544 with the bands listed in Table 4.4 and to calculate the observation times of the absorption bands using

the JWST exposure time calculator (ETC). Observation times were calculated for signal-to-noise (S/N) ratios > 10 for the weak N_2 and O_2 bands and added to Table 4.5. We find that the detection of N_2 is feasible with a calculated total exposure time of 1.4 h with NIRSpec, while for observing O_2 an exposure time 123.6 h is necessary. As the H_2O bending mode is observed with the same instrument configurations as O_2 , its observation time amounts to the same time interval even though it can be detected after shorter exposure times. However, this specific feature can give us information about the layered or mixed nature of icy mantles as well as about abundances of CO and O_2 relative to H_2O . Thus, longer observation times improve the evaluation of the physical and chemical structure of interstellar ices.

Table 4.5: Full width half maximum, line strength S , observation time and signal-to-noise ratio S/N of the bands included in the JWST exposure time calculator.

Molecule	Vibration mode	FWHM (Hz)		S ($\text{erg s}^{-1} \text{cm}^{-2}$)		t_{obs} (s)		S/N	
		Layered	Mixed	Layered	Mixed	Layered	Mixed	Layered	Mixed
H ₂ O	ν_2 OH bend	2.28×10^{12}	2.04×10^{12}	2.08×10^{-15}	2.40×10^{-15}	445105 ^a		151.47	183.48
CH ₃ OH	ν_7, ν_{11} CH ₃ rock	9.00×10^{11}	1.05×10^{12}	2.38×10^{-16}	2.63×10^{-16}	445105 ^b		41.92	40.05
N ₂		9.00×10^{10}	9.00×10^{10}	9.87×10^{-18}	1.17×10^{-17}	5017 ^c		11.23	12.72
O ₂		9.00×10^{10}	-	4.72×10^{-18}	-	445105 ^a		10.21	-

^a Instrument configuration: MIRI MRS Channel 1B.

^b Instrument configuration: MIRI MRS Channel 2B.

^c Instrument configuration: NIRSpec fixed slit G395H/F290LP S400A1.

The observation time of O₂ is too long to be performed with JWST. This however might change when a background light source closer to the dust peak and thus more suitable for O₂ detection is used for the calculation. Future surveys could help to find such a source and make more promising predictions on the detectability of absorption bands.

The purpose of the presented results is providing spectroscopic data that will help future observations to investigate the nature of interstellar ice structures. The available spectral resolutions of $R > 2400$ for MIRI and $R \sim 2700$ for NIRSpec (high resolution gratings) correspond to an upper limit of $0.43 \text{ cm}^{-1} < \Delta\nu < 0.83 \text{ cm}^{-1}$ for the examined bands observed with MIRI and $0.79 \text{ cm}^{-1} < \Delta\nu < 1.38 \text{ cm}^{-1}$ for bands observed with NIRSpec. Hence, all changes in the spectroscopic features recorded in our experiments will be detectable for JWST.

Observations with JWST will not only be able to test state-of-the-art gas-grain model predictions but also constrain the physical and chemical structure of ice mantles. The H₂O stretching, bending and dangling, CH₃OH rocking and O₂ modes help to differentiate between layered and mixed ice structures whereas composition ratios can be estimated via the CH₃OH CH stretching and CH₃ bending modes. We conclude that JWST observations will be sufficient to test our model predictions.

4.7 Conclusion

This work focuses on laboratory spectroscopy of interstellar icy mantle analogues predicted within pre-stellar cores and we characterise the changes of absorption band positions and profiles for ice analogues based on the model of Vasyunin et al. (2017). Previous CH₃OH observations by Dartois et al. (1999), Penteado et al. (2015) and Goto et al. (2021) hint to a layered structure of ice mantles as demonstrated in Müller et al. (2021). This work investigates the spectral features contribution for new species, in addition to CH₃OH, which are suitable for deducing the morphology of interstellar ices. The ice structure is tightly related to the chemical composition of the mixtures that we prepared for our experiments. According to our theoretical predictions we find that in regions close to the dust peak, ice layers rich in H₂O and CH₃OH are covered by watery layers with a significant amount of CO and O₂. We compare this structure with a completely mixed ice and show the differences in the band characteristics. Our experiments, coupled with future JWST observations, will allow us to test our gas-grain models and help us to gain understanding on surface processes.

Chapter 5

Broadband spectroscopy of astrophysical ice analogues. I. Direct measurement of the complex refractive index of CO ice using terahertz time-domain spectroscopy

The contents of this chapter were published in the *Astronomy & Astrophysics* Journal.

Credit: Giuliano, Gavdush, Müller et al., *A&A*, 629, A112, 2019, reproduced with permission ©ESO

I made a major contribution to this work by participating in the assembling of the experimental set-up and by conducting all experiments presented in the following. I took care that the experimental procedures fitted the needs for deriving the optical constants and provided measured data with best possible quality.

5.1 Abstract

Reliable, directly measured optical properties of astrophysical ice analogues in the infrared and terahertz (THz) range are missing from the literature. These parameters are of great importance to model the dust continuum radiative transfer in dense and cold regions, where thick ice mantles are present, and are necessary for the interpretation of future observations planned in the far-infrared region. Coherent THz radiation allows for direct measurement of the complex dielectric function (refractive index) of astrophysically relevant ice species in the THz range. We recorded the time-domain waveforms and the frequency-domain spectra of reference samples of CO ice, deposited at a temperature of 28.5 K and annealed to 33 K at different thicknesses. We developed a new algorithm to reconstruct the real and imaginary parts of the refractive index from the time-domain THz data.

The complex refractive index in the wavelength range 1 mm–150 μm (0.3–2.0 THz) was determined for the studied ice samples, and this index was compared with available data found

in the literature. The developed algorithm of reconstructing the real and imaginary parts of the refractive index from the time-domain THz data enables us, for the first time, to determine the optical properties of astrophysical ice analogues without using the Kramers-Kronig relations. The obtained data provide a benchmark to interpret the observational data from current ground-based facilities as well as future space telescope missions, and we used these data to estimate the opacities of the dust grains in presence of CO ice mantles.

5.2 Introduction

One of the main problems in unraveling the chemical and physical properties of molecular clouds, in which the star and planet formation process takes place, is to estimate correctly the amount of gas contained. The difficulties in the direct observation of molecular hydrogen constrain the possibility to calculate the total mass of a cloud. An easy alternative could be to use carbon monoxide as a tracer of molecular gas, but in dense and cold regions of the interstellar medium and protoplanetary discs, CO is not a good tracer of gas mass because CO molecules preferentially reside on dust grains, forming thick icy mantles (e.g. Dutrey et al. 1998; Caselli et al. 1999). Alternatively, the dust continuum emission is the best available tool to compute a molecular cloud mass, if dust opacities are known.

The advent of Atacama Large Millimeter/submillimeter Array (ALMA) and Northern Extended Millimeter Array (NOEMA) facilities offers the possibility to observe the dust continuum emission in the millimetre and submillimetre part of the electromagnetic spectrum with very high angular resolution and sensitivity. However, to model the dust continuum emission properly it is necessary to have information about its grain size distribution and its chemical composition, since the dust opacity depends directly on these parameters. If we take into account that the dust grains can be covered by ice mantles at the centre of prestellar cores or in protoplanetary disc mid-planes, we also need to investigate how the presence of ices is changing the dust opacities.

Unfortunately, no experimental data are available for these cases, and the interpretation of the dust continuum emission measurements relies on calculated opacity values, such as those tabulated in Ossenkopf & Henning (1994). The goal of our study is to provide laboratory data on the optical properties of CO ice and utilize these data to calculate the opacities of dust grains covered by CO ice mantles. We compare the opacity values obtained by our study to those available in the literature.

The presently available set of data focusses mainly on the determination of the optical constants in the visible and mid-infrared (MIR) range (Hudgins et al. 1993; Ehrenfreund et al. 1997; Baratta & Palumbo 1998; Loeffler et al. 2005; Dartois 2006; Palumbo et al. 2006; Warren & Brandt 2008; Mastrapa et al. 2009).

Far-infrared (FIR) studies on spectral properties of molecular solids, without deriving optical constants, started early, to deepen the understanding of the infrared-active lattice vibrations of simple species. Anderson & Leroi (1966) studied frequencies of CO and N₂ in the range 40-100 cm⁻¹, and Ron & Schnepf (1967) complemented the available information with CO, N₂ and CO₂ intensity studies in the same frequency range. In 1994 Moore and Hudson published a comprehensive study of FIR spectra of cosmic type ices, including ice mixtures. These data

included the analysis of amorphous and crystalline phases of the pure molecular ices, and the authors discussed the implications of the results on the identification based on astronomical observations. An estimation of the band strengths in the FIR region for pure ices and ice mixtures relevant for astrophysical environments can be found in Giuliano et al. (2014; 2016).

Recently, the investigation of the terahertz (THz) spectroscopic properties of ice mantles analogues has gained considerable interest (Allodi et al. 2014; Ioppolo et al. 2014; McGuire et al. 2016). This technique allows direct measurement of the intermolecular vibrations in the ice samples related to the lattice structure, which can be connected to their large-scale structural changes and finally to their thermal history. On the contrary, spectroscopic features measured in the MIR frequency range are indicative of the intramolecular vibrations of the sample, which can provide a wealth of information on the molecular identification and chemical reactivity. A comparison of our THz experimental data with that observed in the MIR range could help us to reveal intra- and inter-molecular vibrations. However, this study is beyond the scope of this paper and will be addressed in our future investigations.

Nowadays, numerous spectroscopic methods are extensively used for dielectric measurements at THz frequencies (Lee 2009); these include the following: Fourier transform infrared (FTIR) spectroscopy (Griffiths & de Haseth 1986), Backward-wave oscillator (BWO) spectroscopy (Komandin et al. 2013), spectroscopy based on photomixing (Preu et al. 2011) or parametric conversion (Kawase et al. 1996; Kiessling et al. 2013), and, finally, THz time-domain spectroscopy (THz-TDS) (Auston 1975; van Exter et al. 1989). These methods exploit either continuous-wave or broadband sources, operate in different spectral ranges, and are characterized with different sensitivity and performance. Among these methods, THz-TDS seems to be the most appropriate for studying laboratory analogues of circumstellar and interstellar ices. In contrast to other approaches, THz-TDS yields detection of both amplitude and phase of sub-picosecond THz pulses in a wide spectral range as a result of a single measurement; thus, the reconstruction of the dielectric response of a sample might be performed without using the Kramers-Kronig relations (Martin 1967) and involving additional physical assumptions. Furthermore, THz-TDS yields analysis of separate wavelets forming the time-domain response of a sample; thus, it is a powerful method for the characterization of multilayered samples. Thereby, we selected THz-TDS as a spectroscopic technique for our experiments.

We aim at the extension of the laboratory data in the FIR/THz region, and we show how the employment of the THz-TDS is able to provide direct measurement of the real and imaginary part of the refractive index of the ice sample. The experimental and theoretical methods employed are explained in Section 5.3, the results obtained and how these data are relevant for astrophysical application are presented in sections Section 5.4.3 and Section 5.5, respectively; the conclusions are illustrated in Section 5.6.

5.3 Experimental and theoretical methods

For this series of experiments a dedicated set-up has been designed and developed in the laboratories of the Center for Astrochemical Studies (CAS) located at the Max Planck Institute for Extraterrestrial Physics in Garching (Germany). The set-up is composed of a closed-cycle

The cryocooler coupled to a THz time-domain spectrometer. The cryocooler vacuum chamber is small enough to be hosted in the sample compartment of the THz spectrometer, and it is mounted on a motor controlled translational stage, which ensures the tuning of the cryostat position with respect to the THz beam. The details of the main components of the apparatus and the ice growing procedure are given in the following subsections.

5.3.1 Cryogenic set-up

The high power cryocooler was purchased from Advanced Research Systems. The model chosen is designed to handle high heat loads thereby ensuring a fast cooling. This instrument is equipped with a special interface capable of reducing the vibration transmitted from the cold head to the sample holder at the nanometer level. This requirement is important in case of spectroscopic measurements in the THz frequency region, where the induced vibration of the sample can cause the increase of the noise level of the recorded spectra.

The cryostat is placed in a 15 cm diameter vacuum chamber, equipped with four ports for optical access and for the gas inlet. The optical arrangement is designed to work in the transmission configuration. The optical windows chosen for the measurements at the desired frequency range are made of high-resistivity float-zone silicon (HRFZ-Si), purchased by Tydex. This material features a high refractive index of $n_{\text{Si}} = 3.415$, negligible dispersion, and impressive transparency in the desired frequency range. The same material was chosen as a substrate for ice growing. In order to suppress the Fabry-Perot resonances in the THz spectra, caused by multiple reflection of the THz pulse within the windows, the thickness of the three Si windows must be different from each other. For this purpose we chose to use the 1 mm thick Si window as substrate for the ice deposition, and we used two windows of 2 mm and 3 mm thickness as optical access to the THz beam.

We performed measurements with a slightly focussed THz beam configuration in order to mitigate vignetting and diffraction of the beam at the metal components of the vacuum chamber. A schematic overview of the chamber arrangement is sketched in Fig. 5.1. The pumping station is composed of a turbomolecular pump (84 l s^{-1} nitrogen pumping speed) combined with a backing rotary pump ($5 \text{ m}^3 \text{ h}^{-1}$ pumping speed), thus providing a base pressure of about 10^{-7} mbar. The minimum temperature measured at the sample holder in normal operation mode is 5 K.

5.3.2 Terahertz time-domain spectrometer

The THz-TDS set-up used for this work was purchased from the company Batop GmbH. The model chosen is the TDS-1008, which has a customized sample compartment in order to allocate the cryostat. This model is based on two photoconductive antennas made of low-temperature-grown gallium arsenide (LT-GaAs), which constitute the emitter and detector of the THz pulse (Lee 2009). The antennas are triggered by a femtosecond laser (TOPTICA, 95 fs, 780 nm) with a pulse repetition rate of 100 MHz and an average input power of 65 mW. Further details on the set-up are provided in the Appendix B.1.

Fig. 5.2 (a) shows the optical path of the laser beam into the optical bench of the spectrometer. Panel (b) in Fig. 5.2 shows standard broadband Fourier spectra. The THz pulse registered

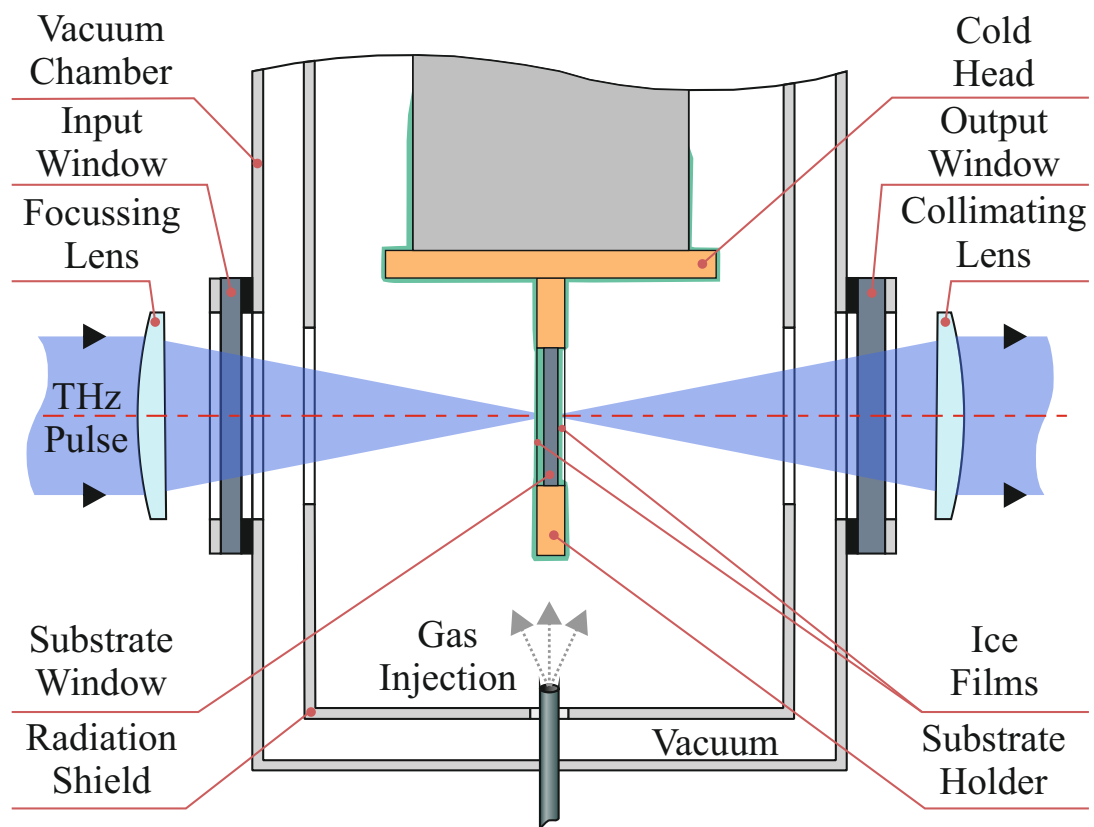


Figure 5.1: Sketch of the vacuum chamber of the cryostat coupled to the THz beam at the CAS.

with the beam path empty is then converted in the blue spectrum spanning the frequency range from 0.05 THz to 3.5 THz with maximal spectral amplitude centred at about 1.0 THz. In TDS, the time-domain THz waveform is converted to the frequency domain using the direct Fourier transform, which yields the frequency-dependent amplitude and phase of the THz wavelet. Since the frequency-domain data are calculated via the direct Fourier transform, the spectral resolution of measurements is determined as $\Delta\nu = 1/\Delta T$, where ΔT is a size of the time-domain apodization filter, chosen to avoid the edge effects (i.e. the Gibbs effect) in the frequency domain. In our experiments we used the 35-ps Tukey apodization filter (see Appendix B.2), which yields the spectral resolution of about 0.03 THz.

The green spectrum was recorded with the cryostat placed in the sample compartment. It is converted from a waveform which contains both a first THz pulse (i.e. a ballistic one) and a train of satellite pulses originating from the multiple THz wave reflections within the windows. The ballistic THz pulse is delayed in the input/output windows and the substrate of the vacuum chamber. The spectrum of this waveform is slightly suppressed owing to the Fresnel losses and modulated due to the interference of the ballistic pulse and the satellites.

In Fig. 5.2 (b), we show the shaded area at lower frequencies, where we expect growing distortions of the experimental data caused by the THz beam diffraction on the aperture of the substrate that is 20 mm in diameter. Assuming that the THz beam spot formed at the substrate is diffraction-limited, the lateral intensity distribution in the spot is defined by the Bessel function of the first kind (Born & Wolf 1980). The resulting width of the first intensity peak is approximately $(3.8/\pi)(f/D)(c/\nu)$, where $D = 25$ mm and $f = 67$ mm stand for the diameter and the back focal distance of the focussing lens, respectively. From this model, we deduce the critical frequency of 0.3 THz, below which less than 95% of the beam energy passes through the substrate aperture. Thereby, considering both the spectral sensitivity of our THz-TDS set-up and the diffraction limits, the spectral operation range of our experimental set-up is approximately limited within 0.3 to 2.0 THz.

The THz-TDS housing is kept under purging with cold nitrogen gas during the entire experiment to mitigate the absorption features due to the presence of atmospheric water in the THz beam path. The residual humidity measured at the sensor was less than $10^{-3}\%$.

5.3.3 Ice preparation

The ices are prepared using a standard technique in which the molecular sample in its gaseous form is allowed to enter the vacuum chamber through a stainless steel 6 mm pipe. The gas flux is controlled by a metering valve. Once the gas is expanding inside the vacuum chamber it condensates on the substrate.

For this set of experiments an ice thickness of the order of millimetre is required to fulfil the sensitivity characteristic of the THz-TDS set-up. This value is orders of magnitude higher than the usual ice thickness reached using this deposition technique, which is of the order of μm . To deposit such a thick ice in a reasonable amount of time, we chose fast deposition conditions, in which a considerable amount of gas is introduced in the vacuum chamber. In these conditions it is very difficult to obtain an ice sample which is homogeneous enough to determine its optical properties. To overcome this problem the gas inlet characteristics must be set accordingly.

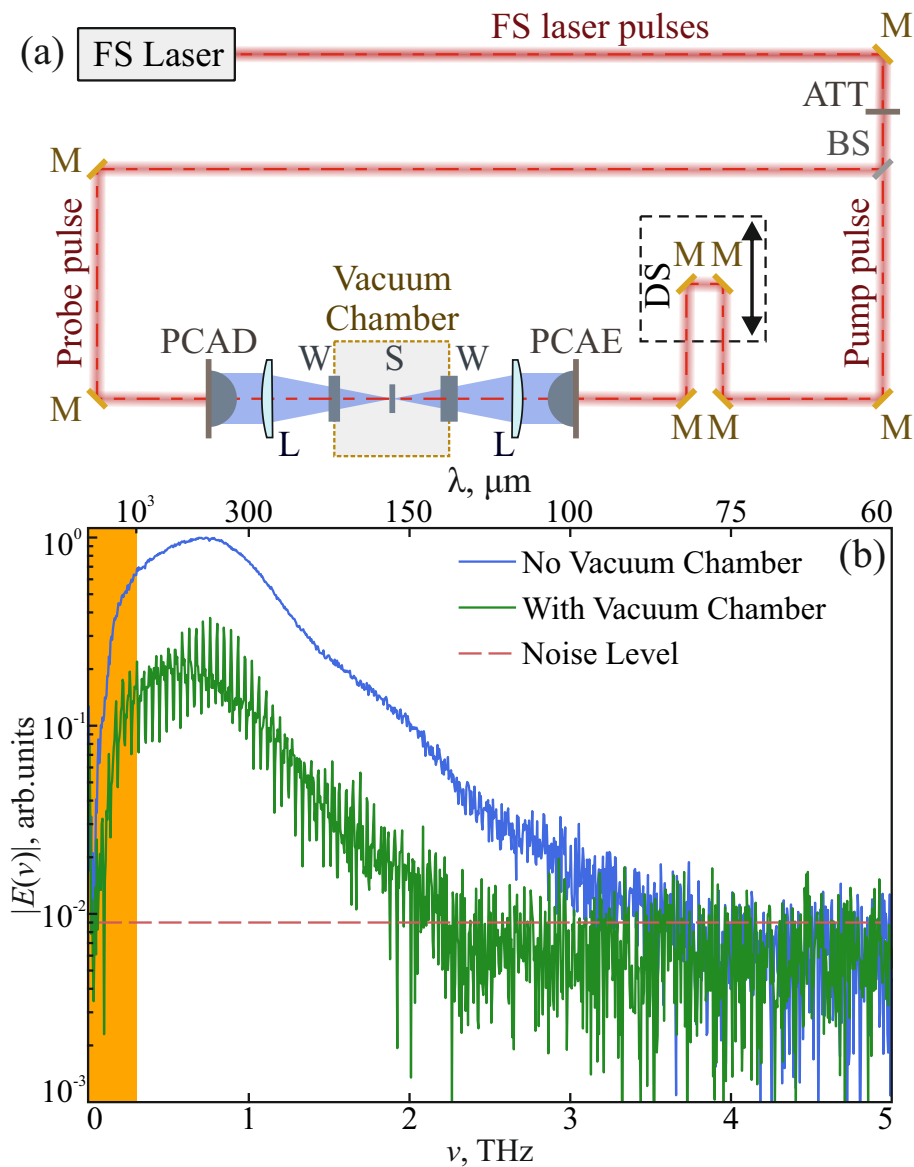


Figure 5.2: Set-up of THz-TDS for the spectroscopy of ices. (a) A schematic of the set-up, where FS laser stands for the femtosecond laser, M stands for the optical mirrors, ATT stands for the attenuator of the laser beam intensity, BS stands for the optical beams splitter, DS stands for the mechanical double-pass delay stage, PCAE and PCAD stand for the photoconductive antenna-emitter and antenna-detector, respectively, L stands for the TPX lenses, and S and W stand for the HRFZ-Si substrate and windows, respectively. (b) Spectra of THz waveforms $E(\nu)$ transmitted through the empty THz beam path or the THz beam path with the cryostat; the shaded region below ≈ 0.3 THz indicates the spectral range in which distortions from the THz beam diffraction on the aperture of the substrate are expected.

We decided to remove any directionality from the gas inlet, keeping the pipe end cut at the vacuum chamber wall at a distance of approximately 7 cm from the substrate (see Fig. 5.1). This configuration creates an ice layer on each side of the substrate. During the deposition, the pressure measured inside the chamber is approximately 10^{-2} mbar. The ice deposition was divided in steps of 4, 5, and 6 min duration, up to a total of 30 min deposition time, in three different experiments. The final temperature was up to 28.5, 31.2, and 33.1 K for each step at 4, 5, and 6 min deposition time, respectively. This increase is due to the condensation of the gas onto the cold surfaces of the cryostat, which is producing a heating rate too fast to be dynamically removed from the cooling system during the deposition. After each step, the THz spectrum has been recorded. This procedure was performed to rule out possible effects on the ice structure due to different deposition temperatures. As interstellar ices can be commonly found at temperatures as low as 10 K, the temperature of the cold substrate has been kept at 14 K, which is the lowest temperature achievable in the set-up in this configuration, because the radiation shield of the sample holder must be removed to ensure that no directionality of the molecular beam is present. Before moving to the next deposition step, the system was allowed to thermalize and spectra recorded after each deposition step have been taken at a temperature of 14 K.

As stated in Urso et al. (2016) the analysis of the Raman and infrared spectra of experiments performed at increasing temperatures from 17 to 32 K show no profile variation in the band at 2140 cm^{-1} , which could be ascribed to a structural change in the ice morphology.

The waveform recorded in the time domain is compared, as reference for the measurements, with the waveform recorded for the substrate without ice, kept at a reference temperature of 14 K as well. After the deposition was completed, we measured the spectra in different regions of the sample, to ensure that the ice morphology is spatially homogeneous. The results obtained from the spectra measured on a grid of 11 points spaced by 2 mm are in agreement within 10%, indicating a uniform ice formation over the substrate.

5.4 Derivation of the optical constants

In order to determine the optical constants, the ice thickness must be known. The laser interference technique is a well-established method to estimate the thickness of an ice sample deposited on a substrate as a function of the time. The absolute accuracy of this method is approximately within 5%, but the maximum CO ice thickness that we can measure with this technique is limited to $5\text{ }\mu\text{m}$ before the reflected laser signal becomes too weak to be detected, due to scattering losses occurring both in the bulk and on surface of the film. Thus, this technique is well suited for studying thin layers, when the ice thickness in total is below $10\text{ }\mu\text{m}$ ($5\text{ }\mu\text{m}$ on each side of the substrate), but is not appropriate for experiments on thick ice samples. In turn, for the thickness estimation of the millimeter-size sample of ice featuring rather low THz absorption, we developed a model to perform an initial estimation of the optical properties and the ice thickness directly from the recorded THz spectra, as described in the following subsections.

5.4.1 Ice parameters modelling

Our model aims to reconstruct the optical properties of ices, which are defined as follows:

$$n(\nu) = n'(\nu) - in''(\nu) \equiv n'(\nu) - i\frac{c}{2\pi\nu}\alpha(\nu), \quad (5.1)$$

where n' and n'' are the real and imaginary parts of the complex refractive index n , c is the light speed, and α is the amplitude absorption coefficient, which is defined as half of the value of the power absorption coefficient.

Equivalently, we can write

$$n^2(\nu) \equiv \varepsilon(\nu) = \varepsilon'(\nu) - i\varepsilon''(\nu), \quad (5.2)$$

where ε' and ε'' are the real and imaginary parts of the complex dielectric permittivity ε .

The model describes the THz wave propagation through the substrate with the ice deposited on both surfaces. The reconstruction of the ice parameters proceeds following three main steps.

The first task is modelling the reference and sample waveforms. Because of the focussed arrangement of the THz beams, the electromagnetic wave is assumed to be planar and to interact with the sample interfaces at the normal angle of incidence. This is a common and conventional assumption widely applied in dielectric spectroscopy (Pupeza et al. 2007; Zaytsev et al. 2014). It allows us to describe all the features of the THz pulse interaction with the multilayered sample using the Fresnel formulas, which define the THz wave amplitude reflection at (and transmission through) the interface between the media and the Bouguer-Lambert-Beer law, which defines the absorption and phase delay of the THz wave in a bulk medium. Further details on these assumptions are given in Appendix B.2.

Figure 5.3 represents the THz wave propagation through the three layers structure: the first ice film, the HRFZ-Si substrate, and the second ice film, where the symbols 0 to 3 and N correspond to different components of the plane wave passing through the multilayered structure. As shown in Fig. 5.3, for the sample spectrum, we took into account the contribution of the ballistic THz pulse (1) and the satellite pulses (2 and 3), caused by the multiple THz wave reflection in the ice films. The mathematical description of the wave propagation can be found in Appendix B.2.

The second step consists in estimating the initial thickness $l_{CO,I}$, $l_{CO,II}$ and the initial complex refractive index n_{init} of the two ice layers as shown in Fig. 5.4. The thickness estimation can be derived from the time delay δt_{01} between the ballistic pulse of the reference and sample waveforms (0 and 1 in Fig. 5.4), the first satellite pulse (2) and the ballistic pulse (1) of the sample waveform δt_{12} , and the second satellite pulse (3) and the ballistic pulse (1) of the sample waveform δt_{13} , in Fig. 5.4 (a). Since the HRFZ-Si has a very high refractive index, we consider that the refractive indexes of ice n satisfies the inequality $n_0 = 1.0 < n < n_{\text{Si}} = 3.415$, where n_0 is the refractive index in vacuum.

Then, by neglecting imaginary parts in the complex refractive indexes of media, the first assumptions for the real part of the complex refractive index of ice films and both their thicknesses $l_{CO,I}$ and $l_{CO,II}$ are described as follows:

$$n'_{\text{init}} = \frac{\delta t_{12} + \delta t_{13}}{\delta t_{12} + \delta t_{13} - 2\delta t_{01}}, \quad (5.3)$$

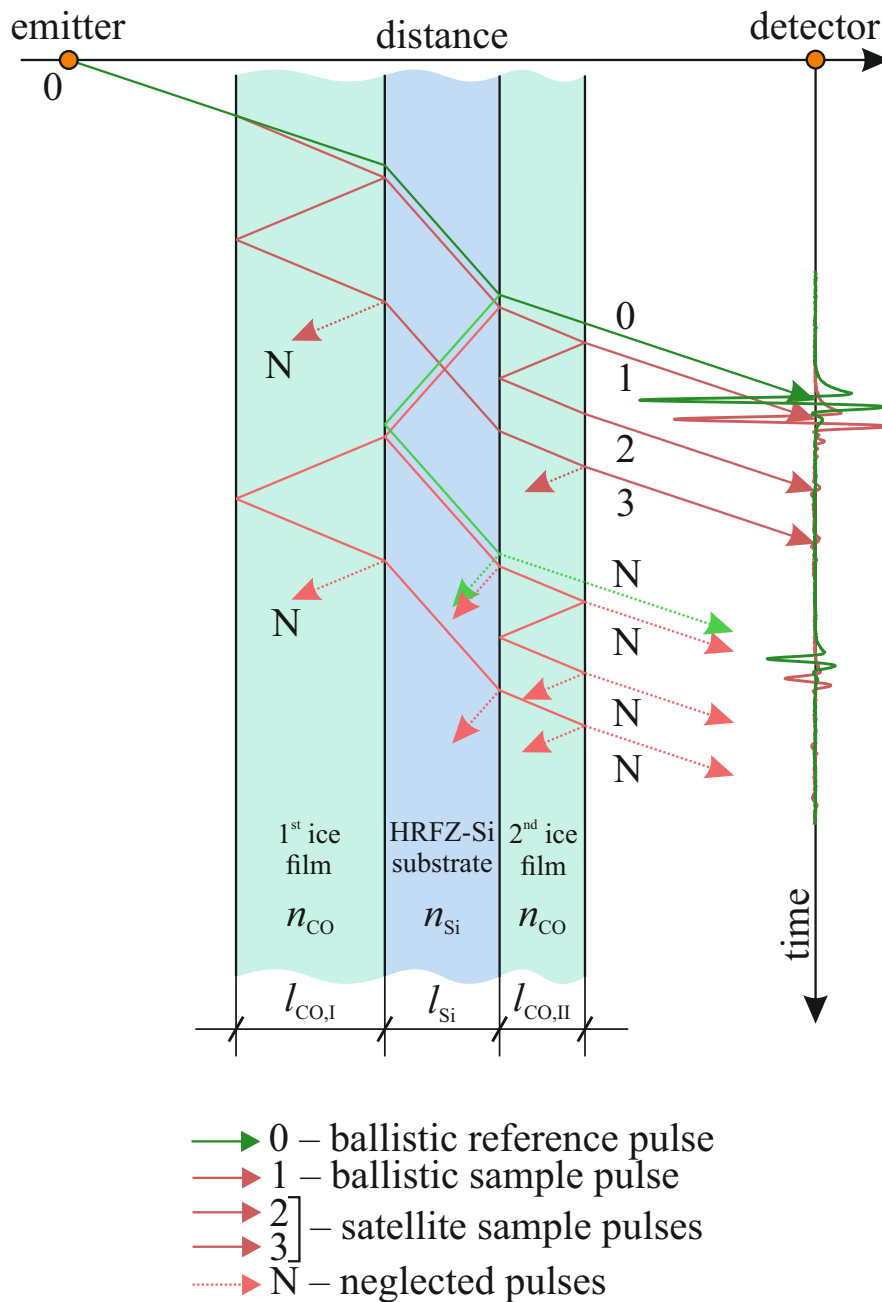


Figure 5.3: Time-distance diagram illustrating the THz wave propagation through the HRFZ-Si substrate with ice films deposited on its surfaces. Lines 0 to 3 illustrate the ballistic pulse and satellite pulses transmitted in the direction of the antenna-detector; N stands for unaccounted satellites with larger time delays. The solid lines represent the pulses used for the analysis, while dotted lines correspond to neglected pulses.

$$l_{\text{CO,I}} = \frac{c \delta t_{13}}{2n'}, \quad l_{\text{CO,II}} = \frac{c \delta t_{12}}{2n'}. \quad (5.4)$$

Eq. (5.3) is obtained from a mathematical model of sample and reference waveform. Further details on the derivation can be found in Appendix B.2. From Eq. (5.4) it is possible to obtain information only on the thicknesses of ice films, while the identification of the specific layer (I or II) is not allowed. We observe a linear increase of the ice thickness with the total deposition time. A first assumption for the real part of the complex refractive index of CO ice is in the range $n'_{\text{init}} = 1.230$ to 1.255 ± 0.035 for all the considered deposition intervals; here, the error accounts for an accuracy of the THz pulse peak position estimation. The first assumption for the imaginary part of the complex refractive index of ice has been done considering $\alpha_{\text{init}} = 0$; thus, $n''_{\text{init}} = 0$.

Finally, from the first estimation of the ice thickness and complex refractive index, it is possible to reconstruct the THz dielectric response of ice. The reconstruction procedure is reported in Appendix B.2, while the results are summarized in Fig. 5.4. Panels (b) and (c) show the growth of the two CO ice layers in time (t), considering different deposition steps of $\Delta t = 4, 5,$ and 6 min.

We can compare the results obtained from the THz spectral data to the thickness calculation performed with the well-established laser interference techniques described in Section 5.4.2 to validate the calculation of the ice thickness using this model. The good agreement between the two methodologies confirm the validity of the present analysis.

5.4.2 Laser interference technique

In the adopted experimental configuration, a He-Ne laser beam ($\lambda = 632.8$ nm) is directed towards the sample and reflected at near normal incidence both by the vacuum-sample and sample-substrate interfaces. The reflected beam is detected by an external diode detector. It is possible to follow the accretion of the ice film by looking at the interference curve (intensity vs. time) of the reflected laser beam. Further details on the laser interference technique can be found in Urso et al. (2016).¹

The results obtained with the two techniques have been compared. The data on the accretion of the ice versus time obtained from the analysis of the interference curve, measured at the early stage of the deposition process, are in good agreement with the data obtained from the THz spectra. In addition, using the laser interference technique, we obtain for the CO ice a refractive index $n_{\text{CO}} = 1.27$, that is close to the value obtained using the THz technique. The good agreement between the two methodologies confirm the validity of the present analysis.

¹A publicly-available interface can be found at <http://www.oact.inaf.it/spess/> to calculate the refractive index of the ice sample and derive the theoretical interference curve from the amplitude of the experimental curve. The sample thickness is obtained by comparing the two curves and using a procedure described in a document available at this web page.

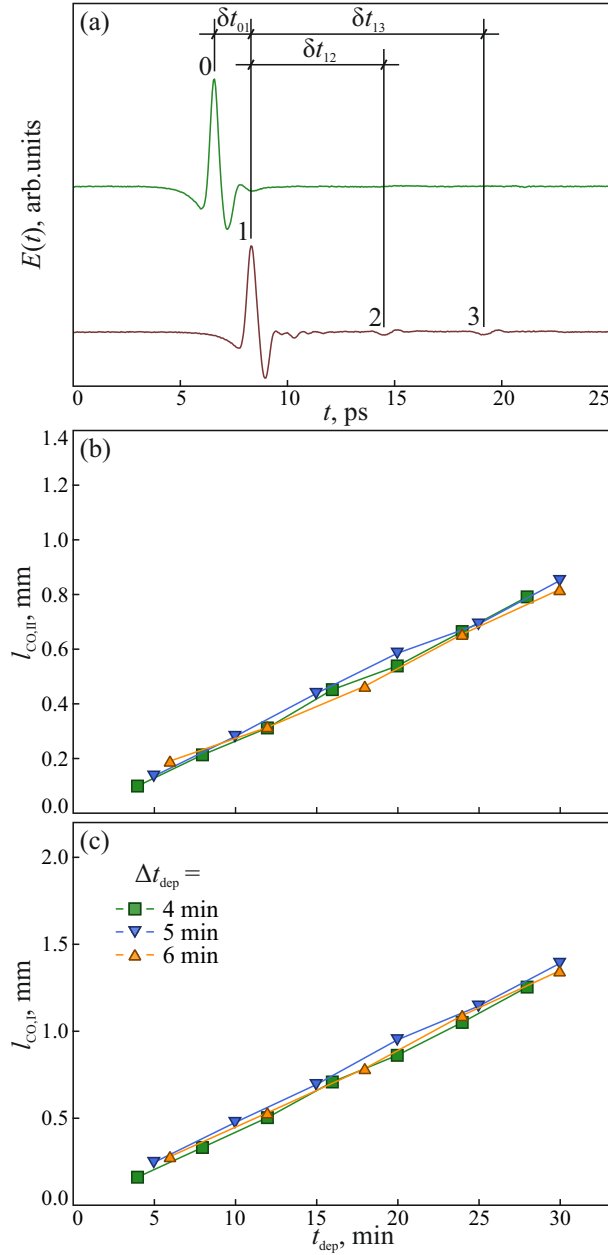


Figure 5.4: Calculation of the thicknesses $l_{CO,I}$, $l_{CO,II}$ and the complex refractive index n of the CO ice films (see Fig. 5.3). (a) Time delays between the ballistic THz pulses of the reference (0) and sample (1) waveforms, δt_{01} ; the first satellite pulse (2) and the ballistic pulse (1) of the sample waveform, δt_{12} ; and the second satellite pulse (3) and the ballistic pulse (1) of the sample waveform, δt_{13} (the pulses are delineated as in Fig. 5.3). (b,c) Estimates for the thicknesses of the two ice films as a function of the total deposition time t_{dep} for the different deposition intervals of $\Delta t_{dep} = 4, 5,$ and 6 min; the first assumption for the real part of the refractive index of ice is between $n'_{init} = 1.230$ and 1.255 ± 0.035 ; for the imaginary part we first set $n''_{init} = 0$.

5.4.3 Reconstruction of the THz response

The recorded THz waveforms and their Fourier spectra are presented in Fig. 5.5 for the optical substrate (used as a reference) and CO ice samples at increasing thicknesses. In panel (a) the waveform $E(t)$ is shown for the reference (green) and five subsequent deposition steps (black to light red) of approximately 0.45 mm total thickness for each step. The thickness reached after the total deposition time is approximately 2.3 mm, split in two ice layers of ≈ 0.85 mm and ≈ 1.45 mm on top of each side of the substrate. A small source of inhomogeneity can be ascribed to the position of the pipe connected to the pumping system, which is located in a lateral position of the vacuum chamber with respect to the cold substrate.

In the THz spectrum of CO ice, we observe a Lorenz-like resonant peak centred near 1.5 THz (50 cm^{-1}) and a second blurred feature close to 2.5 THz (83 cm^{-1}), masked by the sharp bands produced by the atmospheric water contamination in the spectrometer sample compartment. The highest frequency accessible in our set-up is presently limited by the strong absorption features of residual water and carbon dioxide in the spectrometer case. We plan to change the current set-up to an evacuated case to get rid of the contamination from the residual atmosphere, and we expect to extend the accessible frequency range up to 4 THz.

The estimated deposition rate for these deposition conditions is ≈ 0.05 mm/min for layer I and ≈ 0.03 mm/min for layer II. These values are in a reasonable agreement with the results obtained employing the laser technique, with which the deposition rate is calculated to be 0.02 mm/min. This agreement validates our hypothesis that the ice structure of thick ices does not differ significantly from the structure of thin ices, growing homogeneously over time during the deposition. The calculated optical properties are independent from the total thickness of the ice sample, allowing us to relate the laboratory data to the astrophysical ice conditions.

Figure 5.6 shows the determination of CO ice parameters, which are the refractive index (a), the amplitude absorption coefficient (b), and both the real (c) and imaginary (d) parts of the complex dielectric permittivity; see Eqs. (5.1) and (5.2).

5.5 Discussion

A benefit of the direct reconstruction of the optical properties of the ices, provided by THz-TDS, is the detection of the frequency-dependent amplitude and phase of the waveform in a broad frequency range as a result of a single measurement. These data eliminate the need to use the Kramers-Kronig relations for the reconstruction of the optical properties, excluding additional distortion of the experimental data by edge effects, which frequently appears as a result of the Hilbert integral transformation. This is of particular importance when dealing with broadband spectral kernels which are usually present even when operating at low temperature.

We could also compare the refractive index of CO ice at THz frequencies with that previously calculated in the MIR range, from Hudgins et al. (1993), Ehrenfreund et al. (1997), and Baratta & Palumbo (1998) for a CO ice deposited at 10 K. However, a direct comparison between refractive index values found by different authors is not straightforward. As discussed by Loeffler et al. (2005) and Baratta & Palumbo (2017), the density and in turn the refractive index of an ice

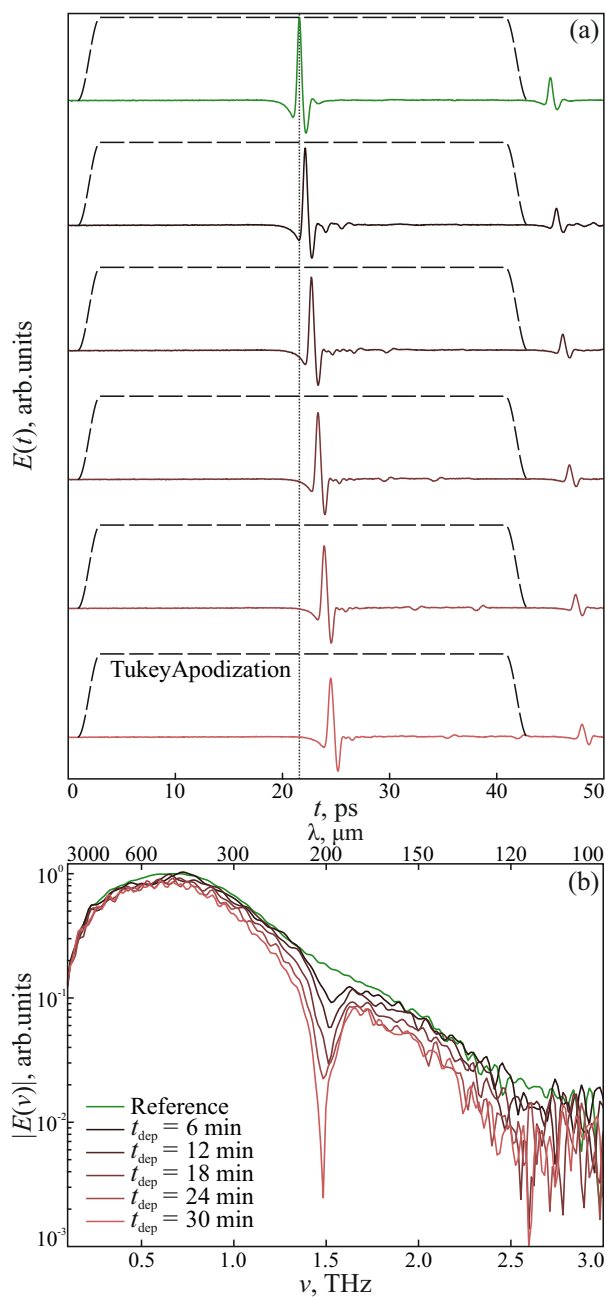


Figure 5.5: Evolution of the THz pulse and its spectra during the CO ice deposition. (a) Reference waveform $E(t)$ transmitted through the cryostat with the empty substrate (green), and sample waveforms (black to light red) transmitted through the substrate with the CO ice deposited on its surfaces. (b) Fourier spectra $|E(\nu)|$ of the reference and sample THz waveforms calculated with the use of Tukey apodization. The waveforms in (a) and spectra in (b) correspond to different values of the total deposition time t_{dep} (indicated); the deposition intervals are $\Delta t_{\text{dep}} = 6$ min.

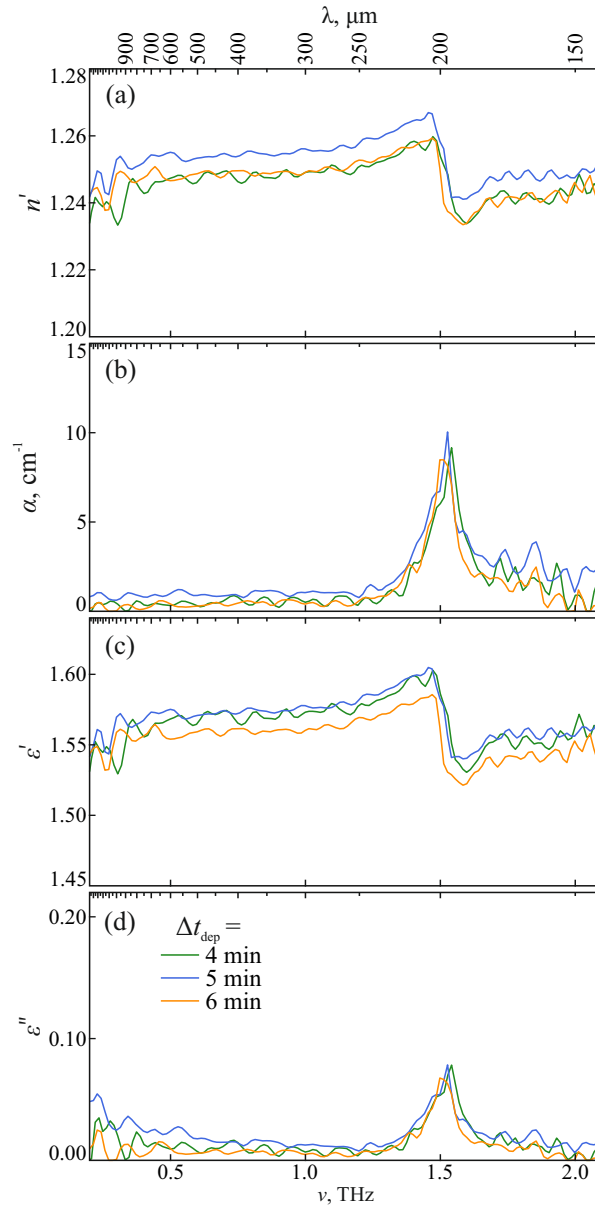


Figure 5.6: Optical properties of CO ice. (a) Real part of the refractive index, (b) amplitude absorption coefficient, and (c) real and (d) imaginary parts of the dielectric permittivity (see Eqs. (5.1) and (5.2)). For all deposition intervals, the dielectric curves demonstrate the existence of a Lorentz-like absorption peak, centred near 1.5 THz and featuring similar bandwidth. Distortions of the results seen at frequencies below 0.3 THz (such as an oscillatory character of n and ϵ' and an increase of ϵ'' with decreasing frequency) are due to diffraction effects (see Sec. 5.3.2).

sample could strongly depend on the experimental conditions such as temperature, growth angle, and deposition rate. We plan to test the effect of the change in the deposition conditions on the ice structure and check if this change will affect the optical constants. These results will be published in a forthcoming paper.

We compare the spectroscopic signature of the CO ice in our experiments with previous studies available in the literature. Data on FIR spectra of solid CO were reported by Anderson & Leroi (1966) and Ron & Schnepp (1967). These studies investigated the absorption spectra of amorphous CO, deposited at 10 K on a crystalline quartz substrate between 250 and 30 cm^{-1} . Two bands are visible at 50 and 83 cm^{-1} (1.5 and 2.5 THz). The spectral features observed in our experiments are in excellent agreement with these data, even though the 2.5 THz feature is masked by atmospheric water bands in our set-up. The THz-TDS technique has a low sensitivity, requiring very thick ice layers to be detectable. Using our fast deposition rate the MIR vibrational bands of CO were strongly saturated within the first 30 seconds of deposition. We did some preliminary tests on the ice growing using the vibrational bands in the NIR range and we were able to follow the ice growing up to approximately $160\text{ }\mu\text{m}$ thickness. Also in this case the ice growing is constant and linear in time during deposition, but the error associated with the thickness estimate using the NIR band is large (20-30%).

It is not surprising then that in the data reported by Ioppolo et al. (2014), on THz and MIR spectroscopy of interstellar ice analogues, the CO ice absorption band in the THz region was not observed. The ice thickness in these experiments was estimated in all cases to be less than $10\text{ }\mu\text{m}$. In our case, the minimum thickness required to be able to observe the 1.5 THz feature is estimated to be of the order of hundreds μm .

The data obtained are then employed to calculate the dust opacity for a given grain size distribution, as reported for example in Ossenkopf & Henning (1994); see Appendix B.3 for additional details on the method we developed to reproduce their results. Following their approach, we report in Fig. 5.7 the calculated dust opacities assuming different ice coatings and different experimental data for the optical constants of ices. Data from Ossenkopf & Henning (1994) are labelled OH94 and reported for bare grains (green dotted line), thin (blue dotted), and thick ice mantles (orange dotted). The labels $V = 0, 0.5,$ and 4.5 indicate the volume ratio of the core of refractory material to the ice mantle (see Appendix B.3). Conversely to the present work, Ossenkopf & Henning (1994) assumed a $\text{H}_2\text{O}:\text{CH}_3\text{OH}:\text{CO}:\text{NH}_3 = 100:10:1:1$ mixture ice mantle composition, i.e. water-based, with a minor amount of methanol, carbon monoxide, and ammonia. As described in detail in Appendix B.3, following the same procedure as in Ossenkopf & Henning (1994), we extended the real and the imaginary parts of the refractive index from Hudgins et al. (1993) to longer wavelengths and we included spherical carbonaceous impurities.

The dielectric functions found by our experiments refer to pure CO ice, which explains the differences in the opacities shown in Fig. 5.7 calculated in the $100 - 1000\text{ }\mu\text{m}$ range (solid lines). To have a more relevant comparison, we calculated the opacity using the same grain distribution and refractory materials as in Ossenkopf & Henning (1994). But in this work we extrapolated the optical values of CO ice coating from Baratta & Palumbo (1998) (labelled BP98), where the refractive index of CO ice deposited at 12 K is calculated from the spectrum recorded in the $4400 - 400\text{ cm}^{-1}$ ($2.27 - 25\text{ }\mu\text{m}$) infrared spectral range. The opacities of Baratta & Palumbo (Fig. 5.7, dashed lines) show an agreement with our results, except for the contribution from the presence

of a CO ice absorbing feature at approximately $200 \mu\text{m}$, which is absent in the extrapolated data, as expected.

When we compare the refractive index, we note that the real part by BP98 ($n' = 1.28$) is reasonably close to our data ($n' = 1.24$), while for the imaginary part the discrepancy is very large, since n'' is completely determined by the absorption feature at 200 microns that is out of the range investigated by Baratta & Palumbo (1998) (see Figure 5.6). It is worth mentioning that Anderson & Leroi (1966) and Ron & Schnepp (1967) reported a CO absorption feature at 2.5 THz, which is not visible in our spectra because it is masked by the atmospheric water contamination. This feature should further decrease the actual value of n' at higher frequencies (above 2.5 THz). If we could measure the 2.5 THz feature and extend the calculation of the optical properties to this value, we would probably obtain a lower value of n' , slightly increasing the discrepancy with the data by Baratta & Palumbo (1998). The reconstruction of the THz dielectric response of ices without the use of the Kramers-Kronig relations, which is provided by THz pulsed spectroscopy, can provide an independent methodology to determine the optical properties of ice samples and validate the previous studies.

Since the real and imaginary parts of the dielectric constant are employed to compute the opacity, we can infer from the calculated opacity curve that the imaginary part, which shows the biggest difference from the data presented by Baratta & Palumbo (1998), does not play a major role in the determination of the opacity. This conclusion might be different for other absolute values or in a different spectral range.

Table 5.1: Opacities calculated at selected wavelengths and parameters of the fitting function $\kappa = \kappa_0 (\lambda/\lambda_0)^\beta$, where $\lambda_0 = 1 \mu\text{m}$, for the two models with different volume ratios (cf. solid lines in Fig. 5.7). The value κ_0 is in units of $10^5 \text{ cm}^2 \text{ g}^{-1}$.

$\lambda/\mu\text{m}$	$\kappa_{V=0.5}$	$\kappa_{V=4.5}$
200	14.94	38.12
250	8.16	12.58
350	4.28	6.28
500	2.27	4.13
800	0.97	2.22
$\kappa_0/10^5$	2.28	1.28
β	-1.85	-1.65

Values of opacities for some selected wavelengths are also given in Table 5.1. The motivation for the choice of CO ice arises from the need of investigating the ice mantle properties for sources in which drastic CO depletion is expected, such as prestellar cores or protoplanetary discs mid-planes (e.g. Caselli et al. 1999; Pontoppidan et al. 2003). In these cases, an ice mantle rich in CO can be formed and influence the optical properties of the dust grains. Thus, it is interesting to compare how the opacities change when ice mantles with diverse chemical composition are present. The common molecular species in astrophysical ices, such as H_2O , CO_2 , NH_3 and

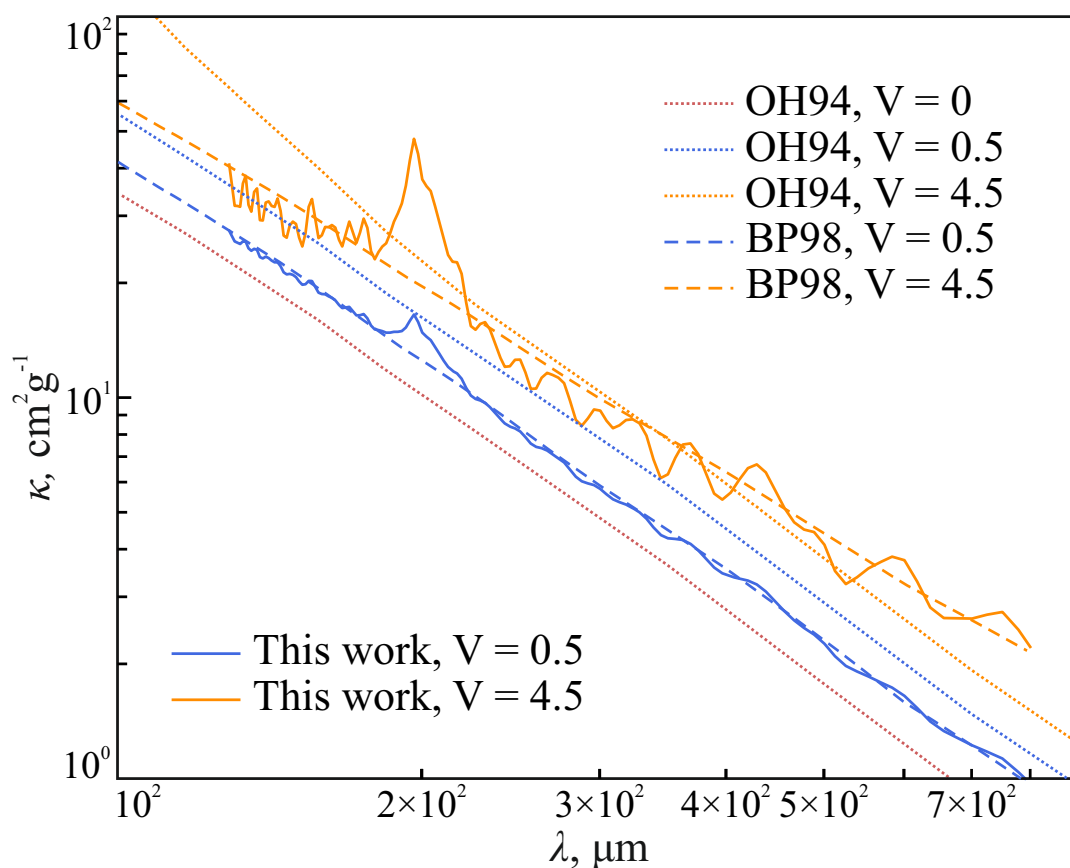


Figure 5.7: Calculated and reference opacities of astrophysical dust with CO ice and ice mixtures as a function of the wavelength. The dotted lines labelled with OH94 refer to bare grains and ice mixtures by Ossenkopf & Henning (1994), the dashed lines with BP98 to CO ice by Baratta & Palumbo (1998), and the solid lines to the CO data by the present work. The value V indicates the volume ratio of refractory core to ice mantle, for which we follow Ossenkopf & Henning (1994), where $V = 0$ (black) is the bare grain, $V = 0.5$ (blue) thin ice, and $V = 4.5$ (orange) thick ice. See text for additional details.

possibly N_2 , present absorption features in the FIR range. Therefore, the study of the influence of the spectroscopic features on the opacity of the ice mantles is important and we plan to extend this study to other pure ices and ice mixtures, which could be representative of the different molecular ice compositions in various astrophysical environments.

5.6 Conclusions

In this work we have presented a study on the optical properties of solid CO at temperature and pressure conditions significant for astrophysical applications. While previous data in the MIR frequency range are available in the literature, to the best of our knowledge, this study is the first to provide the complex refractive index and complex dielectric permittivity of CO ice in the THz range.

We have shown that the ability of THz-TDS to measure both the amplitude and phase information about the transmitted pulse provides direct reconstruction of the complex dielectric function of ices without the use of the Kramers-Kronig relations. The THz spectral features of ices can have a large bandwidth, such as the CO absorption line at 1.5 THz. In this case, an implementation of the Kramers-Kronig relations (i.e. the Gilbert transform), relying only on the power transmission/reflection spectrum, could lead to edge effects and resulting distortion of the dielectric response. Such distortions are of particular importance when a spectral feature of the sample is located near the border of the spectral operation range. Our results justify that THz-TDS set-up is an appropriate instrument for accurate measurements of dielectric properties of ices at THz frequencies.

These results have been used to calculate the opacities of the dust grains covered by a CO ice layer. Discrepancies with currently available opacities suggest that measurements such as those presented in this work are needed to provide a better interpretation of dust continuum emission, including dust and gas mass estimates. In addition, they will provide further insight into the radiative transfer processes based on ice analogues optical and physical properties.

Chapter 6

Conclusion and future prospects

6.1 Summary

This thesis has presented spectroscopic, laboratory work on interstellar water containing ice analogues using the advantages of Fourier transform infrared spectroscopy. The recorded spectral data were further processed to estimate absorption band strengths and consequently observation times in the pre-stellar core L1544. Moreover, obtained results on changes in the band positions and profiles were used to check if they are resolvable and if observations of even weak absorption bands are feasible using the James Webb Space Telescope (JWST).

Chapter 2 - O₂ signature in thin and thick O₂-H₂O ices. Motivated by the non-detection of molecular oxygen in interstellar ice mantles of star forming regions as well as by prior laboratory work found in the literature, I examined the band strength of O₂ in different mixing ratios with H₂O. Relative abundances reach from mixtures with an excess of water, O₂:H₂O = 1:9, to composition ratios with an excess of oxygen, O₂:H₂O = 9:1. I quantitatively analysed the recorded spectra for the increasing O₂ band strength following an increasing portion of oxygen in the ice analogues. Comparison with Ehrenfreund et al. (1992) showed similar but slightly weaker band strengths which is most likely due to differences in the compositions of the corresponding ices. Based on a chemical model of the pre-stellar core L1544 developed by Vasyunin et al. (2017), I combined predicted O₂:H₂O ratios along the line of sight with the obtained absorption coefficient values from the experiments to calculate the transmittance and optical depth of O₂ in L1544. I used the result in the JWST exposure time calculator (ETC) to estimate the observation time of the weak O₂ band, however, I found that with an exposure of > 100 h the detection is not feasible.

Chapter 3 - Spectroscopic measurements of CH₃OH in layered and mixed interstellar ice analogues. Here, I presented the spectral features of the CH₃OH ν_3 CH stretching and ν_8 CO stretching bands for different compositions and ice structures. I analysed the changes in band position and shape for ice analogues with an increasing number of molecular species in the probes. Starting from a two component ice with H₂O and CH₃OH both in a mixed and layered morphology, step by step I added CO₂ and CO to the H₂O and CH₃OH ices, respectively. For

ice analogues where CH₃OH-CO mixtures were deposited on top of H₂O, I analysed spectral features for varying composition ratio of the top ice layer. In the last steps, the ices consisted of all four mentioned components either in a completely mixed ice or in a layered structure with CH₃OH-CO on top of CO₂-H₂O. Additionally, I heated all ices to temperatures of 100 K. I found that changes in the absorption spectra clearly reflect the differences in ice structure and composition and that the band positions and profiles are also dependent on the temperature of the ice analogues. With its spectral resolution, the recently launched JWST will be able to observe the changes presented in this study and my results will help to better understand the structure of ice mantles in future observations of L1544.

Chapter 4 - Laboratory spectroscopy of theoretical pre-stellar core ices. Here, I used the chemical model of L1544 provided by Vasyunin et al. (2017) to provide the composition of ice mantles in regions close to the dust peak of the pre-stellar core. The theoretical predictions provide the fractional abundances for each single layer of the 161 monolayer (ML) thick ice mantle and I used these values to calculate average compositions for a mixed and layered ice structure. For the mixed ice, I averaged over all 161 MLs and used the four most abundant species, namely H₂O, CH₃OH, CO and N₂ for the ice composition. For the layered ice consisting of two layers, I averaged over the first 131 MLs for the bottom ice composition and over the outer 30 MLs for the ice deposited on top of the bottom ice analogue. Thus, a mixture of H₂O, CO, N₂ and O₂ was deposited on top of H₂O, CH₃OH and N₂. I found noticeable differences in the spectral features when comparing mixed and layered ices which will also be observable with JWST. Clear conclusions on interactions between molecules depending on the presence or absence as well as on the mixing ratio of species could be drawn from the band shifts and changes in their shape. Moreover, I investigated the detectability of the weak N₂ and O₂ bands with JWST and found that for signal-to-noise ratios of 10, N₂ will be observable with an exposure time of 1.4 h while O₂ detection with observation times of 123.6 h is not feasible.

Chapter 5 - Broadband spectroscopy of astrophysical ice analogues. I. Direct measurement of the complex refractive index of CO ice using terahertz time-domain spectroscopy. So far, optical properties of interstellar ice analogues in the IR and THz range have been provided only by theoretical calculations. Especially in dense and cold regions, they are important parameters for modelling the dust continuum radiative transfer and interpreting future observations in the FIR regime. With the THz TDS, however, it is possible to directly measure the complex refractive index of CO ice by examining ices of millimetre thickness in the time-domain and frequency-domain. With the data that I recorded in a set of experiments, the real and imaginary parts of the refractive index could be reconstructed with a newly developed algorithm without using the Kramers–Kronig relations. I compared the obtained data to theoretical calculations found in the literature and used this to estimate the opacities of dust grains in presence of CO ice mantles, revealing differences between theoretical and experimental results.

6.2 Future work

Detecting O₂ is an important task necessary to understand the complex chemistry of interstellar ices and the spectroscopic work on **molecular oxygen in a water matrix** was just one step in the investigation of relative O₂ abundances in interstellar ice mantles. I have shown that O₂ band strengths in a two component O₂-H₂O mixture are by a factor of ≈ 2 weaker than values observed by Ehrenfreund et al. (1992). The major difference in their study is the presence of CO and CO₂ in the ice matrix and therefore it can most probably be concluded that CO and CO₂ have an enhancing effect on the O₂ band strength. Even though a mixture of O₂ and CO has been included in the investigation of theoretical ice mantles of L1544 (Chapter 3), a systematic analysis on the effect of molecular species other than H₂O on the O₂ band strength has yet to be done.

Thus, I have once more conducted experiments with O₂-H₂O ice but this time I added CO, CO₂ or both species to the ice composition. As for the chosen O₂-H₂O mixtures, this time I limited them to a set of O₂:H₂O from 1:1 to 1:9 without compositions that show excess of oxygen. Instead, I added CO or CO₂ or both with observation based ratios of CO:H₂O = 1:3 and CO₂:H₂O = 1:4 to each of the O₂-H₂O ices. The analysis of the recorded data has yet to be completed but the results will be published in a future paper and enlighten the influence of two of the most abundant ice species on the observability of the weak oxygen band.

The examination of ice analogues based on **modelled compositions in L1544** should provide useful information on the abundance of chemical species and the structure of ice mantles when they are observed with JWST. However, in the presented experiments, one compound that is usually found in high amounts in interstellar ices was omitted in the ice mixtures that were examined in the CAS ice laboratory: CO₂. Since we investigated ices as they are predicted by the model of Vasyunin et al. (2017) close to the dust peak, CO₂ was not included in the ice analogue mixtures. The subsequent calculations of observation times for some of the H₂O, CH₃OH, N₂ and O₂ bands on the other hand took abundances in the whole modelled pre-stellar core into account. Thus, the motivation is high to also include CO₂, as a major component in interstellar ices along the line of sight, into the spectroscopic examination of L1544 ice analogues. In general, laboratory work in the CAS ice laboratory strives to understand complex interactions between molecules in thorough investigations of ice analogues that reflect the actual composition in the interstellar medium in an increasingly realistic way.

The work shown in Chapter 5 is not only important because it presents the first **direct measurement of the optical constants** of CO. Connecting to the overall topic of this thesis, among other species, I also used H₂O as a compound of major interest as it is the most abundant interstellar molecule in the solid phase. During the analysis however, it was revealed that the estimation of the ice thickness is not possible because the satellite pulses that are necessary to do so are so weak that they were not detectable. However, in order to calculate the complex refractive index and dielectric permittivity the thickness has to be known. Thus, our collaboration consisting of members of the Center for Astrochemical Studies and the Prokhorov General Physics Institute has reached out to the group of Thomas Lörting at the Institute of Physical Chemistry in Inns-

bruck, Austria. With their laboratory equipment, the group is able to produce any phase of water ice with a high precision in thickness and they can therefore provide the CAS ice laboratory with exactly those amorphous solid water samples that are needed for the THz TDS experiments and the consecutive analysis. Moreover, the experiments with the THz spectrometer will be complemented by studies with the FTIR spectrometer that will conduct measurements at frequencies directly extending the spectral range of the THz TDS towards the FIR regime.

6.2.1 Raman Microscope

Theoretical parts of this section are based on Colthup et al. (1990) and Latychevskaia (2019).

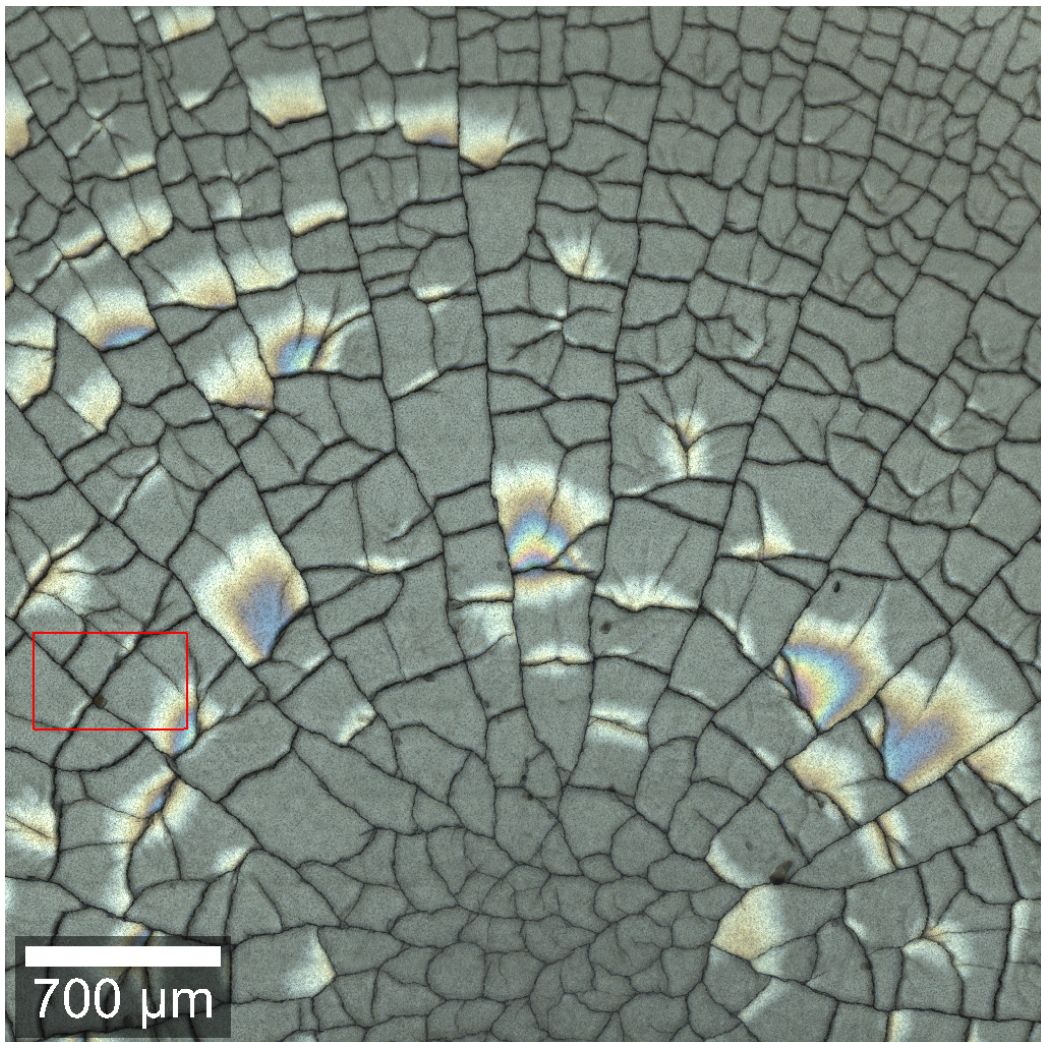


Figure 6.1: Structure of CO ice after fast deposition. A zoomed-in section of the red framed area is shown in the bottom left panel of Figure 6.4.

The Raman microscope uses the principles of scattering that occurs when a molecule is hit by monochromatic radiation of an incoming laser beam with frequency ν_i , which is much greater than molecular vibration frequencies. The collision of a photon and molecule can happen in two ways: elastic or inelastic. In the first case, this implies conservation of the vibrational and rotational energy of the molecule and the scattered photon leaves the molecule without changing its frequency. This elastic collision is called Rayleigh scattering and dominates interaction of molecules and photons. According to the Raman effect however, a small portion of the beam does not experience elastic scattering. In inelastic collisions, some of the molecules convert a part of the incoming energy to vibrational or rotational energy of the amount ΔE_m with:

$$h\nu_i - h\nu_{sc} = \Delta E_m = h\nu_m. \quad (6.1)$$

ν_{sc} here is the frequency of the scattered light and depending on the condition if $h\nu_{sc} < h\nu_i$ or $h\nu_{sc} > h\nu_i$ the new signal in a spectrum is referred to as the Stokes line or anti-Stokes line, respectively. Raman spectroscopy investigates the anti-Stokes lines with $\nu_m > 0$, as seen in Figure 6.2.

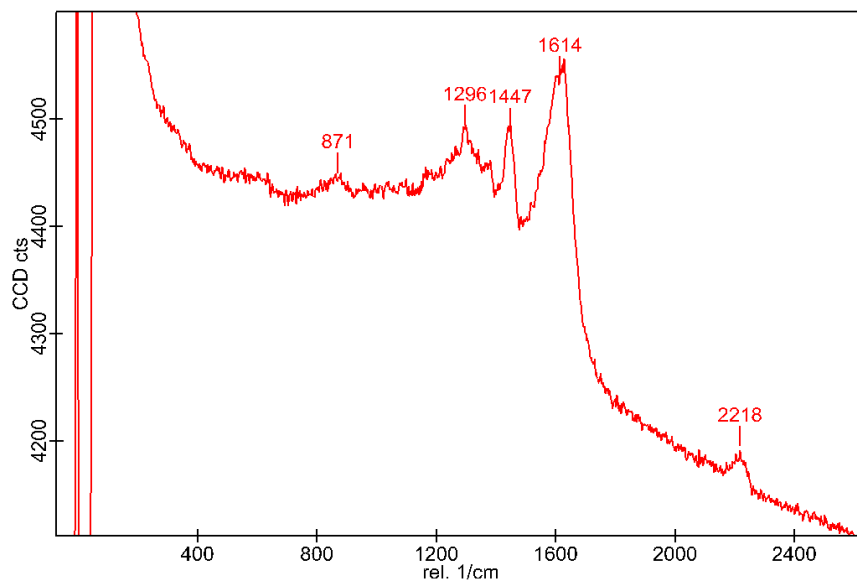


Figure 6.2: Anti-Stokes lines for residue material produced in an UV irradiation experiment of a $\text{CH}_4:\text{N}_1 = 1:8$ mixture.

As most of the molecules are present in ground state $\nu = 0$ rather than in an excited state $\nu = 1$, Stokes lines are usually stronger than anti-Stokes lines and the ratio of the number of molecules n in the respective states follows the Boltzmann distribution:

$$\frac{n_1}{n_0} = \exp(-h\nu_m/kT). \quad (6.2)$$

This correlation however has to be corrected for the polarizability α of the molecule. As the electrons and protons get displaced in opposite directions due to the electric field E that comes

along with the photons, this induces a dipole moment $\mu = \alpha E$ onto the molecule which becomes Raman active when the dipole moment is changing. If the frequency of the normal coordinate in this displacement process is ν_n then the relation of irradiation intensity I and its frequency ν , which is $I \propto \nu^4$, can be used to correct Eq. 6.2 for the polarization effect:

$$\frac{n_1}{n_0} = \frac{(\nu + \nu_n)^4}{(\nu - \nu_n)^4} \exp(-h\nu_n/kT). \quad (6.3)$$

This equation describes the ratio of the anti-Stokes lines intensity to the Stokes lines intensity. Rotation of molecules cause the polarizability to be directed into different directions perpendicular to the rotation axis and even symmetric molecules such as CO_2 or N_2 are observable.

Raman spectroscopy is sensitive to photons with frequencies dictated by fluorescence processes. Fluorescence proceeds when an absorbed photon causes the molecule to reach an excited electronic singlet state. Then, after transitioning to a lower excited level of this singlet state, the molecule returns to its ground state by emitting in fluorescence frequencies. These frequencies can superpose the anti-Stokes lines and hinder the analysis of the observed bands.

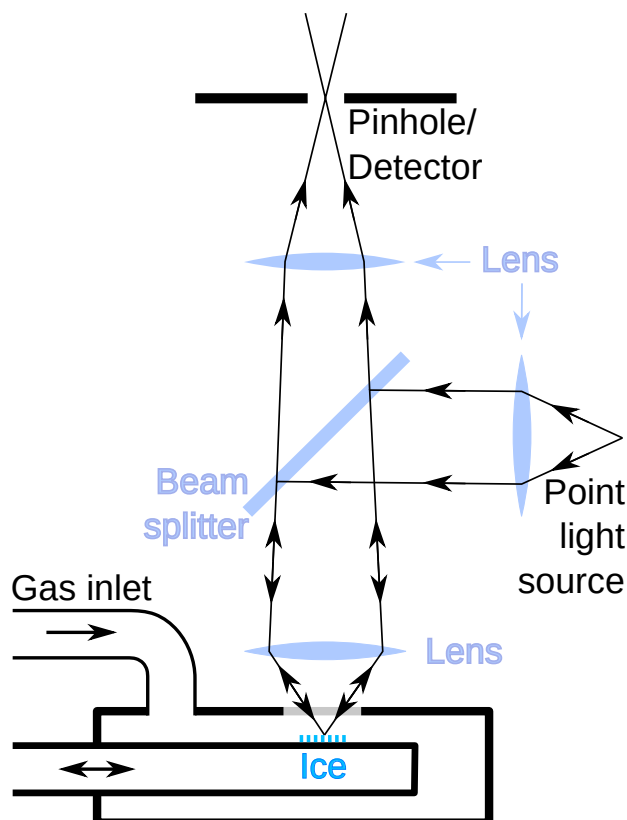


Figure 6.3: The Raman microscope. Left: complete view. Right: illustration of the combined Raman microscope and customized cryostat. The set-up of the Raman microscope is adapted from WITec.

The Raman spectrometer is also combined with a confocal Raman microscope that enables it to visualize the probe and scan its surface with a beam of diameter d that is restricted by the diffraction limit:

$$d = \frac{1.22\lambda}{n \sin\Theta}, \quad (6.4)$$

where n is the refraction index of the medium that the lens is in (usually air) and Θ is the aperture angle. $n \sin\Theta = NA$ is also known as numerical aperture. The resolution along the lateral xy plane, meaning that two points can be resolved, depends on the limits given by the Rayleigh criterion R_{xy} . If the separation of two points is $< R_{xy}$, they appear as one point and only for greater distances they can be resolved. The lateral resolution is given as:

$$R_{xy} = \frac{0.61\lambda}{NA}, \quad (6.5)$$

while the resolution along the axial z direction is:

$$R_z = \frac{2n\lambda}{(NA)^2}, \quad (6.6)$$

The Raman microscope located in the CAS ice laboratory can be combined with a cryostat specifically designed for the necessary horizontal alignment of the substrate so that the probes can be examined under the objectives of the microscope. The challenge in this set-up lies in the fact that the gas inlet can not be in line with the measuring laser that is reflected by the sample and guided back to a spectrometer. Because of that the cryocooler has a movable interior sample holder so that the substrate can be locked at two positions: below the gas inlet and below the objective lenses of the microscope, as shown in Figure 6.3. The Raman microscope is equipped with two lasers of wavelength 488 nm and 785 nm and its combination with the cryostat allows it to examine ice structures, observe diffusion processes and investigate properties in ices and between ice layers and the substrate. The possibility to examine the samples in two and three dimensions also makes studies of multi-component samples possible - including the effect of the material used as substrate.

The possibility to map different components of a sample was first tested on a residue of a $\text{CH}_4:\text{N}_2 = 1:8$ mixture that has experienced UV irradiation. The sample, as shown in the top left panel of Figure 6.4, is characterised by smooth areas, dark channels and bright clusters, and after recording spectra at each of these three regions, a map of the different components was generated, as seen in the top right panel of Figure 6.4. First experiments at low temperatures of 10 K were performed with CO ices, as shown in Figure 6.1 and the two bottom panels of Figure 6.4. The left panel shows the fissured and untransparent structure of CO ice after fast deposition with a background pressure of 50 mbar. In contrast, after slow deposition with a background pressure of 5 mbar the CO ice shows a smooth and transparent distribution resembling a calm lake with a dark dust grain protruding like an island. With its high abundance in astrophysical ice mantles, CO is a highly interesting compound for study, but a huge variety of interstellar compounds are just waiting to be analysed. In this context, I will soon work in the research group for functional nanomaterials located at the Technical University of Munich in Garching. They are able to produce metal and oxide nanoclusters resembling the sizes of small dust grains and study dynamics

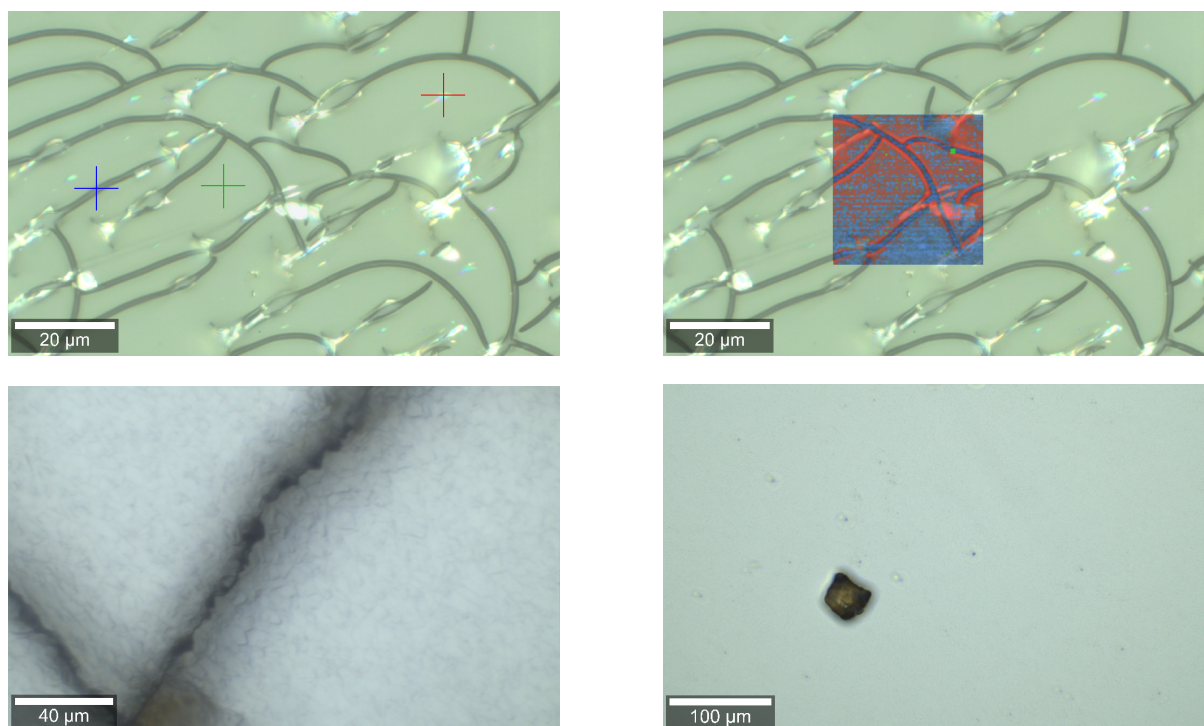


Figure 6.4: Top left: Measurement points for Raman spectra of $\text{CH}_4:\text{N}_2 = 1:8$ irradiation residue at different regions of the probe. Top right: Mapping of the measured species according to their spectra. Bottom left: Fissured CO ice structure after fast deposition with a background pressure of 50 mbar. Bottom right: Smooth CO ice structure after slow deposition with a background pressure of 5 mbar. The dark spot is a dust grain protruding from the CO "sea".

on the surface of these clusters. With a new set-up that will work at cryogenic temperatures, there will be some good connection points for collaborative studies of ice molecules (e.g. water) on the surface of clusters (e.g. SiO).

The chemistry during star formation shows a rich variety of atomic and molecular compounds. By now over 250 species have been detected both in gas and solid phase and still there are many more unknown molecules to be found. Our understanding of chemical and physical processes on the way to the birth of stars, planets and eventually life is an ongoing quest that provides many open questions, at least some of which I have striven to help answer.

Appendix A

Complementary Material for Chapter 4

A.1 Layered ice - Comparison of measurements and computational addition

During the analysis of the ice mixtures used for the layered experiments, we noticed some discrepancies in the position and shape of some absorption bands when we compared the spectra of layer 1 and layer 2 with the spectral features of the layered ice where layer 2 was deposited on top of layer 1. While most of the absorption bands show no differences in the layered ice and the computational addition of the vibrational modes observed in layer 1 and 2, this is not the case for the H₂O dangling bonds, the O₂ band and the 1130 cm⁻¹ CH₃ rocking band. The differences are shown in Fig. A.1.

When we compare the computational addition of layer 1 and 2 with the experimentally layered ice, we see for the dangling bonds that the intensity of the right local maximum at 3662 cm⁻¹ is remarkably weaker than the left local maximum. As we already observed a strong dependence of the 3662 cm⁻¹ maximum on the presence of CO and O₂ the high abundance of these two molecules can explain the difference in the relative intensity of the band maxima via the interaction of the freely vibrating OH bonds with CO and O₂ at the interface where layer 2 was deposited on top of layer 1.

This effect can also be seen in the increased band strength of O₂ measured for the layered structure in comparison to the weaker band of the computationally added spectrum. The presence of the two polar species of layer 1, water and methanol, at the interface seems to amplify the intensity of the O₂ band.

While it is true that increasing CO:CH₃OH ratios cause a drop in the intensity of the 1130 cm⁻¹ shoulder features, as seen in Müller et al. (2021), spectroscopic results from the same work also show that the presence of small amounts of CO enhance these features when CH₃OH is layered on top of H₂O. This effect can be seen when experimentally and computationally added layered spectra are compared. Moreover we see that the shoulders are shifted towards lower frequencies in the experimental data whereas the maximum band position does not experience any effect due to the molecular interaction at the interface.

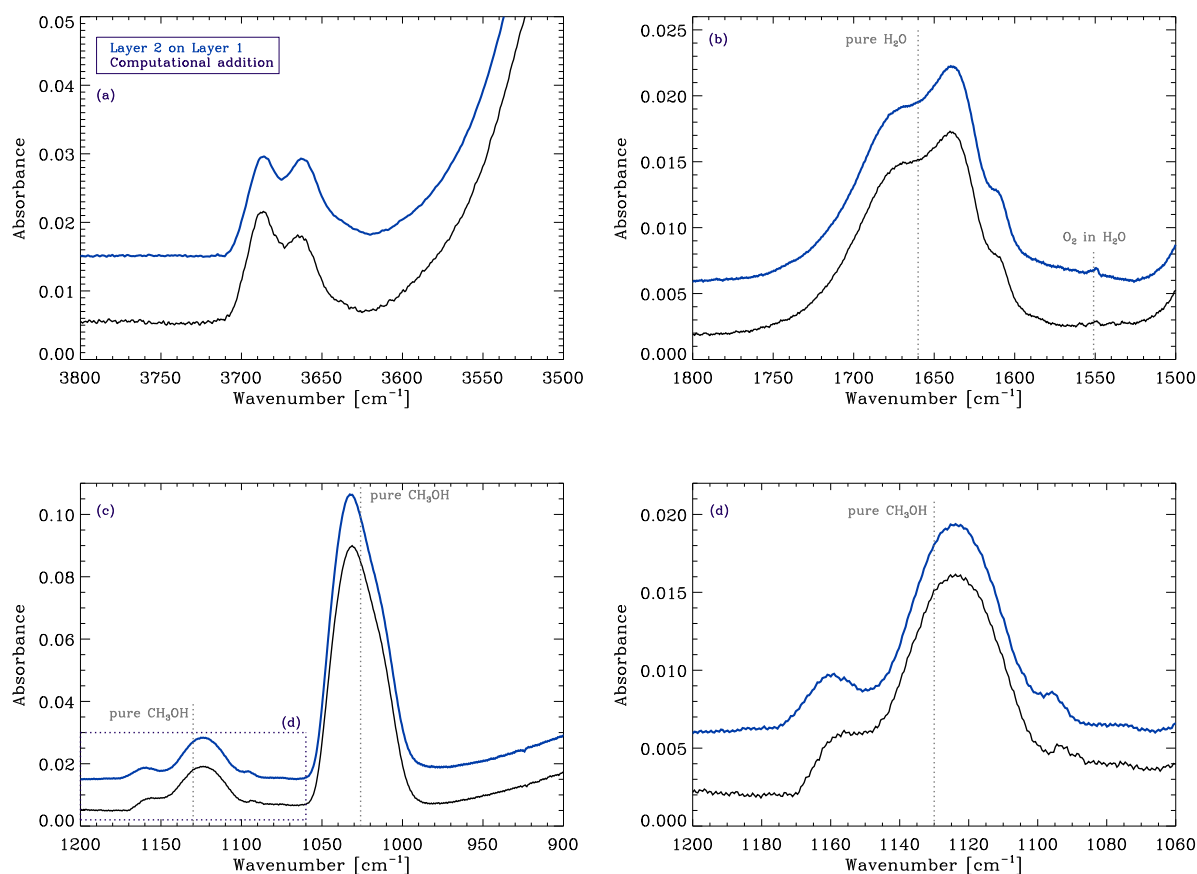


Figure A.1: Comparison of experimentally (dark blue) and computationally added (black) layered ices, zoomed-in around the H₂O dangling bond (a), H₂O OH-bend (b), CO-stretch (c) and CH₃-rock (d) bands. Corresponding to Table 4.1, the spectra are shown for relative abundances of H₂O:CH₃OH:N₂ = 100%:67.5%:27.5% (Layer 1) and H₂O:N₂:CO:O₂ = 100%:46%:146%:38% (Layer 2).

Appendix B

Complementary Material for Chapter 5

B.1 THz-TDS optics

In this section we provide a detailed description of the configuration of the laser beam inside the optical compartment of the set-up, already shown in Fig. 5.2. The power of the laser beam is attenuated and successively divided into equivalent channels. Thus, the antenna-emitter is pumped and the antenna-detector is probed with an equal average power of about 20 mW. The optical delay between the pump and probe beams is varied using a double-pass linear mechanical delay stage from Zaber with the travel range of 101.6 mm and the positioning accuracy of $< 3 \mu\text{m}$. The THz radiation undergoes 10 kHz electrical modulation to detect synchronously the THz amplitude using a lock-in detection principle.

The THz beam emitted by the photoconductive antenna is collimated by an integrated HRFZ-Si hemispherical lens and then focussed on a substrate window using a polymethylpentene (TPX) lens with a focal length of 67 mm and diameter of 25 mm. After passing through the cryostat vacuum chamber, the beam is collimated by an equal TPX lens in the direction of the antenna-detector. Finally, the THz beam is focussed onto the photoconductive gap of the antenna-detector by an equal integrated HRFZ-Si hemispherical lens. In our measurements, during the waveform detection, we used a time-domain stride of 50 fs, which allows for satisfying the Whittaker-Nyquist-Kotelnikov-Shannon sampling theorem (Nyquist 1928), at time-domain window size of 100 ps and an averaging time of 0.1 sec at each time-domain step with no waveform averaging.

The signal measured at the antenna-detector is recorded in the time domain $E(t)$ and converted into its Fourier-spectrum $E(\nu)$ via

$$E(\nu) = \frac{1}{\sqrt{2\pi}} \int_{-\infty}^{+\infty} E(t) e^{-i2\pi\nu t} dt, \quad (\text{B.1})$$

where t and ν stand for time and frequency.

B.2 Reconstruction of the terahertz dielectric permittivity

Eqs. (5.3) and (5.4) are obtained as follows. We defined the complex amplitude of electromagnetic wave $E_0 = |E_0| \exp(i\varphi_0)$, which interacts either with a bare substrate (which we use as reference) or with two ice layers (when detecting the sample waveform). The pulses complex amplitudes depend on the initial complex amplitude of electromagnetic wave E_0 and on ices and reference layers, which define the THz-wave reflection and transmission at the interfaces (R -operators and T -operators, respectively) and its absorption and phase delays in a bulk material (P -operators).

Then, we define the amplitudes of the ballistic reference pulse as follows:

$$\begin{aligned} E_{R,b} &= E_0 P_0 (l_0 - l_{Si}) T_{0,Si} P_{Si}(l_{Si}) T_{Si,0} \\ &= |E_{R,b}| \exp(i\varphi_{R,b}), \end{aligned} \quad (\text{B.2})$$

where l is the thickness of the medium, and the symbols 0 and Si indicate the vacuum and HRFZ-Si, respectively, the ballistic sample pulse as follows:

$$\begin{aligned} E_{S,b} &= E_0 P_0 (l_0 - l_{Si} - l_{CO,I} - l_{CO,II}) T_{0,CO} P_{CO}(l_{CO,I}) \\ &\quad \times T_{CO,Si} P_{Si}(l_{Si}) T_{Si,CO} P_{CO}(l_{CO,II}) T_{CO,0} \\ &= |E_{S,b}| \exp(i\varphi_{S,b}), \end{aligned} \quad (\text{B.3})$$

where $l_{CO,I}$ and $l_{CO,II}$ are defined as in Section 5.4.1, and the two satellite sample pulses as follows:

$$\begin{aligned} E_{S,1s} &= E_0 P_0 (l_0 - l_{Si} - l_{CO,I} - l_{CO,II}) T_{0,CO} P_{CO}(l_{CO,I}) \\ &\quad \times T_{CO,Si} P_{Si}(l_{Si}) T_{Si,CO} P_{CO}(l_{CO,II}) T_{CO,0} \\ &\quad \times R_{CO,Si} P_{CO}^2(l_{CO,I}) R_{CO,0} \\ &= |E_{S,1s}| \exp(i\varphi_{S,1s}), \\ E_{S,2s} &= E_0 P_0 (l_0 - l_{Si} - l_{CO,I} - l_{CO,II}) T_{0,CO} P_{CO}(l_{CO,I}) \\ &\quad \times T_{CO,Si} P_{Si}(l_{Si}) T_{Si,CO} P_{CO}(l_{CO,II}) T_{CO,0} \\ &\quad \times R_{CO,0} P_{CO}^2(l_{CO,II}) R_{CO,Si} \\ &= |E_{S,2s}| \exp(i\varphi_{S,2s}), \end{aligned} \quad (\text{B.4})$$

which are clearly observed in reference and sample TDS waveforms in Fig. 5.4 (a).

Then, by neglecting the phase changes during the reflection at the interfaces of absorbing media as well as the distortion of optical pulses due to dispersion of material parameters, we

calculated the phases of these pulses as

$$\begin{aligned}
\varphi_{R,b} &= \frac{2\pi\nu}{c} (n_0 (l_0 - l_{Si}) + n_{Si} l_{Si}) \\
&= -\frac{2\pi\nu}{c} (l_0 - l_{Si} (n_{Si} - 1)), \\
\varphi_{S,b} &= \frac{2\pi\nu}{c} (n_0 (l_0 - l_{Si} - l_{CO,I} - l_{CO,II}) + n_{Si} l_{Si} \\
&\quad + n_{CO} (l_{CO,I} + l_{CO,II})) \\
&= -\frac{2\pi\nu}{c} (l_0 - l_{Si} (n_{Si} - 1) - (l_{CO,I} + l_{CO,II}) (n_{CO} - 1)), \\
\varphi_{S,1s} &= \frac{2\pi\nu}{c} (n_0 (l_0 - l_{Si} - l_{CO,I} - l_{CO,II}) + n_{Si} l_{Si} \\
&\quad + n_{CO} (3l_{CO,I} + l_{CO,II})) \\
&= -\frac{2\pi\nu}{c} (l_0 - l_{Si} (n_{Si} - 1) - (l_{CO,I} + l_{CO,II}) (n_{CO} - 1) \\
&\quad - 2l_{CO,I} n_{CO}), \\
\varphi_{S,2s} &= \frac{2\pi\nu}{c} (n_0 (l_0 - l_{Si} - l_{CO,I} - l_{CO,II}) + n_{Si} l_{Si} \\
&\quad + n_{CO} (l_{CO,I} + 3l_{CO,II})) \\
&= -\frac{2\pi\nu}{c} (l_0 - l_{Si} (n_{Si} - 1) - (l_{CO,I} + l_{CO,II}) (n_{CO} - 1) \\
&\quad - 2l_{CO,II} n_{CO}),
\end{aligned} \tag{B.5}$$

where n_0 and n_{Si} are defined as in Section 5.4.1 and n_{CO} is the refractive index of the CO ice. The phase changes are weak since we study rather low-absorbing dielectric materials. The dispersion of HRFZ-Si is very low, while the dispersion in ice is negligible owing to its small thickness.

These phases are used to calculate the time delays between the pulses, which are indicated in Fig. 5.4 (a), i.e.

$$\begin{aligned}
\delta t_{01} &= \frac{\varphi_{S,b} - \varphi_{R,b}}{2\pi\nu} = \frac{n_{CO} - 1}{c} (l_{CO,I} + l_{CO,II}), \\
\delta t_{12} &= \frac{\varphi_{S,1s} - \varphi_{S,b}}{2\pi\nu} = \frac{2n_{CO}}{c} l_{CO,I}, \\
\delta t_{13} &= \frac{\varphi_{S,2s} - \varphi_{S,b}}{2\pi\nu} = \frac{2n_{CO}}{c} l_{CO,II}.
\end{aligned} \tag{B.6}$$

Solving this system of equations yields Eqs. (5.3) and (5.4).

Figure 5.5 (b) shows the Fourier spectra $E(\nu)$ of the reference and sample TDS waveforms. In order to filter out the contribution of the satellite THz pulses (caused by the interference in the input and output windows and the substrate) and to improve the analysis of the frequency-domain data, we apply equal apodization procedure (window filtering) to all waveforms,

$$E_{\text{filt}}(t) = E(t) H(t - t_0), \tag{B.7}$$

where $E(t)$ and $E_{\text{filt}}(t)$ stand for the initial and filtered waveforms, $H(t)$ defines the apodization function, and t_0 defines a position of the apodization filter towards the THz waveform, i.e.

$$H(t) = \begin{cases} \frac{1}{2} + \frac{1}{2} \cos \left[\frac{2\pi}{\omega} \left(\frac{t}{\tau} - \frac{\omega}{2} \right) \right], & 0 < \frac{t}{\tau} < \frac{\omega}{2}, \\ 1, & \frac{\omega}{2} < \frac{t}{\tau} < 1 - \frac{\omega}{2}, \\ \frac{1}{2} + \frac{1}{2} \cos \left[\frac{2\pi}{\omega} \left(\frac{t}{\tau} - 1 + \frac{\omega}{2} \right) \right], & 1 - \frac{\omega}{2} < \frac{t}{\tau} < 1. \end{cases} \quad (\text{B.8})$$

The parameter $H(t)$ is a Tukey apodization filter (Tukey et al. 1986) with the width τ , and ω stands for a parameter of the filter smoothness; for $\omega = 0$ the window has a rectangular form and for $\omega = 1$ it is the Hann window Harris (1978). As shown in Fig. 5.5(a), we use the Tukey window centred at the maximum of the reference THz waveform with the smoothness parameter of $\omega = 0.1$ and the width of 40 ps, which yields the frequency-domain resolution of 0.025 THz.

Let us consider the Fresnel formulas (Born & Wolf 1980), defining the THz wave amplitude reflection at (and transmission through) the interface between media m and k as follows:

$$\begin{aligned} R_{m,k}(\nu) &= \frac{n_m(\nu) - n_k(\nu)}{n_m(\nu) + n_k(\nu)}, \\ T_{m,k}(\nu) &= \frac{2n_m(\nu)}{n_m(\nu) + n_k(\nu)}, \end{aligned} \quad (\text{B.9})$$

where $R_{m,k}(\nu)$ and $T_{m,k}(\nu)$ stand for coefficients of the complex amplitude reflection and transmission, respectively, while $n_m(\nu) + in_k(\nu)$ is the complex refractive index of the media. The relation between complex amplitudes of the THz wave right after the emitter ($z = 0$), $E_0(\nu)$ and at the position z along the beam axis, $E(\nu, z)$ is given by

$$E(\nu, z) = E_0(\nu) \exp \left(-i \frac{2\pi\nu}{c} n(\nu) z \right). \quad (\text{B.10})$$

If the thicknesses and refractive indexes of all layers are known, Eqs. (B.9) and (B.10) yield description of all peculiarities of the THz pulse interacting with multilayered structures (Zaytsev et al. 2014, 2015; Gavdush et al. 2019).

We derive the equations describing the complex amplitudes of the reference $E_R(\nu)$ and sample $E_S(\nu)$ spectra, assuming only wavelets inside the Tukey apodization. For the reference spectrum, we obtain

$$E_R/E_0 = P_0(l_0 - l_{\text{Si}}) T_{0,\text{Si}} P_{\text{Si}}(l_{\text{Si}}) T_{\text{Si},0}, \quad (\text{B.11})$$

where the indexes 0 and Si correspond to the free space and the HRFZ-Si medium; l_0 and l_{Si} are the total length of the THz beam path and the thickness of the HRFZ-Si substrate, respectively; $T_{0,\text{Si}}(\nu)$ and $T_{\text{Si},0}(\nu)$ are the transmission coefficients for the respective interfaces (between the free space and the HRFZ-Si), defined by Eq. (B.9); and $P_0(\nu, z)$ and $P_{\text{Si}}(\nu, z)$ are operators describing the THz wave propagation in the free space and the HRFZ-Si, respectively, as given by the exponential factor in Eq. (B.10).

As shown in Fig. 5.3, for the sample spectrum we take into account the contribution of the ballistic THz pulse (1) and the satellite pulses (2 and 3), caused by the multiple THz wave

reflection in the ice films. This yields the following equation:

$$\begin{aligned}
 E_S/E_0 = & P_0 (l_0 - l_{Si} - l_{CO,I} - l_{CO,II}) T_{0,CO} P_{CO} (l_{CO,I}) \\
 & \times T_{CO,Si} P_{Si} (l_{Si}) T_{Si,CO} P_{CO} (l_{CO,II}) T_{CO,0} \\
 & \times \left[1 + R_{CO,Si} P_{CO}^2 (l_{CO,I}) R_{CO,0} \right. \\
 & \left. + R_{CO,0} P_{CO}^2 (l_{CO,II}) R_{CO,Si} \right],
 \end{aligned} \tag{B.12}$$

where the summation terms in the brackets correspond to the wavelets 1, 2, and 3; $l_{CO,I}$ and $l_{CO,II}$ stand for thicknesses of the first and second ice films; $R_{CO,Si}(\nu)$ and $R_{CO,0}(\nu)$ are the transmission coefficients for the respective interfaces, see Eq. (B.9); the definition of the remaining factors (P and T) is similar to that in Eqs. (B.11). We point out that the complex amplitudes (E) and all factors (T , R , and P) in Eq. (B.11) and (B.12) are frequency-dependent. Equations (B.11) and (B.12) form a basis for the reconstruction of the THz dielectric response of ices.

The reconstruction is performed via the following minimization procedure:

$$n(\nu) = \operatorname{argmin}_{n(\nu)} [\Phi(n(\nu), \nu)], \tag{B.13}$$

where argmin is an operator which determines the minimum argument of the vector error functional Φ . The latter is formed from the complex theoretical T_{Th} and experimental T_{Exp} transfer functions

$$\Phi(n(\nu), \nu) = \left(\begin{array}{c} |T_{Th}(n, \nu)| - |T_{Exp}(\nu)| \\ \phi[T_{Th}(n, \nu)] - \phi[T_{Exp}(\nu)] \end{array} \right), \tag{B.14}$$

where $|\dots|$ and $\phi[\dots]$ are the absolute values and phases of the complex functions, respectively.

We define the theoretical transfer function T_{Th} as the sample spectrum (Eq. B.12) normalized by the reference spectrum (Eq. B.11)

$$\begin{aligned}
 T_{Th} = & \frac{T_{0,CO} T_{CO,Si} T_{Si,CO} T_{CO,0}}{T_{0,Si} T_{Si,0}} \\
 & \times P_{CO} (l_{CO,I} + l_{CO,II}) P_0 (-l_{CO,I} - l_{CO,II}) \\
 & \times \left[1 + R_{CO,Si} P_{CO}^2 (l_{CO,I}) R_{CO,0} \right. \\
 & \left. + R_{CO,0} P_{CO}^2 (l_{CO,II}) R_{CO,Si} \right].
 \end{aligned} \tag{B.15}$$

Considering all reflection and transmission operators in Eq. (B.10), we note that T_{Th} depends only on the refractive index of the HRFZ-Si substrate n_{Si} , which is known a priori and on the parameters of the CO ice to be determined; it excludes the contribution of several factors, such as the unknown complex amplitude of the TDS source $E_0(\nu)$, the unknown total length of the THz beam path l_0 , and, finally, the thickness of the HRFZ-Si substrate l_{Si} , which is known, too, but can slightly vary owing to angular deviations of the substrate during the vacuum chamber assembling.

The experimental transfer function T_{Exp} is calculated in a similar manner, relying on the Fourier spectra of the experimental sample E_S and reference E_R waveforms (after applying the Tukey apodization),

$$T_{Exp} = \frac{E_S}{E_R}. \tag{B.16}$$

We note that all the functions and operators in the theoretical and experimental transfer functions are frequency-dependent, and both transfer functions take into account only the ballistic pulses of the reference and sample waveforms, as well as the first and second ice-related satellite pulses of the sample waveform.

By introducing equal confidence intervals for the refractive index n' and the amplitude absorption coefficient α , as $[n'_{\text{init}} - \Delta n', n'_{\text{init}} + \Delta n']$ and $[0, \alpha_{\text{max}}]$ with $\Delta n' = 0.25$ and $\alpha_{\text{max}} = 15 \text{ cm}^{-1}$, we use the non-linear trust region approach (Coleman & Li 1996) to reconstruct the THz dielectric response of the CO ice in the spectral operation range of 0.3 to 2.0 THz.

B.3 Opacity model benchmark

In order to verify the correctness of the machinery employed to calculate the opacity from the dielectric constants, we reproduce the results found by Ossenkopf & Henning (1994) in their Fig. 5, panels a-c, compact grains case. We describe the methodology employed. The results described can be reproduced by running `test_04.py` from the publicly available code¹, while Fig. 5.7 from our paper can be reproduced with `test_05.py`.

B.3.1 Dielectric constants

The complex dielectric functions $\varepsilon' - i\varepsilon''$ of the refractory components are taken from Ossenkopf et al. (1992) (cool oxygen-rich silicates, their Fig. 10) and from Preibisch et al. (1993) (amorphous carbon, their Table 1), while ice is assumed to be a $\text{H}_2\text{O}:\text{CH}_3\text{OH}:\text{CO}:\text{NH}_3 = 100:10:1:1$ mixture at 10 K from Hudgins et al. (1993) (their Table 2A).

For the aims of this work we need to extrapolate the ice data relative to the $\text{H}_2\text{O}:\text{CH}_3\text{OH}:\text{CO}:\text{NH}_3 = 100:10:1:1$ mixture to longer wavelengths, as done by Ossenkopf & Henning (1994). First we fit the last 45 data points² of the imaginary part (i.e. approximately $71 - 194 \mu\text{m}$) with a $f(\lambda) \propto \lambda^{-1}$ function (Ossenkopf, priv. comm.), and we use this to extrapolate ε'' with 200 linearly spaced wavelength points, in the range $71 - 800 \mu\text{m}$. To retrieve the real part of ε at each $\omega = 2\pi c\lambda^{-1}$ point, we apply the Kramers-Kronig (e.g. Bohren & Huffman 1983) relations in the discrete form

$$\varepsilon'(\omega) = 1 + \frac{2}{\pi} \Omega(\omega), \quad (\text{B.17})$$

with $\Omega(\omega)$ the discrete integral over the positive frequency ranges using the composite trapezoidal rule with the integrand $\frac{\varepsilon''(\omega_i)\omega_i}{\omega_i^2 - \omega^2}$, and excluding ω , where the denominator of the argument vanishes (i.e. the Cauchy principal value of the corresponding finite integral).

After the extrapolation, the ice dielectric functions are modified by mixing spherical inclusions of amorphous carbon using the Bruggeman effective medium approximation (Bruggeman 1935), with a volume filling fraction of 0.11 and 0.013 for the thin and the thick ice cases, respectively.

¹https://bitbucket.org/tgrassi/compute_qabs, commit: 8c0812f

²This number is chosen manually to select the λ^{-1} decaying part of the data after the last available resonance.

B.3.2 Absorption coefficients

The absorption efficiency $Q_{abs}(\lambda, a)$ is function of the wavelength and grain size a , and computed with the routine `BHMIE.PY` for the bare grains³ and with `BHCOAT.PY` for the coated grains⁴, both from Bohren & Huffman (1983). In Ossenkopf & Henning (1994) there are three cases: bare grains without ice; thin ice, which has a volume ratio of $V = 0.5$; and thick ice, where $V = 4.5$. The radius of the refractory core a and the fraction V determine the radius of the mantle $a_{coat} = a(V + 1)^{1/3}$.

B.3.3 Opacities

With Q_{abs} it is possible to retrieve the opacities averaged on the grain size distribution $\varphi(a)$ as

$$\kappa(\lambda) = \frac{\pi}{C} \int_{a_{min}^{coat}}^{a_{max}^{coat}} \varphi(a) a^2 Q(\lambda, a) da, \quad (\text{B.18})$$

where a_{min}^{coat} to a_{max}^{coat} is the range in which the size distribution is valid including coating, and

$$C = \frac{4}{3} \pi \rho_0 \int_{a_{min}}^{a_{max}} \varphi(a) a^3 da, \quad (\text{B.19})$$

where a_{min} to a_{max} is the range where the size distribution is valid, but considering only the refractory material, i.e. silicates or carbonaceous dust.

Ossenkopf & Henning (1994) assume $a_{min} = 5 \times 10^{-7}$ cm, $a_{max} = 2.5 \times 10^{-5}$ cm, $\rho_0 = 2.9$ g cm⁻³ (silicates) and $\rho_0 = 2$ g cm⁻³ (amorphous carbon), and $\varphi(a) = a^{-3.5}$.

The total opacity is $\kappa_{tot}(\lambda) = 0.678\kappa_{Si}(\lambda) + 0.322\kappa_{AC}(\lambda)$, where the two terms are, respectively, the silicates and carbonaceous opacities including ice coating, and the two coefficients are calculated from the volume ratio discussed in Sect. 3.1 of Ossenkopf & Henning (1994). In particular, Ossenkopf & Henning assume a volume ratio of the refractory components $V_{AC}/V_{Si} = 0.69$ (their Sect. 3.1), which can be converted into the corresponding mass ratio $M_{AC}/M_{Si} = 0.4758$ using the relation $M_i = \rho_i V_i$, where ρ_i are the bulk densities of the two refractory components (being in Ossenkopf & Henning the opacity defined per unit mass of the refractory material), so that $\kappa_{tot} = (M_{AC}\kappa_{AC} + M_{Si}\kappa_{Si})/(M_{AC} + M_{Si})$.

³<http://scatterlib.wikidot.com/mie>

⁴Adapted here from the FORTRAN version at <http://scatterlib.wikidot.com/coated-spheres>.

Bibliography

- Allodi, M. A., Ioppolo, S., Kelley, M. J., McGuire, B. A., & Blake, G. A. 2014, *Phys. Chem. Chem. Phys.*, 16, 3442
- Anderson, A. & Leroi, G. E. 1966, *J. Chem. Phys.*, 45, 4359
- Auston, D. H. 1975, *Applied Physics Letters*, 26, 101
- Ayotte, P., Smith, R. S., Stevenson, K. P., et al. 2001, *Journal of Geophysical Research: Planets*, 106, 33387
- Bahr, S., Toubin, C., & Kempter, V. 2008, *J. Chem. Phys.*, 128, 134712
- Bar-Nun, A., Dror, J., Kochavi, E., & Laufer, D. 1987, *Phys. Rev. B*, 35, 2427
- Baratta, G. A. & Palumbo, M. E. 1998, *Journal of the Optical Society of America A: Optics and Image Science, and Vision*, 15, 3076
- Baratta, G. A. & Palumbo, M. E. 2017, *A&A*, 608, A81
- Bates, J. 1978, *Comput. Math. Appl.*, 4, 73
- Bergin, E. A., Melnick, G. J., Stauffer, J. R., et al. 2000, *The Astrophysical Journal Letters*, 539, L129
- Bernstein, M. P. & Sandford, S. A. 1999, *Spectrochimica Acta Part A: Molecular Spectroscopy*, 55, 2455
- Bieler, A., Altwegg, K., Balsiger, H., et al. 2015, *Nature*, 526, 678
- Bizzocchi, L., Caselli, P., Spezzano, S., & Leonardo, E. 2014, *A&A*, 569, A27
- Bohren, C. F. & Huffman, D. R. 1983, *Absorption and scattering of light by small particles* (Wiley)
- Boogert, A. A., Gerakines, P. A., & Whittet, D. C. 2015, *Annu. Rev. Astron. Astrophys.*, 53, 541
- Born, M. & Wolf, E. 1980, *Principles of Optics*. 6th Edition (UK: Pergamon Press)
- Bottinelli, S., Boogert, A. C. A., Bouwman, J., et al. 2010, *ApJ*, 718, 1100

- Bouwman, J., Ludwig, W., Awad, Z., et al. 2007, *A&A*, 476, 995
- Breukers, R. J. L. H. 1991, PhD thesis, Univ. of Leiden
- Bruggeman, D. A. G. 1935, *Annalen der Physik*, 416, 636
- Burke, D. J., Wolff, A. J., Edridge, J. L., & Brown, . A. 2008, *Phys. Chem. Chem. Phys.*, 10, 4956
- Carty, D., Goddard, A., Köhler, S. P. K., Sims, I. R., & Smith, I. W. M. 2006, *The Journal of Physical Chemistry A*, 110, 3101, pMID: 16509632
- Caselli, P., Keto, E., Bergin, E. A., et al. 2012, *ApJ*, 759, L37
- Caselli, P., Pineda, J. E., Sipilä, O., et al. 2021, submitted, *ApJ*
- Caselli, P., Pineda, J. E., Zhao, B., et al. 2019, *ApJ*, 874, 89
- Caselli, P., Stantcheva, T., Shalabiea, O., Shematovich, V. I., & Herbst, E. 2002a, *Planet. Space Sci.*, 50, 1257
- Caselli, P., Walmsley, C. M., Tafalla, M., Dore, L., & Myers, P. C. 1999, *ApJ*, 523, L165
- Caselli, P., Walmsley, C. M., Zucconi, A., et al. 2002b, *ApJ*, 565, 344
- Cazaux, S., Minissale, M., Dulieu, F., & Hocuk, S. 2016, *A&A*, 585, A55
- Cernicharo, J., Cabezas, C., Agúndez, M., et al. 2021, *A&A*, 648, L3
- Chacón-Tanarro, A., Caselli, P., Bizzocchi, L., et al. 2019, *A&A*, 622, A141
- Chuang, K.-J., Fedoseev, G., Qasim, D., et al. 2018, *ApJ*, 853, 102
- Ciaravella, A., Muñoz Caro, G. M., Jiménez-Escobar, A., et al. 2020, *Proc. Natl. Acad. Sci. U.S.A.*, 117, 16149
- Coleman, T. & Li, Y. 1996, *SIAM Journal on Optimization*, 6, 418
- Collings, M., Dever, J., Fraser, H., & McCoustra, M. 2003, *Astrophysics and Space Science*, 285, 63
- Collings, M. P., Anderson, M. A., Chen, R., et al. 2004, *MNRAS*, 354, 1133
- Collings, M. P., Dever, J. W., & McCoustra, M. R. S. 2005, *Chemical Physics Letters*, 415, 40
- Collings, M. P., Dever, J. W., & McCoustra, M. R. S. 2014, *Phys. Chem. Chem. Phys.*, 16, 3479
- Colthup, N. B., Daly, L. H., & Wiberley, S. E. 1990, *Introduction to Infrared and Raman Spectroscopy (Third Edition)*, third edition edn. (San Diego: Academic Press)

- Cooke, I. R., Öberg, K. I., Fayolle, E. C., Peeler, Z., & Bergner, J. B. 2018, *ApJ*, 852, 75
- Crapsi, A., Caselli, P., Walmsley, M. C., & Tafalla, M. 2007, *A&A*, 470, 221
- Crapsi, A., Devries, C. H., Huard, T. L., et al. 2005, *A&A*, 439, 1023
- Cuppen, H. M. & Herbst, E. 2007, *ApJ*, 668, 294
- Dame, T. M., Hartmann, D., & Thaddeus, P. 2001, *ApJ*, 547, 792
- Dartois, E. 2006, *A&A*, 445, 959
- Dartois, E., Chabot, M., Bacmann, A., et al. 2020, *A&A*, 634, A103
- Dartois, E., Schutte, W., Geballe, T. R., et al. 1999, *A&A*, 342, L32
- Davidsson, J. & Stenholm, L. G. 1990, *A&A*, 230, 504
- Dawes, A., Mason, N. J., & Fraser, H. J. 2016, *Phys. Chem. Chem. Phys.*, 18, 1245
- D’Hendecourt, L. B. & Allamandola, L. J. 1986, *A&A*, 64, 453
- Dickey, J. M. & Lockman, F. J. 1990, *Annu. Rev. Astron. Astrophys.*, 28, 215
- Dohnálek, Z., Kimmel, G. A., Ayotte, P., Smith, R. S., & Kay, B. D. 2003, *J. Chem. Phys.*, 118, 364
- Dulieu, F., Amiaud, L., Congiu, E., et al. 2010, *A&A*, 512, A30
- Dutrey, A., Guilloteau, S., Prato, L., et al. 1998, *A&A*, 338, L63
- Ehrenfreund, P., Boogert, A. C. A., Gerakines, P. A., Tielens, A. G. G. M., & van Dishoeck, E. F. 1997, *A&A*, 328, 649
- Ehrenfreund, P., Breukers, R., D’Hendecourt, L., & Greenberg, J. M. 1992, *A&A*, 260, 431
- Ehrenfreund, P., Dartois, E., Demyk, K., & D’Hendecourt, L. 1998, *A&A*, 339, L17
- Ehrenfreund, P., Gerakines, P. A., Schutte, W. A., van Hemert, M. C., & van Dishoeck, E. F. 1996, *A&A*, 312, 263
- Ehrenfreund, P., Kerkhof, O., Schutte, W. A., et al. 1999, *A&A*, 350, 240
- Ehrenfreund, P. & van Dishoeck, E. 1998, *AdSpR*, 21, 15
- Ewen, H. I. & Purcell, E. M. 1951, *Nature*, 168, 356
- Fraser, H. J. 2004, in *The Dense Interstellar Medium in Galaxies*, ed. S. Palfzner, C. Kramer, C. Straubmeier, & A. Heithausen (Berlin, Heidelberg: Springer Berlin Heidelberg), 491–496

- Fraser, H. J., Collings, M. P., Dever, J. W., & McCoustra, M. R. S. 2004, *MNRAS*, 353, 59
- Gálvez, O., Ortega, I. K., Maté, B., et al. 2007, *A&A*, 472, 691
- Garrod, R. T., Vasyunin, A. I., Semenov, D. A., Wiebe, D. S., & Henning, T. 2009, *ApJ*, 700, L43
- Gavdush, A. A., Chernomyrdin, N., Malakhov, K., et al. 2019, *Journal of Biomedical Optics*, 24, 027001
- Gerakines, P. A. & Hudson, R. L. 2015, *The Astrophysical Journal*, 808, L40
- Gerakines, P. A., Schutte, W. A., Greenberg, J. M., & van Dishoeck, E. F. 1995, *A&A*, 296, 810
- Gerlich, D., Herbst, E., & Roueff, E. 2002, *Planetary and Space Science*, 50, 1275, special issue on Deuterium in the Universe
- Giuliano, B. M., Escribano, R. M., Martín-Doménech, R., Dartois, E., & Muñoz Caro, G. M. 2014, *A&A*, 565, A108
- Giuliano, B. M., Gavdush, A. A., Müller, B., et al. 2019, *A&A*, 629, A112
- Giuliano, B. M., Martín-Doménech, R., Escribano, R. M., Manzano-Santamaría, J., & Muñoz Caro, G. M. 2016, *A&A*, 592, A81
- Givan, A., Loewenschuss, A., & Nielsen, C. J. 1997, *J. Phys. Chem. B*, 101, 8696
- Goldsmith, P. F., Liseau, R., Bell, T. A., et al. 2011, *ApJ*, 737, 96
- Goldsmith, P. F., Melnick, G. J., Bergin, E. A., et al. 2000, *ApJ*, 539, L123
- Goto, M., Vasyunin, A. I., Giuliano, B. M., et al. 2021, *A&A*, 651, A53
- Griffiths, P. & de Haseth, J. 1986, *Fourier Transform Infrared Spectroscopy* (New York, NY, USA: John Wiley + Sons)
- Hagen, W., Tielens, A., & Greenberg, J. 1981, *Chem. Phys.*, 56, 367
- Halliday, D., Resnick, R., & Walker, J. 2010, *Fundamentals of Physics*, Halliday & Resnick Fundamentals of Physics (John Wiley & Sons Canada, Limited)
- Hama, T. & Watanabe, N. 2013, *Chem. Rev.*, 113, 8783
- Harris, F. J. 1978, *Proceedings of the IEEE*, 66, 51
- Hasegawa, T. I. & Herbst, E. 1993, *MNRAS*, 261, 83
- He, J., Emtiaz, S., Boogert, A., & Vidali, G. 2018a, *ApJ*, 869, 41
- He, J., Emtiaz, S., & Vidali, G. 2018b, *ApJ*, 863, 156

- He, J., Emtiaz, S. M., & Vidali, G. 2017, *ApJ*, 837, 65
- He, J., Emtiaz, S. M., & Vidali, G. 2017, *ApJ*, 851, 104
- He, J. & Vidali, G. 2018, *MNRAS*, 473, 860
- Herbst, E. & Millar, T. J. 2008, *The Chemistry of Cold Interstellar Cloud Cores*, I. W. M. Smith edn. (Imperial College Press), 1–54
- Herrero, V. J., Gálvez, Ó., Maté, B., & Escribano, R. 2010, *Phys. Chem. Chem. Phys.*, 12, 3164
- HI4PI Collaboration:, Ben Bekhti, N., Flöer, L., et al. 2016, *A&A*, 594, A116
- Hudgins, D. M., Sandford, S. A., Allamandola, L. J., & Tielens, A. G. G. M. 1993, *ApJS*, 86, 713
- Ioppolo, S., Cuppen, H. M., Romanzin, C., van Dishoeck, E. F., & Linnartz, H. 2008, *ApJ*, 686, 1474
- Ioppolo, S., McGuire, B. A., Allodi, M. A., & Blake, G. A. 2014, *Faraday Discuss.*, 168, 461
- Ioppolo, S., van Boheemen, Y., Cuppen, H. M., van Dishoeck, E. F., & Linnartz, H. 2011, *MNRAS*, 413, 2281
- Ivlev, A. V., Padovani, M., Galli, D., & Caselli, P. 2015, *ApJ*, 812, 135
- Jiang, G. J., Person, W. B., & Brown, K. G. 1975, *J. Chem. Phys.*, 62, 1201
- Jiménez-Serra, I., Vasyunin, A. I., Caselli, P., et al. 2016, *ApJ*, 830, L6
- Jing, D., He, J., Brucato, J. R., et al. 2012, *ApJ*, 756, 98
- Kalberla, P. M. W., Burton, W. B., Hartmann, D., et al. 2005, *A&A*, 440, 775
- Kawase, K., Sato, M., Taniuchi, T., & Ito, H. 1996, *Applied Physics Letters*, 68, 2483
- Keeney, B. A., Stern, S. A., A’Hearn, M. F., et al. 2017, *MNRAS*, 469, S158
- Keto, E. & Caselli, P. 2008, *ApJ*, 683, 238
- Keto, E. & Caselli, P. 2010, *MNRAS*, 402, 1625
- Keto, E., Caselli, P., & Rawlings, J. 2015, *MNRAS*, 446, 3731
- Kiessling, J., Breunig, I., Schunemann, P. G., Buse, K., & Vodopyanov, K. L. 2013, *New Journal of Physics*, 15, 105014
- Klessen, R. S. & Glover, S. C. O. 2016, *Saas-Fee Advanced Course*, 43, 85

- Komandin, G. A., Chuchupal, S. V., Lebedev, S. P., et al. 2013, *IEEE Transactions on Terahertz Science and Technology*, 3, 440
- Larsson, B., Liseau, R., Pagani, L., et al. 2007, *A&A*, 466, 999
- Latychevskaia, T. 2019, *Appl. Opt.*, 58, 3597
- Lee, Y.-S. 2009, *Principles of Terahertz Science and Technology* (New York, NY, USA: Springer)
- Leger, A., Jura, M., & Omont, A. 1985, *A&A*, 144, 147
- Liseau, R., Goldsmith, P. F., Larsson, B., et al. 2012, *A&A*, 541, A73
- Loeffler, M. J., Baratta, G. A., Palumbo, M. E., Strazzulla, G., & Baragiola, R. A. 2005, *A&A*, 435, 587
- Martin, P. C. 1967, *Physical Review*, 161, 143
- Mastrapa, R. M., Sandford, S. A., Roush, T. L., Cruikshank, D. P., & Dalle Ore, C. M. 2009, *ApJ*, 701, 1347
- Maté, B., Gálvez, Ó., Herrero, V. J., & Escribano, R. 2009, *ApJ*, 690, 486
- Maté, B., Gálvez, Ó., Martín-Llorente, B., et al. 2008, *J. Phys. Chem. A*, 112, 457
- McGuire, B. A., Ioppolo, S., Allodi, M. A., & Blake, G. A. 2016, *Physical Chemistry Chemical Physics*, 18, 20199
- Millar, T. J. 1992, in *Astrochemistry of Cosmic Phenomena*, ed. P. D. Singh (Dordrecht: Springer Netherlands), 211–215
- Millar, T. J. 2005, *Astron. Geophys.*, 46, 2.29
- Minissale, M., Dulieu, F., Cazaux, S., & Hocuk, S. 2016, *A&A*, 585, A24
- Miyauchi, N., Hidaka, H., Chigai, T., et al. 2008, *Chemical Physics Letters*, 456, 27
- Mokrane, H., Chaabouni, H., Accolla, M., et al. 2009, *ApJL*, 705, L195
- Morse, M. D. 1996, in *Experimental Methods in the Physical Sciences*, Vol. 29, Atomic, Molecular, and Optical Physics: Atoms and Molecules, ed. F. Dunning & R. G. Hulet (Academic Press), 21–47
- Mousavipour, S. H. & Saheb, V. 2007, *Bull. Chem. Soc. Jpn.*, 80, 1901
- Mousis, O., Ronnet, T., Brugger, B., et al. 2016, *ApJL*, 823, L41
- Müller, B., Giuliano, B. M., Bizzocchi, L., Vasyunin, A. I., & Caselli, P. 2018, *A&A*, 620, A46
- Müller, B., Giuliano, B. M., Goto, M., & Caselli, P. 2021, *A&A*, 652, A126

- Nyquist, H. 1928, *Transactions of the American Institute of Electrical Engineers*, 47, 617
- Oba, Y., Miyauchi, N., Hidaka, H., et al. 2009, *ApJ*, 701, 464
- Oba, Y., Tomaru, T., Lamberts, T., Kouchi, A., & Watanabe, N. 2018, *Nature Astronomy*, 2, 228
- Oba, Y., Watanabe, N., Hama, T., et al. 2012, *ApJ*, 749, 67
- Öberg, K. I. 2016, *Chem. Rev.*, 116, 9631
- Öberg, K. I., Boogert, A. C. A., Pontoppidan, K. M., et al. 2011, *ApJ*, 740, 109
- Öberg, K. I., Fayolle, E. C., Cuppen, H. M., van Dishoeck, E. F., & Linnartz, H. 2009, *A&A*, 505, 183
- Öberg, K. I., Fraser, H. J., Boogert, A. C. A., et al. 2007, *A&A*, 462, 1187
- Ohashi, N., Lee, S. W., Wilner, D. J., & Hayashi, M. 1999, *ApJ*, 518, L41
- Ossenkopf, V. & Henning, T. 1994, *A&A*, 291, 943
- Ossenkopf, V., Henning, T., & Mathis, J. S. 1992, *A&A*, 261, 567
- Palumbo, E. M., Baratta, G. A., Collings, M. P., & McCoustra, M. R. S. 2006, *Phys. Chem. Chem. Phys.*, 8, 279
- Palumbo, M. E. 2005, *Journal of Physics: Conference Series*, 6, 211
- Palumbo, M. E. 2006, *A&A*, 453, 903
- Palumbo, M. E. & Baratta, G. A. 2000, *A&A*, 361, 298
- Palumbo, M. E., Baratta, G. A., Leto, G., & Strazzulla, G. 2010, *J. Mol. Struct.*, 972, 64
- Palumbo, M. E., Geballe, T. R., & Tielens, A. G. G. M. 1997, *ApJ*, 479, 839
- Peiponen, K.-E. & Zeitler, J. A. 2017, in *Encyclopedia of Spectroscopy and Spectrometry (Third Edition)*, third edition edn., ed. J. C. Lindon, G. E. Tranter, & D. W. Koppenaal (Oxford: Academic Press), 439–443
- Penteado, E. M., Boogert, A. C. A., Pontoppidan, K. M., et al. 2015, *MNRAS*, 454, 531
- Perotti, G., Rocha, W. R. M., Jørgensen, J. K., et al. 2020, *A&A*, 643, A48
- Persson, M. V. 2014, *Current view of protostellar evolution (ENG)*
- Pontoppidan, K. M., Fraser, H. J., Dartois, E., et al. 2003, *A&A*, 408, 981
- Potapov, A., Jäger, C., & Henning, T. 2018, *ApJ*, 865, 58

- Prasad, S. S. & Tarafdar, S. P. 1983, *ApJ*, 267, 603
- Preibisch, T., Ossenkopf, V., Yorke, H. W., & Henning, T. 1993, *A&A*, 279, 577
- Preu, S., Döhler, G. H., Malzer, S., Wang, L. J., & Gossard, A. C. 2011, *Journal of Applied Physics*, 109, 061301
- Pupeza, I., Wilk, R., & Koch, M. 2007, *Optics Express*, 15, 4335
- Romanzin, C., Ioppolo, S., Cuppen, H. M., van Dishoeck, E. F., & Linnartz, H. 2011, *J. Chem. Phys.*, 134, 084504
- Ron, A. & Schnepf, O. 1967, *J. Chem. Phys.*, 46, 3991
- Sandford, S. A. & Allamandola, L. J. 1990, *ApJ*, 355, 357
- Sandford, S. A. & Allamandola, L. J. 1993, *ApJ*, 417, 815
- Scibelli, S. & Shirley, Y. 2020, *ApJ*, 891, 73
- Sipilä, O., Caselli, P., & Harju, J. 2019, *A&A*, 631, A63
- Snels, M., Horká-Zelenková, V., Hollenstein, H., & Quack, M. 2011, in *Handbook of High-resolution Spectroscopy*, Vol. 2 (John Wiley & Sons, Ltd.), 1021–1067
- Stahler, S. W. & Palla, F. 2004, *The Formation of Stars* (WILEY-VCH)
- Tafalla, M., Mardones, D., Myers, P. C., et al. 1998, *ApJ*, 504, 900
- Tafalla, M., Myers, P. C., Caselli, P., & Walmsley, C. M. 2004, *A&A*, 416, 191
- Tafalla, M., Santiago-García, J., Myers, P. C., et al. 2006, *A&A*, 455, 577
- Taquet, V., Furuya, K., Walsh, C., & van Dishoeck, E. F. 2016, *MNRAS*, 462, 99
- Tielens, A. G. G. M. 2005, *The Physics and Chemistry of the Interstellar Medium* (Cambridge University Press)
- Tielens, A. G. G. M. & Hagen, W. 1982, *A&A*, 114, 245
- Tukey, J., Cleveland, W. S., & Brillinger, D. R. 1986, *The Collected Works of John W. Tukey. Volume I: Time Series, 1949-1964* (Wadsworth Statistics/Probability Series) 1st Edition (Wadsworth Advanced Books & Software)
- Ungerechts, H. & Thaddeus, P. 1987, *ApJS*, 63, 645
- Urso, R. G., Scirè, C., Baratta, G. A., Compagnini, G., & Palumbo, M. E. 2016, *A&A*, 594, A80
- van Broekhuizen, F. A., Groot, I. M. N., Fraser, H. J., van Dishoeck, E. F., & Schlemmer, S. 2006, *A&A*, 451, 723

-
- van Exter, M., Fattinger, C., & Grischkowsky, D. 1989, *Applied Physics Letters*, 55, 337
- Vandenbussche, B., Ehrenfreund, P., Boogert, A., et al. 1999, *A&A*, 346, L57
- Vastel, C., Quénard, D., Le Gal, R., et al. 2018, *MNRAS*, 478, 5519
- Vasyunin, A. & Herbst, E. 2013, *ApJ*, 762
- Vasyunin, A. I., Caselli, P., Dulieu, F., & Jiménez-Serra, I. 2017, *ApJ*, 842, 33
- Viti, S., Roueff, E., Hartquist, T. W., des Forêts, G. P., & Williams, D. A. 2001, *A&A*, 370, 557
- Ward-Thompson, D., Motte, F., & Andre, P. 1999, *MNRAS*, 305, 143
- Warren, S. G. & Brandt, R. E. 2008, *J. Geophys. Res.*, 113, D14220
- Williams, J. P., Myers, P. C., Wilner, D. J., & Di Francesco, J. 1999, *ApJ*, 513, L61
- Wolff, A. J., Carlstedt, C., & Brown, W. A. 2007, *J. Phys. Chem. C*, 111, 5990
- Woodall, J., Agúndez, M., Markwick-Kemper, A. J., & Millar, T. J. 2007, *A&A*, 466, 1197
- Yamamoto, S. 2017, *Introduction to Astrochemistry: Chemical Evolution from Interstellar Clouds to Star and Planet Formation* (Springer)
- Zasowski, G., Kemper, F., Watson, D. M., et al. 2009, *ApJ*, 694, 459
- Zaytsev, K., Gavadush, A., Chernomyrdin, N., & Yurchenko, S. 2015, *IEEE Transactions on Terahertz Science and Technology*, 5, 817
- Zaytsev, K., Gavadush, A., Karasik, V., et al. 2014, *Journal of Applied Physics*, 115, 193105
- Zinth, W. & Zinth, U. 2018, *Optik: Lichtstrahlen – Wellen – Photonen* (De Gruyter)

Acknowledgments

First and foremost I want to thank my supervisor Paola Caselli. Paola, you gave me the possibility to do my PhD in your group and you supported me in any possible way. I have learned so much during my time at the Center for Astrochemical Studies. Thank you for all the fruitful discussions, the shared joy about our research and all the other things that I could never list but nevertheless made my PhD under your supervision unforgettable.

I will forever be grateful to Michela Giuliano. Michela, working with you in the laboratory was one of the very best parts on my long road from my first day in university to the end of my PhD at the CAS group. You have not only taught me all the important things that are fundamental for the laboratory work but it was also a great pleasure to work with you as a person. You were always so incredibly supportive and I will always happily look back to all the work travels as well as the discussions and conversations we had outside of scientific topics.

Thank you, Angie. You literally are the CAS group angel! Wherever you were, laughter was never far away. You were always lending a helping hand and I enjoyed the many joyful conversations that we had!

Members of the CAS group, you are next! First, one thing: You are awesome! Every one of you! You have made my PhD just so so sooo much better. Just where should I start? Thanks go to my office mates. Ana, who in spite of her fear of spiders and spontaneous escape-the-room-actions, was a very pleasant office mate and this is also true for Anna with her calm personality. Vlas, who is one of the funniest guys I ever met. Boy, did we laugh a lot! Especially together with Linda, his better second half.

Spandan, who is such a nice and polite person and Joaquin, who also gave me many happy moments full of laughter. Max, with whom I shared my love for Lord of the Rings, dinosaurs and manga/anime and who gave me the final push to dive into the Star Trek universe. Live long and prosper! Franciele, who is an amiable office mate that I could also share my fondness for anime with. Thank you, my other dear PhD fellows Ash, Carolina, Dome, Elena and Johanna! With you I had as much fun as with every other student at the CAS group.

My happy lunch and afternoon break people! Your list is long and I will for sure forget someone's name to mention because many people went and came during my years at the CAS group! But what I won't forget are you all! Thank you for the so very important and enjoyable social component of working at the MPE! In this regard, I also want to thank Luca who enlightened me together with Michela on many Italian traditions. Luca also taught me some important things in the lab and working with him just like with Alexei and Anton was a great experience.

Thank you, Chris, for many entertaining conversations during the lunch break that really

gave me a good time, Felipe, for the many great movie and show recommendations, Jake, for entertaining conversations about various video games, Pavol, for your delicious Apfelstrudel and my Pokemon-Team Jaime, Victor and Dominique who pulled me away from the screen when I needed a break every now and then. Nooow, this guides me to the "last but not least"! My two dear fellow witches Anika and Dom! We were not only connected by burning clothes, but with you two I had some of the best moments in the CAS group. I will miss our lunch break moments on the beach couch. Everyone who has not been mentioned by name here, please be sure, that you are still in that part of my memories that I greatly enjoy to look back to!

Thank you also to Christian Deysenroth who was always there when we needed something to be improved or repaired in the lab!

I want to thank Andi Burkert and Stella Seitz who have guided me through very important parts of my Bachelor and Master studies.

Thanks go to all my friends who supported me from near and afar. Thank you, Dolly, Lilli and Nora. You are the best! To a great part I am who I am because of you! I love you happy, crazy, endearing bunch. Thank you, Luv, Na and Steffi. Our friendship is so important to me and diving into other worlds, writing our own stories has always immensely helped me to relax after work. Thank you, Nici, for many funny Sunday movie evenings that sent me refreshed to a new working week. And thank you, Sophie, Stefan, Sabrina, Michael, Markus and Meli for the great time at the LMU.

Most importantly I want to thank my family for their enormous support and never ending love. No matter what, you have always been there for me in good and in bad times. Thank you, Papa, until we had to say Goodbye, you have always encouraged me to follow the path that was guided by my curiosity for natural science and especially astronomy. Thank you, Mama, you have always watched my back. I can't even describe how many important things you taught me. I'm so proud to be your and Papa's daughter. Thank you, Christina, please never forget how important you are to me and how much I love you. We not only share so many common interests but we have always known each other inside out and this probably will never change.

Everyone, I cannot express how grateful I am to every single one of you! You have made the past years to one of the best times in my life. Thank you so much! You are my stars down here on Earth so stay as great as you are!

Danksagung

Zuallererst möchte ich meiner Betreuerin Paola Caselli danken. Paola, du hast mir die Gelegenheit gegeben, meine Doktorarbeit in deiner Gruppe zu schreiben und du hast mich in absolut jeder Hinsicht unterstützt. Ich habe so viel in meiner Zeit im Center für astrochemische Studien gelernt. Danke für all die ertragreichen Diskussionen, die geteilte Freude an unserer Forschung und die vielen anderen Dinge, die ich niemals aufzählen könnte, die aber mein Doktorat unter deiner Aufsicht trotzdem unvergesslich gemacht haben.

Ich werde Michela Giuliano für immer dankbar sein. Michela, mit dir im Labor zu arbeiten, war einer der allerbesten Teile meines langen Weges vom ersten Tag in der Universität bis zum Ende meiner Doktorarbeit in der CAS Gruppe. Du hast mir nicht nur all die wichtigen Dinge beigebracht, die fundamental für das Arbeiten im Labor sind, sondern es war auch ein großes Vergnügen mit dir als Mensch zu arbeiten. Du warst immer so unglaublich hilfsbereit und ich werde mich immer gerne an all die Dienstreisen sowie die Diskussionen und Unterhaltungen außerhalb wissenschaftlicher Themen erinnern.

Danke, Angie. Du warst wortwörtlich der Engel der CAS Gruppe. Wo immer du warst, war ein Lachen nicht weit entfernt. Du hast immer eine helfende Hand gereicht und ich habe die vielen fröhlichen Gespräche mit dir immer genossen.

Mitglieder der CAS Gruppe, ihr seid die nächsten! Zuerst, eine Sache: Ihr seid großartig! Jeder einzelne von euch! Ihr habt die Zeit meiner Doktorarbeit so, so, sooo viel besser gemacht. Wo soll ich da nur anfangen? Dank geht an meine Bürogefährten. Ana, die trotz ihrer Angst vor Spinnen und spontanen Flucht-aus-dem-Raum-Aktionen eine sehr angenehme Kollegin war und das gilt auch für Anna mit ihrer ruhigen Art. Vlas, der einer der lustigsten Kerle ist, die ich jemals getroffen habe. Junge, haben wir viel gelacht! Ganz besonders zusammen mit Linda, seiner besseren Hälfte.

Spandan, der eine so freundliche und höfliche Person ist und Joaquin, mit dem ich auch viele Momente voller Lachen hatte. Max, mit dem ich meine Liebe für Herr der Ringe, Dinosaurier und Manga/Anime geteilt habe und der mir den letzten Anstoß gegeben hat, in das Star Trek Universum einzutauchen. Lebe lang und in Frieden! Franciele, die eine liebenswürdige Bürogenossin ist, mit der ich ebenfalls meine Vorliebe für Anime geteilt habe. Danke, meine anderen lieben Doktorandengefährten Ash, Carolina, Dome, Elena und Johanna! Mit euch hatte ich genauso viel Spaß wie mit jedem anderen Studenten in der CAS Gruppe.

Meine fröhlichen Leute der Mittags- und Nachmittagspause! Eure Liste ist lang und ich werde ganz sicher den Namen von jemandem vergessen, weil in meinen Jahren in der CAS Gruppe viele gegangen und gekommen sind. Aber was ich nicht vergessen werde, seid ihr alle!

Danke für die so unglaublich wichtige und genussvolle soziale Note während meiner Arbeit am MPE! Dahingehend will ich auch Luca danken, der mich zusammen mit Michela über viele italienische Traditionen erleuchtet hat. Luca hat mir auch einige wichtige Dinge im Labor beigebracht und mit ihm zu arbeiten war genauso wie im Fall von Alexei und Anton eine großartige Erfahrung.

Danke, Chris, für viele unterhaltsame Gespräche während der Mittagspause, die mir eine wirklich gute Zeit beschert haben, Felipe, für die vielen tollen Film- und Serienempfehlungen, Jake, für unterhaltsame Gespräche über Videospiele, Pavol, für deine köstlichen Apfelstrudel und mein Pokemon-Team Jaime, Victor und Dominique, die mich vom Bildschirm weggezogen haben, wenn ich hin und wieder mal eine Pause gebraucht hab. Nuuun, das führt mich zum "zu guter Letzt"! Meine zwei lieben Hexengefährtnen Anika und Dom! Wir waren nicht nur durch brennende Kleidungsstücke miteinander verbunden, sondern mit euch beiden hatte ich einige der besten Momente in der CAS Gruppe. Ich werde unsere Mittagspause-Momente auf der Strandcouch vermissen. Jeder, der hier nicht namentlich erwähnt wurde, bitte seid versichert, dass ihr trotzdem in dem Teil meiner Erinnerungen seid, an den ich gerne zurückdenke!

Danke auch an Christian Deysenroth, der immer da war, wenn etwas im Labor verbessert oder repariert werden musste!

Ich möchte auch Andi Burkert und Stella Seitz danken, die mich durch wichtige Teile meiner Bachelor- und Masterstudien geleitet haben.

Dank geht an all meine Freunde, die mich von nah und fern unterstützt haben. Danke, Dolly, Lilli und Nora. Ihr seid die besten! Zu einem großen Teil bin ich, wer ich bin, dank euch! Ich liebe euch fröhlichen, verrückten, bezaubernden Haufen. Danke, Luv, Na und Steffi. Unsere Freundschaft ist mir so wichtig und in andere Welten zu tauchen und unsere eigenen Geschichten zu schreiben hat mir sehr dabei geholfen, mich nach der Arbeit zu entspannen. Danke, Nici für viele lustige Sonntag-Filmabende, die mich erholt in eine neue Arbeitswoche geschickt haben. Danke, Sophie, Stefan, Sabrina, Michael, Markus und Meli für die tolle Zeit an der LMU.

Am allerwichtigsten will ich meiner Familie für ihre gewaltige Unterstützung und unendliche Liebe danken. Egal wann, ihr wart sowohl in guten wie auch in schlechten Zeiten immer für mich da. Danke, Papa, bis wir uns voneinander verabschieden mussten, hast du mich immer dazu ermutigt, den Weg zu gehen, den mir meine Wissbegierde für Naturwissenschaften und ganz besonders Astronomie angegeben hat. Danke, Mama, du hast mir immer den Rücken freigehalten. Ich kann nicht ansatzweise beschreiben, wie viele wichtige Dinge du mir beigebracht hast. Ich bin so stolz deine und Papas Tochter zu sein. Danke, Christina, bitte vergiss niemals, wie wichtig du mir bist und wie sehr ich dich liebe. Wir teilen nicht nur viele gemeinsame Interessen, sondern wir haben uns schon immer in- und auswendig gekannt und das wird sich vermutlich auch niemals ändern.

Ihr alle, ich kann nicht beschreiben, wie dankbar ich jedem einzelnen von euch bin! Ihr habt die letzten Jahre zu einer der schönsten Zeiten meines Lebens gemacht. Ich danke euch so sehr! Ihr seid meine Sterne hier unten auf der Erde, also bleibt so großartig, wie ihr seid!